Synthesis and spectral investigations of rare earth doped metasilicate phosphor for optoelectronic applications

THESIS

Submitted to

Delhi Technological University

In partial fulfilment of the requirements for the degree of

DOCTOR OF PHILOSOPHY

IN

ENGINEERING PHYSICS

by

Ms. DEEPALI

(Reg. No. 2K18/Ph.D./AP/30)

Under the Supervision
of

Dr. M. JAYASIMHADRI

Assistant Professor

DEPARTMENT OF APPLIED PHYSICS

DELHI TECHNOLOGICAL UNIVERSITY

SHAHBAD DAULATPUR, BAWANA ROAD

DELHI-110 042, INDIA

OCTOBER 2023


To my mummy and papa who always
encourages me and never let me down in
any circumstances

DELHI TECHNOLOGICAL UNIVERSITY

Formerly Delhi College of Engineering
(Govt. of National Capital Territory of Delhi)
Shahbad Daulatpur, Bawana Road, Delhi-110042

CERTIFICATE

This is to certify that the thesis entitled **"Synthesis and spectral investigations of rare earth doped metasilicate phosphor for optoelectronic applications"** is being submitted by ***Ms. Deepali*** with registration no. ***2K18/Ph.D./AP/30*** to Delhi Technological University, Delhi for the award of degree of Doctor of Philosophy in Engineering Physics. The work embodied in this thesis is a record of bonafide research work carried out by me in the Department of Applied Physics, Delhi Technological University, Delhi under the supervision of ***Dr. M. Jayasimhadri***. It is further certified that the work embodied in this thesis has neither been partially nor fully submitted to any other university or institution for the award of any degree or diploma.

Deepali
Research Scholar
Reg. No. **2K18/Ph.D./AP/30**

This is to certify that the above statement made by the candidate is correct to the best of our knowledge.

Dr. M. Jayasimhadri
Supervisor & Assistant professor
Department of Applied Physics
Delhi Technological University
Delhi-110 042, India

Prof. A.S. Rao
Head
Department of Applied Physics
Delhi Technological University
Delhi-110 042, India

ACKNOWLEDGEMENTS

"Gratitude turns what we have into enough, and more. It turns denial into acceptance, chaos into order, confusion into clarity…it makes sense of our past, brings peace for today and creates a vision for tomorrow". ~Melody Beattie

In the above sense of words, I would like to express my sincere gratitude to all who have accompanied me in the successful journey of last five years at Delhi Technological University (DTU) and specifically at Luminescent Materials Research Lab (LMRL). Above all I bow down to the ***Lord Almighty*** *whose grace provided me the wisdom and strength to accomplish my research work with lot of wavering span during this journey. Throughout the course of this work, I encounter God's Grace at every turn, which constantly sharpened my intellect even in times of despair, propelled me ahead and brought unexpected opportunities to my attention.*

I would like to extend my heartfelt and sincere acknowledgement to my supervisor ***Dr. M. Jayasimhadri,*** *Assistant Professor, Department of Applied Physics, DTU, Delhi for his continual assistance and encouragement in my doctoral education and associated research with the constant perseverance, inspiration and insightful remarks. I am really grateful to achieved the opportunity to perform my research under his guidance. His immense knowledge of subject, analytic gaze, farsightedness and tenacity were a constant source of inspiration during the course of my thesis work. He has also encouraged me to be vocal and mingle with research and off-research exposure with ethics.*

The support and direction of many individuals, in addition to my own efforts, play a significant role in the accomplishment of this thesis. I would intend to personally acknowledge everyone who contributed to the successful completion of my journey.

I express reverence towards Honorable Vice Chancellor ***Prof. Yogesh Singh (former) & Prof. Jai Prakash Saini (Current), Prof. Rinku Sharma (Academic Dean- PG) and Prof. A.S. Rao (Head and DRC chairperson),*** *Department of Applied Physics, DTU for providing fundamental infrastructural facilities and timely essential support to carry out the research work. My heartfelt recognitions for* ***Prof. S.C. Sharma,*** *former DRC Chairperson, Department of Applied Physics, DTU, my SRC & DRC committee members for his valuable support and advices,*

I would like to sincerely thank ***Dr. G.A. Basheed (Principal Scientist CSIR-NPL)*** *and his student* ***Ms. Lalita Nehra and Dr. Swapna Koneru*** *(Associate Professor, K.L. University) for providing necessary facilities to carried out the characterization techniques for my research work.*

It's my pleasure to express my deepest regards to ***Prof. A.S. Rao*** *for his candid support and advices to encourage move ahead in future. I owe my sincere gratitude towards all the faculty members of Department of Applied Physics to establish a friendly environment for discussion and conversation associated with research. I would sincerely thank to* ***Mr. Jawed Alam*** *and* ***Mr. Sandeep Mishra****, Advanced Instrumentation Centre (AIC), and other technical and non-technical staff members for their support and cooperation during this tenure.*

To successfully accomplish this expedition, I wish to express my sincere thanks to my former and current labmates, ***Dr. Amit K. Vishwakarma, Dr. Kaushal Jha, Dr. Sumandeep Kaur, Dr. Shankar Subramanian, Dr. Harpreet Kaur, Dr. Mukesh K. Sahu, Mr. Vikas, Mr. Inderjeet Maurya, Ms. Vertika Siwach, Mr. Anupam*** *whose support and company helped me in accomplishment of my thesis. I feel grateful to thank my colleagues from MASRL lab* ***(Mr. Aman Prasad, Mr. Rajat Bajaj, Mrs. Ravita, Ms. Pooja Rohilla, Mr. Mohit Mann, Mrs. Shristi Malik, Ms. Anu, Ms. Sheetal)*** *and other batchmates* ***(Mr. Bhavya Kumar, Ms. Kanika Sharma, Ms. Km. Komal, Mr. Vishal Singh, Ms. Anshu Dahiya, Ms. Megha Sharma, Ms. Anchali Jain)*** *for their immense support. I would also like to thank all other scholars of Department of Applied Physics, Delhi Technological University, Delhi, for their help and advice.*

The love, support, encouragement and blessings from my parents and family gave me the strength and courage to initiate the work and accomplish it with the best of my abilities, With heartful gratitude, respect and love, I express my gratefulness to my grandfather ***Lt. Sh. Jaswant Singh****, grandmother* ***Lt. Smt. Kamlesh****, father* ***Sh. Ramgopal****, mother* ***Smt. Pramila,*** *elder brother* ***Mr. Himanshu Kumar,*** *my extended maternal and paternal family who have always been my pillars of strength and enabled me to maintain positive attitude throughout my research. I would love to share my immense feeling of gratitude to my friends or equivalent to family in just few months* ***Mr. Amol Ahire*** *and* ***Mr. Ritesh Sonje*** *to provide unconditional help and support during my thesis work. I am forever grateful and would thank my beloved family for being there with me during the time of happiness as well as sorrow.*

I wish to express my sincere gratitude towards Delhi Technological University for extending all the necessary facilities and providing financial assistance as a Junior Research Fellowship and Senior Research Fellowship during the period of my Ph.D. course. Finally, I wish to thank one an all for your prompt interventions that made my life more pleasant and meaningful. Thank you all!!

Deepali

LIST OF PUBLICATIONS

Publication from thesis work:

1. **Deepali,** M. Jayasimhadri, "UV excited blue to green emitting Tb^{3+} activated sodium calcium metasilicate color tunable phosphor for luminescent devices" **Luminescence** 37 (2022) 1465. ***(Impact Factor: 2.90)***
2. **Deepali,** M. Jayasimhadri, "Structural and spectroscopic analysis of thermally stable Dy^{3+} activated $Na_4Ca_4Si_6O_{18}$ phosphor for optoelectronic device applications" **Journal of Materials Science: Materials in Electronics** 33 (2022) 19218. ***(Impact Factor: 2.80)***
3. **Deepali,** M. Jayasimhadri, *"*Thermally stable and color-tunable bi-activated (Dy^{3+}/Eu^{3+}) alkaline earth metasilicate phosphor for luminescent **devices*" RSC Advances*** *13 (2023) 21105.* ***(Impact Factor: 3.90)***
4. **Deepali,** M. Jayasimhadri, **"**Effect of sensitizer on the luminescence of thermally stable Eu^{3+} activated metasilicate phosphor for solar cell applications" **Journal of Materials Science: Materials in Electronics** 34 (2023) 1999. ***(Impact Factor: 2.80)***
5. **Deepali,** M. Jayasimhadri, "Structural and photoluminescence features of thermally stable red emitting Pr^{3+} doped sodium calcium metasilicate phosphor for w-LED applications" **Bulletin of Materials Science** (Accepted: In Press, 2023) ***(Impact Factor: 1.80)***

Publications other than thesis work:

1. **Deepali,** Ruchira Bisi, Vandana, Harpreet Kaur**, M. Jayasimhadri, "**Structural and spectroscopic properties of Sm^{3+}-doped $NaBaB_9O_{15}$ phosphor for optoelectronic device applications" **Journal of Materials Science: Materials in Electronics** 32 (2021) 1650-1658. ***(Impact Factor: 2.80).***

2. Animesh Verma, Mukesh K. Sahu, **Deepali,** Mrinal Pandey, P. Koteswara Rao, M. Jayasimhadri. *"*Structural and photoluminescent features of Eu^{3+} activated single phase niobate phosphor for lighting applications" **International Journal of Applied Ceramic Technology** (2023) (Accepted: In Press, 2023). ***(Impact factor: 2.10).***

3. Muskan, Pranjali Sharma, **Deepali,** M. Jayasimhadri, **Exploration of efficient photoluminescence properties of intense green emitting Er^{3+} activated $NaBi(MoO_4)_2$ phosphor for white LED applications" Journal of Materials Research** (Accepted: In Press, 2023). ***(Impact Factor: 2.70).***

ABSTRACT

In the recent era, the usage of conventional light sources such as incandescent and fluorescent bulbs have diminished significantly due to the enormous benefits of solid state lighting (SSL) technology. These conventional sources rely on either heat or discharge of gases and associated with large energy losses due to high temperature and large stokes shifts. Phosphor converted light emitting diodes (pc-LEDs) are strongly acknowledged due to their unprecedented features which include longer lifetime, high efficiency, swift response, affordable, stable and environmentally benign. In general, the pc-LEDs are designed by coating the phosphor on the LED chip and produce the emission output in the desirable spectral region upon specific excitation. On the basis of previously mentioned advantages, SSL based pc-LEDs have emerged as a long-term solution for unceasing advancement of human civilization and will bring about a revolutionary shift in the lighting sector. Especially, white light emitting pc-LEDs (or w-LEDs) have been the most endorsed SSL devices for various indoor and outdoor lighting applications. Moreover, the phosphor based w-LEDs can be fabricated via layering a mixture of red (R), green (G) and blue (B) phosphors over the UV LED chip and coating a yellow emitting phosphor on blue LED chip. However, the former approach lead to inadequacy of reabsorption of blue color by red and green phosphor while later one reflects white light with deteriorated color rendering index (CRI), high correlated color temperature (CCT) and low color saturation due to lack of red color. Thus, the above-mentioned flaws can be eliminated by developing single phase phosphor activated with the combination of bi- or trivalent rare earth ions to produce efficient white light via energy transfer mechanism with improved luminous efficiency, significant CCT and CRI values.

Moreover, phosphor materials possess noteworthy qualities to be employed in versatile applications. One of the most crucial and promising applications is solar cell, which rely on abundant and renewable solar energy to get an electricity. In solar cells, the contribution of phosphor materials has shown prodigious potential to substitute other non-renewable sources of energy. In general, the solar cell efficiency has been limited due to the spectral mismatch between

the incident solar spectrum and spectral response of the solar cell, which mainly arises due to two reasons; (i) transmittance loss and (ii) thermalization loss. Although, these losses can be exceeded by the use of phosphor material as a conversion layer to improve the conversion efficiency of the solar cell. The RE doped phosphor materials are frequently sought for the purpose of transformation of light by means of photon down-conversion (DC) approach. Thus, illuminating high brightness, multimodal spectral region, effective color purity and thermal stability are the implausible features of phosphor materials which encourages them to utilize in solar cell applications to improve the luminous and conversion efficiency, respectively. In general, phosphor materials are essentially associated with the host lattice (inorganic crystal) and an activator ion (luminescent centre) possess excellent chemical, physical, thermal and luminescent properties. Usually, most inorganic hosts are chosen as an effective host lattice since the contribution of effective host is to provide proficient luminescent properties. Among inorganic hosts, silicates have been the preferential choice as they possess good physical, thermal, chemical stability with wide band gap and low thermal expansion coefficient. Also, silicates can be synthesized via physical, physico-chemical and chemical routes at significantly low temperature using economical precursors. Recently, RE doped silicates have been speculated as the most promising contender for w-LED and solar cell applications as they provide proficient luminescent characteristics due to probability of *f-f* transitions in RE ions. By considering above factual advantages, silicates especially metasilicate ($Na_4Ca_4Si_6O_{18}$) phosphors doped with specific RE ions have been studied for w-LEDs and solar cell applications. Indeed, the incorporation of suitable RE ions into host ($Na_4Ca_4Si_6O_{18}$) has yielded the favourable results for both proposed applications.

Based on the detailed analysis of thermal, structural, morphological and luminescent properties, the outcomes of the research undertaken to achieve research objectives has been organized in various chapters. The brief summary of each chapter is outlined below:

Chapter 1 preferably summarize the introduction of basic terminology, brief history and recent development, challenges and influential opportunities in w-LEDs and solar cell

applications. This chapter focused on the fundamental concepts of luminescence and their classifications. The luminescence mechanisms appear in the RE ions and luminescent properties of RE ions have been described in detail. The chapter outlines the brief explanation about the targeted applications, challenges, prerequisites and alternative strategies to improve the materials quality. This chapter also describes various parameters such as chromaticity coordinates, CCT, color purity and activation energy, which are necessarily required to analyse the luminescence performance of the synthesized phosphor. Moreover, importance of the selection of host and activator ions in the current research work have been discussed. Finally, the objectives of the thesis have been framed on the basis of literature review.

Chapter 2 makes a comprehensive discussion on the synthesis technique chosen to synthesize single phase sodium calcium silicate ($Na_4Ca_4Si_6O_{18}$: NCMS) phosphors activated with distinct as well as combination of rare earth ions (Tb^{3+}, Pr^{3+}, Dy^{3+}, Eu^{3+} and Sm^{3+}). In this chapter, experimental procedure and merits of adopted synthesis approach have been explained in detail. This chapter elucidates the characterization techniques used to investigate thermal, structural, morphological, optical and photoluminescent features of NCMS phosphor along with their principle, instrumentation, formulation and graphical data analysis. Moreover, thermal, structural and morphological studies have been accomplished via thermogravimetric analysis (TGA), x-ray diffraction (XRD) and field emission scanning electron microscopy (FE-SEM) techniques. Moreover, optical properties have been analysed through diffuse reflectance spectral (DRS) measurement. Excitation, emission, chromaticity coordinates, color purity and decay studies associated with photoluminescent (PL) properties of NCMS phosphors have been executed through spectrofluorophotometer.

Chapter 3 emphasizes on the green emitting Tb^{3+} activated $Na_4Ca_4Si_6O_{18}$ phosphor synthesized via solid state reaction method. XRD patterns identified the phase and confirmed the phase purity by comparing the diffraction patterns with standard JCPDS card no.: 75-1687 for NCMS compound. The morphology and size of the particles have been illustrated with FE-SEM

micrographs. PLE spectrum of Tb^{3+} doped $Na_4Ca_4Si_6O_{18}$ phosphor depicts the strong excitation peak obtained in UV spectral region. The trivalent terbium activated NCMS phosphors excited under UV region (λ_{ex}=232 nm) exhibit intense emission in the blue (350-470 nm) and green (470-650 nm) spectral regions. With increasing the concentration of Tb^{3+} ions in the host matrix, the emission color shifts from blue to green region due to cross relaxation (CR) mechanism and shows the tunable behaviour of Tb^{3+} activated as-synthesized NCMS phosphor. The aforementioned results manifest that Tb^{3+} activated sodium calcium metasilicate phosphor has an immense potential to contribute as a green and blue-green emitting component in lighting and display device applications.

This research work has been published in ***Luminescence, 37 (2022) 1465 (Impact Factor: 2.90)***

Chapter 4 describes about the synthesis, characterizations and the outcome analysis of Pr^{3+} activated NCMS phosphor. Microcrystalline pure phase praseodymium doped $Na_4Ca_4Si_6O_{18}$ (NCMS: Pr^{3+}) phosphors have been synthesized and systematically characterized for implementation in w-LED applications. In this chapter, high temperature solid state reaction methodology has been opted to synthesize a series of NCMS: xPr^{3+} (x= 0.0, 1.0, 2.0, 3.0 and 4.0 mol%) phosphor. X-ray diffraction patterns confirmed the phase purity and crystallinity of the as-synthesized phosphor via comparing all the diffraction peaks with the standard pattern. Luminescent studies have been carried out in n-UV and visible regions to illustrate the excitation and emission spectra of NCMS: Pr^{3+} phosphor. PL spectrum exhibits the radiative emission at 611 nm under the most intense excitation peak at 480 nm for 1.0 mol% of Pr^{3+} doped NCMS phosphors. The optimized concentration of the dopant ion has been achieved by following the energy transfer-based concentration quenching mechanism and found to be 1.0 mol% for NCMS crystal. The chromaticity diagram represents the integrated emission color of the optimized NCMS:1.0 mol% Pr^{3+} phosphor falls in the red region with a color purity of 97.0% when stimulated with the blue light. Temperature dependent luminescence studies are evident that the thermal stability of the prepared phosphor is quite high when utilized under the operating temperature of LEDs. Thus, the

investigated outcomes encourage that the promising red-emitting NCMS phosphor can be utilized in w-LED applications.

This research work has accepted in the ***Bulletin of Material Science (Accepted: In Press, 2023) (Impact Factor: 1.80)***

Chapter 5 demonstrates the structural and spectroscopic analysis of thermally stable yellow emitting component and its usage in optoelectronic applications. In modern days, researchers are focused into developing the strategies for production of white light having high quantum efficiency, better performance, and high CRI. Recently, high quality white light has been achieved via adopting fundamental phosphor-based approaches in lighting industries. The white light can be generated by stimulating the yellow emitting phosphor with blue LED excitation. Thus, Dy^{3+} activated phosphors have great potential to contribute as thermally stable yellow emitting phosphor in the w-LED applications. In this chapter, a series of Dy^{3+} doped sodium calcium metasilicate ($Na_4Ca_4Si_6O_{18}$) phosphors have been synthesized by adopting the conventional solid-state reaction route. Phase identification has been carried out through XRD technique. Under near-UV excitation, PL spectra exhibit two characteristic bands with blue and yellow colour emitting light. The concentration quenching was achieved beyond the 5.0 mol% of Dy^{3+} ion in NCMS host lattice. The temperature-dependent PL studies display that the as-synthesized phosphor has high thermal stability. All investigations listed above demonstrate the tremendous potentiality of yellow emitting NCMS phosphor for optoelectronic device applications.

This research work has been published in ***Journal of Materials Science: Materials in Electronics 33 (2022) 19218 (Impact Factor: 2.80)***

Chapter 6 proposes the description of energy transfer induced color tunability behaviour of bi-activated NCMS phosphor for luminescent device applications. As it is commonly known that commercial w-LEDs are fabricated by coating a yellow emitting YAG: Ce^{3+} (Ce^{3+} ion doped yttrium aluminium garnet) phosphor with reasonably broad spectrum on blue emitting InGaN LED chip. One such fabricated w-LED shows deprived value of color rendering index and correlated

colour temperature caused by the dearth of red colour emitting component. In order to achieve sufficient CRI and lower CCT with improved luminous stability, researchers and scientists have to delve into an alternative approach with the suitable amalgamation of RGB (red: R, green: G and blue: B) mono phase phosphor. Solid state reaction methodology has been adopted to synthesize Dy^{3+}/Eu^{3+} co-activated thermally persistent $Na_4Ca_4Si_6O_{18}$ (NCMS) phosphors and investigated their structural, morphological and luminescent characteristics. In PL studies, as-synthesized NCMS phosphors co-activated with Dy^{3+}/Eu^{3+} ions have been excited with near-ultraviolet light (λ_{ex}=348 nm) and shows the utmost energy transfer up to 97.80% from sensitizer to activator. Dy^{3+} activated NCMS phosphor shows the illumination shift from yellow to red region with varying the Eu^{3+} ions concentration and also observed colour tunability by altering the excitation energy. Thus, Dy^{3+}/Eu^{3+} co-doped NCMS phosphors embrace tremendous thermally stable behaviour with flexible color tunability to emerge as a promising contender for w-LED applications.

This research work has been published in ***RSC Advances*** 13 (2023) 21105 ***(Impact Factor: 3.90)***

Chapter 7 discusses on the effect of sensitizer on the luminescence of Eu^{3+} activated metasilicate phosphor for solar cell applications. Solar energy has been ascended as a leading renewable energy source to accomplish the massive demand through amalgamating this energy source into technology. The luminescent materials especially downconversion/downshifting (DC/DS) materials have the immense potential to be utilized as an efficient energy conversion source, which absorbs energy in UV/n-UV region and releases energy in the visible region (without heat dissipation). Thus, down-converting features of thermally stable NCMS: Sm^{3+}/Eu^{3+} phosphors are highly preferred for solar cells. Conventional solid state reaction methodology has been opted to synthesize microcrystalline pure phase Sm^{3+}/Eu^{3+} co-doped $Na_4Ca_4Si_6O_{18}$ (NCMS) phosphors. Pure phase has been obtained and confirmed via x-ray diffraction technique. Photoluminescence studies of Sm^{3+} activated and Sm^{3+}/Eu^{3+} co-activated NCMS phosphors have been thoroughly investigated and discussed. The energy transfer mechanism in NCMS: Sm^{3+}/Eu^{3+} phosphors have been studied using PL and lifetime data to facilitate the emission in red region

under n-UV excitation. The chromaticity coordinates of NCMS: Sm^{3+}/Eu^{3+} phosphors exhibit the color tunability from orange to red region excited with n-UV/blue light as the concentration of activator ion increases. Moreover, enhanced luminescence and superior thermal stability of Sm^{3+}/Eu^{3+} co-activated NCMS phosphor demonstrates the viability of the phosphor to be utilized in solar cell applications.

This research work has been published in ***Journal of Materials Science: Materials in Electronics* 34 (2023) 1999.** ***(Impact Factor: 2.80)***

Chapter 8 explicates the summary of the results obtained in the chapters from 3 to 7 and also highlights the scope of the thesis for future applications.

CONTENTS

LIST OF TABLES

LIST OF FIGURES

Chapter 1

Introduction

In view of the current status of inhabitants and their set of circumstances, phosphor based lighting technology can be expected to implement in multipurpose applications, including white light emitting diodes (pc-wLEDs), laser, display devices and solar cell applications due to the fact of their reliability, flexibility, compactness, high brightness, simple fabrication and cost-effectiveness. Furthermore, this emerging technology demands additional study to create innovative multicolour emitting phosphors with high thermally stable luminescent intensity. This chapter covers the luminescence phenomena, including its underlying mechanisms and practical applications. In addition to that, role of the phosphors in solid state lighting and solar cell applications have been elucidated. This chapter also discusses the significance of selected host material ($Na_4Ca_4Si_6O_{18}$) as well as the objectives of the research work.

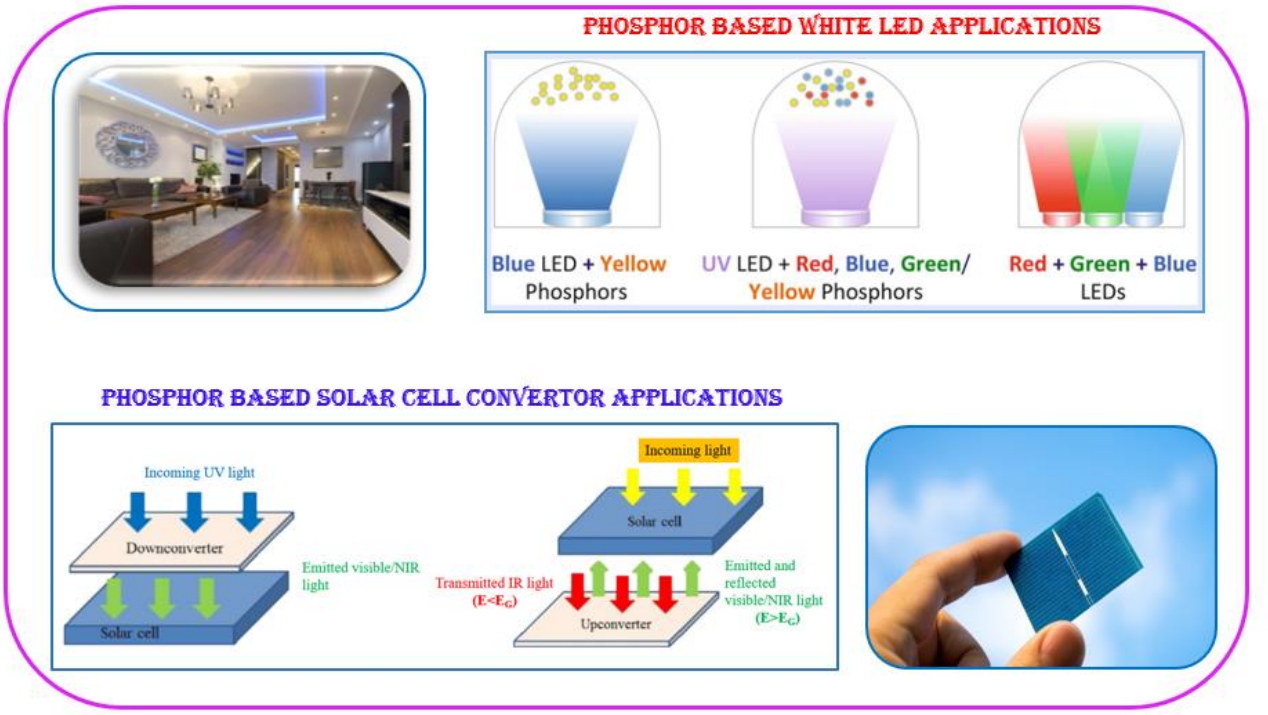

1.1. Luminescence

In the recent era, solid state lighting (SSL) has fundamentally altered the production and utilisation of lighting in all the facets of our lives which enables huge reduction in domestic and global energy consumption. In contrast to conventional lighting sources (with tungsten filament, plasma and toxic gases), SSL based inorganic light emitting diodes (LEDs) have tremendous potential to generate white light with maximum efficiency [1]. The development of useful SSL technology has been significantly demonstrated by the phenomenon of luminescence. 'Luminescence' is the term refers to low temperature emission, which often emits light at a greater wavelength when excited with the lower energy source. Materials which follows the principle of luminescence are known as luminescent materials or phosphor [2]. Moreover, phosphors are light emissive materials consist of host matrix (inorganic/organic) that includes deliberately added impurity in a very small quantity known as activator ions (transition metals or rare earth (RE) ions). These materials are essential for clean and energy saving technologies to address the demand for low voltage stimulated lighting sources due to consequence of rising worldwide energy consumption and have ability to convert high frequency of light to low frequency (Stokes shift) via electronic transition. In addition, due to their usage in cutting-edge technologies includes field emission display, scintillation, plasma display panels, light emitting diodes (LEDs), luminescent paints and photovoltaic cells etc., researchers have been intrigued by these materials over the past few decades [3].

1.2. Classification of Luminescence

The majority of materials emit radiation in the UV, visible and infrared (IR) region, when they are doped with impurity or particular dopant ions. The efficiency of these materials depend on the transforming ability of excitation energy into visible light. Depending on the type of excitation source, luminescent materials are classified into eight categories:

(i) Photoluminescence (PL): Photoluminescence is defined as the emission of photon caused by the excitation of photon/electron carrying higher energy. Based on the relaxation time of the excited electron from higher state to lower state, two well recognized form of photoluminescence are fluorescence and phosphorescence.

Fluorescence is the instantaneous process of the emission of light until the excitation is removed. The lifespan of excited state typically in the range of 10^{-8} to 10^{-4} s. However, phosphorescence is the process of emission of light from a substance exposed to radiation and persisting after an excitation source is removed. The lifespan of the excited state is typically higher than the fluorescence i.e. 10^{-4} to 10^{-2} s.

(ii) Chemiluminescence (CL): Chemiluminescence is a type of emission which takes place due to certain chemical reactions at diverse wavelength from UV-visible to infrared region. With the progression in the reaction, the ensuing vibronic excited state degrades to the lower energy state that eventually emits light. Glowsticks toys are the popular example of chemiluminescence [4].

(iii) Electroluminescence (EL): Electroluminescence is a kind of optoelectronic process where materials generate light when an electric current passing through them. A high electric stimulus can accelerate highly energetic electrons in electroluminescent materials, which then have tendency to generate light. The conversion of electrical energy into non-thermal light is a component of electroluminescent. Technologies like flat screen displays and illumination benefits greatly from electroluminescence [5].

(iv) Thermoluminescence: The phenomenon of thermoluminescence occurs when a specific crystal is stimulated by temperature over a threshold value. Cryoluminescence is one of the type of thermoluminescence, which releases light when the crystal temperature become lower. Archaeological dating and ecological monitoring comes under this type of luminescence [6].

(v) Cathodoluminescence: Cathodoluminescence produces the emission of photon in the visible portion of electromagnetic spectrum, when an electron beam incident on a luminescent material. The primary application of cathodoluminescence is the construction of displays, flat screen displays such as LCDs, traditional cathode ray tube [7].

(vi) Triboluminescence: Triboluminescence is the phenomenon which provides luminescence when the surface of material is fractured or polished by external mechanical force. Diamond is one of the example of triboluminescence as it shows emission during polishing process.

(vii) Radioluminescence: Radioluminescence is the generation of photons from the interaction of ionisation radiation such as alpha (α), beta (β), gamma (γ) and x-rays with matter. Tritium and radium are the examples of radioluminescence [8].

(viii) Bioluminescence: Bioluminescence is subtype of chemiluminescence which generally develop within the body of biological entity as a result of chemical processes. Fireflies, jelly fish and lantern fish etc., reflects light by pursuing the phenomenon of bioluminescence [9].

1.3. Fundamentals of photoluminescence

Photoluminescence is the phenomenon which involves the process of absorption of energy and subsequent emission of light especially in the visible region by the activator ions. The activator is the element added as dopant to the crystal lattice to obtained desired nonhomogeneities. These ions may stimulate to the higher energy levels via absorbing energy in the form of photons and function as a luminescence centres. In general, the photoluminescence process typically occurs in the following order:

- Absorption of energy by the activator ions and promote to the excited states.
- Relaxation of activator ion to the lower excited states.
- Radiative emission due to de-excitation of activator ions to the ground states.

To begin with, the activator ions first absorb the incoming photons, which stimulates the activator ions to reach to their excited states. The ions attained at excited states commence to relax

non-radiatively to lower excited states as phonons (heat or lattice vibrations) and due to the proximity of higher excited states inhibit the radiative relaxation. Moreover, these higher excited states possess very short lifetime to obtain radiative emission. Thus, the de-excitation of activator ions from the lower excited state to the ground state release photons to emit radiatively [10]. This radiative emission leads to the photoluminescence as shown in Fig. 1.1.

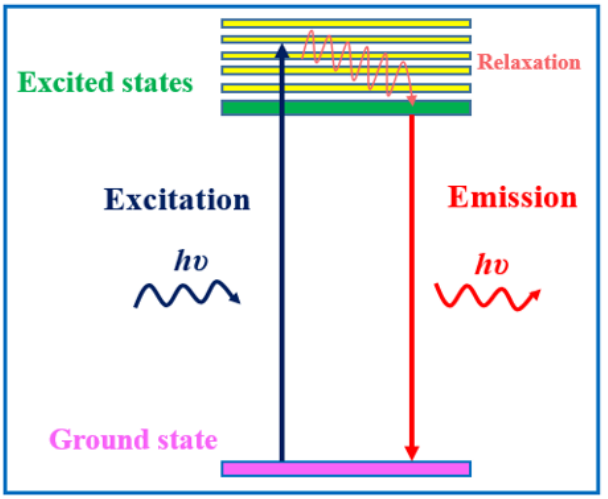

Fig. 1.1. *Schematic representation of photoluminescence.*

The radiative process yields emission in the visible region whereas the non-radiative process does not produce visible emission. The efficient radiative emission can be achieved by reducing the non-radiative emission. Stokes and anti-stokes law have been determined by following the photoluminescence mechanism. When the high energy photons i.e. UV/n-UV strike on the material, a part of this energy may be absorbed and re-emits as a lower energy photon in the visible or NIR region is known as Stokes law and the process is known as down-conversion process. Stokes shift is the energy difference between the excitation and emission wavelengths caused by the excitation energy's prior non-radiative loss. On the other hand, when two or more low energy photons of the NIR region are absorbed and release the energy in UV or visible range, then the process is validated as anti-Stokes law and the process is called as up-conversion. The down-conversion and up-conversion processes are illustrated in Fig. 1.2. Furthermore, photoluminescence can be divided into two categories on the basis of emission time after removing

the excitation sources are *(i) fluorescence and (ii) phosphorescence*. Fluorescence is simply the emission occur from the sample when it is exposed to excitation source of radiation and it is independent of temperature whereas phosphorescence exhibits the persistent emission even after removing the excitation source and also have significant dependency on temperature [11].

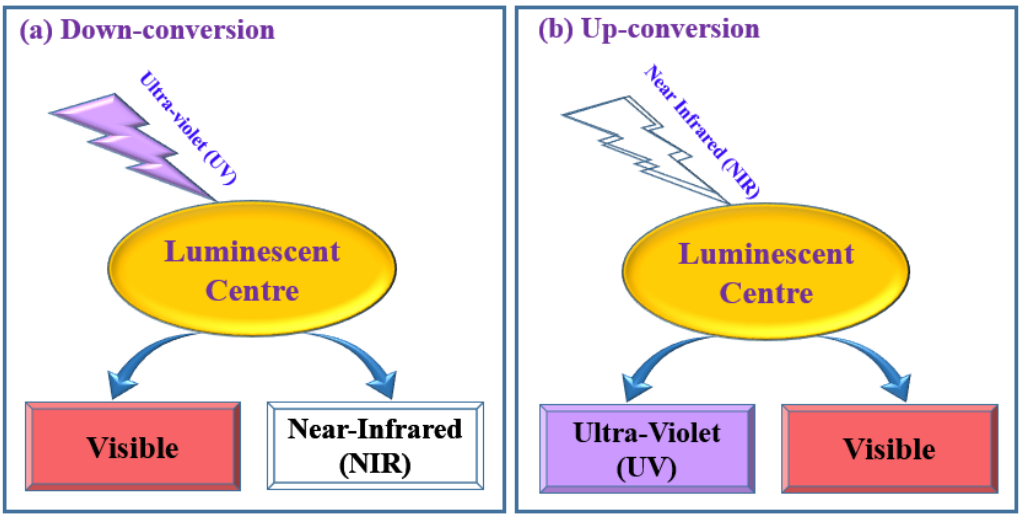

Fig. 1.2. ***(a)*** *Down-conversion and* ***(b)*** *Up-conversion process.*

1.4. Rare earth (RE) ions and its unique properties

Rare earth elements (REEs) are the member of lanthanide series containing fifteen elements begin from Lanthanum (atomic no. 57) to Lutetium (atomic no. 71) element. In addition, scandium and yttrium fall underneath rare earth elements category as they are extracted from the same ore and share comparable characteristics as lanthanide ions. These REEs are non-toxic, exhibit unique luminescent features [12]. These ions play significant role in the field of luminescence as they provide emission in broad range that encompasses ultraviolet (UV), visible and infrared (IR) region of electromagnetic spectrum. Therefore, lanthanide based systems are quite adorable choice for versatile applications in the field material science, chemical, physical sciences and across all other disciplines of science and technology.

Moreover, the chemistry of rare earths is characterised by the trivalent state owing to the most stable behaviour. In general, the electronic configuration of trivalent rare earth ions are represented as $[Xe]4f^n$ (n=0-14), where n is the number of electrons in the f-shell. The

spectroscopic features of RE ions are governed by the shielding effect of $5s^2$ and $5p^6$ over 4f electrons, which gives rise to well defined energy levels and protect the electronic states from the crystal field environment. The characteristic energy levels of the lanthanide ions are investigated by the Dieke diagram as shown in the following figure (Fig. 1.3.).

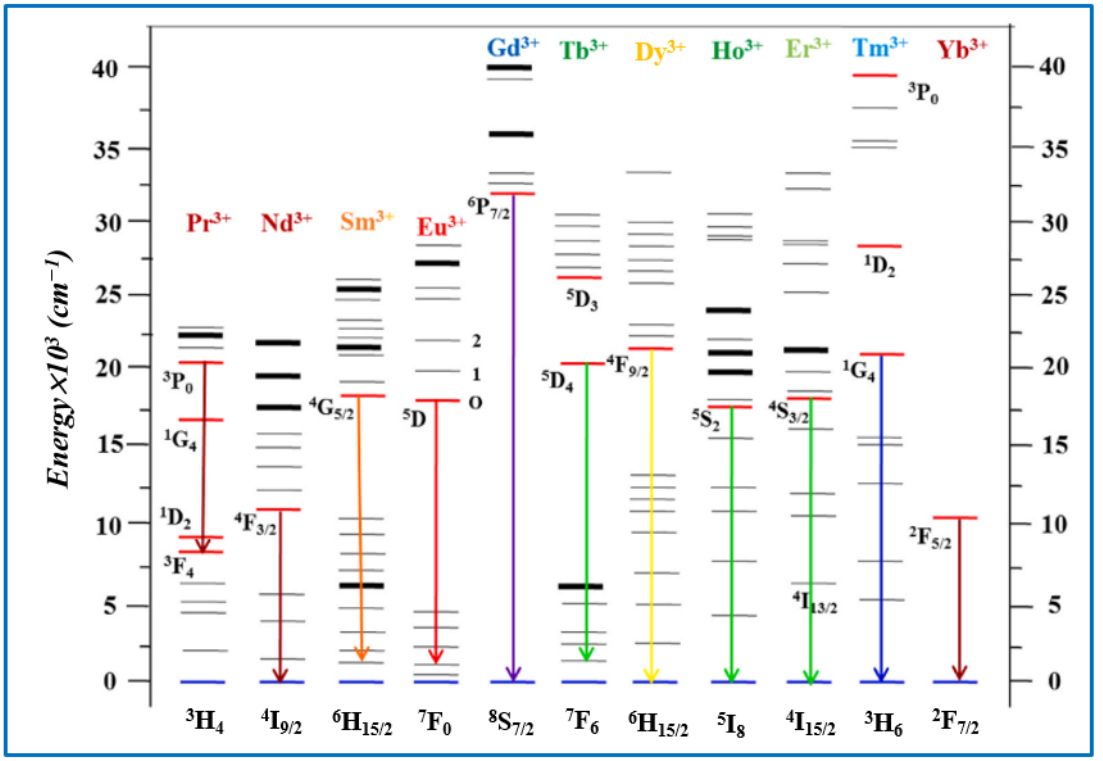

Fig. 1.3. *Dieke's illustration of various energy states of distinct RE ions.*

1.4.1. Unique features of RE ions

Based on the interactions described above, trivalent lanthanide ions or RE ions are extensively used as an activator in various luminescent devices since they possess unique luminescence properties in comparison to other optically active ions.

- RE ions exhibit narrow spectral lines that indicates monochromatic light and have longer emission lifetime.
- RE ions expose large stokes shift upon excitation due to huge gap between excitation and emission spectra.
- RE ions have several excited levels suitable for optical pumping.
- The intra-configuration *f-f* transitions of RE ions possess small homogenous linewidth.

- They manifest luminescence in spectral regions including visible, NIR and IR regions of electromagnetic spectrum.
- Well-developed theoretical models are available for organized study of energy levels, transition intensities in order to contemplate the excited state dynamics.

These exceptional properties of rare earth ions inflate their utility in various applications such as finger printing, display devices, anti-counterfeiting, bio-sensing, solar cell and solid-state lighting [13,14].

1.5. Phosphor and its luminescence mechanism

As the term 'Phosphor' has been already explained in the previous section (section 1.1), phosphors are the inorganic microcrystalline powder composed of host lattice that has traces of activator ions inserted into it as an impurity. It is vital to investigate the light emission process in the phosphor materials due to the fact that these materials are extensively employed in a variety of applications, including display and energy-saving technologies. On absorption of excited energy, the electron of the activator ion excites to the higher state and returns back to the associated ground state via two competitive pathways either by photon emission or phonon energy release. The manifestation of the luminescence phenomenon in the phosphor materials rely on three key features such as absorption, emission and energy transfer, however, these features may vary from host to host. Furthermore, the excitation in the phosphor materials can be either by x-ray, cathode ray, UV-rays, visible or n-UV excited source to achieve preferred excited state [15].

1.5.1. Absorption or excitation process

In general, the absorption of energy takes place either by the deliberately adding impurities (activator ions) or via host matrix itself. The host matrix subsequently transfers absorbed energy to the activator ions. In the host lattice, if the activator ions are not withstanding the enough absorption energy, a supplementary ion as a co-dopant is added named as sensitizer (S). Primarily, the dopant ions absorb the energy and then instantly transfer to the co-dopant ions to emit efficient

light. Lately, the absorption of excited energy via sensitizer results luminescence by transferring the excitation energy to the activator (A) ions, as shown in Fig.1.4.

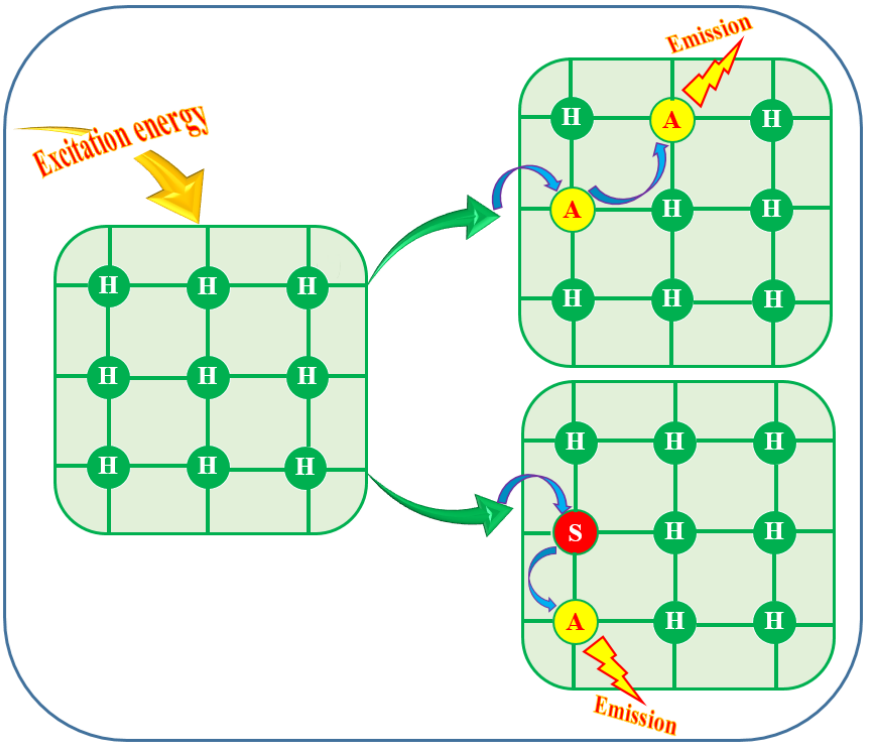

Fig. 1.4. *Absorption of incident energy, energy transfer and emission mechanism.*

1.5.2. Emission process

The analysis of luminescent characteristics of lanthanide ions begins with the configurational coordinate diagram (CCD) model. This model describes the luminescence process (excitation and emission) of the localised centre, notably the impact of lattice vibrations. In solid materials, the spectral location of absorption spectra resides different from emission of spectra especially at the lower wavelength and the phenomenon called as stokes shift. The CCD plot of potential energy curve for activator ion containing ground and excited states against configurational coordinates (internuclear distance) provide more clarity on the preceding phenomenon, as shown in Fig. 1.5. The lowest curve designates the ground state whereas the highest curve represents the excited state with minima which may locate at same or different equilibrium position with respect to the ground state. From the Fig. 1.5, it can be noted that the excited state minima shifted to left from the ground state over the value of ΔR which signifies the

interaction between electron and vibrations of luminescent centre. The potential energy curve follows parabolic shape which describe the harmonic behaviour of the electronic levels of ions. The horizontal lines within the parabola depicts the vibrational states present in both ground and excited states [16].

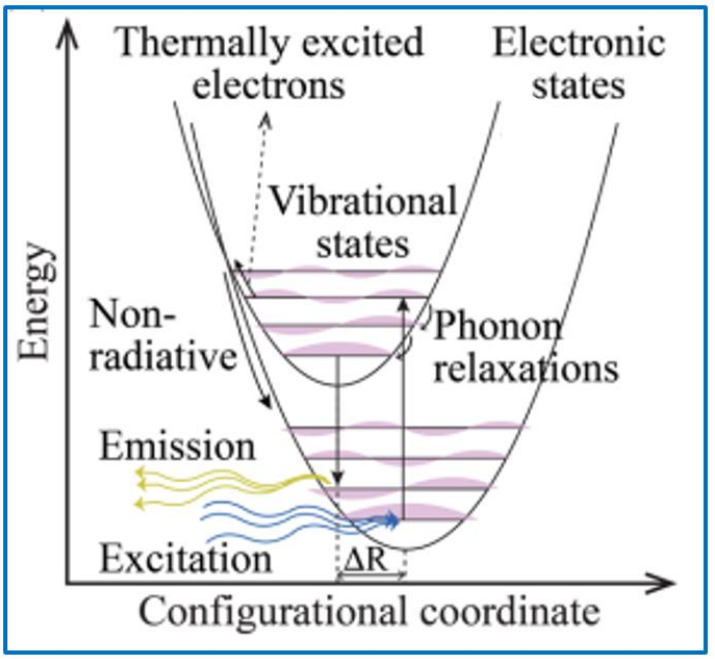

Fig. 1.5. *Configuration coordinate diagram representing excitation and emission process.*

During the process of electronic transition which involves absorption and emission to exhibit luminescence, the electron traces the vertical path while promoting to the excited state via following the Frank-Codon principle. According to the principle, the electronic transition in an atom or a molecule relatively swift than the vibrational transition of nuclei since the nuclei is much more massive than the electron. As a result, vibrational motion of the nuclei remains unaltered and electronic transitions are represented through vertical lines. Furthermore, the bound activator ion gets excited through absorption of energy in the form of photons and migrated vertically from the ground state (equilibrium) to higher non-equilibrium state. The excited ion falls down to the lowest vibrational levels of electronic excited state before reaching to the ground state and triggered as phonon relaxation and exposed with few loss of energy in the form of vibrational or thermal energy. The ion resided at the lowest excited state subsequently returns to the electronic ground

state with the release of photon to exhibit the luminescence. According to the configurational coordinates, it is worthy to accept that the energy required to excite the electron is much more than the energy of the emitted photons and hence satisfies stokes shift. In addition to this, thermal quenching is one of the aspect which can be explained through configurational coordination diagram. At elevated temperature the electron in the excited state can cross the intersection of both the electronic states assisted by the thermal energy, diminish the emission intensity and leads to thermal quenching.

Moreover, the electronic state is indicated by the notation included three quantum numbers S, L and J as $^{(2S+1)}L_J$ due to the spin orbit interaction. All three quantum numbers S, L and J designates as spin angular momentum, orbital momentum and total angular momentum, respectively. Apart from the $4f^n$ configuration, some of the RE ions represent $4f^{n-1}$-5d state where the migration of ion from 4f to 5d level may take place and profoundly affected by the crystal field surroundings. The energy level of free RE ions and the RE^{3+} ions in the host matrix are similar as there is no crystal field environment effect on the energy levels of stable +3 oxidation state of RE ions. Moreover, the incorporated RE ions into the host lattice, accommodate the energy levels of RE ions under the band of host. Despite the similarities between energy levels of free RE ions and RE^{3+} ions in the host lattice, the emission characteristics respond differently. It is worthwhile to notice that the incorporated ions demonstrated the difference in spectral position of excitation and emission generally referred as 'stokes shift', wherein the excitation takes place from ground to higher excited state and the emission occurs from the intermediate energy level to the ground state. Thus, the luminescent features appeared from RE doped phosphors can be recognized through either intra-configurational $4f^n$ transitions or inter-configurational $4f^n$-$4f^{n-1}5d^1$ or charge transfer transitions [17]. There are three types of electronic transition exhibited by RE ions viz. $4f^n$, $4f^n$-$4f^{n-1}5d^1$ and charge transfer transitions which are explained below in detail.

(i) Intra- configurational $4f^n$ transitions: The electronic transitions in $4f^n$ configuration for each lanthanide ion is specified and significant to explore the absorption and emission characteristics. As stated earlier, the 4f-4f transitions are therefore untouched by the crystal field environment due to outlying the screening effect of 5s and 5p orbitals, consequently sharp emission lines are produced by the 4f-4f transition. Thus, the luminescence originated from the 4f-4f intra-configurational transition is primarily due to the electric dipole and magnetic dipole interactions [18].

(a) Electric dipole (ED) transition: An electric dipole transition is caused by the interaction of lanthanide ions with the electric field vector in electromagnetic field. The emergence of electric dipole observed as the movement of charge is linear and have odd parity. In free RE ions, the electric dipole transition is parity forbidden via obeying Laporte selection rule. In induced electric dipole transitions, the non-centrosymmetric interaction permits to combine with the orbitals having different parity and provide the weak electric induced transition. Nevertheless, the 4f-4f transition achieve some intensity and implies that the ligand field around the electric dipole transitions affect their strength. Moreover, the induced electric dipole transitions are characterized by high asymmetry or strong interactions between the ligand fields. The selection rule for induced electric dipole transitions are; $|\Delta l|=\pm1$, $|\Delta S|=0$, $|\Delta L|\leq6$, $|\Delta J|\leq6$, $|\Delta J|=2, 4, 6$; if $J=0$ or $J'=0$. However, in some cases, the electric dipole transitions intensity in the lanthanide ions is highly sensitive to the coordination crystal field environment which either may absent or extremely intense and such transitions are termed as hypersensitive transitions [19]. Hypersensitive transitions are pure quadrupole transition via following selection rule of quadrupole transitions as $\Delta S=0$, $|\Delta L|\leq2$ and $|\Delta J|\leq2$ and also called as pseudo quadrupole transitions. The intensity obtained through hypersensitive transition is excessively high as it follows the quadrupole nature [20].

(b) Magnetic dipole (MD) transition: Magnetic dipole transition induced by the interaction of magnetic field vector of electromagnetism with lanthanide ions. It depicts extremely weak transition and rotational displacement of charge without reversing the direction of rotation under inversion centre. Magnetic dipole transition has even parity which suggest that it possess even transformation properties under inversion and allow transition between states of same parity. Since, the case of parity allowed, the MD transition are negligible influence by the site symmetry. Furthermore, the MD transition follows the selection rule as $\Delta S=\Delta L=0$ and $\Delta J=0$, $\pm 1$and $\Delta J=0$ or $\Delta J'=0$; is forbidden [21].

(c) Electric quadrupole transition: Electric quadrupole transition is achieved when there is a displacement of charge takes place having quadrupole nature. In electric quadrupole, four point charge exists with zero total charge and no dipole moment. It may be visualized as the two dipoles are placed in such a way that their dipole moment cancels and ensues the net dipole moment is zero. For an electric quadrupole transition, the parity tends to be even and found weaker transition in comparison with magnetic dipole and induced electric dipole transition.

(ii) Inter-configurational ($4f^n5d^0$-$4f^{n-1}5d^1$) transition: The inter-configuration ($f^n \rightarrow f^{n-1}d$) transition involves the promotion of 4f electron into the higher 5d energy state and governs the allowed parity by following the Laporte's selection rule. In this, the transition of an electron provides broadband than the f-f transition since the 5d orbital exists at higher energy and very much sensitive to the crystal field environment. Thus, the broad band appears with certain dopants in solid materials is because of two characteristics features as follows: the 5d orbital is much more exposed to the surrounding atom which results the huge splitting of 5d sub-shells owing to crystal field and the second one is the dipole allowed transition. The well-known example of such transition is YAG: Ce^{3+} yellow emitting phosphor [22].

(iii) Charge transfer electronic transition: This transition implies to excite the ion from host matrix ligand to the 4f shell of lanthanide ions to produce broad absorption and emission band

[23,24]. During the charge transfer transition process, the electron transfers from surrounding to the lanthanide ions by absorbing higher energy and often observed in the UV spectral region. It can be illustrated from the well-recognized phosphor (Y_2O_3: Eu^{3+}) in which the electrons transfer from O^{2-} to Eu^{3+} takes place with the broad absorption band in the higher energy state [25].

1.5.3. Energy transfer mechanism

Energy transfer refers to the process through which the excitation energy of one ion migrates to another ion. To develop the effective luminous materials, it is crucial to comprehend the mechanism of energy transfer. In general, there are several types of energy transfers processes (Fig. 1.6) undertaken in the phosphor materials includes (i) resonant radiative energy transfer via emission of sensitizers and re-absorption by activator ions (ii) non-radiative resonant energy transfer between sensitizers and activator ions (iii) phonon assisted non-radiative energy transfer and (iv) cross-relaxation among activator ions. Fig. 1.6 (a) represents the influence of efficient resonant radiative energy transfer from the sensitizer to activator ion by overlapping the spectra of emission of sensitizer and excitation of activator ions. Moreover, the fact that the lifetime of sensitizer's fluorescence is unaffected by increase in concentration of activator ion indicates that the radiative energy transfer is more prevalent. However, in the case of non-radiative resonant energy transfer, the significant decrease in the lifetime of fluorescence of sensitizer ions with increase in the concentration of activator ions takes place (Fig. 1.6 (b)). The non-resonant energy transfer occurs due to phonons, when there is a significant difference between ground and excited states of the sensitizer and activator. The competitive interaction, distinctive transitions and spatial separation of sensitizer and activator are the primary determinants of energy transfer process in phosphors. Moreover, if the two ions are at different excited states then the probability of energy transfer is nominal and the process is known as phonon assisted non-radiative transition, as represented in Fig. 1.6 (c). Furthermore, the phenomenon of cross relaxation observed between

activator ions have two pairs of energy levels shares the same energy gap (ΔE), as shown in Fig. 1.6 (d). The excited energy of one ion lies at higher level transfers its energy to the another ion remains at ground state which absorbs the emitted energy of previous ion. After absorbing energy, the ion migrates to the intermediate level from where it decays non-radiatively to the ground state by sharing some of their energy [26]:

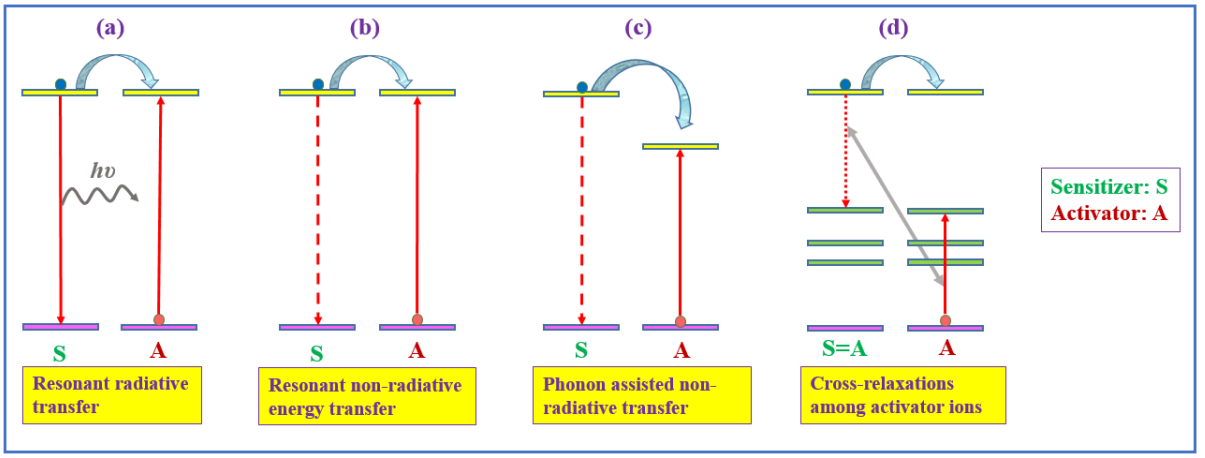

Fig. 1.6. *Schematic diagram for different energy transfer processes between two ions.*

1.6. Theoretical models explaining energy transfer (ET) process

In general, phosphor materials exhibit strongest emission with the optimum concentration of dopant ion in the host lattice. However, the optimum concentration can be figure out by adding the dopant ion up to the limit having highest absorption efficiency. The concentration beyond which emission intensity tend to decline with further increase in dopant concentration is known as concentration quenching. Moreover, the concentration quenching phenomenon widely depend on certain factors such as structure of the host and nature of the dopant ion within the specific crystal lattice. The dopant ions within the lattice possess identical excited states and enhance the probability of ET non-radiatively among the nearest neighbouring ions, since, the distance between the neighbouring ions get reduces with increasing the dopant ion concentration. The energy transfer takes place via following three chief processes including exchange interaction, reabsorption and multipolar interactions. In radiation reabsorption, the excitation and emission band should overlap but it is seldom to occur, whereas to analyse other processes (i.e. multipolar

interaction or exchange interaction), critical distance (R_c) between the dopant ions have to be estimated using Blasse equation given below [27]:

$$R_c = 2\left(\frac{3V}{4\pi x_c N}\right)^{\frac{1}{3}} \quad (1.1)$$

In the above equation, parameters listed such as V, N and x_c represents the volume of unit cell, number of cations per unit cell and critical concentration of the activator ion in the host lattice, respectively. The exchange interaction takes place when the R_c is less than the 5 Å, if both the conditions explained above do not satisfy to support the preliminary two energy transfer mechanisms, therefore, the multipolar interaction will become prominent since the value of R_c is much higher than 5 Å. Thus, Dexter's theory can be employed to determine the energy transfer take place via multipolar interaction.

(a) Dexter theory: Following Dexter's theory, the type of multi-polar interaction can be determined using the derived equations given below [28,29]:

$$\frac{I}{x} = k\left[1 + \beta(x)^{\frac{Q}{3}}\right]^{-1} \quad (1.2)$$

$$\log\left(\frac{I}{x}\right) = -\frac{Q}{3}logx + K' \quad (\text{Assume } \beta x^{\frac{Q}{3}} >> 1) \quad (1.3)$$

where, Q and I are the parameters reveal the type of interaction and emission intensity, respectively, x is the concentration of dopant ions, k and β are the constants. Q denotes the type of interaction associated with the values 6, 8 and 10 denoted as d-d, d-q and q-q interaction, respectively. Furthermore, Dexter and Reisfield's approximation can be used on the data of emission spectra to investigate the existence of type of multipolar interaction in case of double ion (dopant: sensitizer→ co-dopant: activator) doped phosphor.

(b) Dexter and Reisfield's approximation: To recognize the type of multipolar interaction among the sensitizer (S) and activator (A) ions, Reisfield's and Dexter theory can be employed. The quantum efficiencies can be expresses as η_{s0} and η_s, where η_{s0} is the quantum efficiency of

sensitizer emission without activator, η_s is quantum efficiency with activator ions and C is the summation of sensitizer and activator concentrations [30]:

$$\frac{\eta_{s0}}{\eta_s} \propto C_{S+A}^{\frac{n}{3}} \tag{1.4}$$

where *n* designates the type of multipolar interactions for which dipole-dipole (d-d) interaction with the value of 6, dipole-quadrupole (d-q) with 8 and quadrupole-quadrupole (q-q) interaction with 10. The value of quantum efficiency ratio $\left(\frac{\eta_{s0}}{\eta_s}\right)$ for sensitizer ions emission without and with activator ions can be associated to the ratio of emission intensity $\left(\frac{I_{s0}}{I_s}\right)$:

$$\frac{I_{s0}}{I_s} \propto C_{S+A}^{\frac{n}{3}} \tag{1.5}$$

Moreover, $\frac{I_{s0}}{I_s}$ vs $C_{S+A}^{\frac{n}{3}}$ plot unveils the value of *n* by the best linear fitted at 6, 8 and 10 indicating the contribution of type of interaction to elaborate the energy transfer mechanism from sensitizer to activator ions. Moreover, the energy transfer efficiency (η_{ET}) of corresponding sensitizer to activator ions can be determined using below equation:

$$\eta_{ET} = 1 - \frac{I_s}{I_{s0}} \tag{1.6}$$

1.7. Solid state lighting and solar cell applications

In the recent time, solid state lighting is alleged to be an ultimate light source that is in the process of profoundly alter the way of generating and controlling the light for distinct applications by the growing human civilization. Earlier, conventional light sources such as fire (1st generation), incandescent bulbs and fluorescent lamps (2nd and 3rd generations) were exorbitantly utilized due to lack of development of innovative technology [31]. These light sources entail high temperature, more heat dissipation and release of toxic gases which adversely affect the environment [32]. Therefore, considering the challenges on the subject of an escalating demand of energy consumption and environment problems, a substitute of conventional light source is obligatory to develop. In reference to this, solid state lighting (SSL) emerged as an alternative source of light

and currently serve as fourth generation of light owing to the significant reduction of energy usage. SSL rely on the organic or inorganic based light emitting diodes (LEDs) to produce light with maximum efficiency. Moreover, SSL possesses two highly enviable features includes; (i) extremely energy efficient with a great deal of potential to reduce energy usage and carbon emission and, (ii) flexible light source having several configurable characteristics such as spatial emission pattern, colour temperature, temporal modulation and control of spectrum etc [33,34]. The introduction of LEDs over outmoded technology (incandescent and fluorescent bulbs) is to improve the quality of life and reflect benefits in performance, economy, sustainability and ecology [35]. Thus, the current technology generates efficient white light.

1.7.1. Generation of white light

In general, there are three ways to generate white light in fabricating w-LEDs as explained in Fig. 1.7. The prime approach is the most common and phosphor free, in which each monochromatic red (R), green (G) and blue (B) emitting LEDs are combined to attain white light. The above-mentioned RGB-LEDs are inaccessible as individual LED demands different driving currents to provide constant white light emission [36]. Further, different driving currents of each LED trigger the emission color and results unstable color temperature. Second approach is phosphor dependent and produce white light by layering yellow emitting YAG: Ce^{3+} phosphor on the top of blue emitting InGaN LED chip had proven to be advantageous over RGB LEDs due to high brightness, simple fabrication and cost-effectiveness. Despite of these advantages and its on-going commercial practice, people are refraining to use it due to some drawbacks such as less efficiency, halo effect, low color rendering index (CRI<80) and high correlated color temperature (CCT>7000 K). The listed issues mentioned in phosphor based LEDs are due to insufficient availability of red component and can be resolved by adopting third approach that implicates red color emitting component into the phosphor. Thus, final approach embraces two sub approaches, wherein exciting either a mixture of green and red phosphors via blue LED chip or a mixture of

blue-green-red phosphors via UV/near(n)-UV LED chip. Eventually, the final approach indigenously holds red component to produce efficient phosphor [37]. Moreover, the prepared multiphase phosphor causes deteriorated output efficiency due to the re-absorption of blue emission through RG phosphor. Nevertheless, the deteriorated output efficiency can be improved by preparing single phase phosphor activated with double or multiple dopant ions to provide warm white light. Double or multiples dopant ion activated single phosphor yields excellent efficiency with optimum color reproducibility, suitable CCT, appropriate CRI value and color tunability [38].

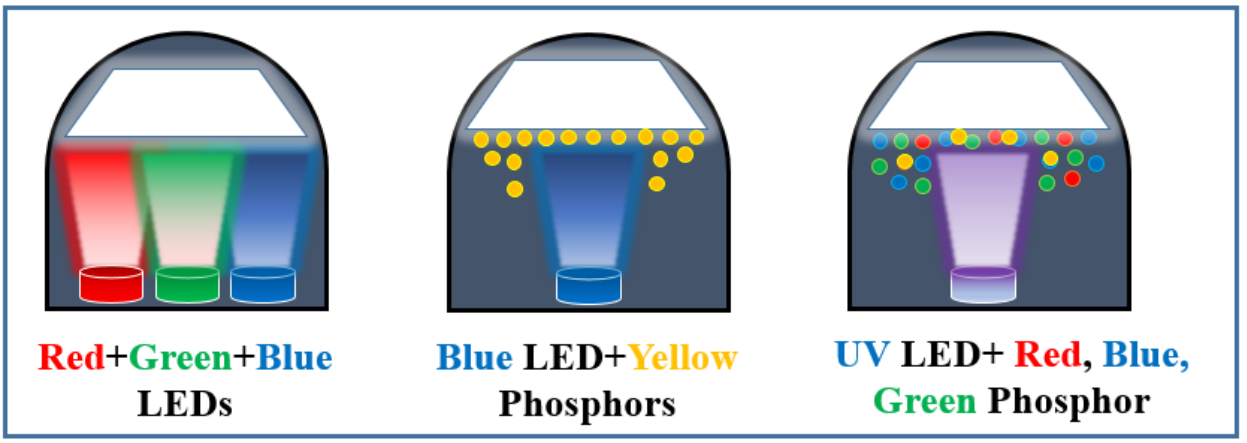

Fig. 1.7. *Generation of white light using phosphors.*

1.7.2. Phosphor based solar cells

In addition to this, solar energy source has immense potential to substitute other sources of energy (wind, biomass, nuclear, and geothermal, etc.), since the solar energy is clean, renewable, environmental friendly and abundant in atmosphere [39]. In recent years, photovoltaic solar cells have been investigated as an efficient and cost effective conversion of solar energy to electrical energy. The most common commercially used photovoltaic cells are produced using silicon crystal with band gap energy E_g=1.12 eV, and have about 14% of solar cell efficiency [40,41]. The solar cell efficiency limits due to spectral mismatch between the incident solar spectrum and spectral response of solar cells and thermalization loss. RE doped phosphor materials played crucial role in the photovoltaic applications due to their outstanding photoluminescence properties. Phosphors are the materials which follows upconversion (UC), downshifting (DS) and down-conversion (DC)

mechanism: UC is the process involves the conversion of longer wavelength to shorter wavelength while DC is the process that convert one high energy photon (UV/blue region) into two or more low energy photon (NIR region) and DS is the process in which one high energy (UV/blue region) photon converts into one low energy photon (visible/NIR region). The DC is the process in which the shorter wavelength convert into longer wavelength phosphor uses on the front side of photovoltaic solar cells while in UC phosphor uses on the backside of solar cells to enhance the conversion efficiency as represented in Fig. 1.8 (a & b) [42,43].

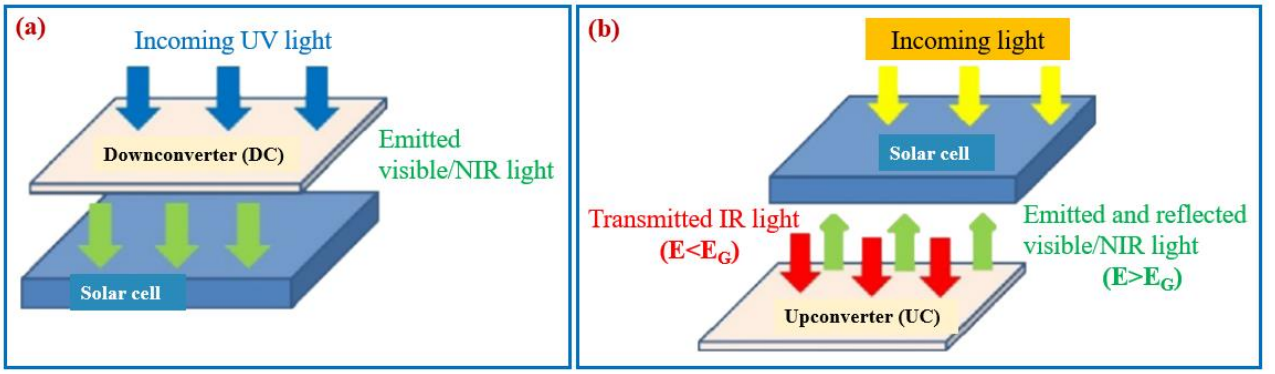

Fig. 1.8 ***(a)*** *A downconversion layer-solar cell system* ***(b)*** *An upconversion layer-solar cell system.*

Furthermore, the photon energy lower than the band gap of the silicon crystals are not absorbed and move to transmission loss while in case where the photon energy higher than the band gap energy, excess energy gets exhausted and way to thermalization loss. However, these losses of energy can be harvested by using the DS or DC process that convert the high or low energy photons into a spectral range that can be utilized by electron hole pair [44,45].

Many DC phosphor materials have improved the performance of the solar cells via increasing the energy conversion efficiency, absorption and reducing the reflection of light. For instance, Eu^{3+} doped $KCaGd(PO_4)_2$ (KCGP) phosphor studied by Y. Chen. et al have shown the effective reduction in the reflection and increment in the absorption of light. The KCGP: Eu^{3+} phosphor coated on the polycrystalline silicon solar cell surface could effectively increase the value of efficiency by 0.64% by simultaneously analysing the increment in parameter such as short circuit current (I_{sc}) open circuit voltage (V_{oc}) [46]. G Shao. et. al has investigated the influence of

high quantum yield bearing and commercial Ce^{3+} doped yttrium aluminium garnet on the monocrystalline silicon solar cell [47]. Moreover, YAG: Ce^{3+} DC material has been used to enhance the energy conversion efficiency of solar cells and improved the efficiency upto 1.05% but the high reflection and internal energy loss issues are still need to be resolved. The appropriate DC luminescence materials are need to satisfy some requirements to improve the efficiency of solar cells: (i) materials should have good quantum yield and low reflectivity (ii) the optimum separation between the absorption and emission bandgap is required (iii) the absorption band should be broad in shorter wavelength regions, where solar cells have low spectral response (iv) the materials need to be transparent for unabsorbed light [48,49].

1.8. Spectral tuning and their influence on luminescence performance

It is widely known that the colour of the luminescent materials depend on the dopant ion incorporated into the host matrix via recorded photoluminescence excitation (PLE) and emission (PL) spectra. In addition to that there are other significant parameters essentially needed to analyse the performance of the materials viz. Commission Internationale de I'Eclairage (CIE), color rendering index (CRI), correlated color temperature (CCT), luminescence efficiency and quantum yield [50,51]. The improved luminous performance with aforementioned luminous parameters can be achieved by tuning the peak width and peak position in the spectra of specific phosphor. Thus, the spectral tuning could be the efficient technique to render the excellent luminescent property and performance of rare earth doped phosphor material to be utilized in the solid state lighting.

1.8.1. CIE color coordinates

It is important to extensively explore the Commission Internationale de I'Eclairage (CIE) coordinates, to reveal the aptness of color array as well as the relevant application of material especially for optoelectronic devices [52]. CIE generated color models are available to represent the tristimulas values of illuminated color (Red: R, Green: G, Blue: B) in the 3 dimensional color

space. The standard CIE 1931 chromaticity diagram and color matching function has shown in Fig. 1.9.

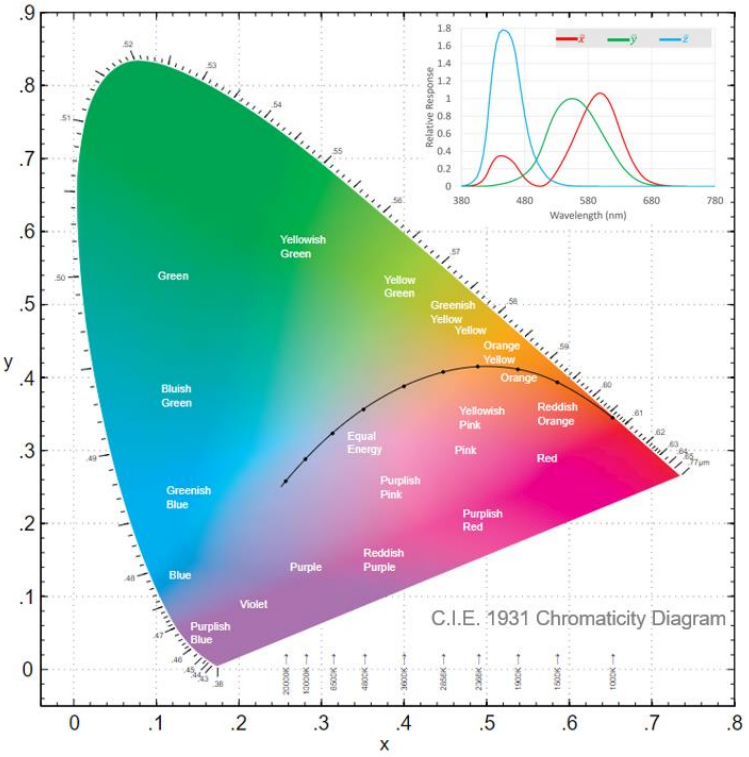

Fig. 1.9. *Standard CIE 1931 chromaticity plot and color matching function plot.*

Since, human eye can possess three separate colors and each color produced with the combination of RGB. The color of any illuminating light can be displayed via color matching function. In color space, $\bar{x}$ (λ), $\bar{y}$ (λ) and $\bar{z}$ (λ) are three color matching functions and a dimensionless quantity.

$$X = \int \bar{x}(\lambda)P(\lambda)d\lambda \tag{1.7}$$

$$Y = \int \bar{y}(\lambda)P(\lambda)d\lambda \tag{1.8}$$

$$Z = \int \bar{z}(\lambda)P(\lambda)d\lambda \tag{1.9}$$

where, tristimulus values (X, Y and Z) provide the degree of stimulus for each primary color (RGB) required to match the power spectral density *P(λ)*. Moreover, the tristimulus values are employed to evaluate the chromaticity coordinates i.e. x and y, as represented in the following equations [53]:

$$x = \frac{X}{X+Y+Z} \tag{1.10}$$

$$y = \frac{Y}{X+Y+Z} \tag{1.11}$$

The location of the CIE chromaticity coordinates across the locus of CIE chromaticity diagram signifies the monochromaticity while multichromic coordinates lie within the area of chromaticity diagram.

Thus, to quantify the monochromaticity of under investigated material using CIE coordinates, the color purity can be evaluated using formula as follows [54]:

$$Color\ purity = \frac{\sqrt{(x-x_{ee})^2+(y-y_{ee})^2}}{\sqrt{(x_d-x_{ee})^2+(y_d-y_{ee})^2}} \times 100\% \tag{1.12}$$

where (x, y) are the coordinates of phosphor, (x_{ee}, y_{ee}) are the coordinates corresponds to the equal energy point and (x_d, y_d) are the coordinates of dominant wavelength point. As stated earlier the monochromatic coordinates locate at the locus with 100% color purity.

1.8.2. Correlated color temperature (CCT)

Correlated color temperature (CCT) is one of the significant luminescence parameter used to measure the color temperature of focused the material and measure it in degree kelvin (K). CCT is defined by the CIE as the temperature of the planckian blackbody whose perceived color is closest to that of a given spectrum at the same brightness and under specified viewing conditions. CCT refers to the coldness and warmness of light. In general, the higher CCT (>5000 K) value denotes to the cooler light with emission of bluish light whereas lower (<5000 K) one signifies the warmer light with emission of yellow and red light. Typically, CCT values has a range of 2000 to 10000 K and access in accordance to specific purpose such as indoor, outdoor, industrial and display etc. It has been accepted commercially that the lighting source lie between 2200-6500 K range is most substantial. The correlated color temperature (CCT) value of luminescent material can be estimated from the equation evaluated by McCamy as follows [55]:

$$CCT = -449n^3 + 3525n^2 - 6823.3n + 5520.33 \tag{1.13}$$

where $n = (x - x_e)/(y - y_e)$ represents inverse slope line and $x_e = 0.332, y_e = 0.186$ are the coordinates for epicentre of convergence.

1.8.3. Color rendering index (CRI)

Color rendering index (CRI) is the quantitative measure to reveal the ability of light source in terms visibility of diverse objects and compare with the natural or standard light source. The CRI is rated on the scale ranging from 0 to 100. The minimum indexing enunciates undistinguishable color whilst higher indexing refers to the "ideal" white light or daylight [56].

1.8.4. Luminous efficacy (K)

Luminous efficacy (*K*) is the measure of the efficient conversion of electricity into light. It is defined as the proportion of luminous flux to power and the SI unit of luminous efficacy is lumens per watt. Depending on the measurement of power, it can either be radiant flux or the overall amount of electrical energy output expended by the source [57].

1.8.5. Fluorescence decay

The study involves the excitation and de-excitation of rare earth ions via f-f electronic transitions provides a deeper insight into the mechanism of excitation. Typically, a time resolved intensity curve described by the integral solutions to specific rate equation which is accountable for the possible excitation and de-excitation mechanism [17]. As stated in previous section that excited ion may relax to the ground state through various processes through either radiative transition or phonon transition or transfer excess energy to the nearby ion. The fluorescence decay curve can be fitted to single exponential function in case of the lower concentration of dopant ions with the negligible interaction among the RE ions. Furthermore, perfect single exponential decay indicates the insignificant energy transfer between the luminescent centres besides that the life of the excited level can be readily estimated by finding the first e-folding times.

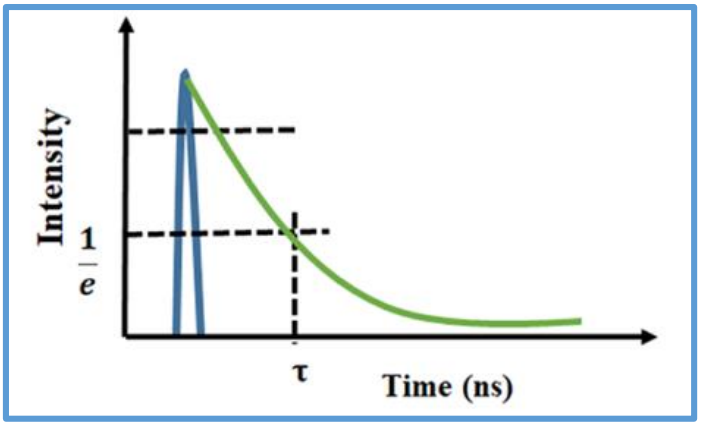

Fig. 1.10. *Time resolved fluorescence spectra.*

A logarithmic plot of intensity versus time is used to determine the lifetime. It is evident from the figure that after time τ, the intensity of excited state has declined to 1/e. However, bi-exponential curve fit obtained at higher concentration of dopant and co-doped phosphors. The fluorescence intensity as a function of time with single or bi-exponential fit can be described by the following equations [58]:

$$I = I_o + Ae^{\left(-\frac{t}{\tau}\right)} \tag{1.14}$$

$$I = I_o + A_1 e^{\left(\frac{t}{\tau_1}\right)} + A_2 e^{\left(\frac{t}{\tau_2}\right)} \tag{1.15}$$

where I_o represents the fluorescence intensity at time (t=0). Moreover, in case of single exponential fit τ denotes the experimental lifetime of excited state that is equivalent to the radiative lifetime, reciprocal to the probability of spontaneous emission from the excited state to ground if there is no energy loss due to non-radiative process. On the other hand, parameters in bi-exponential fit such as τ_1 and τ_2 signifies the fast and slow components of lifetime, A_1 and A_2 are the constants. The average lifetime (τ_{avg}) for bi-exponential fit can be estimated by the relation as follows:

$$\tau_{avg} = (A_1\tau_1^2 + A_2\tau_2^2)/(A_1\tau_2 + A_2\tau_2) \tag{1.16}$$

In general, the fluorescence lifetime relies on the rate of radiative and non-radiative relaxations. The lifetime value decreases with rise in non-radiative relaxation rate due to increase in number of defects as well as quenching centres.

1.8.6. Thermal stability

Thermal stability is one of the significant aspect of the prepared phosphor that predicates the robustness, durability and consistency performance in optoelectronic devices at preferably working temperature (~423 K) of LED from very low to ideal high temperature [59]. Temperature dependent photoluminescence (TDPL) spectra attained at leading excitation frames the dependency of the relative emission intensity of phosphors with respect to the intensity at room temperature. In general, the emission intensity tends to decline with rise in temperature as it follows thermal quenching phenomenon. The current phenomenon arises as a result of non-radiative relaxations in the phosphor materials. The non-radiative emission rate (R_{nr}) based on the higher temperature can be determined with the following equation [60,61]:

$$R_{nr} = Kexp\left(-\frac{\Delta E_a}{K_B T}\right) \quad (1.17)$$

where the above mentioned parameters, ΔE_a represent as activation energy relate with thermal quenching, K is a constant and K_B is Boltzmann's factor with the value 8.6173×10^{-5} *eV/K*. The activation energy is defined as the energy separation between the lower level of the excited state parabola and the intersecting point for the excited and ground state. The relation between temperature and non-radiative emission rate shown in the equation (1.17), clearly explains the increase in non-radiative relaxation rate with rise in temperature, which supresses the emission intensity. To evaluate the activation energy (ΔE_a) of phosphor, Arrhenius equation can be expressed as given below [62,63]:

$$I_T = \frac{I_o}{1+\alpha exp\left(-\frac{\Delta E_a}{K_B T}\right)} \quad (1.18)$$

where, luminescent intensity at initial temperature and at testing temperature represented as I_o and I_T, respectively while α denotes as a constant factor. The linear fitted plot between $\ln\left(\frac{I_o}{I_T}-1\right)$ and $1/K_B T$ aids to estimate activation energy. The obtained value of activation energy depicts the

thermal stability of the phosphor. Moreover, the higher value of activation energy results better thermal stability of focused phosphor.

1.9. Importance of the current host material

Phosphors are widely acknowledged for its usage in technological advancements in numerous applications includes field emission displays, plasma display panels, solar cells and light-emitting diodes (LEDs). Especially in case of LEDs, an efficient single phase phosphor based LEDs with remarkable luminescent features has to be explored. The choice of appropriate host lattice has notable impact on the effective luminescent properties of the phosphors while generating single phase phosphor based LEDs. Recently, focusing on to the unique benefits includes affordability, ease of production, environment friendly, excellent chemical, thermal and photo stability, inorganic oxides have been validated as a viable host material. Undoubtedly, it has been previously described that the efficient host lattices provide an advantageous contribution to synthesize an effective phosphor with proficient luminescence properties. Therefore, despite the availability of numerous oxide hosts such as borates, phosphates, tungstates, molybdates, and vanadates etc., the silicates have been the preferential choice since they have good physical-thermal-chemical stability with wide band gap and low thermal expansion coefficient.

However, silicates are the most abundant in nature and they are categorised as ortho (1:4), meta (1:3) and pyro (2:7) depending upon Si:O ratio. Amongst various metasilicates, the $Na_4Ca_4Si_6O_{18}$ occurs as ternary compound in a Na_2O-CaO-SiO_2 system. Ohsato et. al. determined $Na_4Ca_4Si_6O_{18}$ structure consists of tightly packed six membered $[Si_6O_{18}]^{12-}$ rings of silicate tetrahedral that stacked in a cubic close packed arrangement with alkali and alkaline earth ions. Further, it has been investigated that structure has phase transition with variation in temperature. At elevated temperature, the rhombohedral crystal occurs whereas hexagonal structure of $Na_4Ca_4Si_6O_{18}$ has been formed at lower temperature. The difference in structure may be observed

due to change in temperature and can be expressed in the form of cation coordination polyhedral and arrangement of $[Si_6O_{18}]^{12-}$ rings [64].

Alkaline based metasilicate compounds are the substantial class of phosphor for incorporation of many trivalent luminescent centers. These materials possess interesting features such as good thermal as well as chemical stability, low thermal expansion, wide band gap and better insulation properties for various other applications such as paint, coating and biomedical diagnosis etc.

1.10. Objectives of the present work

Over the past few decades, LEDs fabricated using phosphor materials (pc-wLEDs) are most imperious and promising innovation in the field of artificial lighting since it carries advantageous features such as compactness, better efficient and eco-friendly. Present work is focused on to the synthesis of $Na_4Ca_4Si_6O_{18}$ phosphor with distinct dopant and co-dopant ions in order to produce efficient white light with improved luminescent properties. Moreover, the thermal, structural, optical, morphological and photoluminescence properties were examined which revealed the significant results to fulfil the objective of the present thesis. The chief objectives of the present thesis are:

- To prepare the single phase host matrix.
- To investigate the thermal, structural, morphological, optical and photoluminescent features of the prepared RE ion doped phosphors.
- To improve the luminescence intensity via varying dopant and co-dopant of activator and sensitizer ion into host matrix.
- To optimize the emission intensity and color of the prepared phosphor in the required spectral region for w-LEDs and photovoltaic applications.
- Finally, to develop optimized, thermally stable and eco-friendly phosphor with appropriate luminescent efficiency for optoelectronic device applications.

Chapter 2

Synthesis and characterization techniques

In this chapter, the employed experimental and characterizations techniques for RE doped $Na_4Ca_4Si_6O_{18}$ phosphor have been explained in detail. Traditional solid state reaction methodology has been adopted to prepare various RE activated and co-activated $Na_4Ca_4Si_6O_{18}$ phosphor. The as-prepared phosphors have been studied via distinct characterization tools and technique in order to explain thermal, structural, morphological, optical and photoluminescence features. These properties are advocated with the characterization tools includes thermogravimetric-differential thermal analysis (TG-DTA), X-ray diffraction (XRD), scanning electron microscope (SEM), UV-Visible (UV-Vis) spectrophotometer and spectrofluorophotometer etc.

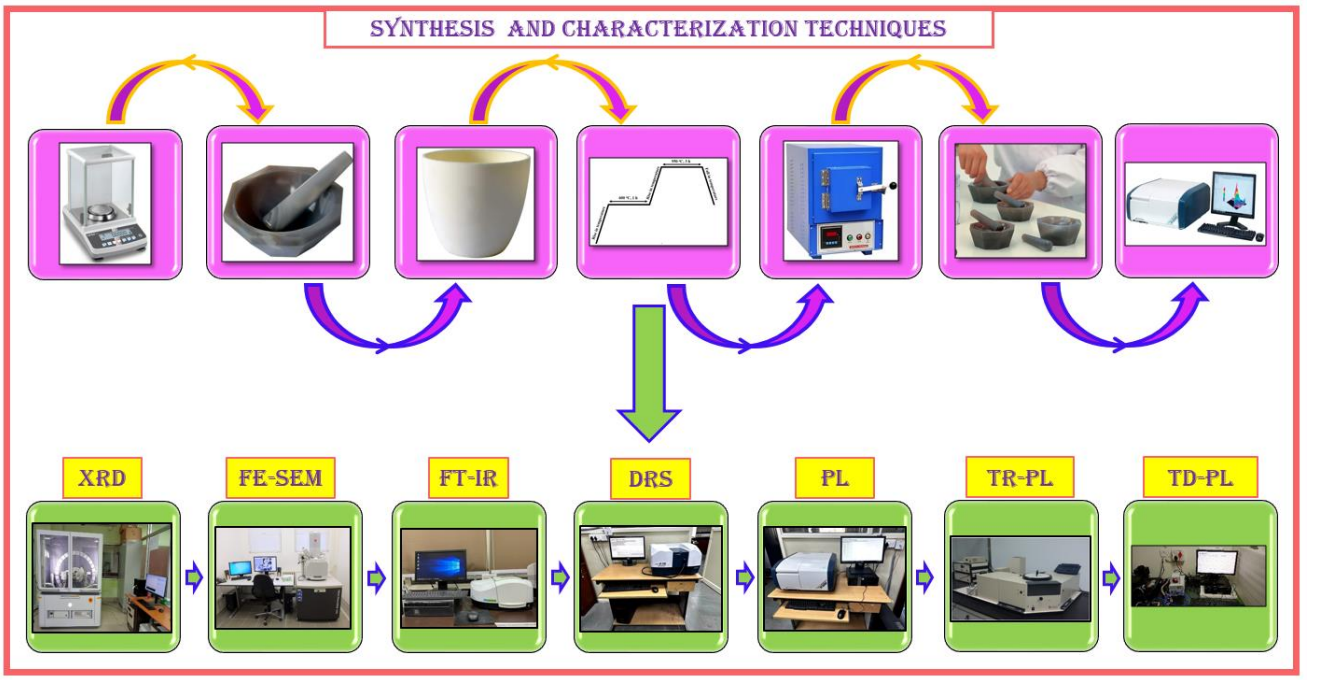

2.1. Experimental

Traditionally, materials are diversified on the basis of their fundamental properties such as structural, morphological, bonding, band gap and photoluminescence. The crystallinity feature is assessed in order to study the crystallographic arrangement. Morphological properties express the shape and size of the particles. The formed crystal with the attached bonds have been figured out with bond analysis technique. The optical properties have been studied to analyse the band gap of the prepared materials. Moreover, luminescence studies have also been accomplished with the help of few characterisation tools.

2.2. Synthesis methodology

2.2.1. Solid State Reaction (SSR) method

Various synthesis techniques viz. solid state reaction, co-precipitation, hydrothermal, spray pyrolysis, microwave and combustion methods are followed to synthesizing different materials. Among all the techniques, solid state reaction (SSR) method is conventional and ubiquitous to prepare crystalline materials. However, SSR approach is quiet ordinary but it is most promising for scaling up the production of the material. SSR approach comprises mechanical force to mix the solid constituents such as carbonates, oxides, fluorides and sulphides etc. The solid constituents are grinded for long time to allow these constituents mix together homogeneously and place this homogeneous mixture at elevated temperatures to undertake the diffusion process. In this methodology, the chemical reaction takes place at the stage where the reactants are in intimate contact with each other. Afterwards, the product layer is formed at the interface between the reactants which further proceed the reaction by the diffusion of each reactant. This process relies on various factors such as structure of product and reactants, size of the diffusion ions, presence of defects and reaction temperature. Several key points must be taken into account before begin the experimental practice for solid state reaction method such as melting temperature, vapour pressure and decomposition temperature etc. Moreover, appropriate environment needs to be

provided in accordance to the requirement and stability of the reactants. Crucible selection is crucial to sinter or calcine the sample at high temperature, a chemically inert as well as thermally stabilized crucible material such as alumina (Al_2O_3) or platinum must be selected [65,66].

Furthermore, continuous grinding of reactants may peel-off the layer formed at the interface of the product and form a contemporary layer while forming a final product. Homogeneous grinding improves the surface area and reduces the particle size as well as diffusion path. However, a non-uniform and larger size particle (usually in micrometer range) are achieved through grinding and mixing process or commonly known as solid state reaction method. There are few merits of the SSR approach which encourage to opt the methodology to prepare the sample using this approach.

2.2.2. Merits of SSR approach

(i) Easy to synthesise

(ii) Availability of precursors

(iii) Low cost production

(iv) Eco-friendly process, no toxic gases liberate

(v) Large scale production

2.2.3. Synthesis procedure to prepare RE doped $Na_4Ca_4Si_6O_{18}$ phosphors

In the current experimental process, a series of samples with empirical formula $Na_4Ca_4Si_6O_{18}$ have been synthesized through conventional solid-state reaction approach. In this, the raw materials listed as Na_2SiO_3, CaO, SiO_2 and RE_2O_3 with high purity were taken and mixed up in the stoichiometric ratio according to chemical reaction given below in presence of acetone (dispersing medium) via manual grinding process. After continuous grinding for 1 h, the powder sample was placed into alumina crucible for the heat treatment. Initially, the sample was heated at 650 °C for 1 h and then further temperature is raised till 900, 950 and 1000 °C for 3h to improve the crystallinity of sample. Finally, the sample was allowed to cool down till the room temperature

and the sintered sample is ground to make fine powder for further investigations. The optimum crystallinity has achieved at 950 °C and all the samples were synthesized at optimum temperature. The detailed process has been represented in the Fig. 2.1.

Chemical Reaction:

$$2\ Na_2SiO_3 * 5\ H_2O + 4\ CaO + 4\ SiO_2 \rightarrow Na_4Ca_4Si_6O_{18} + 10\ H_2O$$

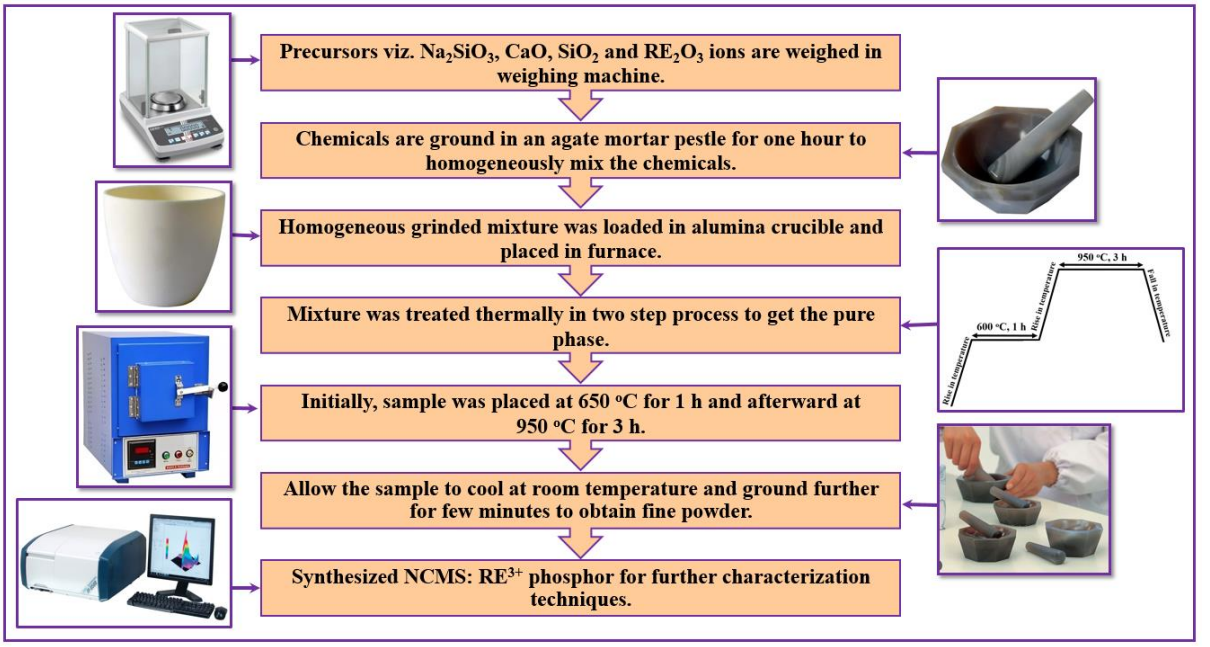

Fig. 2.1. *Flow chart of SSR method to synthesize NCMS: RE^{3+} phosphor.*

2.3. Characterization techniques

This chapter describes the essential characterization techniques to investigate the structural, morphological, photoluminescence and lifetime decay properties of as-synthesized rare earth doped $Na_4Ca_4Si_6O_{18}$ phosphors for optoelectronic applications. In order to optimize the sample and various other parameters of the materials, the relevant characterization techniques are vital to explore and has been discussed in further sections given below.

2.3.1. Thermal Analysis

In the field of physicochemical science, thermal analysis is a technique which study the behaviour of materials and quantified in response to change in temperature. Thermal analysis is used for investigation of various other studies such as mass, enthalpy, dimension, melting

temperature, cooling temperature, freezing temperature and dynamic characteristics etc. In addition, thermal analysis is widely applicable in a variety of disciplines remarkably from pharmaceutical to polymer and material sciences to understand the behaviour with respect to time and temperature but it is not feasible technique to understand the structure of materials [67]. In order to analyse the thermal properties of the materials, most basic thermal analytical techniques are as follows: thermogravimetric analysis (TGA) and differential thermal analysis (DTA).

2.3.1.1. Thermogravimetric analysis (TGA)

TGA is a technique in which the mass of sample is measured with respect to gradual increase in temperature and leads to interpret thermal events that happened during the process such as decomposition, absorption, adsorption, desorption, vaporization, sublimation, reduction and oxidation etc. The evaluation of volatile or gaseous products or byproducts loss during chemical reaction for materials viz. polymer, composites, nanomaterials, fibres and thin films can be observed using TGA [68]. Fig. 2.2 (a) represent the block schematic of thermogravimetric instrument which is most widely used for TGA analysis is thermobalance and the recorded data in the form of TGA curve is known as thermogram. An alternative and complimentary representation of TGA curve with respect to temperature is the first derivative of TGA, generally known as differential thermogravimetric analysis or DTG which clearly show the rate at which weight loss taking place [69]. There are certain factors and conditions that are necessary to take in notice while performing the TGA analysis are as: weight and volume of sample, physical form of sample, shape and nature of sample holder, nature of atmosphere under which the analysis performed, pressure of the atmosphere maintained in the chamber and rate of heating as well as cooling. Thermal analysis has been carried out using Labsys Evo instrument from Setaram, as shown in Fig. 2.2 (b).

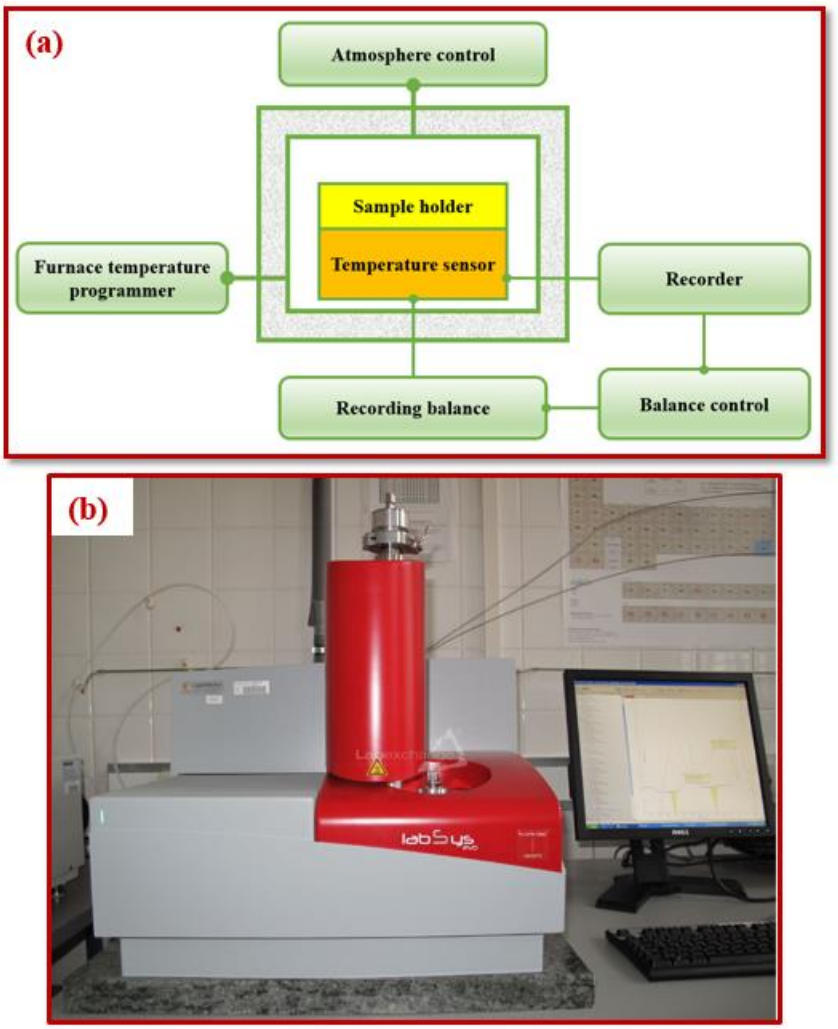

Fig. 2.2. ***(a)*** *Schematic diagram of thermogravimetric analysis* ***(b)*** *Setaram Labsys EVO TGA/DTA analysis instrument.*

2.3.1.2. Differential thermal analysis (DTA)

It is one of the crucial thermal analysis technique which measures the temperature difference between analyte (sample) and reference (mainly alumina) as a function of temperature whilst both analyte and reference are treated thermally at a controlled atmosphere. The thermogram or DTA curve is basically a plot between differential temperature (ΔT) and reference temperature (T) which reveals the variation in the mass of sample due to absorption (endothermic) and evolution (exothermic) of heat associated with the reference during gradual heat process [70,71]. DTA is used to determine various other aspects of material such as heat of reactions, sample mass and thermal conductivity etc.

2.3.2. X-ray diffraction (XRD)

2.3.2.1. Basic principle

X-ray diffraction is a non-destructive and versatile technique used for identification of crystal structure, crystallite size and strain of materials employed in various institutions/industries. Diffraction technique can recognize the chemical compositions from crystal structure instead the elements [72]. X-ray diffraction is the phenomena in which an incident x-ray beam's wave interferes with one another as a result of the uniform spacing of the atoms in the crystal structure. The crystalline structure is an array of atoms ordered in a systematic pattern in three dimensional space known as lattice. The smallest reoccurring element of the crystal is called unit cell in which the size and shape of the unit cell are expressed by the angle between axes as α, β, γ and the length of the three translational axes are *a, b, c*. In a crystal structure, based on the angles between axes, length and symmetry, seven crystal systems are categorised, which further sub-divided into 14 Bravais lattices. This technique was discovered by Von Laue in 1912 for both quantitative and qualitative investigation of polycrystalline materials. Each crystalline material has a unique diffraction pattern, including a precise location of diffraction lines and their peak intensities. Such diffraction patterns are complicated and impossible to have similar diffraction peak profile of the materials. Thus, x-ray diffraction contributes significantly to the identification of a crystalline materials as "fingerprints" [73,74].

2.3.2.2. Instrumentation

X-ray diffractometer is an instrument used to examine the crystal structure of single and crystalline samples. A spectrum for diffraction intensity versus angle between incident and diffracted beam is recorded via continuous change in the incident angle of X-ray beam. Fig. 2.3. represents the geometric arrangement of diffractometer consists essentially X-ray source, sample and detector. In the X-ray diffraction, diffractometer is to detect the diffracted x-rays from the materials and measure the intensity as a function of diffraction angle (2θ). The generated X-rays

in the X-ray tube passes through a slits which collimate the X-ray beam and prevents the beam divergence while incident on the specimen. The specimen is in the form of flat plate which is supported by the specimen table (sample holder) [75,76]. The incident X-rays are diffracted from the sample and forms a convergent beam which passes through the monochromator (monochromatic filter) before entering into the detector for further record. The monochromatic filter is generally placed in the path of diffracted beam instead of incident beam in order to suppress the wavelengths other than K_α radiation and reduce the background radiation generated within the sample.

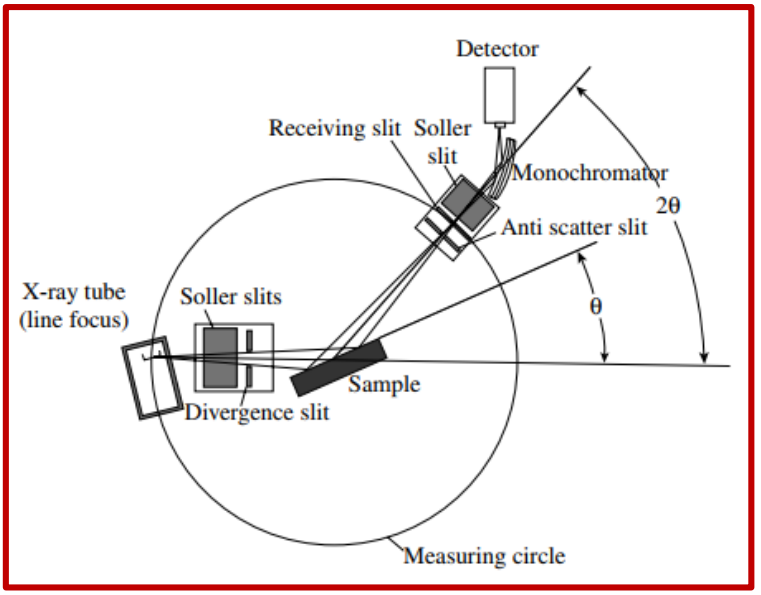

Fig. 2.3. *Schematic diagram of geometric arrangement of x-ray diffractometer.*

2.3.2.3. Bragg's law

According to Bragg's analysis, the crystal lattice planes or the atomic planes are assumed to be arranged in the layered format and these layers are separated by a distance d in the crystal. Furthermore, when a monochromatic x-ray beam incident on the crystalline solid sample which will get diffracted by the lattice plane with the equal angle between the incident ray and the equivalent diffracted beam, as shown in Fig. 2.4. In order to produce a constructive interference, the path difference must be equal to the integer multiples of the wavelength. The general

relationship between the incident x-ray wavelength, angle of incidence and the spacing between the crystal lattice plane has been explained by the Bragg's law as mentioned below:

$$n\lambda = 2d \sin\theta \qquad (2.1)$$

where, n is the integer signifies the order of diffraction, λ is the wavelength of incident x-rays, d is the interplanar spacing and θ is the diffraction angle.

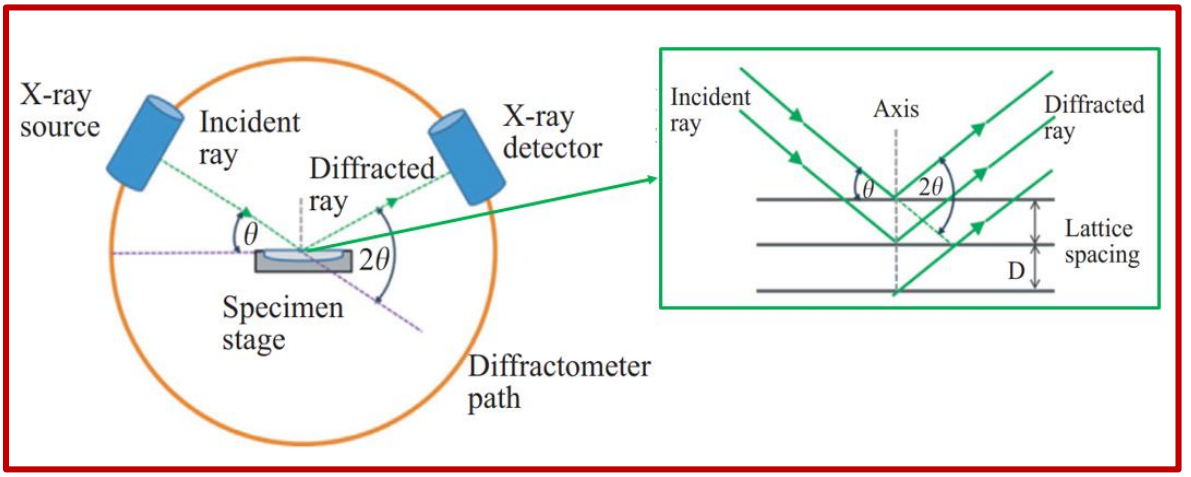

Fig. 2.4. *Schematic diagram of x-ray diffraction from the crystal lattice plane.*

2.3.2.4. Data collection and analysis

The diffraction measurement output is obtained when a plot against x-ray diffraction intensity and Bragg's angle is drawn. In general, the diffraction pattern measured in the *2θ* range of 10-70° is sufficient to determine the phase of inorganic material. The scan time can be optimized to obtain better diffraction pattern with good intensity of diffraction peaks [77]. In the current analysis, the obtained diffraction pattern was associated with the JCPDS (Joint Committee on Powder Diffraction Standard) database available for the reported crystalline samples. Moreover, when assessing the size of grains, it is based on the idea that smaller grains or crystals will result in wider diffraction patterns, also referred to as peak broadening [75]. Therefore, broadening of an XRD peak indicates that a small crystallite does not have sufficient viable planes to provide fully destructive interference. Using the Debye Scherrer's equation shown below, one may determine a average crystallite size (*D*) of the samples:

$$D_{hkl} = \frac{k\lambda}{\beta_{hkl} Cos\theta_{hkl}} \quad (2.2)$$

where, λ denotes the x-ray wavelength of Cu-K_α radiation used in XRD, β indicates the FWHM of the diffraction peak corresponds to a particular angle θ. Furthermore, the Williamson-Hall (W-H) equation was employed to calculate the crystallite size (D) and strain (ε) of the sample using below equation (2.3) [76]:

$$\beta Cos\theta = {K\lambda}/{D_{hkl}} + 4\varepsilon\, Sin\theta; \text{ where } K \text{ is the shape factor} \quad (2.3)$$

The XRD pattern in the current work has been recorded using Smartlab high resolution X-ray diffractometer from Rigaku as shown in Fig. 2.5 (a). The PANalytical EMPYREAN X-ray diffractometer (Fig. 2.5 (b)) is the another diffractometer used to measure the diffraction pattern. The diffractometer consists of X-rays of Cu-Kα beam (λ = 1.5406 Å) as radiation source. The scanning rate and the angular detection range of XRD machine are 0.013° sec^{-1} and $10 \leq \theta \leq 70°$, respectively with an accelerating voltage of 40 kV and current 30 mA.

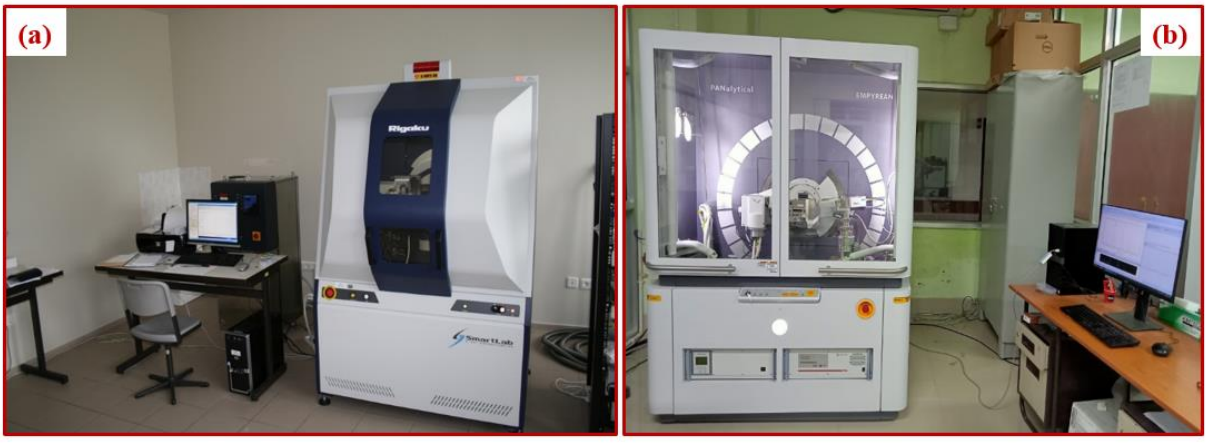

Fig. 2.5. ***(a)*** *Rigaku high resolution x-ray diffractometer* ***(b)*** *PANalytical EMPYREAN x-ray diffractometer.*

2.3.3. Field emission scanning electron microscope (SEM/FE-SEM)

SEM or FE-SEM is a microscopic analytical technique that creates a highly magnified image based on the reflection of electrons while scanning by the electron beam produced from the mounted probe arranged to eject electrons. SEM has the capability to scan the sample surface up to few microns. Following the instrumental description, SEM is conducted into the vacuum

chamber which holds the sample to be measured. The scanned sample's morphology is determined by the electrons that are reflected from the dark chamber after the electron is emitted from the probe to that chamber. The image captured from the SEM may vary due to compositional and topographical or morphological (shape) features of the prepared samples.

2.3.3.1. Instrumentation and basic principle

Initially, the electron gun (probe) placed at the top ejects electron beam in the vacuum chamber and follows the downward path through the electromagnetic fields. The electron beam focused onto the specimen using objective lenses fixed in the same chamber. This focused beam scans over the specific area of the specimen surface where the beam is rastered (point by point scan) across the material's surface using deflector coils, which is controlled by the scan generator. The size of the rastered region on the sample can be adjusted by the variation in magnification, as magnification controls the size of the rastered area. When the electron beam strikes on the surface of the material, large number of signals are produced from the specimen such as electrons (secondary and backscattered) and x-rays [78,79]. These propagated signals are detected by the detector and converted into the signals which further produced the images (topology and morphology) of the specimen. The schematic diagram represent the principle followed to collect the SEM images, as shown in Fig. 2.6.

Before capturing the SEM image of the specimen, some pre-requisite has to be followed in order to obtain the high quality image. In the beginning, the applied accelerating voltages should be modulated according to the nature of the sample. The high accelerating voltage elevate the probe current which may reduce the contrast and signal to noise ratio. Indeed, high accelerating voltage may cause overcharging for conductive or non-conductive samples and reflect extreme brightness and poor image. Therefore, optimum high accelerating voltage is required to capture highly magnified image with good resolution. Moreover, non-conductive samples such as

polymer, fibres, glass and ceramics are sputtered with a layer of carbon or metals such as gold/platinum/gold-palladium to prevent the sample from the cause of overcharging.

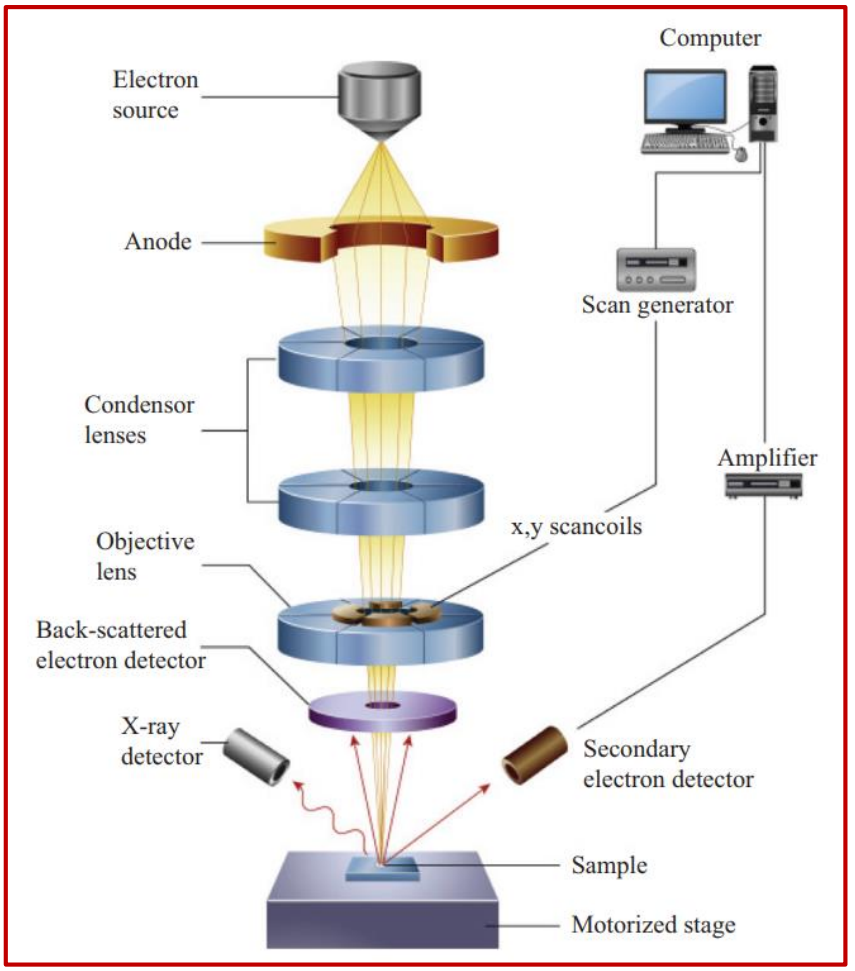

Fig. 2.6. *Schematic diagram of scanning electron microscope (SEM).*

The length of the line (or longitudinal area) that is scanned or "rastered" by the electron beam, as described in earlier section, directly affect the magnification (M). The magnification can be defined as the ratio of the length of the line on the screen (L) to the length of the rastered line on the material (l) and represented as M=L/l. Since, the size of the monitor is fixed, thus the variation on the length of rastered line can change the magnification of the reflected image. A wide area of scan results lower magnification whereas smaller scan area provides higher magnification. Thus, SEM proved to be a versatile technique to obtain a remarkable features of the materials such as morphology includes size, shape and organization of particles etc. [80,81].

In the current study, FE-SEM images were recorded using NOVA NanoSEM 450 scanning electron microscope, as shown in Fig. 2.7. NOVA NanoSEM 450 is a modern field emission scanning electron microscope with 1 nm ultimate resolution, large sample chamber with advanced motorized stage and navigation supported by an in-chamber camera. In this, high as well as low vacuum operation is possible. This microscope is equipped with additional features such as energy dispersive x-ray analysis (EDAX) and scanning transmission electron microscope (STEM) etc.

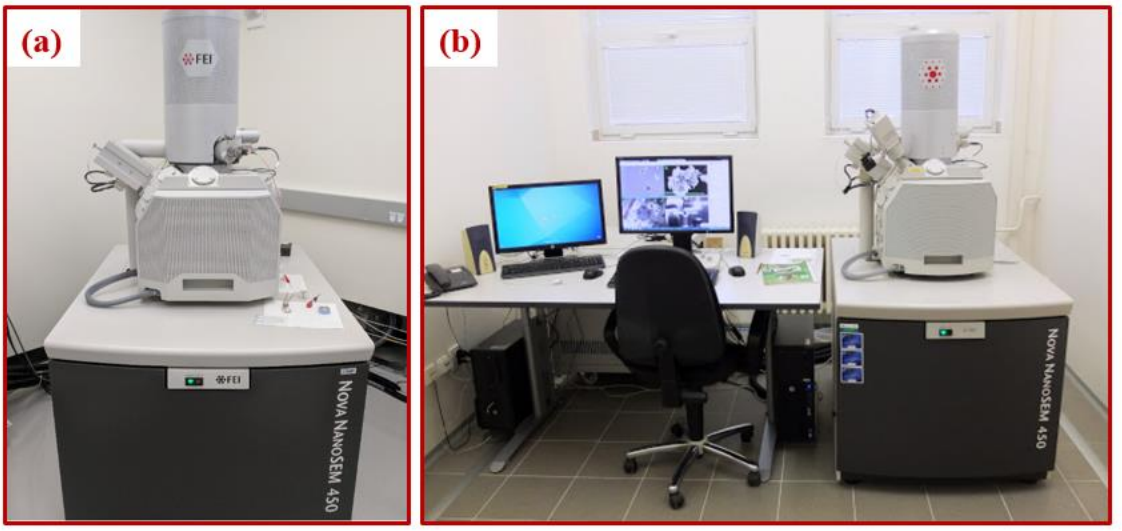

Fig. 2.7. *NOVA NanoSEM 450 field emission scanning electron microscope.*

2.3.3.2. Energy dispersive analysis of x-rays (EDAX)

EDAX is a powerful technique and applied along with SEM/FESEM to analyse the types and quantity of the elements at the materials surface or in the vicinity of surface to provide specimen image. EDAX explained as the generation of x-rays from the sample through electron beam. Following the basic principle of EDAX technique, the x-rays are produced according to the characteristics and nature of the elements present in the material. Three principal components exist in the EDAX systems are x-ray detector, pulse processor (measure corresponding voltage of emitted x-ray) and a computer system. In the EDAX system, x-rays emitted from the sample are measured by the x-ray detector in which x-rays generates current. The small generated current further converted into voltage pulse associated with the x-rays produce by the particular element to accomplish the elemental analysis [82].

2.3.4. Fourier transform infrared spectroscopy (FT-IR)

2.3.4.1. Instrumentation and basic principle

Fourier transform infrared spectroscopy is one of the most widely used analytical techniques for the identification of functional groups in inorganic, organic and biological compounds. This versatile technique signifies the quality and consistency of the components. The IR source, interferometer, sample chamber, detector, and display screen are the main parts of the FT-IR system, which operates based on the Michelson interferometer fundamental concept. Fig. 2.8 (a) represents the schematic of fourier transform infrared (FT-IR) spectroscopy. In the FT-IR system, interferometer contains two mirrors (movable and stationary) and one beam splitter. Initially, before reaching to the sample, the beam passes through interfere wherein the beam splits the radiation into two rays headed towards stationary and movable mirror. Once the rays reunite after travelling through different path with different mirrors, it results a signal called interferogram which consists information regarding the emitted IR radiation from the source. This information coded signals in the form of radiation strikes the sample where some part of the radiation is absorbed whilst some part is get transmitted. Further, specific signal is recollected in the detector based on the type of material and the bonds among the present components. Since, the signal detected by the detector is difficult to read, thus it is decoded using well known mathematical tool known as fourier transformation and the technique is called as fourier transformation infrared spectroscopy [83].

2.3.4.2. Sample preparation

To prepare the sample for FT-IR analysis, the sample was mixed with the KBr powder in a specific ratio of 1:300 (sample: KBr) in mg and ground this mixture in an agate mortar for 10-15 min to make fine and homogeneously mixed powder. Afterwards, the pellet is formed using hydraulic press in a circular shape and specific size. The KBr pellet technique is used to record FT-IR signals for our samples, as the KBr has strong tendency to pass all IR radiation [84]. In this

research work, Perkin Elmer spectrum two FT-IR spectrometer has been used to analyse the FT-IR analysis of our sample, as shown in Fig. 2.8 (b).

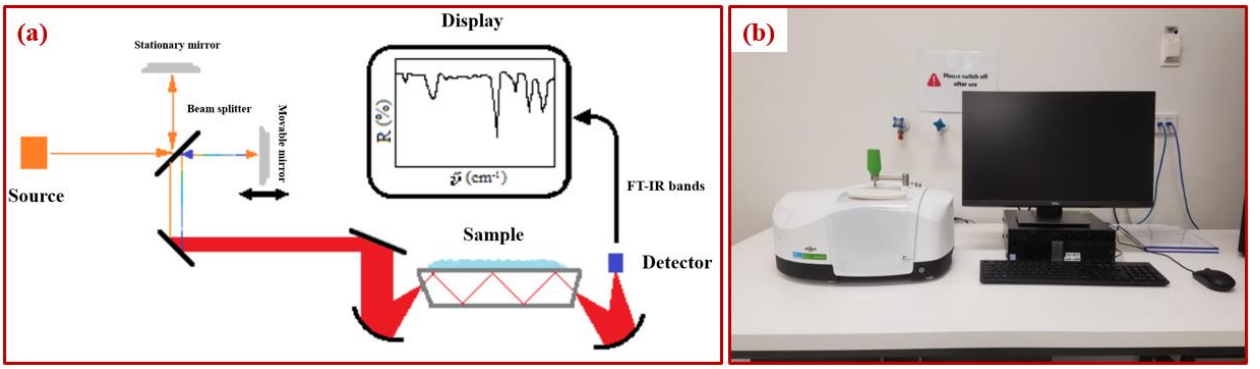

Fig. 2.8 ***(a)*** *Schematic diagram of FT-IR spectroscopy* ***(b)*** *Perkin Elmer spectrum two FTIR spectrometer.*

2.3.5. Diffuse reflectance (DR) spectroscopy

2.3.5.1. Principle of DR spectroscopy

DR spectroscopy (DRS) is one of the most crucial spectroscopic techniques based on the reflection of light in ultraviolet, visible and near-infrared regions in order to determine the optical band gap of the powder sample for various optoelectronic applications. In addition, the reflection of electromagnetic light generally occurs on the basis of the texture of the sample. In powder sample, the randomly oriented particles of variable sizes reflected the incident light in all angles into the hemisphere of provenance of light. Contrary to the regular (directed) reflection from the plane phase boundary, the phenomena caused by reflection, refraction, diffraction and absorption by particles oriented in all direction is known as diffuse reflection. Fig. 2.9 (a). illustrates that the incident light reflected in all directions by two types of reflection (i.e. specular and diffuse reflection) after interacting with the sample [85,86].

When a beam of electromagnetic radiation incident on the surface of the sample then the parts of incident light get reflected, absorbed and transmitted from the sample. The potential to reflect radiant energy is referred to as its reflectance. It is the portion of incident electromagnetic

energy that is reflected at an interface. Reflectance versus wavelength plot reveal the reflectance spectrum.

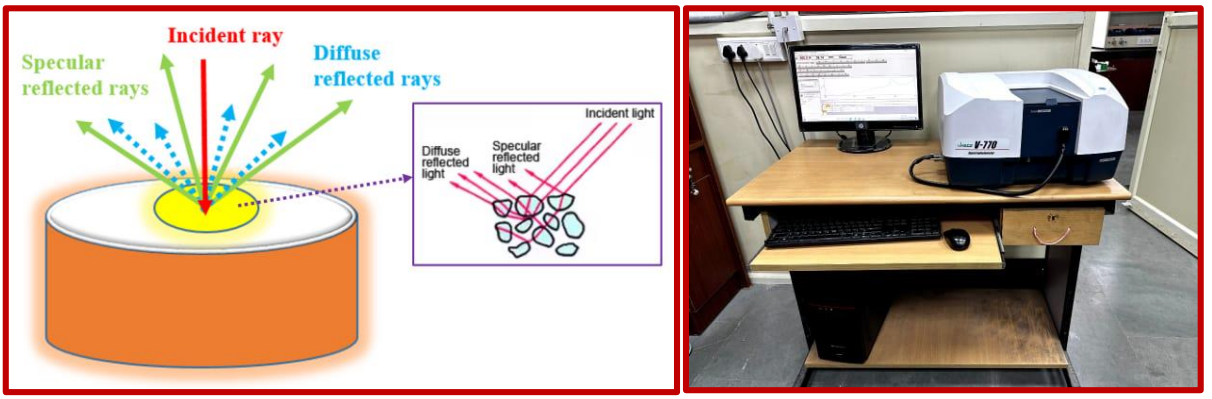

Fig. 2.9 (a) *Schematic diagram of reflectance from the sample (b) V-770 Jasco spectrophotometer*

2.3.5.2. Formulation and data analysis of diffuse reflectance spectra

As expressed earlier, DRS is an essential technique to determine the optical band gap of the powder samples. To evaluate the band gap (E_g) of the as-prepared materials, Tauc method has been followed using the scientific relationship between E_g and α (optical absorption coefficient) shown below:

$$\alpha h\upsilon = A(h\upsilon - E_g)^n \qquad (2.4.)$$

where, α refers as the absorption coefficient, $h\upsilon$ is the energy of incident photons, A is the proportionality constant and n is the coefficient that reveals the type of electronic transition. The electronic transition depends upon the value of coefficient 'n' expressed as the direct allowed transition for n equal to 1/2, indirect allowed transition for n equal to 2, direct forbidden transition for n equal to 3/2 and indirect forbidden transition for n equal to 3. Since, absorption is the factor essentially required to assess the Tauc method successfully. However, the scattering component is rather acknowledgeable in case of powder samples. The recorded DR spectrum has been transformed into the equivalent absorption spectra using the function known as Kubelka-Munk (K-M) function or reemission factor $F(R_\infty)$, is expressed as given below [87]:

$$F(R_\infty) = \frac{K}{S} = \frac{(1-R_\infty)^2}{2R_\infty} \quad where, R_\infty = \frac{R_{sample}}{R_{standard}} \qquad (2.5)$$

$$(F(R)h\upsilon) = B(h\upsilon - E_g)^n \quad (2.6)$$

In the above equation, R_∞ denotes as the reflectance of the sample with "infinite thickness", and other parameters such as *K*, *S* and *B* represent absorption coefficient, scattering coefficient, and proportionality constant, respectively. The R_∞ is the ratio between the reflectance of the sample (R_{sample}) and diffuse reflectance of standard material ($R_{standard}$) where the standard material is typically are $BaSO_4$ or polytetrafluoroethylene (PTEE). Consequently, the optical band gap can be ascertained by extrapolating the linear streak to $(F(R)h\upsilon)^{\frac{1}{n}}$ =0 in $(F(R)h\upsilon)^{\frac{1}{n}}$ versus $h\upsilon$ plot, using equation (2.6). In this experimental work, the diffuse reflectance measurement has been carried out at room temperature using V-770 Jasco spectrophotometer as shown in Fig. 2.9 (b).

2.3.6. Photoluminescence (PL) spectroscopy

Photoluminescence (PL) spectroscopy is a contactless, non-destructive and powerful technique to investigate the luminescent properties of the focused material. It involves the principle of photoluminescence in which the material undergoes the photoexcitation and eventually provides emission of light. A graph of photoluminescence expresses the relation between emission intensity versus wavelength. The intensified emission peak signifies the energy required to perceive the excitation spectrum, which further utilized to observe the exact emission spectrum of the phosphor material. Both excitation and emission spectra plotted against the wavelength lie on x-axis (abscissa) whereas the intensity as arbitrary unit lie on y-axis (ordinate).

2.3.6.1. Instrumentation and data analysis

The spectrofluorophotometer contains four basic components includes excitation light source, sample holder and detector. The prime component is the excitation source which gives continuum spectrum light instead of line spectra. For the present research, xenon lamp employed spectrofluorophotometer is used as an excitation source which provide a continuous emission of light with constant intensity covers 200-800 nm range. The light emitted from the excitation source

spread in all possible directions, which narrowed down with the help of monochromator assembled in the instrument. Furthermore, the monochromator includes diffraction grating having large aperture to collect intensified excitation light to transmit to sample holder loaded with phosphor sample. The sample first absorb the excitation light and then emit light in the visible region, which will be collected by the detector. Photomultiplier tube (PMT) is used as a detector that provide considerable spectral response associated with the collective luminescence light. For some cases, the sample exhibit unstable and non-uniform emitted light from the source results greater noise and signal distortion. To prevent the issue, an additional system (source compensation system) is used wherein a PMT with a reference cell is placed beside the excitation monochromator to monitor and fix the distorted signal and transmit smooth signal back to the detector. Both photoluminescence excitation and emission spectra were measured at room temperature by adjusting parameters such as scan rate, sensitivity, response time, bandwidth, measurement range and data interval etc. [88,89].

However, the photoluminescence studies of phosphor sample have been accomplished at elevated temperature up to few 150 °C temperature using temperature dependent photoluminescent (TDPL) equipment in which the temperature is raised by an additional heating component attached with it. TDPL is the most effective and powerful technique used to analyse the thermal stability of the material. Determining the thermal stability is fundamental and technologically approved approach before implementing the material for optoelectronic device applications since these devices already have excess heat liberation issue. Moreover, the PL profile should not change while performing the TDPL characterization, but the intensity may vary in order to inspect the thermal stability of the samples. In general, the thermal stability is associated with the phenomenon is called as thermal quenching which have been explained in section 1.8.6. The minimum thermal quenching revealed at higher temperature implies higher thermal stability and provide a thermally stable phosphor.

Time resolved (TR)-PL spectroscopy is used to measure the lifetime of the excited state. Generally, the overall PL data obtained by the radiative (τ_R) and non-radiative (τ_{NR}) recombination lifetimes. The lifetime can be recorded as the summation of radiative and non-radiative decay rates. The lifetime plot of the material generally exhibits an exponential curve which can be fitted either with single or bi- or tri- exponential equations. Thus, the non-radiative relaxation can be contemplated from the fitted TR-PL data which elucidates the significance of TR-PL spectroscopy [90–92].

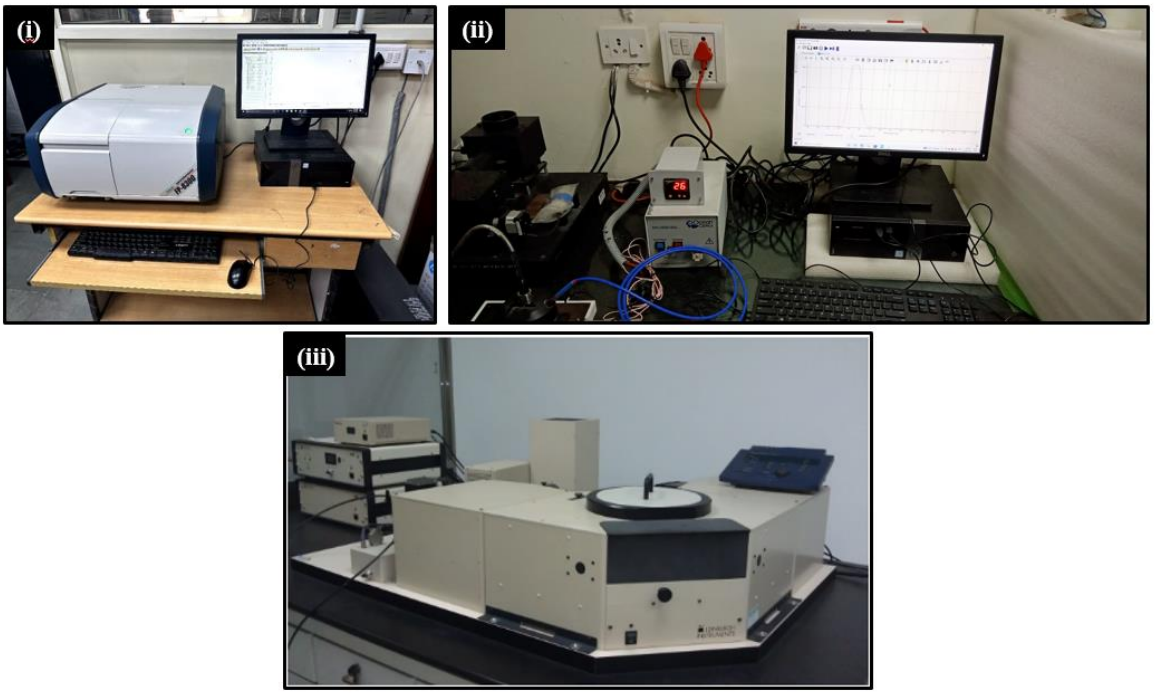

Fig. 2.10 *(i) JASCO FP-8300 spectrofluorophotometer for PL measurement (ii) Ocean Optics spectrofluorophotometer (FLAME-S-XR1-ES) for TDPL studies (iii) Edinburgh FLS980 to measure lifetime.*

Altogether, the luminescent features of the phosphor materials are measured using different spectrofluorophotemeters in the present thesis work listed as: (i) JASCO FP-8300 spectrofluorophotometer for PL measurement (ii) Ocean Optics spectrofluorophotometer (FLAME-S-XR1-ES) for TDPL studies (iii) Edinburgh FLS980 to measure lifetime.

Chapter 3

Photoluminescence studies of UV excited blue to green emitting Tb^{3+} activated sodium calcium metasilicate color tunable phosphor for luminescent devices

Tb^{3+} doped $Na_4Ca_4Si_6O_{18}$ (NCMS: Tb^{3+}) phosphors have been synthesized via solid state reaction route with increasing dopant concentration. The phase identification studies for NCMS: Tb^{3+} phosphors have been done through XRD technique. The XRD patterns for as-synthesized phosphors showed satisfactory agreement with the standard pattern (JCPDS card no. 75-1687) of $Na_4Ca_4Si_6O_{18}$ compound. The morphology and size of particles have been illustrated with FE-SEM *micrographs. PLE spectrum of Tb^{3+} doped $Na_4Ca_4Si_6O_{18}$ phosphor depicts the strong excitation peak obtained in UV spectral region. The trivalent terbium activated NCMS phosphors excited under UV region (232 nm wavelength) exhibit intense emission in blue (350-470 nm) and green (470-650 nm) spectral regions. With increasing the concentration of Tb^{3+} ions in host matrix, the emission color shifts from blue to green region due to cross relaxation energy transfer (CRET) mechanism and shows the tunable behaviour of Tb^{3+} activated as-synthesized NCMS phosphor. The aforementioned results manifest that Tb^{3+} activated sodium calcium metasilicate phosphor has an immense potential to contribute as a green and blue-green emitting component in lighting and display device applications.*

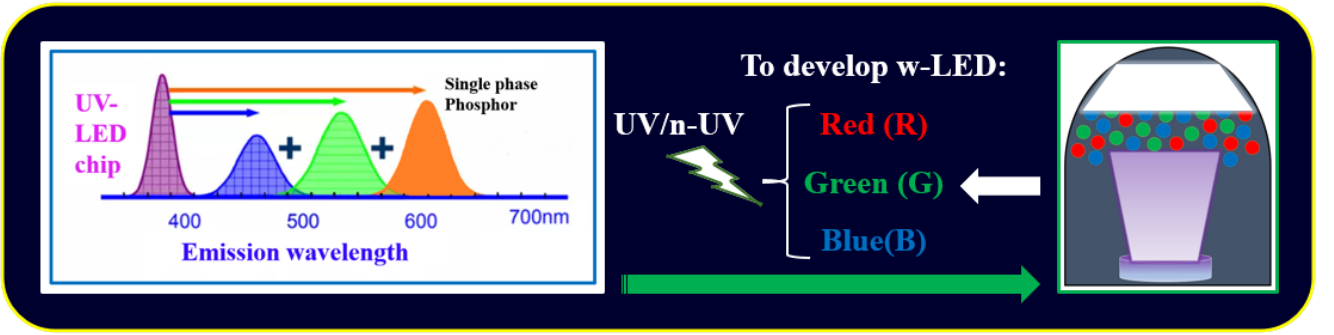

3.1. Introduction

In recent years, rare-earth (RE) activated phosphor materials have offered a substantial input in bringing a revolutionary change in the modern lighting technology [93,94]. In this technology, phosphors have become the center of sight to the researchers owing to their crucial role in solid state lighting (SSL) as white light emitting diodes (w-LEDs). Moreover, phosphors have found potential utility in other fields such as fluorescence detection, artificial photosynthesis, anti-counterfeiting, temperature sensing and bio-imaging etc. [95,96]. The phosphor converted (pc)-w-LED is accepted as a smart lighting source for future generation on the account of conspicuous features such as high illumination, low energy consumption, less emission of toxic gases, longer working lifetime, better performance and potential to substitute conventional incandescent and fluorescent lamps [97,98]. The conventional w-LEDs can be fabricated with the conjunction of red (R), green (G) and blue (B) LEDs to achieve efficient white light. However, the above-mentioned combined LEDs are inaccessible as individual LED demands different driving currents to provide constant white emission. However, pc-w-LEDs that are fabricated by layering yellow emitting phosphor (YAG: Ce^{3+}) on the top of blue emitting InGaN LED chip have proven to be advantageous over RGB LEDs due to high brightness, simple fabrication and cost-effectiveness [99]. Despite of these advantages and its on-going commercial practice, people are refraining to use it due to some drawbacks such as less efficiency, halo effect, low color rendering index (CRI<80) and high correlated color temperature (CCT>7000 K) [100]. The issues raised in phosphor based LEDs, can be resolved by exciting either a mixture of green and red phosphors via blue LED chip or a mixture of blue-green-red phosphors via UV/near(n)-UV LED chip. Therefore, the efficient blue-green light emitting phosphor is crucially required to get the effective white light with higher values of CRI and lower CCT values.

The trivalent terbium (Tb^{3+}) ions with $4f^n$ electronic configuration employed as a green emitting centers based on the transitions between their 4f levels. Tb^{3+} ion is an efficient absorber

for UV region and it also shows absorption in the n-UV region with most of the hosts. Hien et. al. presents Tb^{3+} doped ZnS quantum dots with multiple excitation peaks in the UV and n-UV range [101]. The excitation and emission of Tb^{3+} ions are affected by the symmetry of metal ions and nature of bonding with coordination ligands [102]. The strong visible emission can be obtained from the cross relaxation energy transfer (CRET) process among Tb^{3+} ions [103,104]. Appropriate host lattice is mandatory with suitable Tb^{3+} ion concentration in order to achieve intense green emission from Tb^{3+} activated phosphors. Undoubtedly, the efficient host lattices provide an advantageous contribution to synthesize an effective phosphor with proficient luminescence properties. Despite the availability of numerous oxide hosts such as borates, phosphates, tungstates, molybdates, and vanadates etc., the silicates have been the preferential choice since they have good physical-thermal-chemical stability with wide band gap and low thermal expansion coefficient [105].

However, silicates are the most abundant in nature and they are categorised as ortho (1:4), meta (1:3) and pyro (2:7) depending upon Si:O ratio [106]. Amongst various metasilicates, the $Na_4Ca_4Si_6O_{18}$ occurs as ternary compound in a Na_2O-CaO-SiO_2 system. Ohsato et. al. determined $Na_4Ca_4Si_6O_{18}$ structure consists of tightly packed six membered $[Si_6O_{18}]^{12-}$ rings of silicate tetrahedral that stacked in a cubic close packed arrangement with alkali and alkaline earth ions [107]. Further, it has been investigated that the structure has phase transition with the variation in temperature. At elevated temperature, the rhombohedral crystal occurs, whereas hexagonal structure of $Na_4Ca_4Si_6O_{18}$ has been formed at lower temperature. The difference in structure may be observed due to change in temperature and can be expressed in the form of cation coordination polyhedral and arrangement of $[Si_6O_{18}]^{12-}$ rings [64,108]. Alkaline based metasilicate compounds are the substantial class of phosphors for incorporating many trivalent luminescent centres. These materials possess exciting features such as good thermal as well as chemical stability, low thermal

expansion, wide band gap and better insulation properties for the applications in paint, coating and biomedical diagnosis etc [109].

In this chapter, Tb^{3+} ions doped $Na_4Ca_4Si_6O_{18}$ phosphor have been synthesized via adopting conventional solid state reaction method to explore structural, optical, morphological and photoluminescence properties. A series of $Na_4Ca_4Si_6O_{18}$: xTb^{3+} phosphors have been synthesized by varying the concentration of Tb^{3+} ions to achieve optimum concentration with effective green emission. The efficiently green color can be discerned in the CIE color chromaticity plot for the optimized concentration of Tb^{3+} ion and color tunablity from blue to green region can be noticed depending on the concentration of Tb^{3+} ion in the host lattice. The aim of this work is to produce an efficient blue and green component for the utility in generation of pc-w-LEDs with as-synthesized NCMS: Tb^{3+}phosphor.

3.2. Sample synthesis and characterisation techniques

A series of xTb^{3+} doped $Na_4Ca_{4-x}Si_6O_{18}$ (x= 1.0, 3.0, 5.0, 7.0, 9.0 and 11.0 mol%) phosphors were synthesized via conventional solid-state reaction methodology as described in the section 2.2.3. The detailed procedure is represented through the flow chart as shown in Fig. 2.1. Moreover, various characterization techniques have been carried out to investigate the crystalline, morphological and luminescent behaviour of the as synthesized phosphors, described in detail in the section 2.3. (chapter 2).

3.3. Results and discussion

3.3.1. Thermogravimetric analysis (TGA)

Thermogravimetric analysis (TGA) has been done for $Na_4Ca_4Si_6O_{18}$ in the temperature range of 35-1050 °C. The TGA graph illustrates the weight loss that occurred in three distinct steps during the formation of the crystalline $Na_4Ca_4Si_6O_{18}$ sample, as shown in Fig. 3.1. Each step shows a certain percentage of weight loss for various by-products released while forming the crystalline phase of $Na_4Ca_4Si_6O_{18}$. In the prior step (35-220 °C temperature range), maximum

amount of weight loss (about ~18.29 %) has been observed, which arose due to release of H_2O water molecule [110]. Following the prior step, slope of the TGA curve changes with increasing temperature from 220 to 470 °C showing 5.18 % weight loss attributed to the removal of hydroxyl group present in the sample [111]. Following loss till 420 °C, the curve becomes constant until 620 °C which infer that there is no loss occur in this region. Finally, the weight loss appeared in the range of 620-820 °C is around 2.45%, which could be due to the removal of water molecules, carbonates and carbon monoxide. The TGA curve is progressing to flat with a nominal loss after 820 °C temperature, and it has shown a flat curve after 900 °C, indicating that the pure phase can be achieved after 900 °C temperature. Thus, the mixture was calcined at 950 °C to obtain the pure phase of $Na_4Ca_4Si_6O_{18}$ sample.

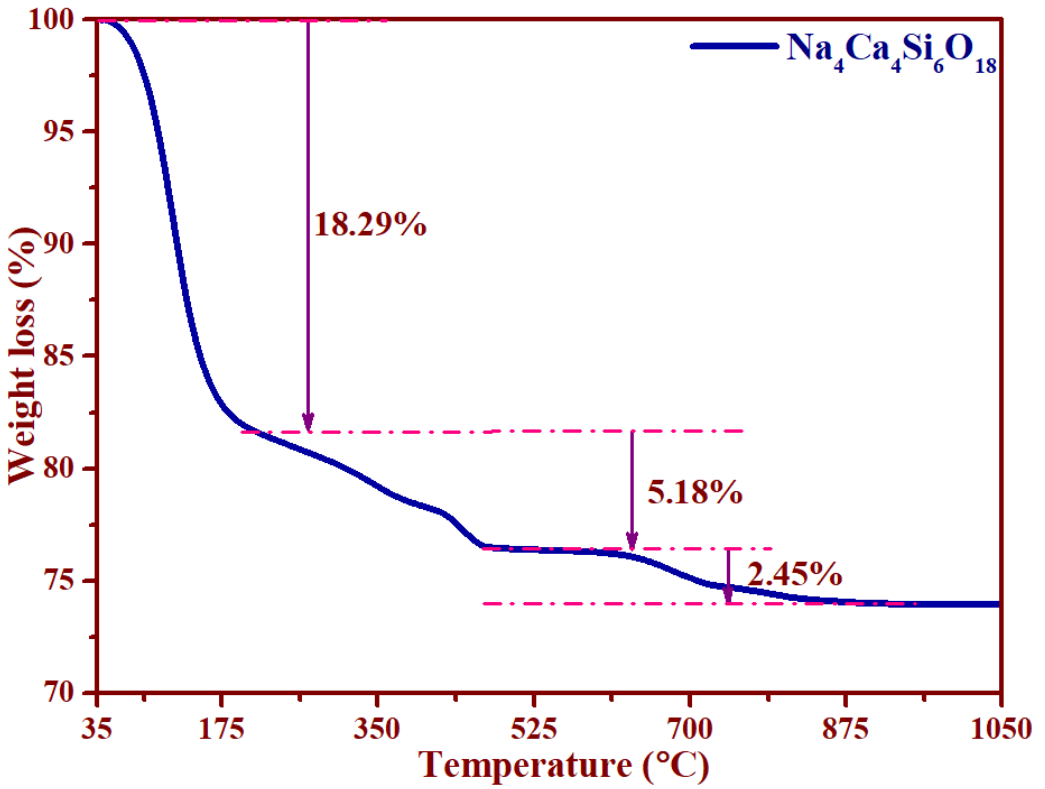

Fig. 3.1. *TGA curve for $Na_4Ca_4Si_6O_{18}$ sample.*

3.3.2. X-ray diffraction

Fig. 3.2(a) depicts the XRD patterns of $Na_4Ca_4Si_6O_{18}$ sample and 1.0 mol% Tb^{3+} doped $Na_4Ca_4Si_6O_{18}$ phosphor calcined at 950 °C temperature along with the standard pattern (JCPDS card no. 75-1687). Fig 3.2(b) explicates the schematic view of $Na_4Ca_4Si_6O_{18}$ sample structure from the c-axis. The diffraction peaks of the undoped and doped samples are well matched with the standard JCPDS pattern indicating that the pure hexagonal $Na_4Ca_4Si_6O_{18}$ crystalline phase has been achieved with space group $P3_2$ and lattice parameters a=10.46 Å; b=10.46 Å; c=13.17 Å and V=1249.42 $Å^3$. The dearth of any additional peak for the as-synthesized phosphor indicates that the dopant ion has been successfully incorporated into the host lattice. The successful incorporation may become possible due to the accomplishment of certain criteria such as comparable ionic radii and nearly same valence state of dopant ion with the substituted ion present in the host lattice [112].

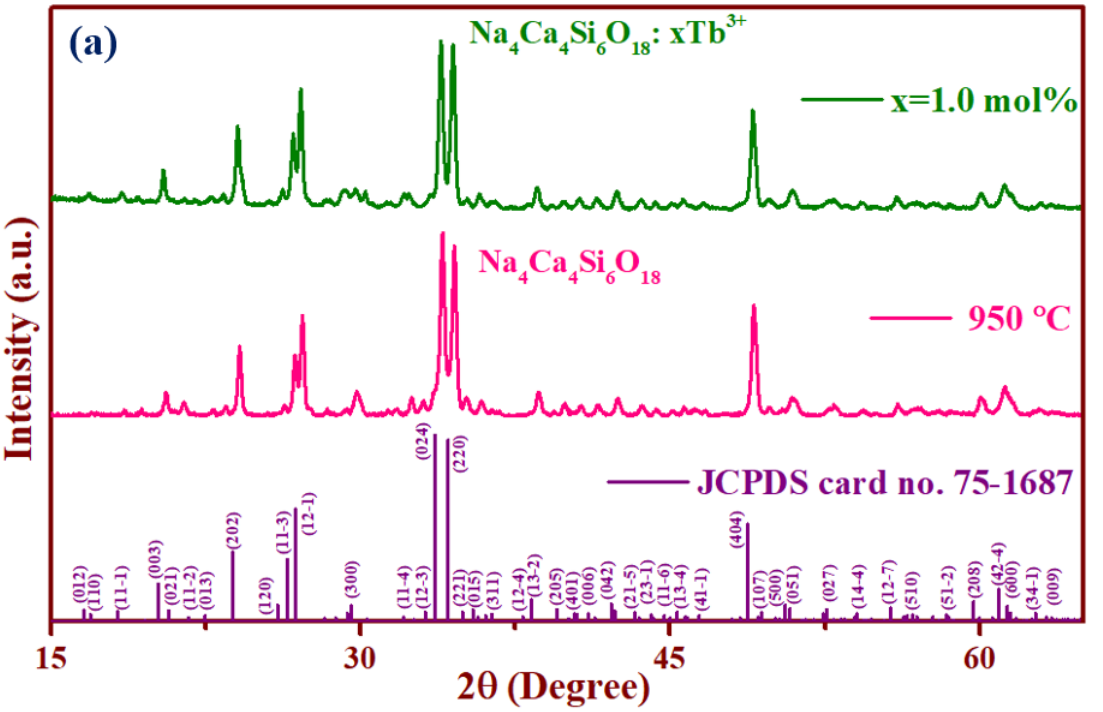

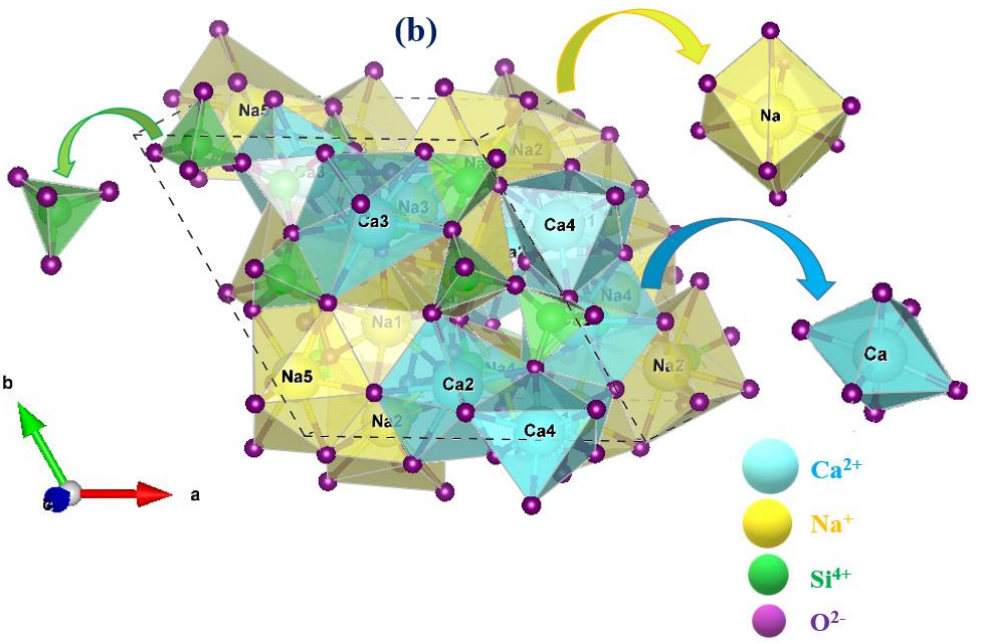

Fig. 3.2. ***(a)*** *XRD patterns of 1.0 mol% of Tb^{3+} doped and undoped $Na_4Ca_4Si_6O_{18}$ phosphor calcined at 950 °C for 3 h along with standard data.* ***(b)*** *Schematic view of crystal structure of $Na_4Ca_4Si_6O_{18}$ from c-axis.*

The ionic radii of ions present in the host lattice Na^+, Ca^{2+} and Si^{4+} are 1.02, 1.00 and 0.4 Å, respectively whereas the ionic radii of Tb^{3+} ion is 0.92 Å. It has been reported that to approach the efficient doping, the percentage difference (%) of ionic radii (D_r) of substituted (R_s) and dopant (R_d) should be below 30%. The lesser percentage difference between ionic radii enhances the site occupying probability. The percentage difference of ionic radii (D_r) can be estimated by employing the following relation [113]:

$$D_r = \frac{R_s - R_d}{R_s} \tag{3.1}$$

where R_s is the respective ionic radii of substituted ion while $R_d$is the ionic radii of dopant ion. The percentage difference of ionic radii is figured as 9.8, 8.0, and 130.0% for ions listed as Na^+, Ca^{2+} and Si^{4+}, respectively. Thus, ionic radii of dopant ions are much favourable to substitute in Ca^{2+} as the computed percentage difference of ionic radii is smaller and feasible to accommodate Tb^{3+} ion without influencing the host lattice. The well-known Debye-Scherrer equation has been employed to estimate the crystallite size (D) of as-synthesized sample given as [114]:

$$D = \frac{k\lambda}{\beta Cos\theta} \quad (3.2)$$

where, k represents the shape factor with a constant value of 0.9, λ denotes the incident X-ray wavelength, β represents full width at half maxima (FWHM) and θ is the Bragg's diffraction angle. The crystallite size of un-doped $Na_4Ca_4Si_6O_{18}$ sample is found to be 38.68 nm.

3.3.3. Diffuse reflectance spectra

Diffuse reflectance spectra were measured to analyse the band gap energy (E_g) lies between higher state of valence band (VB) and lower state of the conduction band (CB) [115]. The band gap values for undoped and 1.0 mol% of Tb^{3+} doped $Na_4Ca_4Si_6O_{18}$ phosphors have been estimated from Fig. 3.3. In the inset of Fig. 3.3, DR spectra exhibit a reflectance band in undoped $Na_4Ca_4Si_6O_{18}$ sample while two bands observed in 1.0 mol% Tb^{3+} doped $Na_4Ca_4Si_6O_{18}$ phosphor, which corresponds to the 4f→5d transition in the range of 200-300 nm.

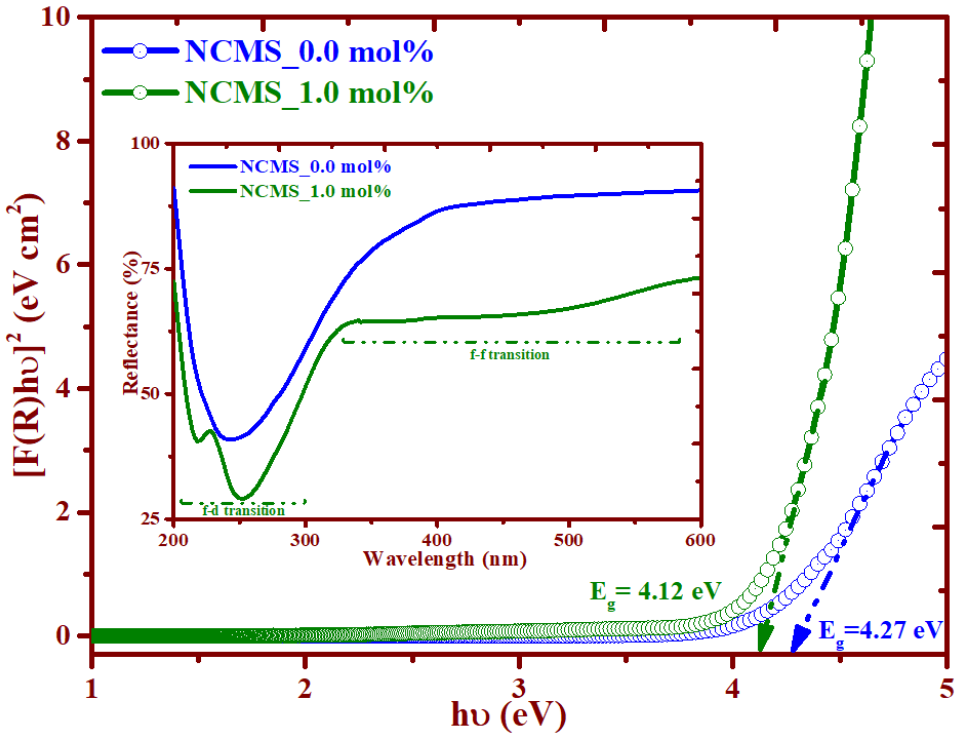

Fig. 3.3. *The band gap spectra via K-M function (inset: Diffuse reflectance spectra) of un-doped and Tb^{3+} doped $Na_4Ca_4Si_6O_{18}$ samples.*

The absorption bands occurred in 1.0 mol% Tb^{3+} doped $Na_4Ca_4Si_6O_{18}$ phosphor after 300 nm resembles to 4f→4f transitions [116]. The DRS has shown in plateau of near 80%

reflectance in the wavelength range of 200-600 nm [117]. To evaluate the optical band gap energy (E_g) of un-doped and 1.0 mol% Tb^{3+} doped $Na_4Ca_4Si_6O_{18}$ phosphors from Fig. 3, Kubelka-Munk (K-M) function (F(R)) has been applied on the data of diffuse reflectance spectra. The well-known K-M (F(R)) function expresses as given below [118]:

$$F(R) = \frac{K}{S} = \frac{(1-R)^2}{2R} \quad (3.3)$$

The parameters in the above equation such as *K*, *S* and *R* represent absorption coefficient, scattering coefficient, and reflectance constant, respectively. Furthermore, the optical band gap E_g can also be estimated using absorption spectra from the well-known Tauc equation expressed below [119]:

$$\alpha h\upsilon = A(h\upsilon - E_g)^n \quad (3.4)$$

where, α refers as the absorption coefficient, $h\upsilon$ is the energy of incident photons, *A* is the proportionality constant and n is the coefficient that reveals the type of electronic transition. The electronic transition depends upon the value of coefficient '*n*' expressed as the direct allowed transition for *n* equal to 1/2, indirect allowed transition for *n* equal to 2, direct forbidden transition for *n* equal to 3/2 and indirect forbidden transition for *n* equal to 3 [85]. The absorption coefficient in Tauc equation is proportional to the K-M function deduced from equation (3.3) and (3.4) are represented below:

$$(F(R)h\upsilon) = B(h\upsilon - E_g)^n \quad (3.5)$$

The optical band gap can be ascertained by extrapolating the linear streak to $(F(R)h\upsilon)^{\frac{1}{n}}$ =0 in $(F(R)h\upsilon)^{\frac{1}{n}}$ versus $h\upsilon$ plot and evaluated the direct allowed band gap for n=1/2 as 4.27 and 4.12 for un-doped and 1.0 mol% Tb^{3+} doped $Na_4Ca_4Si_6O_{18}$ samples, respectively.

3.3.4. Field emission scanning electron microscopy

Fig. 3.4. (a) and (b) depict the FE-SEM micrographs of un-doped $Na_4Ca_4Si_6O_{18}$ sample and Fig. 3.4. (c) and (d) display the micrographs for 1.0 mol% Tb^{3+} doped $Na_4Ca_4Si_6O_{18}$ phosphor to

reveal the morphology and particle size at different magnifications. FE-SEM images disclose that the size of particles is in micro range and irregularity is obtained with some agglomeration. Energy-dispersive X-ray analysis (EDAX) of un-doped $Na_4Ca_4Si_6O_{18}$ sample has been carried out and epitomized elements such as Na, Ca, Si and O present in the host matrix along with their atomic and weight percentage, as shown in Fig. 3.4 (e & f).

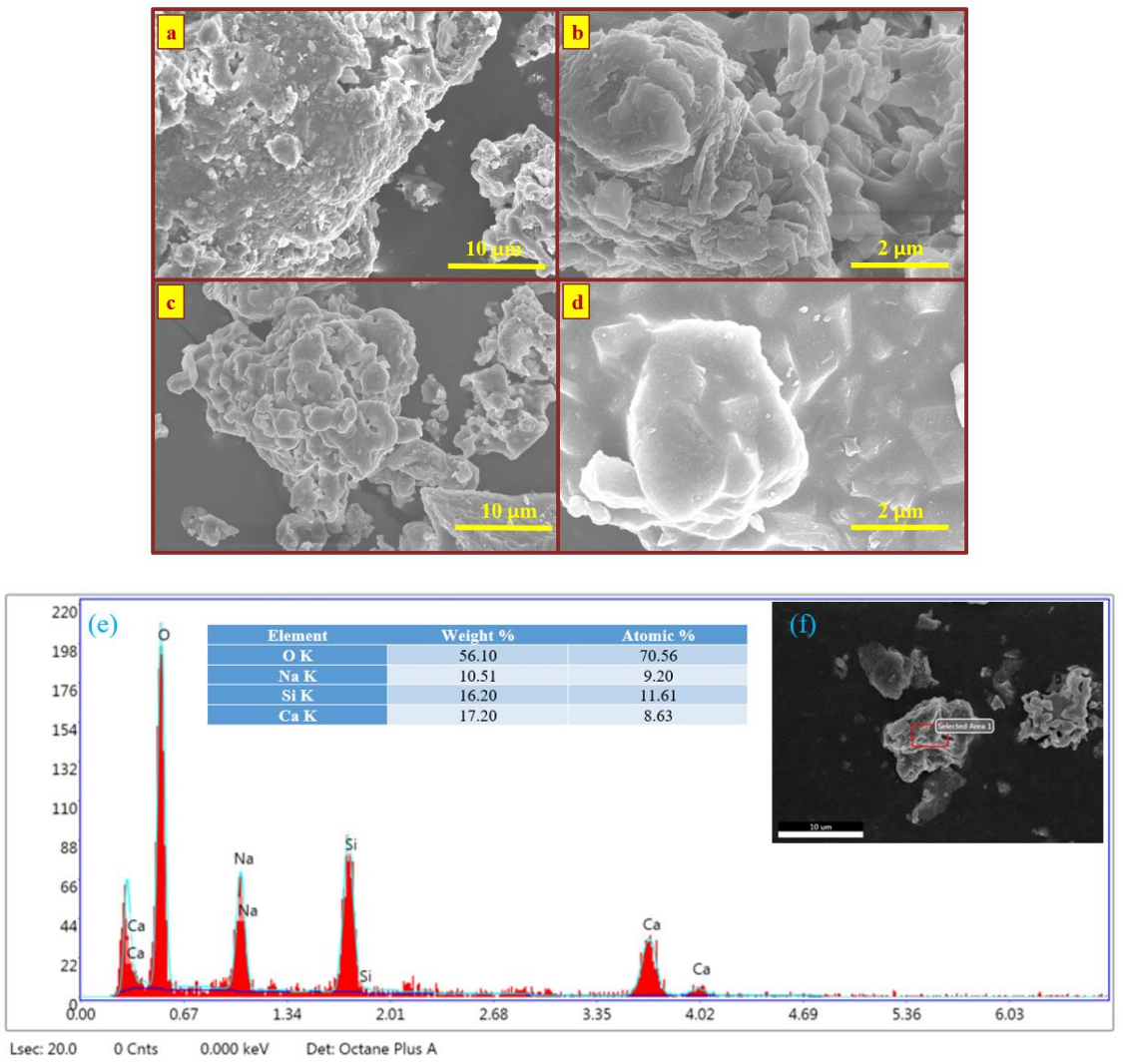

Fig. 3.4. ***(a & b)*** *FE-SEM micrographs for un-doped and (c & d) 1.0 mol% of* Tb^{3+} *doped* $Na_4Ca_4Si_6O_{18}$ *phosphor at different magnifications. (e & f) EDAX image of* $Na_4Ca_4Si_6O_{18}$ *sample.*

Recently, the pc-w-LEDs available in the market are using the phosphors with micro size particles to achieve intense luminescence, which indicates that the proposed NCMS: Tb^{3+} phosphors may provide better performance in terms of commercial usage [120].

3.3.5. Photoluminescence analysis

3.3.5.1. Photoluminescence excitation and emission spectra

Fig. 3.5 (a) illustrates the photoluminescence excitation (PLE) and emission (PL) spectra of 9.0 mol% Tb^{3+} doped sodium calcium silicate ($Na_4Ca_4Si_6O_{18}$) phosphor by monitoring emission wavelength at 542 nm and excitation wavelength at 232 nm, respectively. In Fig. 3.5 (b), the PLE spectra have been carried out in the range of 220-400 nm by fixing the emission wavelengths at 542 and 552 nm. The strong intense band obtained at 232 nm is spin allowed while at 266 nm is spin forbidden $4f^8 \rightarrow 4f^7 5d^1$ transition of Tb^{3+} ion [121,122]. The inset of Fig. 3.5 (b) shows the magnified PLE spectrum of $Na_4Ca_{4-x}Si_6O_{18}$: xTb^{3+} (x=9.0 mol%) phosphor at a fixed emission wavelength of 542 nm in a range of 300-400 nm to discern less intense peaks. In the inset of Fig. 3.5 (b), few peaks appeared due to f-f transitions centred at 318, 352 and 378 nm that are attributed to $^7F_6 \rightarrow {}^5H_7$, $^7F_6 \rightarrow {}^5L_9$ and $^7F_6 \rightarrow {}^5D_3$ transitions, respectively [123]. The stronger excitation peaks endorse the higher light absorptivity due to f-d transitions than f-f transitions in the present work [124].

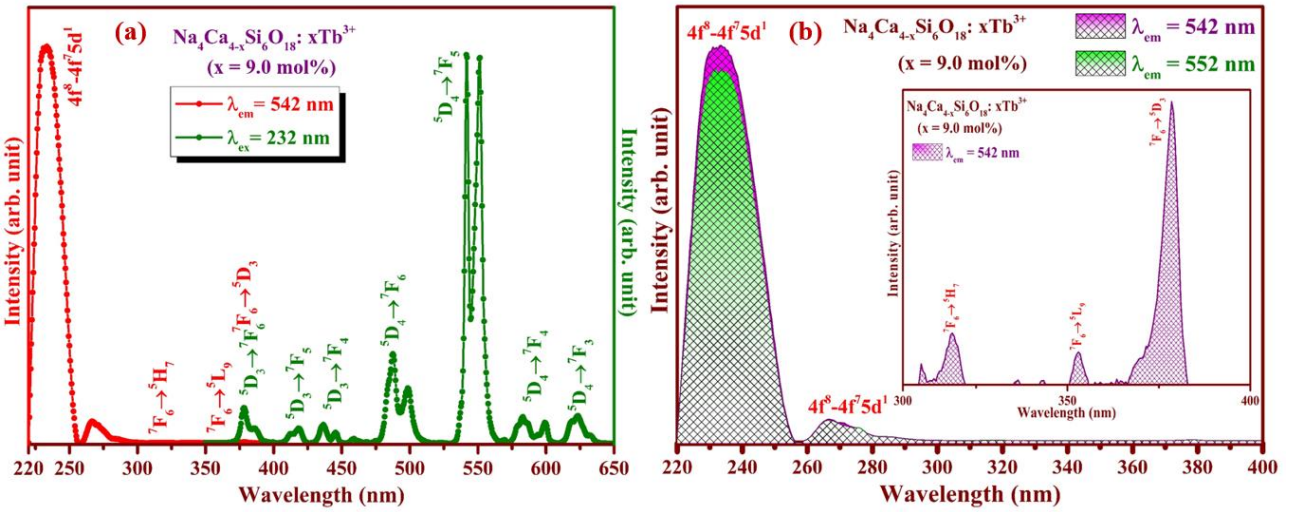

Fig. 3.5. ***(a)*** *PLE and PL spectra of 9.0 mol% of Tb^{3+} doped $Na_4Ca_4Si_6O_{18}$ phosphor* ***(b)*** *Comparison of PLE spectrum of 9.0 mol% of Tb^{3+} doped $Na_4Ca_4Si_6O_{18}$ phosphor monitored at emission wavelengths of 542 and 552 nm. (Inset: Magnified PLE spectrum of 9.0 mol% of Tb^{3+} doped $Na_4Ca_4Si_6O_{18}$ phosphor monitored by emission wavelength of 542 nm).*

Fig. 3.6 (a) and (b) depict the emission spectra of $Na_4Ca_4Si_6O_{18}$: xTb^{3+} (x=1.0, 3.0, 5.0, 7.0, 9.0 and 11.0 mol%) with 232 (UV) and 378 (n-UV) nm excitation wavelengths in the ranges of 350-650 nm and 475-650 nm, respectively. In Fig. 3.6 (a), the most prominent peak attained at 542 nm with a splitting of nearly same intensity at 552 nm corresponds to $^5D_4 \rightarrow {}^7F_5$ transition and is responsible for the bright green emission. The emission spectra of $Na_4Ca_{4-x}Si_6O_{18}$: xTb^{3+} (x =1.0, 3.0, 5.0, 7.0, 9.0 and 11.0 mol%) have been categorised in two sets of range, one is from 350-475 nm that exhibits the transitions from $^5D_3$ excited level to various ^7F_J ground state levels and other is in 475-650 nm range from $^5D_4$ excited level to various ground state energy levels [125,126]. In the emission spectra, the peaks originated in the preliminary range located at 377, 419, 436 and 458 nm correspond to $^5D_3 \rightarrow {}^7F_6$, $^7F_5$, $^7F_4$ and $^7F_3$ transitions, respectively. The peaks located in further range at 487, 542, 582 and 622 nm are resembled to $^5D_4 \rightarrow {}^7F_6$, $^7F_5$, $^7F_4$ and $^7F_3$ transitions, respectively.

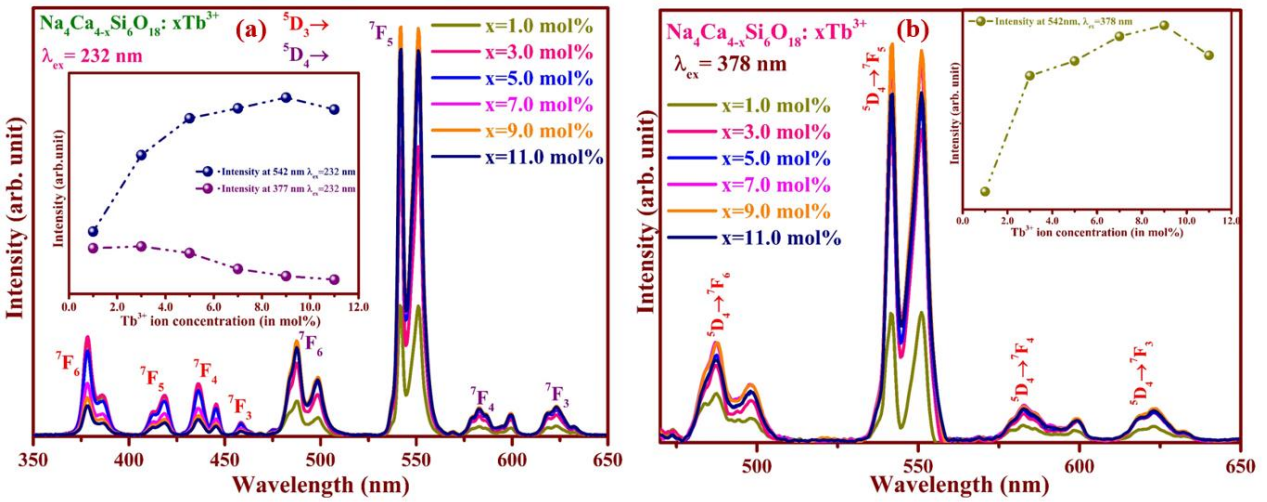

Fig. 3.6. *PL spectra of $Na_4Ca_4Si_6O_{18}$: xTb^{3+} (x= 1.0, 3.0, 5.0, 7.0, 9.0 and 11.0 mol%) phosphors at **(a)** λ_{ex} = 232 nm **(b)** λ_{ex} = 378 nm. Inset of **(a)**: Variation of emission intensity at 542 and 377 nm by varying the concentration of Tb^{3+} ion at λ_{ex} = 232 nm. Inset of **(b)**: Variation of emission intensity at 542 by varying the concentration of Tb^{3+} ion at λ_{ex} = 378 nm.*

These emission transitions observed under 378 nm excitation are positioned at same wavelengths as excited at 232 nm. Each band in PL spectra positioned at 487, 542, 582 and

622 nm shows splitting, which arises due to crystal field effect. In addition, the $^5D_4 \rightarrow {}^7F_6$ transition corresponds to an electric dipole (ED) transition in a blue region by obeying the selection rule ($\Delta J = 2$), which depends on the local environment as well as symmetry of crystal field while $^5D_4 \rightarrow {}^7F_5$ transition resembles to magnetic dipole (MD) transition in a green region following the selection rule ($\Delta J = \pm 1$), which is independent on the crystal field strength [127]. The ratio of integrated intensities of peaks due to electric and magnetic dipoles (I_{ED}/I_{MD}) defines the asymmetric behaviour of dopant ions in the host lattice. In the present work, the ratio was lesser than 1, which indicates that the dopant ion has occupied the sites of symmetric environment in the crystal lattice [128,129].

3.3.5.2. Effect of Tb^{3+} ion concentration

The emission intensity of the transitions originating from $^5D_3$ state decreases as the concentration of dopant ion increases up to 11.0 mol% of Tb^{3+} ion doped NCMS phosphor. On the other hand, the emission intensity of the transitions from $^5D_4$ state increases until 9.0 mol% and then decreases with increasing the concentration of dopant ions as shown in Fig. 3.6 (a & b).

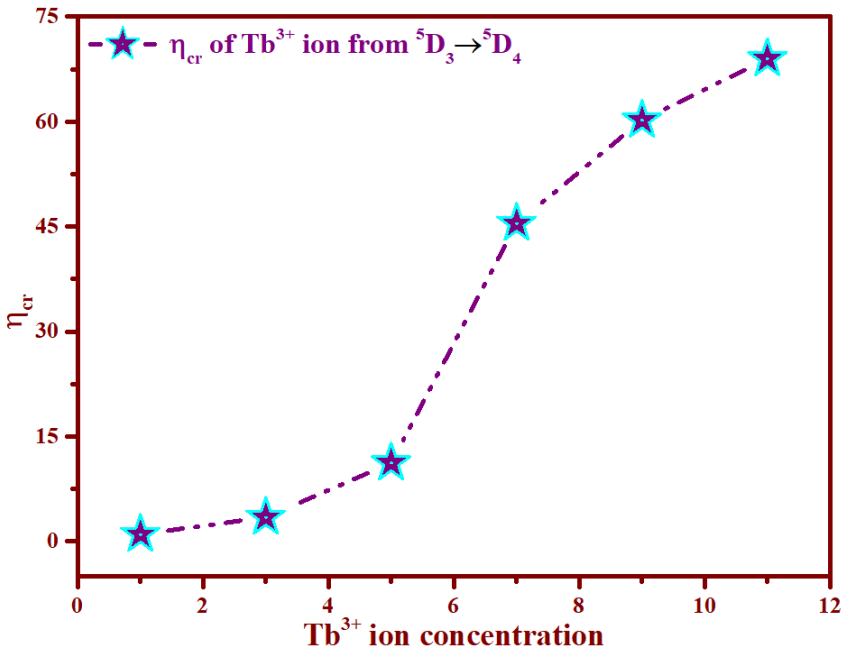

Fig. 3.7. *Cross-relaxation efficiency of Tb^{3+} ion doped $Na_4Ca_4Si_6O_{18}$ phosphor.*

The inset of Fig. 3.6 (a) shows the variation in emission intensity of peaks positioned at 542 and 377 nm with an increase in the concentration of Tb^{3+} ion under 232 nm excitation wavelength, whereas the inset of Fig. 3.6 (b) shows the variation of emission intensity at 542 nm under 378 nm excitation wavelength with an increase in dopant concertation. The gradual decrease in $^5D_3$ state and simultaneous rise in $^5D_4$ state with Tb^{3+} ion concentration occurs due to cross relaxation. It could be possible to estimate the cross-relaxation efficiency of Tb^{3+} ion from $^5D_3$ to $^5D_4$ state via expression as mentioned below [130]:

$$\eta_{CR} = 1 - \left(\frac{I_x}{I_0}\right) \tag{3.6}$$

where I_x and I_0 are represented as emission intensity of $^5D_3$ at a given Tb^{3+} ion concentration and at the lower Tb^{3+} ion concentration [128]. The estimated cross-relaxation efficiency is found to be 1.0, 3.46, 11.21, 45.44, 60.19 and 68.97 % for 1.0, 3.0, 5.0, 7.0, 9.0 and 11.0 mol% concentration of dopant ion in the silicate matrix, respectively. The variation of cross-relaxation efficiency with the dopant ion concentration is shown in Fig. 3.7. The distance among Tb^{3+} ions reduces with an increment in dopant ion concentration that promotes the faster cross-relaxation from $^5D_3$ to $^5D_4$ state, as observed in Fig.3.7.

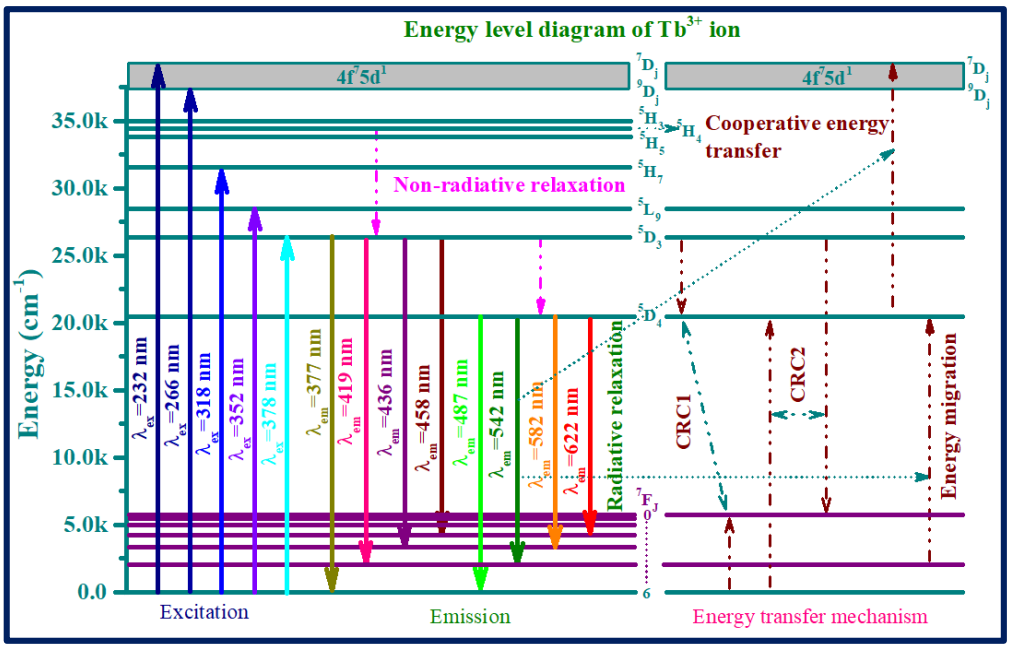

Fig. 3.8. *Partial energy diagram of Tb^{3+} ion doped $Na_4Ca_4Si_6O_{18}$ phosphor.*

Further, the drop in emission intensity from $^5D_4$ state after 9.0 mol% of dopant concentration may occur either due to cross-relaxation (CR) processes via resonant energy transfer (CRC1: $^5D_3+^7F_6 \rightarrow {}^5D_4+{}^7F_0$ and CRC2: $^5D_3+^7F_6 \rightarrow {}^7F_0+{}^5D_4$) or cooperative energy transfer or energy migration as depicted in the energy level diagram (Fig. 3.8) [131,132]. The cross-relaxation mechanism depends on the critical distance between Tb^{3+}-Tb^{3+} ions [133]. The critical distance (R_c) between Tb^{3+}-Tb^{3+} ions in NCMS: Tb^{3+} phosphor can be evaluated by Blasse's equation as given below:

$$R_c = 2\left(\frac{3V}{4\pi x_c N}\right)^{\frac{1}{3}} \quad (3.7)$$

In the above equation, the parameters such as N, V, and x_c represent the number of cations per unit cell, volume of the given unit cell and critical concentration of dopant ions in the host matrix, respectively. In the NCMS host matrix, the values for N, V and x_c are 3, 1249.42 $Å^3$ and 0.09 mol. Using the equation (3.7), the critical distance (R_c) has been found to be 20.67 Å. As the estimated value of R_c is much larger than 5 Å, the multipolar interaction will takes place in NCMS: xTb^{3+} phosphor while exchange interaction takes place, when the value of R_c is lesser than 5 Å as per the Van Uitert [134,135].

3.3.5.3. CIE chromaticity coordinates

The accurate color emission from Tb^{3+} doped $Na_4Ca_4Si_6O_{18}$ phosphor has been estimated from the emission spectra measured at 232 and 378 nm excitation wavelengths presented on Commission Internationale de I'Eclairage (CIE 1931) chromaticity diagram as shown in Fig. 3.9. The CIE chromaticity coordinates at 1.0, 3.0, 5.0, 7.0, 9.0 and 11.0 mol% of Tb^{3+} ion concentrations excited at 232 nm are found to be (0.25, 0.40), (0.27, 0.49), (0.28, 0.52), (0.29, 0.55), (0.29, 0.57) and (0.30, 0.58) (marked as star in Fig. 3.9), whereas the chromaticity coordinates under 378 nm excitation are to be (0.30, 0.55), (0.31, 0.60), (0.31, 0.60), (0.30, 0.60), (0.31, 0.60) and (0.31, 0.60), respectively (marked as solid circle in Fig. 3.9). The optimized

phosphor (9.0 mol% Tb^{3+} doped NCMS) CIE coordinates under UV and n-UV excitation wavelengths are located near to European broadcasting union illuminant green phosphor coordinates (0.29, 0.60) [136]. The CIE coordinates reflect the pure green emission color under 378 nm excitation wavelength, whereas under 232 nm, the color tunability from blue to green region observed with increasing concentration of Tb^{3+} ions in $Na_4Ca_4Si_6O_{18}$ phosphor. Thus, the observed color tunability in NCMS: Tb^{3+} phosphor under efficient UV chip excitation may be useful for lighting and display device applications [137].

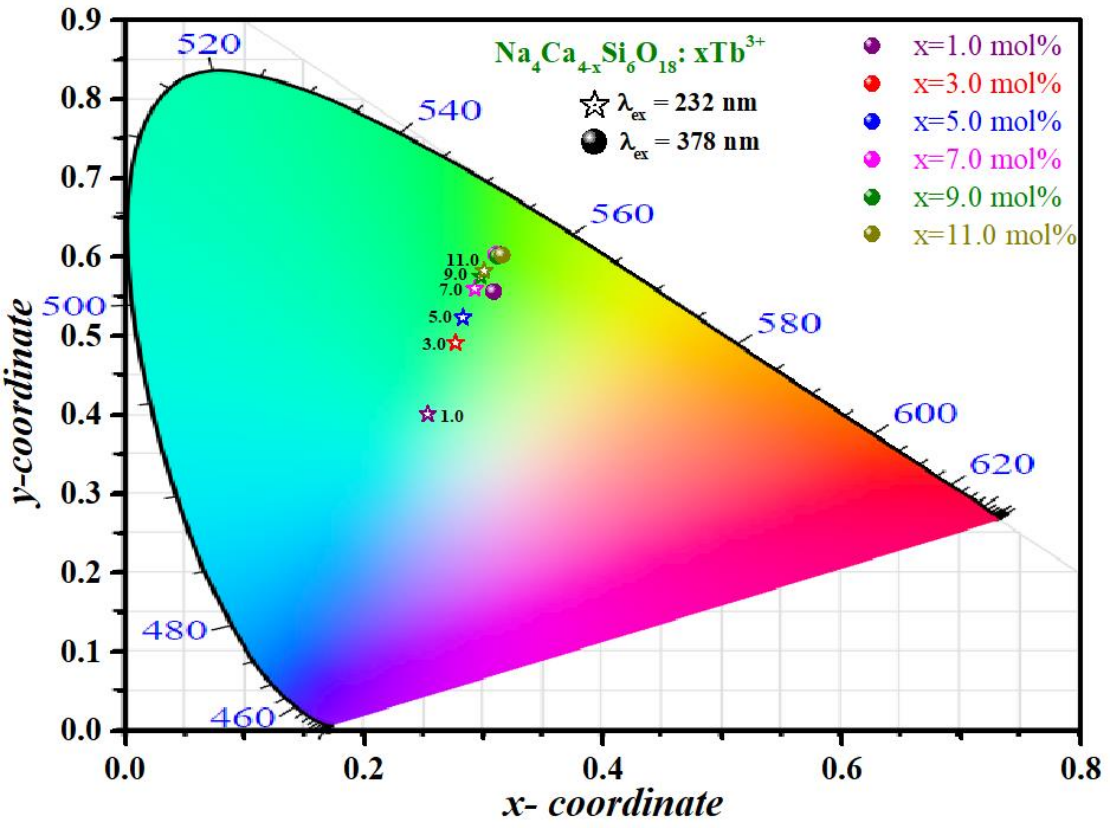

Fig. 3.9. *CIE plot of $Na_4Ca_{4-x}Si_6O_{18}$: xTb^{3+} (x= 1.0, 3.0, 5.0, 7.0, 9.0 and 11.0 mol%) phosphors at λ_{ex} = 232 nm and λ_{ex} = 378 nm.*

The correlated color temperature (CCT) value can be estimated from the equation evaluated by McCamy as follows [55]:

$$CCT = -449n^3 + 3525n^2 - 6823.3n + 5520.33 \quad (3.8)$$

where $n = (x - x_e)/(y - y_e)$ represents inverse slope line in which x_e and y_e are the coordinates for epicentre of convergence with the value of $x_e = 0.332, y_e = 0.186$. The CCT values for

$Na_4Ca_{4-x}Si_6O_{18}$: xTb^{3+} ($1 \leq x \leq 11$ mol%) phosphors are found to be in a range of 5500-8500 K. The higher CCT values fall under the cool region of visible color gamut. The purity of color for the optimized Tb^{3+} doped phosphor has been evaluated using the formula [138]:

$$Color\ purity = \frac{\sqrt{(x-x_{ee})^2+(y-y_{ee})^2}}{\sqrt{(x_d-x_{ee})^2+(y_d-y_{ee})^2}} \times 100\ \% \quad (3.9)$$

where (x, y) are the coordinates of 9.0 mol% of Tb^{3+} ion incorporated in $Na_4Ca_4Si_6O_{18}$ phosphor, (x_{ee}, y_{ee}) are the coordinates correspond to the equal energy point and (x_d, y_d) are dominant wavelength point coordinates.

Table 3.1. *Comparison of color purity of Tb^{3+} ion doped $Na_4Ca_4Si_6O_{18}$ with other host materials under n-UV and UV excitation sources.*

Excitation	Sample composition	Color Purity	References
n-UV	$Na_5Lu_9F_{32}$: $0.07Tb^{3+}$	57.3%	[140]
	ZrO_2: $0.02Tb^{3+}$	60.0%	[143]
	$Na_4Ca_4Si_6O_{18}$: $0.09Tb^{3+}$	82.0%	This work
UV	$Ca_3La_3(BO_3)_5$: $0.08Tb^{3+}$	63.63 %	[139]
	$KNa_3Al_4Si_4O_{16}$: $0.13Tb^{3+}$	62.80 %	[141]
	YPO_4: $0.08Tb^{3+}$	41.56 %	[142]
	$Na_4Ca_4Si_6O_{18}$: $0.09Tb^{3+}$	64.00 %	This work

The color purity for the optimized Tb^{3+} doped NCMS phosphor has been estimated as 82% and 64% for the excited under n-UV region and UV region, respectively for providing strong green emitting phosphor. Table 3.1 reveals the comparison of color purity for optimized Tb^{3+} ion doped $Na_4Ca_4Si_6O_{18}$ and other phosphor materials reported elsewhere under UV and n-UV excitation [139–143] Among various phosphors, present NCMS: Tb^{3+} phosphor showed excellent green emission to use as one component for developing efficient pc-w-LEDs.

3.4. Conclusions

Depending on the excitation source (UV/n-UV), tunable blue-green and intense green emitting Tb^{3+} doped $Na_4Ca_4Si_6O_{18}$ phosphors have been synthesized by solid state reaction method. The pure phase of the $Na_4Ca_4Si_6O_{18}$ structure has been confirmed via diffraction pattern as the XRD peaks are well agreed with the standard diffraction pattern (JCPDS card no. 75-1687). The calculated crystallite size through Debye-Scherer's equation is found to be 38.68 nm for un-doped $Na_4Ca_4Si_6O_{18}$ sample. The FE-SEM micrographs of un-doped and Tb^{3+} ion doped $Na_4Ca_4Si_6O_{18}$ sample revealed the irregular, non-uniform, agglomerated morphological structures with sizes in micro-range. The optical band gap of the un-doped and Tb^{3+} doped sample was obtained through DRS spectra, found to be 4.27 and 4.12 eV. PLE spectra exhibit the strong excitation wavelengths at 232 and 378 nm by fixing emission wavelength at 542 nm. PL emission occurred in two ranges that exhibit the transitions from $^5D_3$ (350-475) and $^5D_4$ (475-650) excited levels to various ^7F_J ground state levels. The emission intensity reduces with an increase in the concentration of dopant ions till 11.0 mol% in the range of 350-475 nm under 232 nm (UV) excitation. The decrease in emission intensity from $^5D_3$ state increases the intensity in $^5D_4$ level with an increment in dopant ion concentration is due to cross relaxation. However, the PL intensity under 378 nm (n-UV) excitation wavelength rises up to 9.0 mol% concentration of Tb^{3+} ions and then begin to decrease due to the effect of concentration quenching. The similar effect observed under 232 nm excitation in the wavelength range of 475-650 nm. Hence, the optimized concentration is estimated to be 9.0 mol% for the Tb^{3+} ions doped $Na_4Ca_4Si_6O_{18}$ phosphor. PL spectra and CIE coordinates revealed the tunable blue to green emission by exciting under UV light while intense green emission was obtained via n-UV excitation source. The features mentioned above indicate that Tb^{3+} doped $Na_4Ca_4Si_6O_{18}$ phosphor could be a viable choice to be utilized as a green emitting component in the development of w-LED applications.

Chapter 4

Spectroscopic features of thermally stable red emitting Pr^{3+} doped sodium calcium metasilicate phosphor for w-LED applications

Microcrystalline pure phase praseodymium doped $Na_4Ca_4Si_6O_{18}$ (NCMS: Pr^{3+}) phosphors have been synthesized and systematically characterized for implementation in w-LED applications. High temperature solid state reaction methodology has opted to prepare a series of NCMS: xPr^{3+} (x= 0.0, 1.0, 2.0, 3.0 and 4.0 mol%) phosphor. X-ray diffraction pattern has confirmed the phase purity and crystallinity of the as-prepared phosphor via comparing all the diffraction peaks with the standard pattern. Luminescence studies have been carried out in n-UV and visible regions to illustrate the excitation and emission spectra of NCMS: Pr^{3+} phosphor. PL spectrum exhibits the radiative emission at 611 nm under the most intense excitation peak at 480 nm for 1.0 mol% of Pr^{3+} doped NCMS phosphors. The optimized concentration of dopant ion has been achieved by following the energy transfer-based concentration quenching mechanism and found to be 1.0 mol% for NCMS crystal. The chromaticity diagram represents the integrated emission color of the optimized NCMS:1.0 mol% Pr^{3+} phosphor falls in the red region with a color purity of 97.0% when stimulated with the blue light. Thus, the investigated outcomes encourage that the promising red-emitting NCMS phosphor can be utilized in w-LED applications.

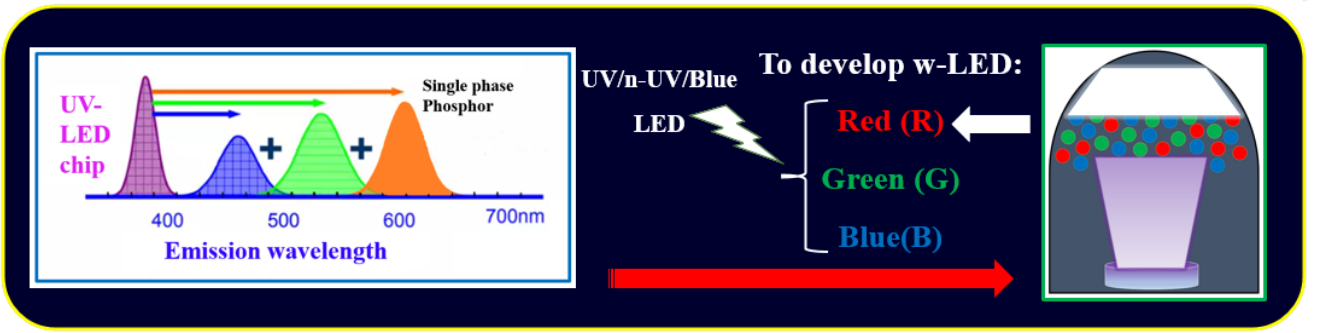

4.1. Introduction

Considering the next generation lighting sources, phosphor converted white LEDs (pc-wLEDs) have recently been persuasive in producing white light since it furnishes substantial benefit over conventional incandescent and fluorescent bulbs [144–146]. Phosphor based w-LEDs are highly scrutinized by the researcher around the world as it provides a multitude of unique characteristics such as longer lifetime, high efficiency, swift response, affordable, steady and environmentally benign [147,148]. Traditionally, pc-wLEDs were manufactured by layering a yellow-emitting YAG: Ce^{3+} phosphor upon a blue emitting LED chip but relinquished due deprived performance of CCT (high) and CRI (low) with effect of scarcity of red component. To resolve these issues, red component can amalgamate with the yellow emitting phosphor in order to achieve white light with good color purity, high CRI and low CCT values [146]. The CRI and CCT values provide better results by adjusting the ratio of the existing color components in the pc-wLEDs. Therefore, the involvement of red component is much significant to upgrade the luminescent performance of w-LEDs [149].

Rare-earth ions manifest themselves as an excellent dopant ion due to their unique property of yielding extremely sharp emission lines in the visible spectrum due to the existence of partially filled 4f orbitals which are shielded by the $5s^2$ and $5p^6$ electrons [150]. Among these, the trivalent praseodymium (Pr^{3+}) ion with a [Xe] $4f^2$ electronic configuration has garnered great interest due to its many unique optical properties. Moreover, the emission due to Pr^{3+} is attained in the red region with distinct host materials excited under blue light [151]. Among various host materials, metasilicate compounds are considered to be the excellent host matrices for trivalent rare earth ion activators due to their excellent chemical stability, ease of synthesis and exceptional photoluminescence properties [152].

In the current investigation, red emitting Pr^{3+} doped $Na_4Ca_4Si_6O_{18}$ phosphor materials have been synthesized via utilizing the traditional solid-state synthesis method. The crystal structure

and morphological studies have been confirmed via x-ray diffraction and FE-SEM techniques, respectively. The exploration of photoluminescence studies represents that the radiative red emission occurs under blue excitation and indeed investigated the optimized concentration of dopant ion via concentration quenching process. The CIE diagram and temperature dependent photoluminescence studies illustrate that the as-synthesized phosphor is lying in the intense red region with good thermal stability. Hence, the aforementioned studies demonstrate that Pr^{3+} doped $Na_4Ca_4Si_6O_{18}$ phosphor is a potential candidate to use as a red component in the production of white light for w-LED applications.

4.2. Sample synthesis and characterisation techniques

Sodium calcium metasilicate ($Na_4Ca_{4-x}Si_6O_{18}$) phosphor doped with Pr^{3+} ions were synthesized via conventional solid-state reaction methodology as described in the section 2.2.3. The detailed procedure is represented through the flow chart as shown in Fig. 2.1. Moreover, various characterization techniques have been used to examine the crystalline, morphological and luminescent behaviour of the as synthesized phosphors, described in the section 2.3 (chapter 2).

4.3. Results and discussion

4.3.1. Structural phase analysis

Fig. 4.1. illustrates the x-ray diffraction pattern of 1.0 mol% Pr^{3+} doped NCMS phosphor along with the standard pattern of $Na_4Ca_4Si_6O_{18}$ crystal. Diffraction pattern without any significant additional peaks have been obtained which confirms the pure crystalline phase formation of NCMS crystal. The obtained diffraction peaks of Pr^{3+} doped NCMS phosphor are well allied with standard JCPDS (card no. 75-1687) pattern of $Na_4Ca_4Si_6O_{18}$ crystal [153]. Pure hexagonal NCMS crystal has lattice parameters as a=b=10.46 Å; c=13.17 Å and V=1249.42 $Å^3$ along with the space group $P3_2$ [154]. The well-matched profile signifies the successful accommodation of dopant ion into host matrix. The dopant ion can be properly accommodated in the host when the ionic radii of dopant ion is comparable to the substituted ion [155]. The well-recognized Debye-Scherrer

formula written as $D=K\lambda/\beta Cos\theta$ has been used to estimate the average crystallite size. Here, K is the shape factor, λ, β and θ represents the incident x-ray wavelength, full width at half maxima and Bragg's diffraction angle, respectively [156]. Using above formula, the average crystallite size for 1.0 mol% Pr^{3+} doped $Na_4Ca_4Si_6O_{18}$ phosphor is found to be 51.75 nm.

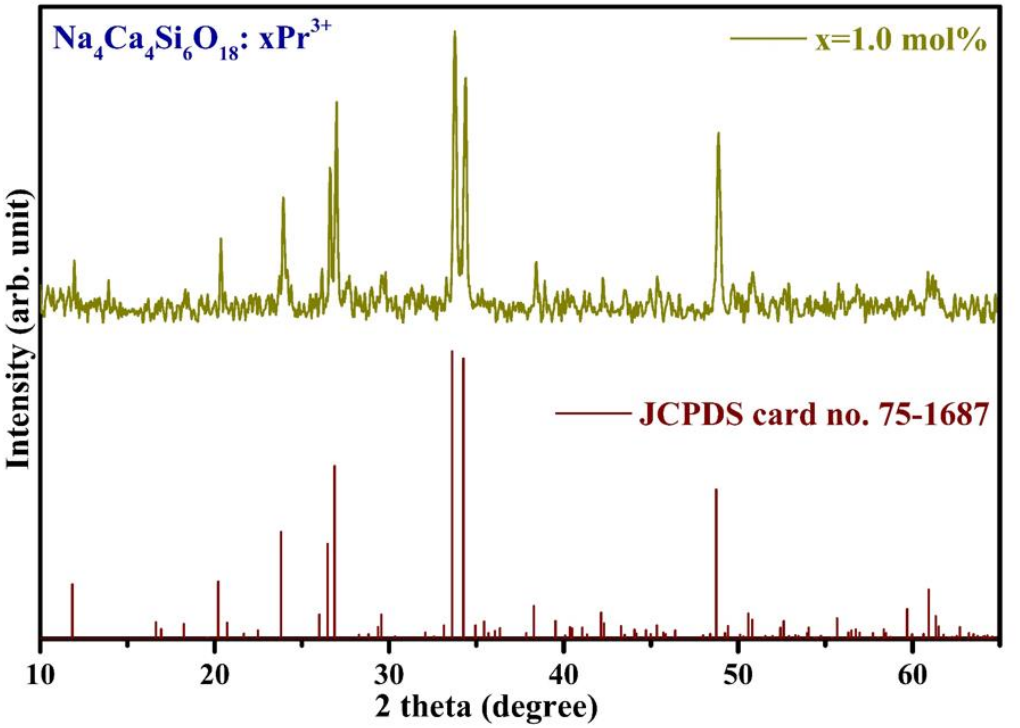

Fig. 4.1. *XRD patterns of 1.0 mol% of Pr^{3+} doped $Na_4Ca_4Si_6O_{18}$ phosphor along with standard data.*

4.3.2. Morphological studies

Field emission scanning electron microscopy (FE-SEM) have been performed to ascertain the particle size and morphology of the as-synthesised Pr^{3+} (1.0 mol%) doped NCMS phosphor, as shown in Fig. 4.2. The particles are visible in the micrograph with irregular small size clustered on large particles under the resolution of 5 μm. The agglomerated and massive particles formation occurs at high temperature and is essential to perform better for w-LEDs applications [120].

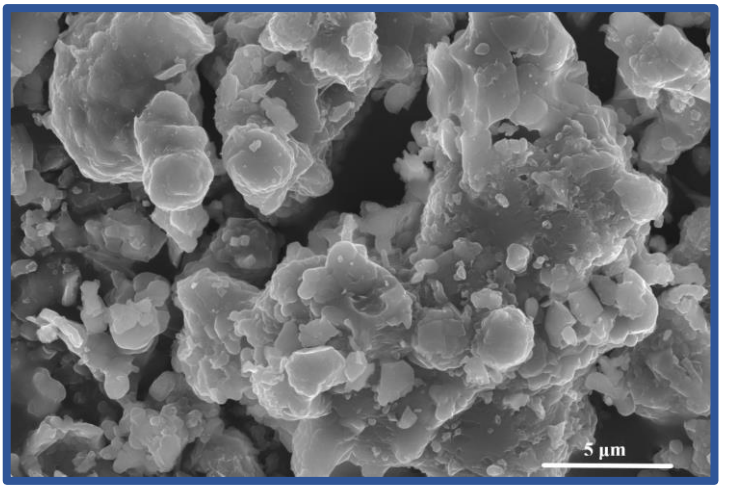

Fig. 4.2. *FE-SEM micrographs for 1.0 mol% of Pr^{3+} doped $Na_4Ca_4Si_6O_{18}$ phosphor.*

4.3.3. Luminescent studies

Excitation and emission spectra have been measured to explore the photoluminescence properties of as-synthesised Pr^{3+} doped NCMS phosphor, as depicted in Fig. 4.3 (a & b). The excitation spectrum of 1.0 mol% Pr^{3+} doped NCMS phosphor was captured by keeping the emission wavelength at 611 nm in a range of 350-500 nm, as presented in Fig. 4.3 (a). The excitation spectrum has shown three characteristic peaks positioned at 439, 467 and 480 nm resembles to the ground state to various excited states ($^3H_4 \rightarrow {}^3P_2$, $^3P_1$ and $^3P_0$) [157]. The highest intense peak was obtained at 480 nm which was employed to record emission spectra. Fig. 4.3 (b) represents the emission spectrum of NCMS: 1.0 Pr^{3+} phosphor under 480 nm excitation wavelength in 550-800 nm range. The peaks emerged at distinct wavelengths 578, 595, 603, 611, 652 and 704 nm imputed to specific transitions $^3P_0 \rightarrow {}^3H_5$, $^3P_1 \rightarrow {}^3H_6$, $^1D_2 \rightarrow {}^3H_4$, $^3P_0 \rightarrow {}^3H_6$, $^3P_0 \rightarrow {}^3F_2$ and $^3P_0 \rightarrow {}^3F_4$, respectively [158]. The peak with highest emission intensity was obtained at 611 nm, divulges the emission in red region which can be implemented as intense red component in the w-LED fabrication.

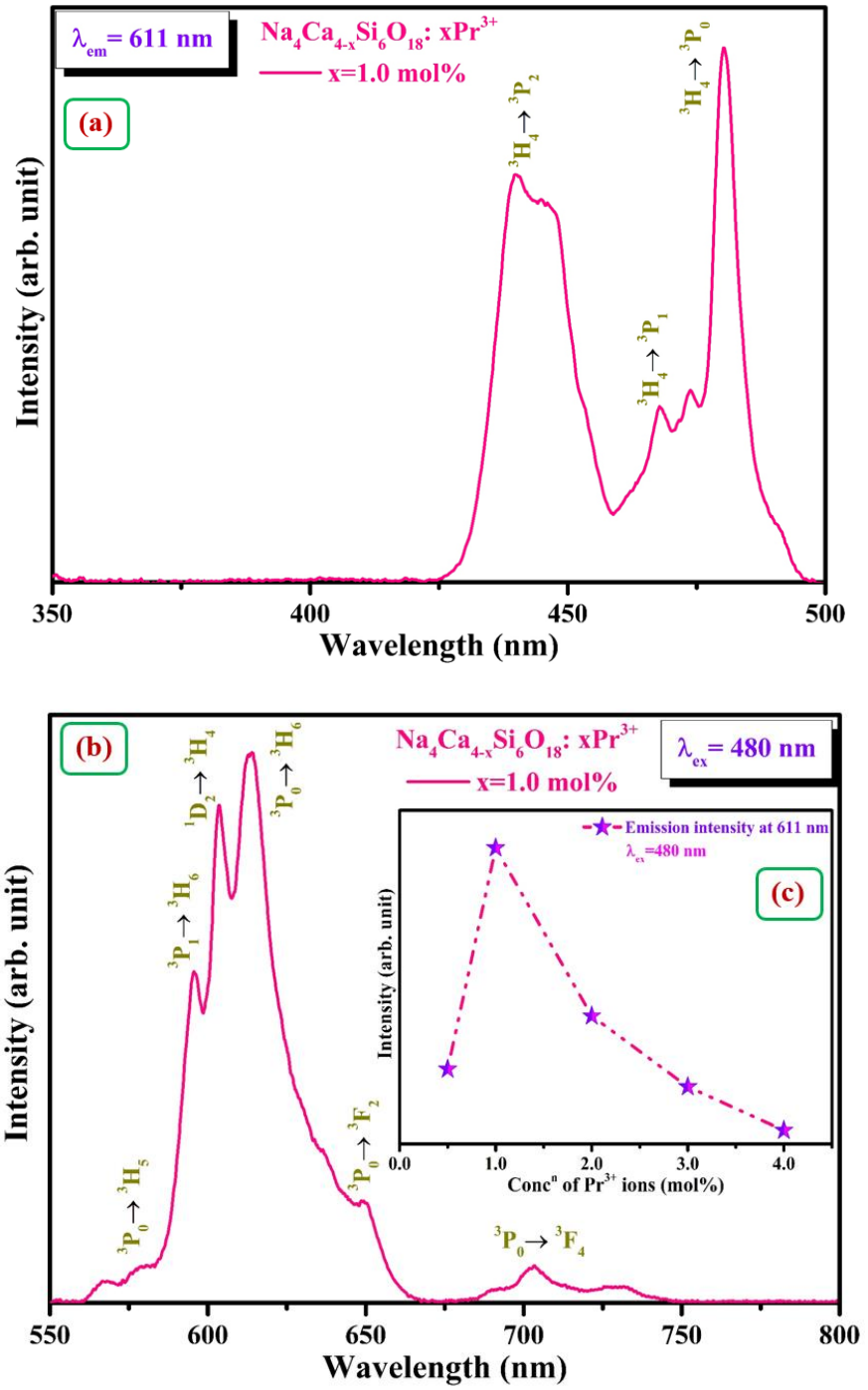

Fig. 4.3. ***(a)*** *PLE and* ***(b)*** *PL spectra of 1.0 mol% of Pr^{3+} doped $Na_4Ca_4Si_6O_{18}$ phosphor under λ_{em}=611 nm and λ_{em}=480 nm, respectively.* ***(c)*** *Variation of emission intensity at 611 nm by varying the concentration of Pr^{3+} ion at λ_{ex} = 480 nm.*

Fig. 4.3 (c) depicts the intensity vs dopant ion concentration plot which shows the variation in the emission intensity with the concentration of Pr^{3+} ions (0.5, 1.0, 2.0, 3.0 and 4.0 mol%) in the host matrix. The plot indicates that the emission intensity rises until 1.0 mol% of Pr^{3+} dopant ion, and further rise in dopant concentration leads to the decrement in emission intensity by

following concentration quenching phenomenon [159]. In general, at higher concentration the distance between dopant ion reduces due to which the absorbed energy was dissipated at quencher sites, which further relaxed back to ground state via non-radiative multi-phonon emission [160,161]. In order to estimate critical distance among dopant ions, Blasse's equation has been followed [162]. The R_c has been evaluated as 43.01 Å by using V=1249.42 Å^3, N=3 and x_c=0.01 mol values. Thus, high R_c values facilitates multi-polar interaction among dopant ions for non-radiative transition. Following Dexter's theory, the type of multi-polar interaction can be determined by using the derived equation below [163]:

$$\frac{I}{x} = k\left[1 + \beta(x)^{\frac{Q}{3}}\right]^{-1} \quad (4.1)$$

where, Q and I are the parameters reveal type of interaction and emission intensity, respectively, x is the concentration of Pr^{3+} ions, k and β are the constants. Moreover, Q denotes the type of interaction associated with the values 6, 8 and 10 expresses as d-d, d-q and q-q interaction [164]. Fig. 4.4. exhibits the log (I/x) versus log (x) plot with the slope of 2.39 ensues that the value of Q as 7.18, which is close to 8 and implies dipole-quadrupole interactions among the dopant ions [165].

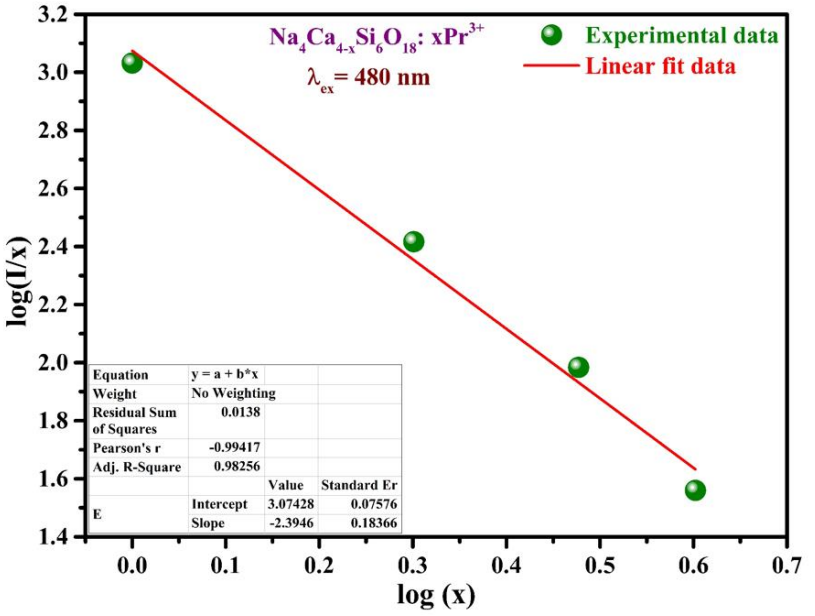

Fig. 4.4. *Log(I/x) versus Log(x) plot for $Na_4Ca_4Si_6O_{18}$ phosphor.*

In Pr^{3+} doped NCMS phosphor, the process of distinct transitions such as radiative and non-radiative transitions have been comprehended through partial energy level diagram as illustrated in Fig. 4.5. Predominantly, the energy incident on NCMS: Pr^{3+} phosphor excites Pr^{3+} ions from the lower energy state i.e. $^3H_4$ to higher excited states (^3P_J: J=0, 1 and 2). Afterward, the ions at higher excited state relax back to divergent states by liberating energy non-radiatively and radiatively [166]. The radiative emission takes place when the ion jumps from emitting states as $^3P_1$, $^3P_0$ and $^1D_2$ to the ground states and emitting energy in the visible region at 578 ($^3P_0 \rightarrow {}^3H_5$), 595 ($^3P_1 \rightarrow {}^3H_6$), 603 ($^1D_2 \rightarrow {}^3H_4$), 611 ($^3P_0 \rightarrow {}^3H_6$), 652 ($^3P_0 \rightarrow {}^3F_2$) and 704 ($^3P_0 \rightarrow {}^3F_4$) nm wavelength, respectively. The energy state $^3P_0$ envisage as a most populated level since the ions relax from $^3P_0$ to give strong emission with the peak attained at 611 nm wavelength. In addition, there are other pathways which exhibit non-radiative transition such as phonon assisted transitions from different excited levels between $^3P_2$ and $^1D_2$ and cross relaxation channels (CRC1: $^1D_2 + {}^3H_4 \rightarrow {}^1G_4 + {}^3F_4$; CRC2: $^3P_0 + {}^3H_4 \rightarrow {}^3H_6 + {}^1D_2$) [167].

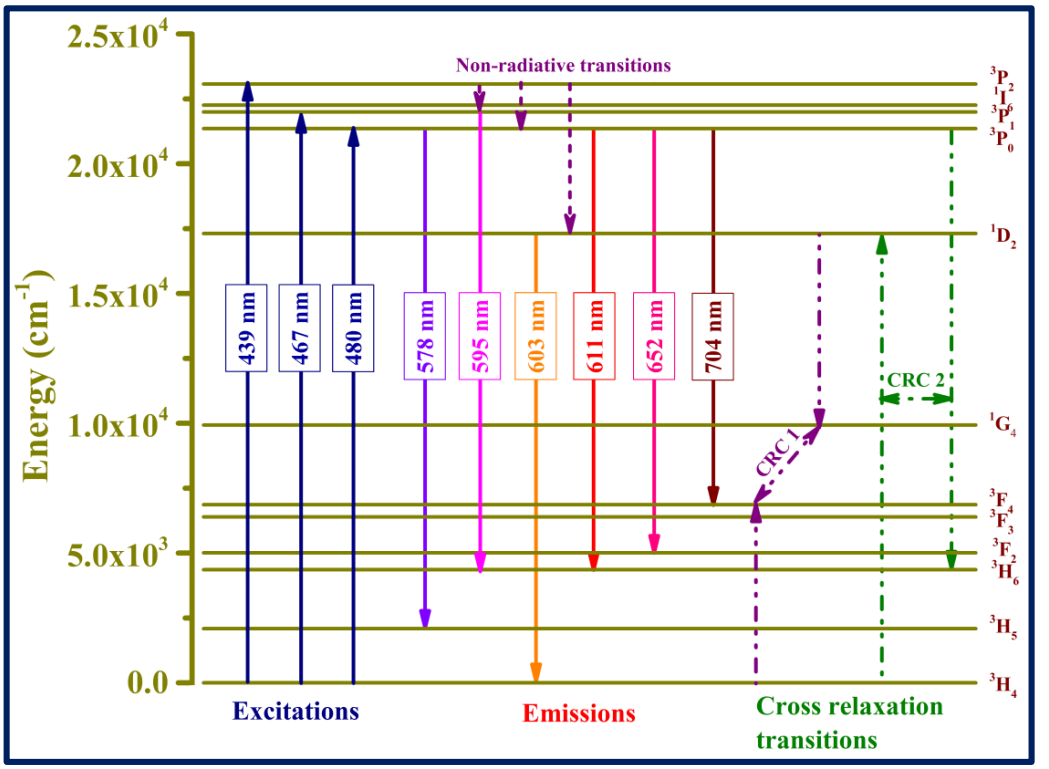

Fig. 4.5. *Partial energy level diagram of Pr^{3+} ion doped $Na_4Ca_4Si_6O_{18}$ phosphor.*

4.3.4. CIE chromaticity coordinates

The colorimetric studies have been performed to analyse the integrated color of emitted light via Commission International de I'Eclairage (CIE) 1931 coordinates [168]. Fig. 4.6. depict the color coordinates (0.64, 0.35) of the optimized NCMS: 1.0 mol % Pr^{3+} phosphor fall in the red region under 480 nm wavelength of excitation. The evaluated chromaticity coordinates of the optimized Pr^{3+} doped NCMS phosphor located quite near to the commercially available red emitting Eu^{3+} doped Y_2O_2S phosphor coordinates (0.62, 0.35) as marked in Fig. 4.6.

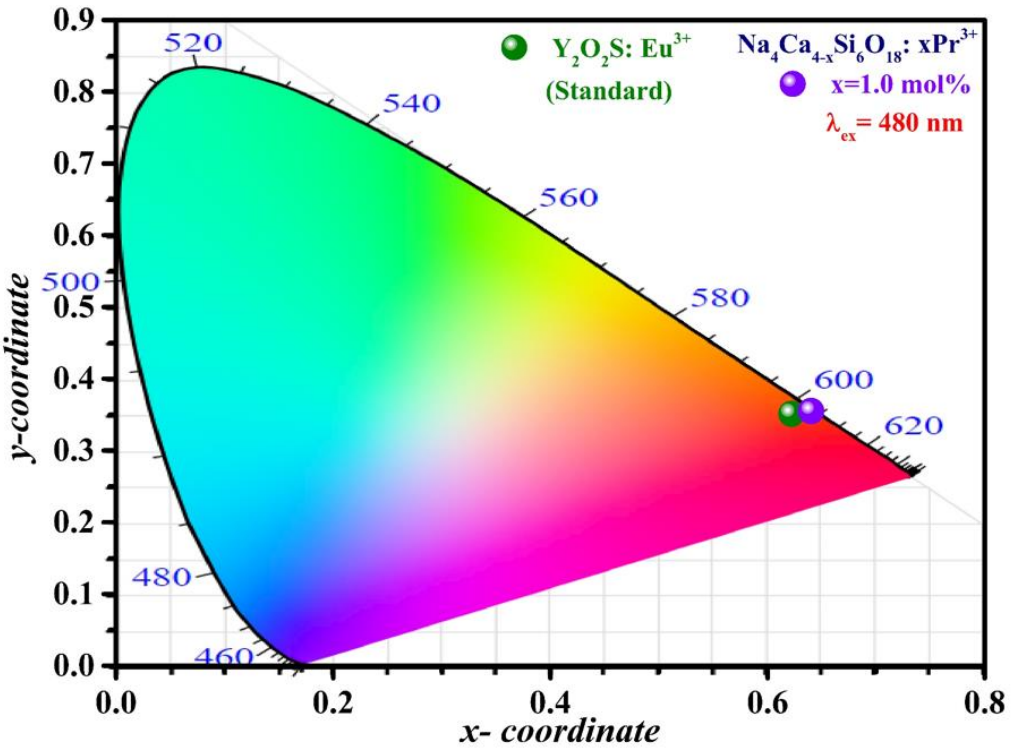

Fig. 4.6. *CIE plot of $Na_4Ca_{4-x}Si_6O_{18}$: xPr^{3+} (x= 1.0 mol%) phosphors at λ_{ex} = 480 nm.*

The color correlated temperature (CCT) value for the optimized NCMS phosphor has been estimated using McCamy's empirical formula and found to be 2322 K using the emission data recorded under 480 nm excitation wavelength [169]. Furthermore, the color purity is a significant parameter to be determined to recognize the color quality of the phosphor and can be estimated using below equation [170]:

$$Color\ purity = \frac{\sqrt{(x-x_{ee})^2+(y-y_{ee})^2}}{\sqrt{(x_d-x_{ee})^2+(y_d-y_{ee})^2}} \times 100\ \% \qquad (4.2)$$

where, the chromaticity coordinates of the phosphor, dominant wavelength and standard white points are represented as (x, y), (x_d, y_d) and (x_{ee}, y_{ee}), respectively. The color purity obtained from above equation is found to be 97.0% for NCMS: 1.0 Pr^{3+} phosphor and suggest that the as-prepared phosphor embrace high potential to emit light in pure red region under blue excitation may be useful especially for w-LED applications.

4.3.5. Temperature dependent PL studies

Evaluation of thermal stability of the phosphor is significant for practical purpose [171]. Temperature dependent PL (TDPL) spectra for 1.0 mol% of Pr^{3+} doped NCMS phosphor has been recorded under 500-800 nm range at 480 nm excitation wavelength as represented in Fig. 4.7 (a). The emission intensity of NCMS phosphor begins to drop with elevation of temperature from RT to 190 °C. Inset of Fig. 4.7 (a) depicts that the relative emission intensity specifically at 611 nm sustained up to 64.0% when the temperature reaches to 150 °C (operating temperature of w-LED).

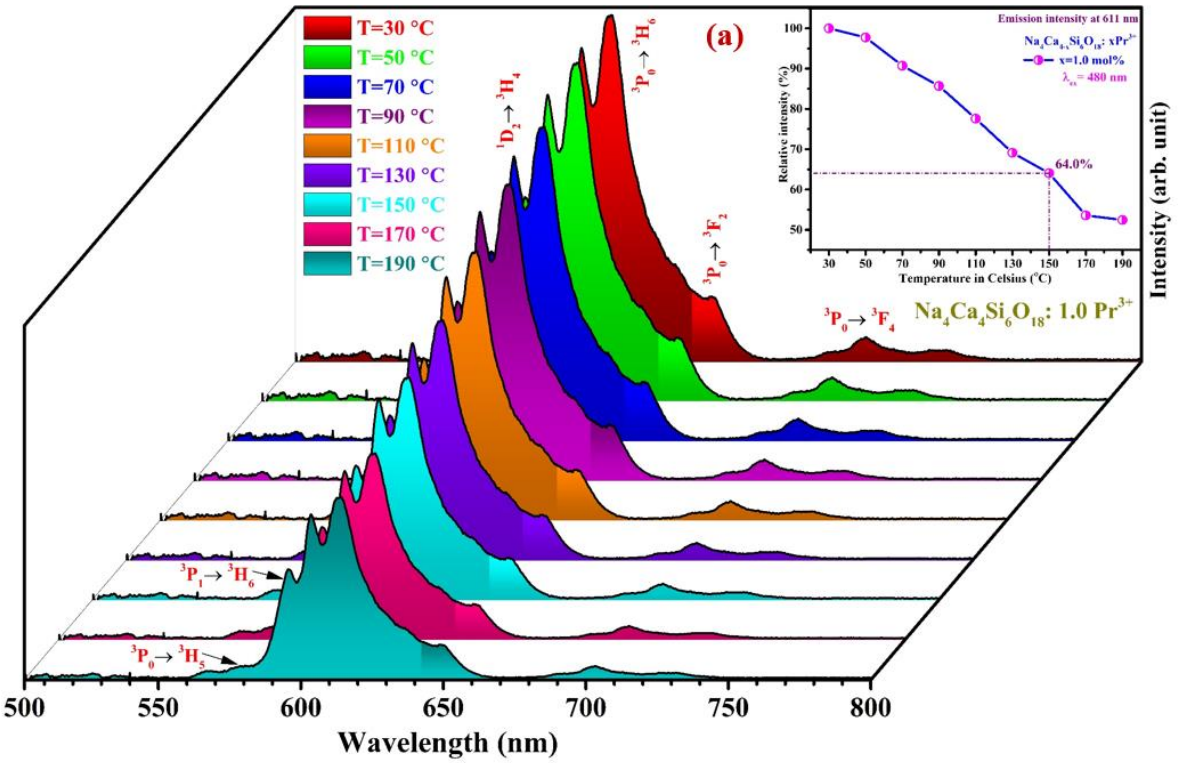

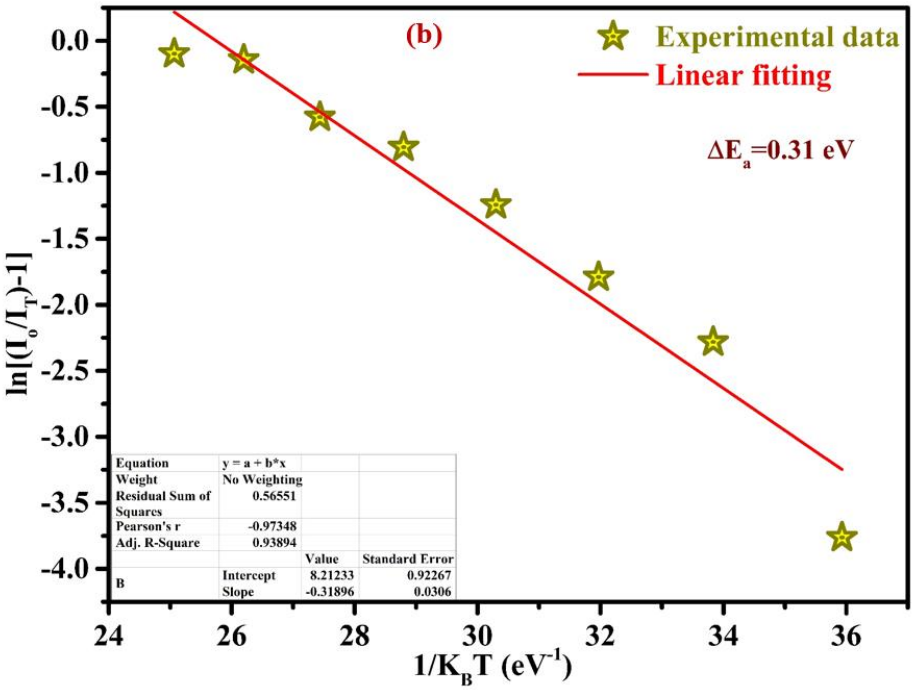

Fig. 4.7. ***(a)*** *Temperature-dependent PL spectra of NCMS: 1.0 mol% Pr^{3+} phosphor [inset: shows the relative emission intensity variation in temperature range RT to 190 °C]* ***(b)*** *Plot of $ln\left[\left(\frac{I_O}{I_T}\right)-1\right]$ with $1/K_BT$ for 1.0 mol% Pr^{3+} doped $Na_4Ca_4Si_6O_{18}$ phosphor.*

Furthermore, the activation energy (ΔE_a) can be calculated using Arrhenius equation by linearly fitted the graph between $\ln[(I_o/I_T)-1]$ vs $1/K_BT$ (Fig. 4.7 (b)) and found the activation energy as a slope of the value 0.31 *eV* [172]. Thus, the aforementioned TDPL study demonstrates relatively strong thermal stability of the optimized phosphor and could be utilized for w-LED applications.

4.4. Conclusions

A sequence of samples for Pr^{3+} doped red emitting phosphor have been prepared using conventional solid state reaction method. Phase purity and crystal structure affirms by the x-ray diffraction patterns when compared with the comparison of standard diffraction peaks. Morphology of the as-prepared phosphor has been expressed by the FE-SEM image unveil that the particles size are in micron range. The excitation spectrum shows three characteristic peaks in the blue region and the strongest excitation peak emerge at 480 nm ($^3H_4 \rightarrow {}^3P_0$) is used to record the emission spectra of NCMS: Pr^{3+} phosphor. The emission spectrum for 1.0 mol% of Pr^{3+} doped

NCMS phosphor depicts the various radiative peaks obtained under 480 nm excitation wavelength with the highest intensity at 611 nm wavelength. The concentration of dopant ion in the host matrix has been finalized at 1.0 mol% due to the effect of concentration quenching phenomenon. Dexter's theory expresses the type of interaction among the dopant ions in NCMS phosphor as dipole-quadrupole interaction. Chromaticity coordinates illustrate the emitting color of the optimized Pr^{3+} doped NCMS phosphor as intense red with the high color purity of 97.0%. Hence, the above-mentioned studies indicated the promising features of thermally stable red emitting Pr^{3+} doped NCMS phosphor for w-LED applications.

Chapter 5

Structural and spectroscopic analysis of thermally stable Dy^{3+} activated $Na_4Ca_4Si_6O_{18}$ phosphor for optoelectronic device applications

A series of yellow light emitting Dy^{3+} doped sodium calcium metasilicate (NCMS: $Na_4Ca_4Si_6O_{18}$) phosphors have been synthesized by adopting the conventional solid-state reaction route. Phase identification has been carried out through XRD technique. The diffraction peaks of $Na_4Ca_4Si_6O_{18}$ sample are well-matched with the standard JCPDS (card no. 75-1687) pattern. DRS have been used to determine the optical band gap of as-synthesized NCMS material. Morphological studies and particle size estimation have been done through FE-SEM. *Under near-UV excitation, PL spectra exhibit two characteristic bands with blue and yellow colour emitting light. The concentration quenching was achieved beyond the 5.0 mol% of Dy^{3+} ion in NCMS host lattice. The temperature-dependent PL studies display that the as-synthesized phosphor has high thermal stability. All investigations listed above demonstrate the tremendous potentiality of NCMS phosphor for optoelectronic device applications.*

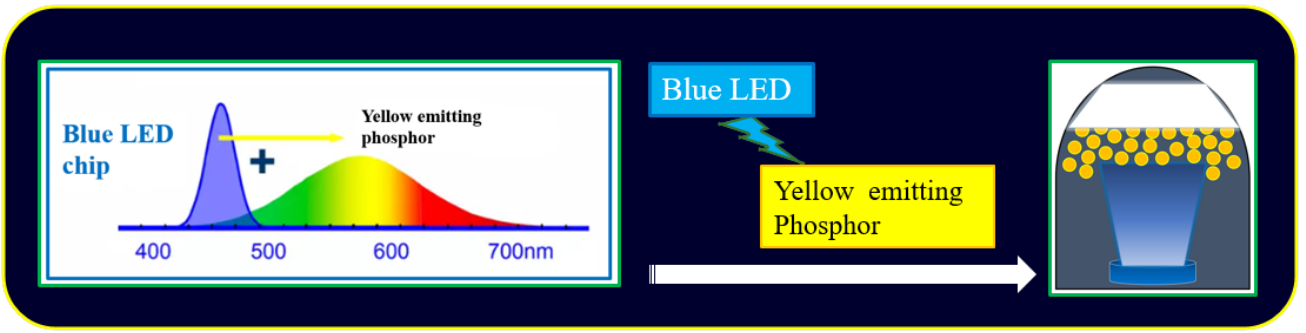

5.1. Introduction

In recent years, white light-emitting diode (w-LED) has been ascending as a peculiar source of light due to abundance advances in lighting technology. Moreover, w-LEDs exhibit marvellous potential to proliferate the current technology in respect to the generation of white light [173,174]. In modern days, researchers are focused onto developing the strategies for production of white light having high quantum efficiency, better performance, and high CRI. Recently, high quality white light has been achieved via adopting two fundamental phosphor-based approaches in lighting industries. Primarily, the white light has been generated by stimulating the yellow phosphor with blue LED and secondarily, the blue LED chip is combined with Red (R), Blue (B) and Green (G) phosphors [175]. Further, phosphor manifest pivotal role in lighting industry owing to their fascinating luminescent properties based on their chemical compositions, host lattices, concentration of rare earth ions, reaction condition, size as well as morphology of the as-prepared phosphor. Specifically, the rare earth incorporated inorganic phosphor reflects extensive behaviour in various applications including display panels, w-LEDs, temperature detectors, solid state lasers and solar cells etc [176].

Among rare earth ions, Dy^{3+} ion act as a prospective activator for its incorporation into suitable host lattice owing to its unique spectral characteristics. Dy^{3+} is an eminent rare earth ion with two characteristic emission bands including blue and yellow emission band [177]. The hypersensitive electronic dipole in yellow region is highly influenced from its crystal field environment whereas magnetic dipole in blue region hardly varies with local symmetry [178,179]. Thus, tweaking the yellow to blue (Y/B) ratio and choosing appropriate host matrix may improve the possibility of achieving near white light from Dy^{3+} activated luminescent materials. Numerous host matrices have been explored in terms of their thermal, structural and optical properties in order to produce efficient luminescent material. In spite of various inorganic oxide hosts such as phosphates, borates, vanadates, molybdates and tungstates, silicates have come out to be the most

fascinating host matrix owing to their stable crystal lattice, economically inexpensive preparation and good thermal, physical and chemical stability [180,181]. Dy^{3+} doped sodium metasilicate phosphor has shown exclusive properties in terms of optical band gap, luminescence, thermal and chemical stability [177,178]. Hence, Dy^{3+} activated $Na_4Ca_4Si_6O_{18}$ phosphor will be highly fascinating material for w-LEDs, display and various other optoelectronic device applications.

In the present study, pure phase Dy^{3+} activated $Na_4Ca_4Si_6O_{18}$ phosphors have been synthesized via solid state reaction route to explore thermal, structural, optical, morphological, photoluminescence and temperature dependent PL properties. The identification of pure and crystalline phase has been done from XRD patterns. The morphological and optical studies exhibit the particle size/morphology and band gap of as-prepared material from FE-SEM micrograph and DRS spectra, respectively. The PL and temperature dependent PL express the luminescent intensity depending on Dy^{3+} ion concentration and temperature for NCMS phosphor. The above mentioned properties indicate the potential utilization of white light emitting NCMS phosphor for w-LED applications.

5.2. Sample preparation and characterisation techniques

Conventional solid-state reaction methodology has been used to synthesize microcrystalline sodium calcium metasilicate ($Na_4Ca_{4-x}Si_6O_{18}$) phosphor doped with Dy^{3+} ions, as described in section 2.2.3. The detailed procedure is represented through the flow chart as shown in Fig. 2.1. Moreover, various characterization techniques have been carried out to investigate the crystalline, morphological and luminescent behaviour of the as synthesized phosphors, described in detailed in section 2.3 from chapter 2.

5.3. Results and discussion

5.3.1. Thermal analysis

Thermogravimetric analysis (TGA) and differential thermogravimetric (DTG) analysis have been done to determine the weight loss and identification of weight loss processes [182,183]. TGA

and DTG of powder sample $Na_4Ca_4Si_6O_{18}$, contained raw materials (Na_2SiO_3, CaO, and SiO_2) in stoichiometric amounts have been shown in Fig. 5.1. The weight loss and corresponding DTG spectra with several endothermic peaks from RT to 1000 °C have been depicted in Fig. 5.1.

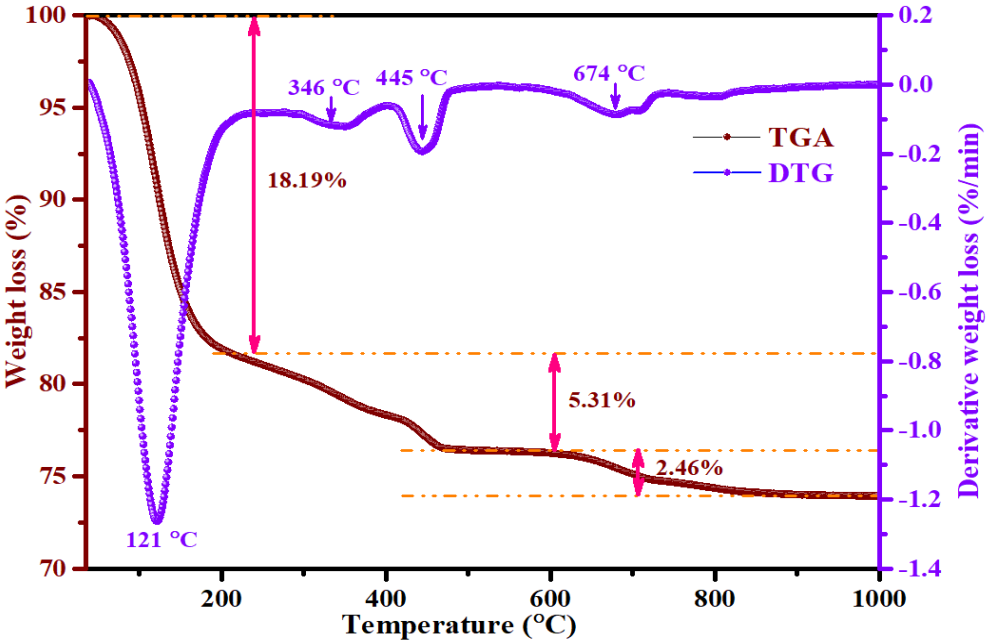

Fig. 5.1. *TGA and DTG curve for $Na_4Ca_4Si_6O_{18}$ sample.*

The weight loss takes place in three stages. Predominantly, the significant weight loss of about 18% occurred in the range from RT to 200 °C as seen by the prominent endothermic peak at 121 °C in DTG spectra which is due to removal of absorbed water. Secondly, the weight loss appeared in the temperature range from 200 to 600 °C with two derivative weight loss peaks at 346 and 445 °C. The weight loss percentage took place in the second step is approximately 5%, which resembles due to hydroxyl group present in the structure [184]. At third step, weight loss (~2 %) observed due to decomposition of oxides residuals in the sample at temperature between 600-850 °C with derivative peaks position at 674 °C [185]. Thus, the optimum temperature to obtain pure phase could be achieved beyond 800 °C as the weight loss curve become flat and maximum decomposition have been completed before this temperature [186]. Hence, the raw mixture has been sintered at various temperatures beyond 800 °C to get the crystalline $Na_4Ca_4Si_6O_{18}$ sample.

5.3.2. X-ray diffraction

Fig. 5.2 (a) reveals the XRD patterns (2θ=10-65°) of as-synthesized $Na_4Ca_4Si_6O_{18}$ powders synthesized via solid state reaction route at different temperatures and compared with the standard pattern (JCPDS card no. 75-1687). The phase formation takes place in the range of 900-1000 °C and achieved the crystallinity. The pure phase with higher crystallinity obtained at 950 °C among three different temperatures. Therefore, the sample is sintered at 950 °C for un-doped and Dy^{3+} doped $Na_4Ca_4Si_6O_{18}$ samples. The hexagonal $Na_4Ca_4Si_6O_{18}$ crystal structure was first explored by H. Ohsato et. al. in 1986 having space group P 32 and lattice parameter a=10.46 Å; b=10.46 Å; c=13.17 Å and V=1249.42 $Å^3$ [107].

Fig. 5.2 (b) represents the XRD pattern of 1.0 mol% of Dy^{3+} doped $Na_4Ca_4Si_6O_{18}$ phosphor compared with the standard pattern of $Na_4Ca_4Si_6O_{18}$. The XRD pattern of Dy^{3+} doped $Na_4Ca_4Si_6O_{18}$ phosphor has shown good agreement with the diffraction peaks of standard pattern at 2θ values with absence of any impurity in the as-synthesized phosphor. The absence of peaks apart from standard pattern indicates the successful incorporation of dopant ion in the host lattice which may be possible due to comparable ionic radii of rare earth ion and ion present in the host lattice. Fig. 5.2 (c) shows the schematic of hexagonal $Na_4Ca_4Si_6O_{18}$ structure built of six membered $[Si_6O_{18}]^{12-}$ rings stacked with alkali and alkaline earth ions [64].

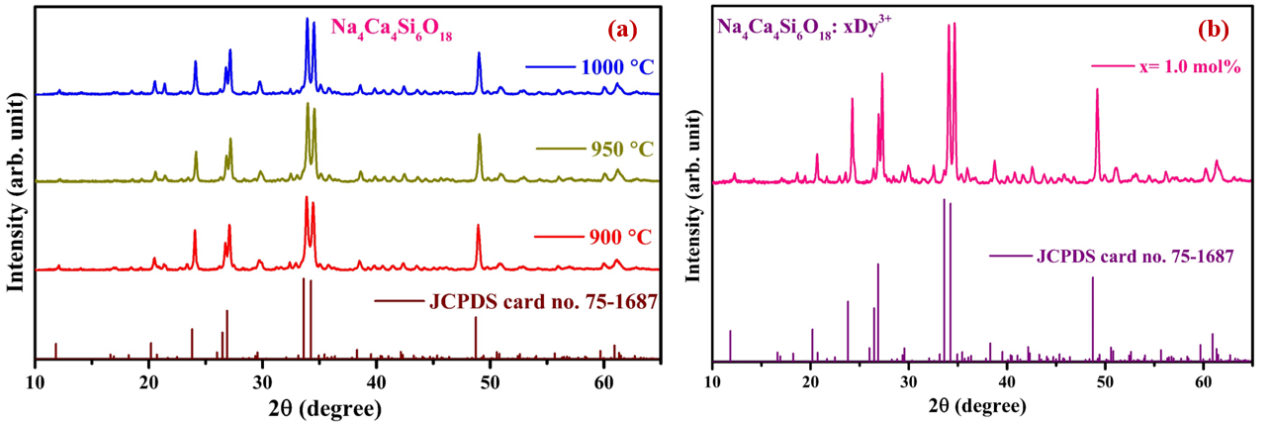

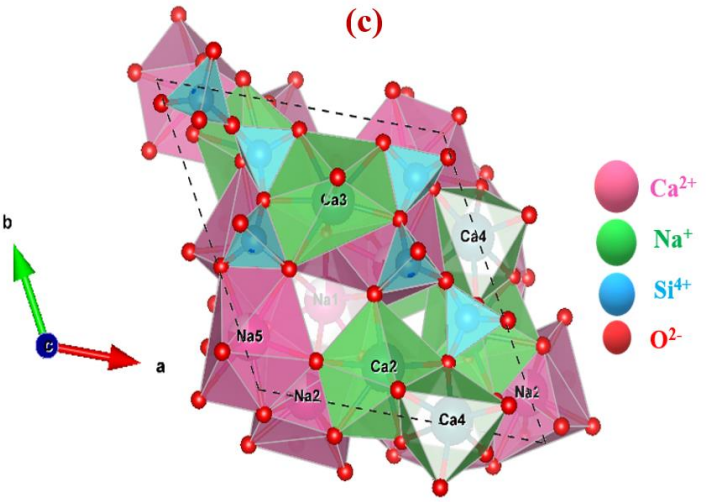

Fig. 5.2. ***(a)*** *XRD patterns of $Na_4Ca_4Si_6O_{18}$ samples at different calcination temperatures (900, 950, and 1000 °C for 3h) compared with standard JCPDS data.* ***(b)*** *XRD pattern of 1.0 mol% Dy^{3+} doped $Na_4Ca_4Si_6O_{18}$ phosphor compared with standard data* ***(c)*** *Schematic view of crystal structure of $Na_4Ca_4Si_6O_{18}$ from c-axis.*

The ionic radius of Dy^{3+} ion is much more approachable to replace Ca^{2+} ion as the assessed percentage difference is much smaller than other ions. Furthermore, the presence of dopant ion has not influenced the crystal structure of $Na_4Ca_4Si_6O_{18}$ that uplift the concept of successful incorporation of dopant ion into the crystal lattice. The crystallite size (D) has been computed by employing the well-known Debye-Scherrer equation as give below [187,188]

$$D = \frac{k\lambda}{\beta Cos\theta} \tag{5.1}$$

where, k is the shape factor with value $k = 0.9$, θ is the diffraction angle, λ represents as wavelength of incident X-ray and β denotes full width half maxima (FWHM). The crystallite size of $Na_4Ca_4Si_6O_{18}$ powder at temperature 900, 950 and 1000 °C have been calculated and found to be 35, 37 and 42 nm. The increase in crystallite size with rise in temperature indicates the crystal growth with temperature and peaks become narrow [189].

5.3.3. Band gap calculation

The diffuse reflectance spectrum (DRS) analysis have been carried out to determine the band gap energy (E_g) of un-doped 1.0 mol% of Dy^{3+} doped $Na_4Ca_4Si_6O_{18}$ phosphor, as represented in inset of Fig. 5.3. Primarily, an intense absorption band is perceived at 245 nm resembles to the

band of as-synthesized $Na_4Ca_4Si_6O_{18}$ sample [190]. However, in Dy^{3+} doped samples additional absorption band can be observed in a range of 300-500 nm.

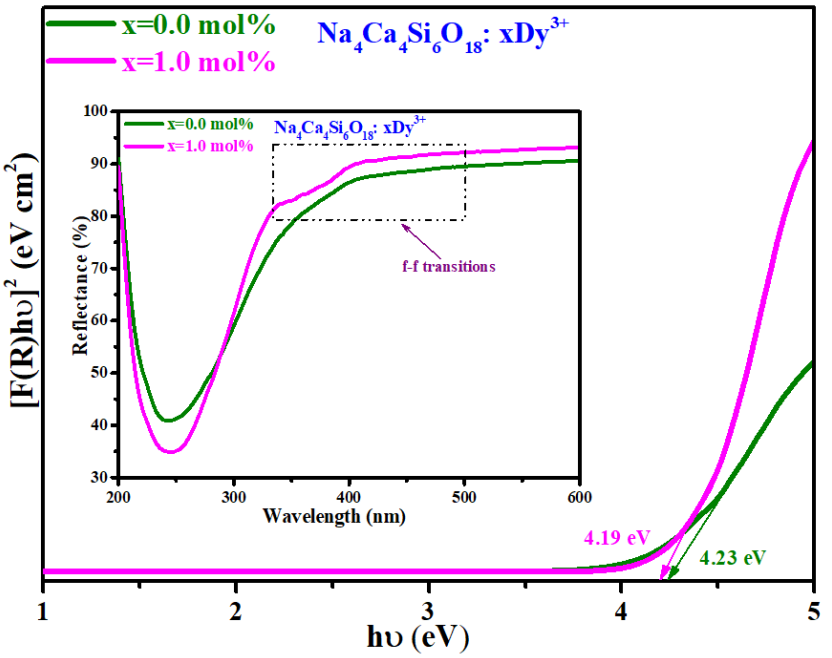

Fig. 5.3. *Band gap spectra for un-doped and 1.0 mol% of Dy^{3+} doped $Na_4Ca_4Si_6O_{18}$ phosphor using Kubelka-Munk function (inset: Diffuse reflectance spectra).*

The weak broad band consisting of peaks in the f-f transition region, which positioned at similar location traced as the excitation peaks of Dy^{3+} doped phosphor. Moreover, the energy band gap value has been estimated utilising Kubelka-Munk (K-M) relation as expressed below in equation (5.2):

$$F(R) = \frac{(1-R)^2}{2R} = \frac{K}{S} \tag{5.2}$$

where R is the ratio between reflectance of sample to the reference sample or standard $R = \frac{R_{sample}}{R_{standard}}$ and S is the scattering coefficient, K is absorption coefficient and $F(R)$ is Kubelka-Munk function. Furthermore, the band gap energy (E_g) and linear absorption coefficient (α) of the as-prepared material can be associated with the Tauc equation given as [191]:

$$\alpha h\upsilon = A(h\upsilon - E_g)^n \tag{5.3}$$

where $h\upsilon$ and A represent energy of incident photon and proportionality constant, respectively. In equation (5.3), n=1/2, 2, 3/2, 3 shows the electronic transition ascribe to allowed direct, allowed

indirect, forbidden direct and forbidden indirect [192]. If a sample scatters light in an absolutely diffuse manner, then the absorption coefficient K become equivalent to twice of α (K = 2α), [193,194]. Further taking S as constant with regards to wavelength and applying Kubelka-Munk function to the equation (5.3), we get the expression as shown below:

$$(F(R)hv) = B(hv - E_g)^n \quad (5.4)$$

As a result, the value for band gap energy (E_g) may be calculated by projecting the linear streak region where $[F(R)hv]^2=0$, as shown in Fig. 5.3. According to $[F(R)hv]^2$ vs hv plot in Fig. 5.3, direct allowed band gap energies for un-doped and 1.0 mol% of Dy^{3+} doped $Na_4Ca_4Si_6O_{18}$ samples were found to be 4.23 and 4.19 eV, respectively.

5.3.4. FT-IR spectroscopy

Fig. 5.4. depicts the Fourier transform infra-red spectra for un-doped $Na_4Ca_4Si_6O_{18}$ samples at different calcination temperatures and doped $Na_4Ca_4Si_6O_{18}$ samples with varying dopant (Dy^{3+}) concentrations in the range of 500-1400 cm^{-1}. The peaks identified in FT-IR spectra at specific wavenumber resembles to particular chemical bonding among molecules [109]. In the FT-IR spectra, multiple prominent peaks have been observed and located at 529, 624, 696, 729, 914, 1030, 1095 and 1385 cm^{-1} position for all samples. Absence of any extra peak confirms that there is no significant change occur on structure due to change in temperature and concentration of Dy^{3+} ions. The peak located at 529, 624, and 696 cm^{-1} reflects the bending vibration mode of linkages between silicon and oxygen atoms [195]. Additionally, the peaks centred at 729, 914 and 1030 cm^{-1} are assigned to Si-O-Si asymmetric stretching, Si-O symmetric stretching and Si-O-Si symmetric stretching mode, respectively [196,197]. The peaks observed at 1095 and 1385 cm^{-1} are produced by the vibrational mode of metal-oxygen (M-O: Ca, Na-O) bonds [198].

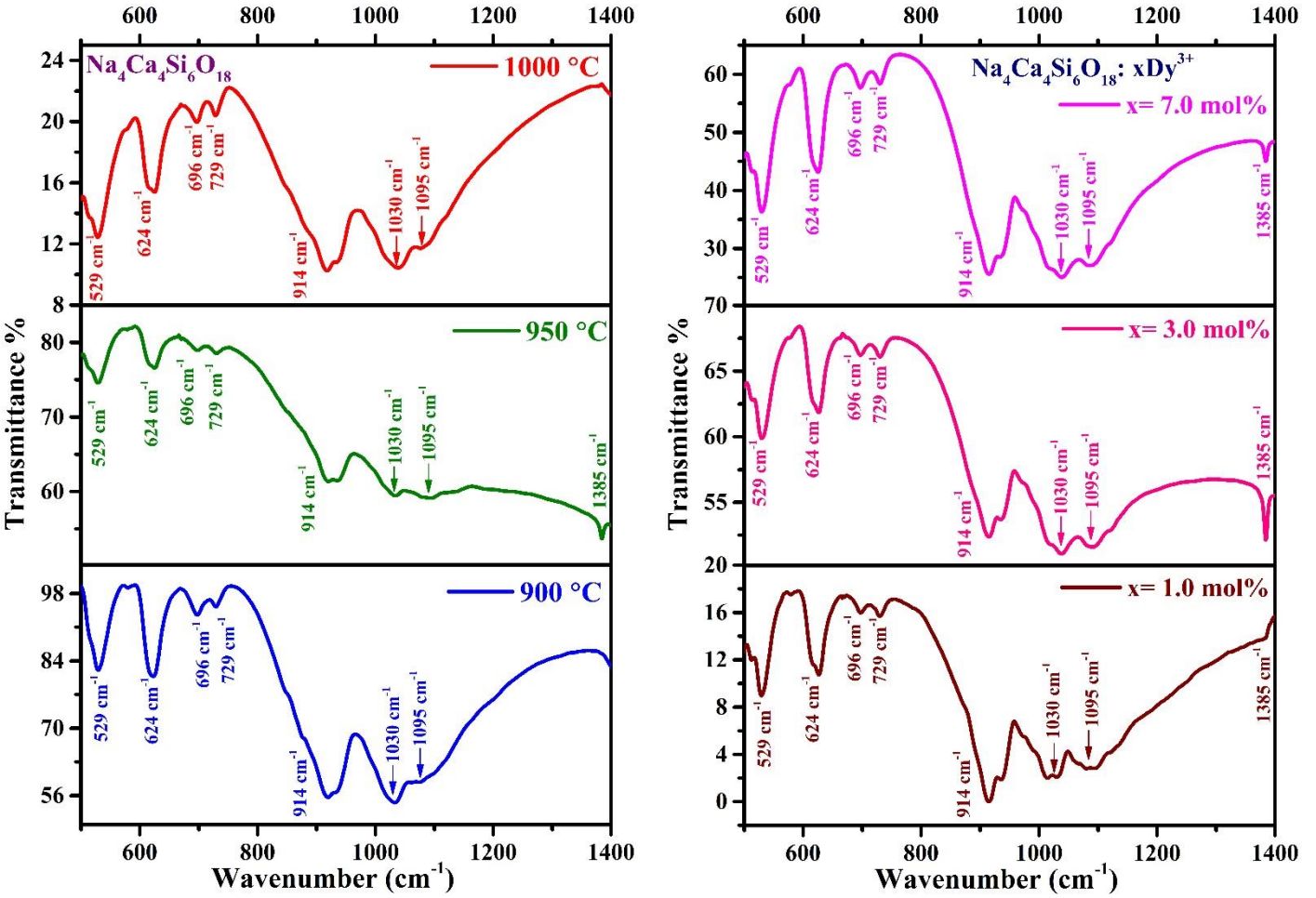

Fig. 5.4. *FT-IR spectra of un-doped $Na_4Ca_4Si_6O_{18}$ samples at different calcination temperatures & FT-IR spectra of $Na_4Ca_4Si_6O_{18}$: xDy^{3+} (x=1.0, 3.0 and 7.0 mol%) phosphors at 950 °C.*

5.3.5. Morphological studies

Scanning electron microscope (FE-SEM) is a technique that exhibit the particle size and morphological analysis of as-synthesized NCMS samples. The FE-SEM micrographs of undoped and 1.0 mol% of Dy^{3+} doped NCMS phosphor at same resolution, respectively are represented in Fig. 5.5 (a) and (b). Both doped and un-doped samples are expressing the agglomeration of particles, inhomogeneity and rough surface due to opting the same synthesis method.

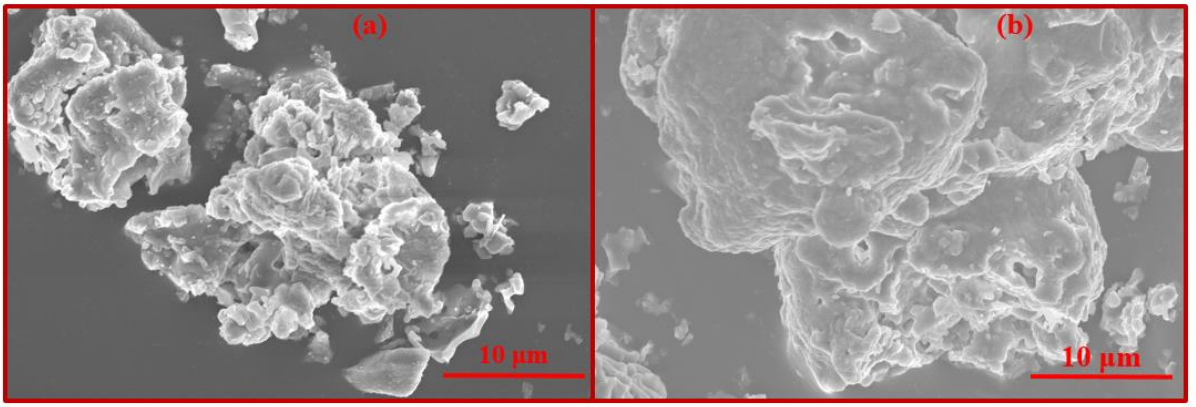

Fig. 5.5. ***(a & b)*** *FE-SEM micrographs for un-doped and 1 mol% of Dy^{3+} doped NCMS phosphor at same magnification*

It can be seen that due to aggregation of small inhomogeneous particles, the final particle size is lie within the micro-range. However, recent available pc-w-LEDs fabricated with the micro-size phosphor to acquire strong luminescence. Therefore, as-synthesized micro-size Dy^{3+} doped $Na_4Ca_4Si_6O_{18}$ phosphor may provide an influential performance for commercial usage [120,135].

5.3.6. Down-conversion emission measurement

The PL excitation (PLE) and emission spectra of xDy^{3+} (x= 1.0, 3.0, 5.0 and 7.0 mol%) doped $Na_4Ca_4Si_6O_{18}$ phosphors have shown in Figs. 5.6. and 5.7, respectively. The PLE spectra under the emission wavelength of 576 nm in the range of 300-460 nm depicted in Fig. 5.6. depicts. There are several peaks in the excitation spectra at 321, 348, 360, 382, 421 and 450 nm, with the emission wavelength at 576 nm. These excitation peaks are ascribed to several excited states $^6P_{3/2}$, $^6P_{7/2}$, $^6P_{5/2}$, $^4F_{7/2}$, $^4G_{11/2}$ and $^4I_{15/2}$ i.e. respective transitions to these excited levels from ground state $^6H_{15/2}$ [199]. The intense excitation peak is observed at 348 nm among various excitation peaks in the PLE spectra of Dy^{3+} (1.0, 3.0, 5.0 and 7.0 mol%) activated $Na_4Ca_4Si_6O_{18}$ phosphor. Therefore, NCMS phosphors with Dy^{3+} concentration of 1.0, 3.0, 5.0 and 7.0 mol% are excited at 348 nm wavelength, which locate three characteristic bands in the visible region at 488 nm with blue emission, 576 nm with yellow emission and 675 nm with red emission in Fig. 5.7.

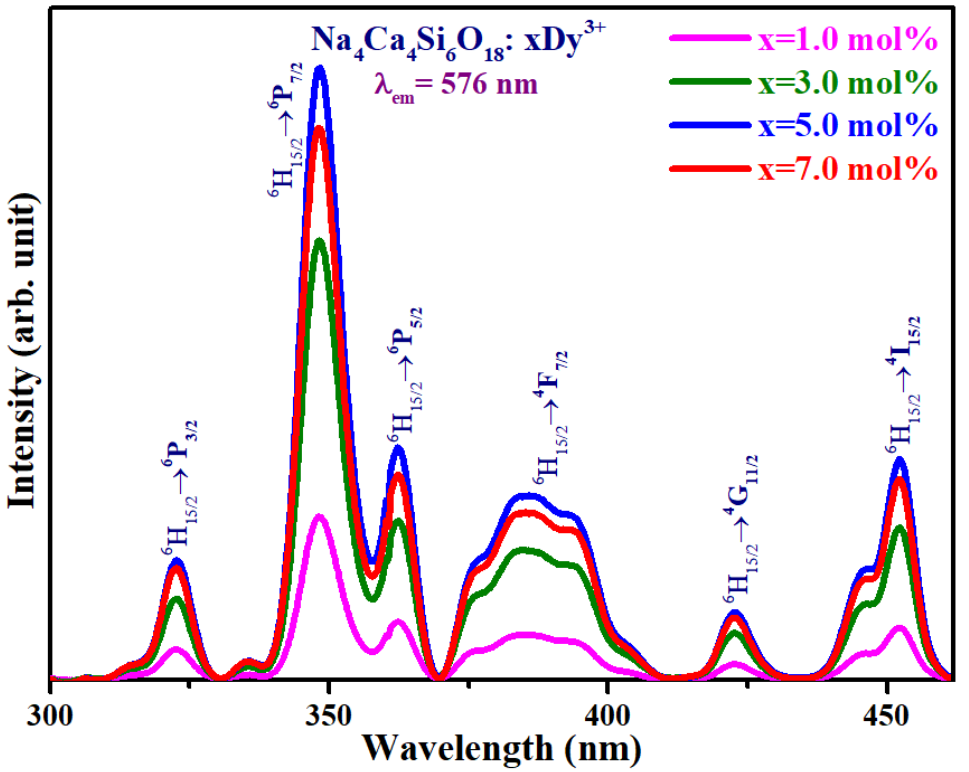

Fig. 5.6. *PLE spectra of Dy^{3+} doped $Na_4Ca_4Si_6O_{18}$ phosphor with 1.0, 3.0, 5.0 and 7.0 mol% Dy^{3+} concentration monitored at emission wavelength 576 nm.*

The emission peaks at 488, 576 and 675 nm wavelengths are ascribed to $^6H_{15/2}$, $^6H_{13/2}$ and $^6H_{11/2}$ from the excited state $^4F_{9/2}$, respectively. In PL spectra of Dy^{3+} activated $Na_4Ca_4Si_6O_{18}$ phosphor, it can be observed that the emission at 576 nm is dominating among three characteristic peaks and responsible for yellow colour emission. The peak at 488 nm in the PL spectra corresponds to $^4F_{9/2}\rightarrow{}^6H_{15/2}$ shows magnetic dipole (MD) transition and insensitive to crystal field environment whereas the peak at 576 nm relates to $^4F_{9/2}\rightarrow{}^6H_{13/2}$ (a forced electric dipole (ED) transition obeying the selection rule as ($\Delta J=0$ or $\Delta J=\pm2$) [200]. The ED transition, which is strongly impacted by the surrounding environment and responsible for the dominant with substantial yellow emission [201]. In general, when the Dy^{3+} ion is positioned at low symmetry site with no inversion centre, yellow emission is more apparent than blue emission, whereas when the dopant ion is positioned at a high symmetry site with an inversion centre then the blue emission is more prominent. The enhanced emission in yellow region in the current Dy^{3+} ion doped $Na_4Ca_4Si_6O_{18}$ phosphor indicates that the dopant ion occupies low symmetry sites with no inversion centre [202].

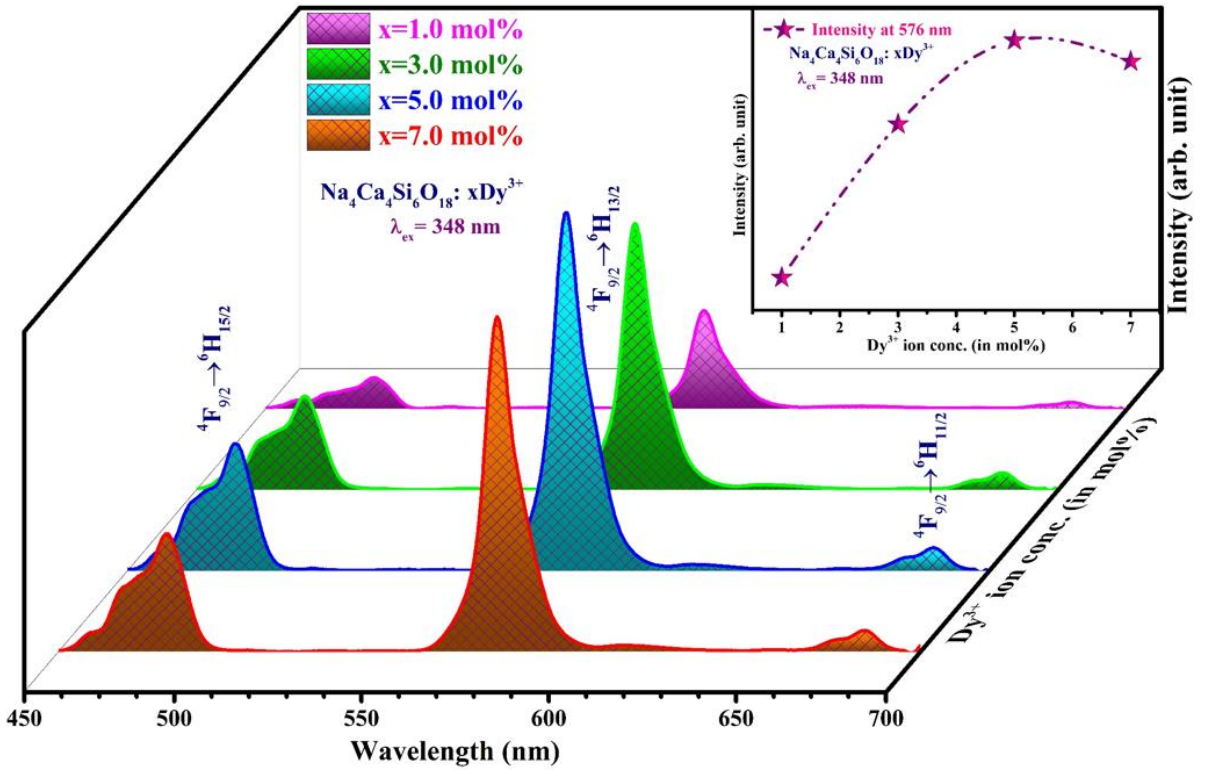

Fig. 5.7. *PL spectra of $Na_4Ca_4Si_6O_{18}$: xDy^{3+} (x= 1.0, 3.0, 5.0 and 7.0 mol%) phosphors at λ_{ex} = 348 nm. Inset: Variation of emission intensity at 576 nm wavelength at λ_{ex} = 348 nm with concentration of Dy^{3+} ion.*

Fig. 5.7. depicts the PL emission spectra recorded with varying the concentration of dopant ions witness that the peak positions are same but the intensity varies [203,204]. The inset of Fig. 5.7, discerns that emission intensifies with increment in concentration of dopant ions up to 5.0 mol% in the NCMS host lattice. Thereafter, further enhancement in the Dy^{3+} ion concentration reduces the distance between dopant ions which causes more non-radiative energy transfer between them. The enhanced probability of non-radiative energy transfer among dopant ions suppress the emission intensity and lead to upsurge in concentration quenching effect [100]. The energy transfer between the dopant ions rely on the critical distance (R_c) between them which can be estimated by the equation suggested by Blasse as follows [162]:

$$R_c = 2\left(\frac{3V}{4\pi x_c N}\right)^{\frac{1}{3}} \quad (5.5)$$

In the above equation, parameters listed such as V, N and x_c represents the volume of unit cell, number of cations per unit cell and critical concentration of the activator ion in the host lattice,

respectively. Herein, for Dy^{3+} doped $Na_4Ca_4Si_6O_{18}$ phosphor the values are V=1249.42 $Å^3$, N=3 and x_c=0.05 mol. Thus, the critical distance estimated via above equation are found to be 25.15 Å. The multipolar interaction will become prominent since the value of critical distance (R_c) is much higher than 5 Å. In the current study, the emission intensity ratio between yellow to blue (Y/B) varies from 3.10 to 2.80 with rise in concentration of dopant ion which is higher than 1 and endorses yellow emission. Thus, the as-synthesized Dy^{3+} doped $Na_4Ca_4Si_6O_{18}$ phosphor have the potential to be used as a yellow emitting phosphor pumped with n-UV source in the pc-w-LED applications. Variation in Y/B ratio could achieve white light emitting colour with variable CCT value.

The partial energy level diagram of Dy^{3+} doped $Na_4Ca_4Si_6O_{18}$ phosphor in which the different levels of excitation and emission can be observed in Fig. 5.8. The $Na_4Ca_4Si_6O_{18}$ phosphors have been excited from the ground state $^6H_{15/2}$ to various upper states ascribed to respective transitions at 321 ($^6P_{3/2}$), 348 ($^6P_{7/2}$), 360 ($^6P_{5/2}$), 382 ($^4F_{7/2}$), 421 ($^4G_{11/2}$) and 450 ($^4I_{15/2}$) nm. Further, the 4f electron of dopant ion descends to lower excited state ($^4F_{9/2}$) through non-radiative transition due to minute energy difference between upper levels.

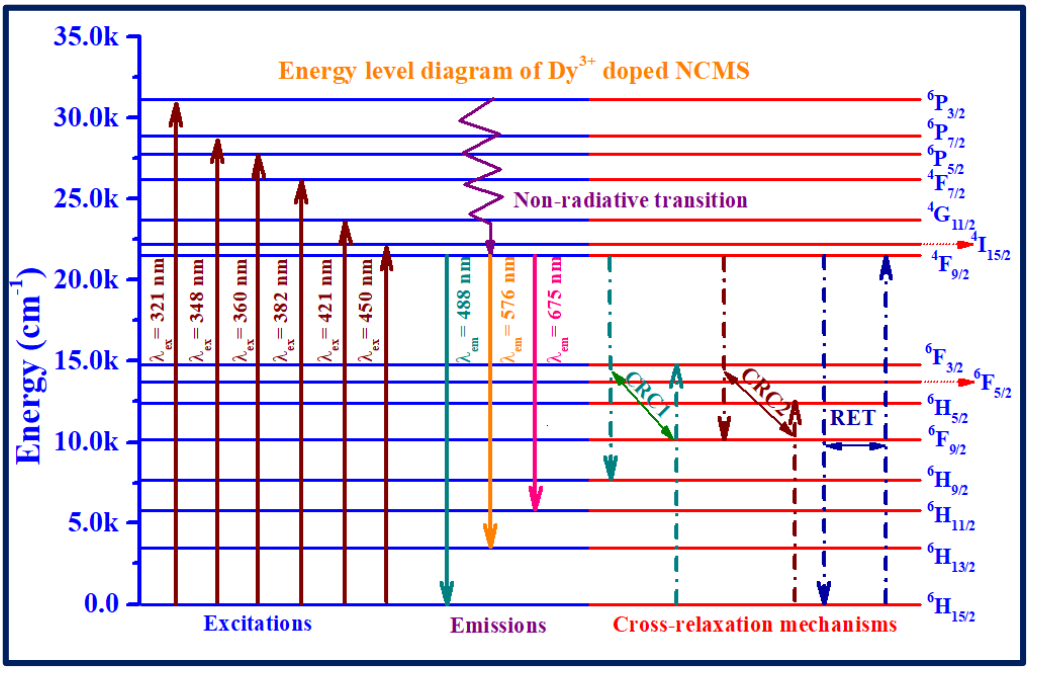

Fig. 5.8. *Partial energy level diagram of Dy^{3+} doped $Na_4Ca_4Si_6O_{18}$ phosphor.*

Radiative emission, on the other hand, results from the relaxation of electrons from the $^4F_{9/2}$ level to distinct lower levels such as $^6H_{15/2}$, $^6H_{13/2}$ and $^6H_{11/2}$ as a result of sufficient energy difference between them. However, the cross-relaxation channels (CRC) as well as resonance energy transfer (RET) in the Dy^{3+} doped $Na_4Ca_4Si_6O_{18}$ phosphor, may cause non-radiative energy transfer and concentration quenching. The following are possible cross-relaxation channels (CRC1 and CRC2) and RET, as shown in Fig. 5.8 [205]:

$$\text{CRC1: } {}^4F_{9/2}+{}^6H_{15/2}\rightarrow{}^6H_{9/2}+{}^6F_{3/2}$$

$$\text{CRC2: } {}^4F_{9/2}+{}^6H_{15/2}\rightarrow{}^6F_{9/2}+{}^6F_{5/2}$$

$$\text{RET: } {}^4F_{9/2}+{}^6H_{15/2}\rightarrow{}^6H_{15/2}+{}^4F_{9/2}$$

5.3.7. Colorimetric analysis

To study the behaviour of as-prepared Dy^{3+} doped $Na_4Ca_4Si_6O_{18}$ phosphor, the Commission International de l'Eclairage (CIE) coordinates were used. Fig. 5.9 depicts the CIE coordinates for the optimized sample (5.0 mol% Dy^{3+} doped $Na_4Ca_4Si_6O_{18}$ phosphor), which are located in yellow region with the points (0.423, 0.433) at an excitation wavelength of 348 nm.

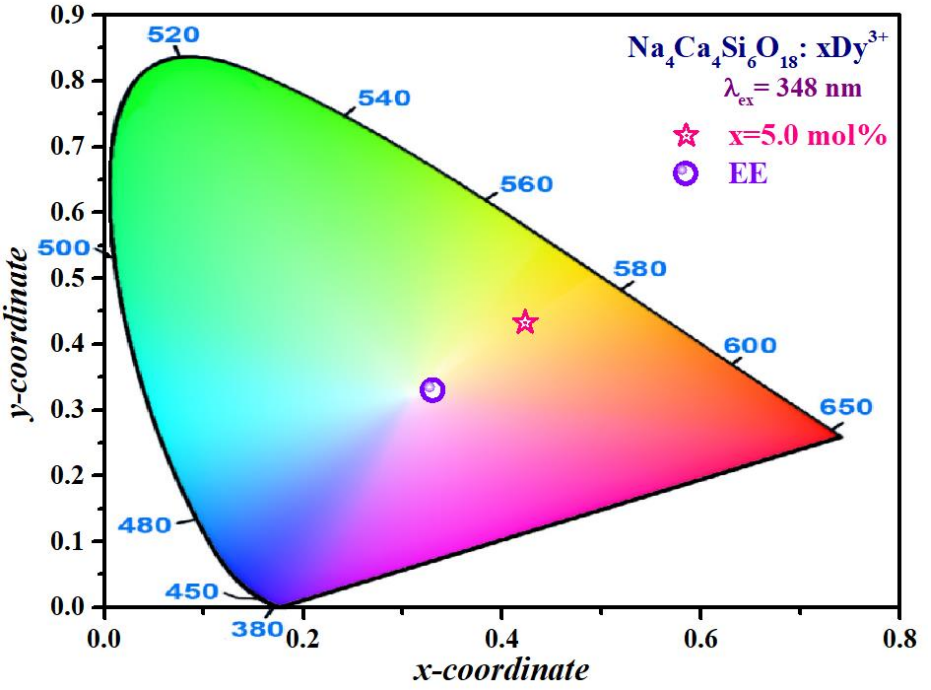

Fig. 5.9. *CIE plot of $Na_4Ca_4Si_6O_{18}$: xDy^{3+} (x= 5.0 mol%) phosphors at λ_{ex} = 348 nm.*

The correlated colour temperature (CCT) is defined as Planckian black-body radiator with an emitting colour approaches to the white light source [206]. Thus, this aid to determine the quality of white colour and offers the idea about coolness and warmness of light in accordance with temperature [207]. Moreover, the CCT value of phosphor lower than 5000 K is considered as warm light source while greater than 5000 K encourages the phosphor to be utilize as a cool light source. The CCT value has been evaluated from the equation proposed by McCamy given below [55,208]:

$$CCT = -437n^3 + 3601n^2 - 6861n + 5514.31 \quad (5.6)$$

where n represents the inverse slope line and equivalent to $\frac{(x-x_e)}{(y-y_e)}$, $x_e = 0.332\ and\ y_e = 0.186$ are the coordinates for epicentre of convergence. Therefore, the CCT value for Dy^{3+} doped $Na_4Ca_4Si_6O_{18}$ phosphor has been calculated using the above-mentioned equation, which was found to be 3459 K for 5.0 mol% of dopant ion. Hence, the estimated values of CCT are less than 5000 K that make the phosphor to be used as a warm light based LED applications [209].

5.3.8. Photoluminescence decay analysis

Fig. 5.10 (a-d) depicts the decay profile for Dy^{3+} (1.0, 3.0, 5.0 and 7.0 mol%) doped $Na_4Ca_4Si_6O_{18}$ phosphor measured at 348 nm excitation wavelength. The decay profile estimated to measure the lifetime of $^4F_{9/2}$ excited level at 576 nm emission wavelength. The decay curves were fitted to different exponential equations but the best fit was observed for bi-exponential equation for all the concentration of Dy^{3+} ion which indicates the significant interaction between dopant ions and energy transfer between the excited Dy^{3+} ion (donor) to unexcited Dy^{3+} ion (acceptor). The intensity of PL spectra is given by the equation below [210]:

$$I = I_o + A_1 exp\left(\frac{-t}{\tau_1}\right) + A_2 exp\left(\frac{-t}{\tau_2}\right) \quad (5.7)$$

where I_o and I are the luminescence intensity at initial time (t=0) and instantaneous time (t), respectively. Moreover, τ_1 and τ_2 denotes the lifetime decay components whereas $A_1$and A_2 are the fitting constants.

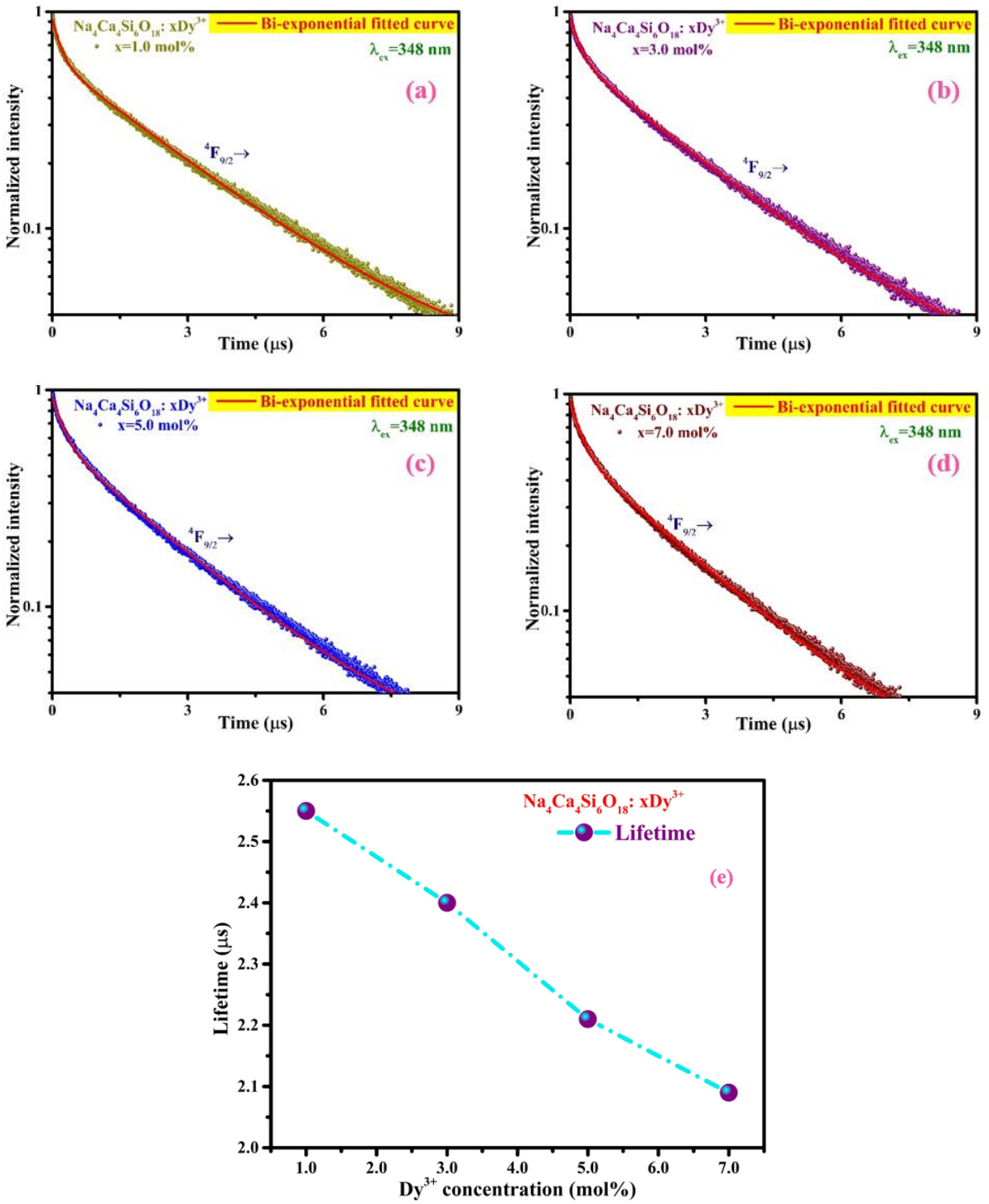

Fig. 5.10 ***(a-d)*** *Decay curves of Dy^{3+} (1.0, 3.0, 5.0 and 7.0 mol%) doped $Na_4Ca_4Si_6O_{18}$ phosphors for λ_{ex}=348 nm, λ_{em}=576 nm,* ***(e)*** *Lifetime versus concentration of Dy^{3+} ions of $Na_4Ca_4Si_6O_{18}$ phosphor plot.*

The average lifetime (τ) of as-synthesized Dy^{3+} doped $Na_4Ca_4Si_6O_{18}$ phosphor for bi-exponentially fitted decay profile can be evaluated as:

$$\tau = \frac{A_1\tau_1^2 + A_2\tau_2^2}{A_1\tau_1 + A_2\tau_2} \quad (5.8)$$

On account of fitted curve data, the average lifetime (τ) value for each concentration (1.0, 3.0, 5.0 and 7.0 mol%) of Dy^{3+} doped $Na_4Ca_4Si_6O_{18}$ phosphor has been calculated and found to be 2.55, 2.40, 2.21 and 2.09 μs, respectively. Fig. 5.10 (e) shows the decrease in average lifetime with rise in concentration of Dy^{3+} that indicates the energy transfer between donor and acceptor. The computed average lifetime of $Na_4Ca_4Si_6O_{18}$ phosphor in micro seconds could make a preferable choice for optoelectronic applications.

5.3.9. Temperature dependent PL studies

In general, the thermal stability is a significant characteristic to be hold for phosphor utilising in w-LED applications in reference to light intensity output and service life [211]. To investigate the thermal stability of the optimized 5.0 mol% Dy^{3+} doped $Na_4Ca_4Si_6O_{18}$ phosphor, the PL emission intensity at 576 nm under excitation of 348 nm have been compared with varying the temperature from 303 to 463 K, as shown in Fig. 5.11 (a).

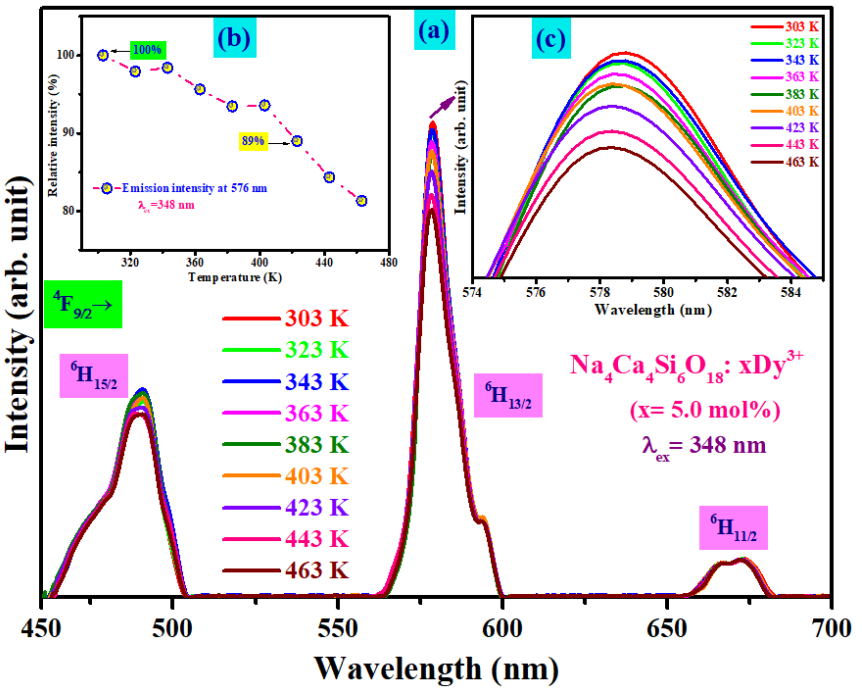

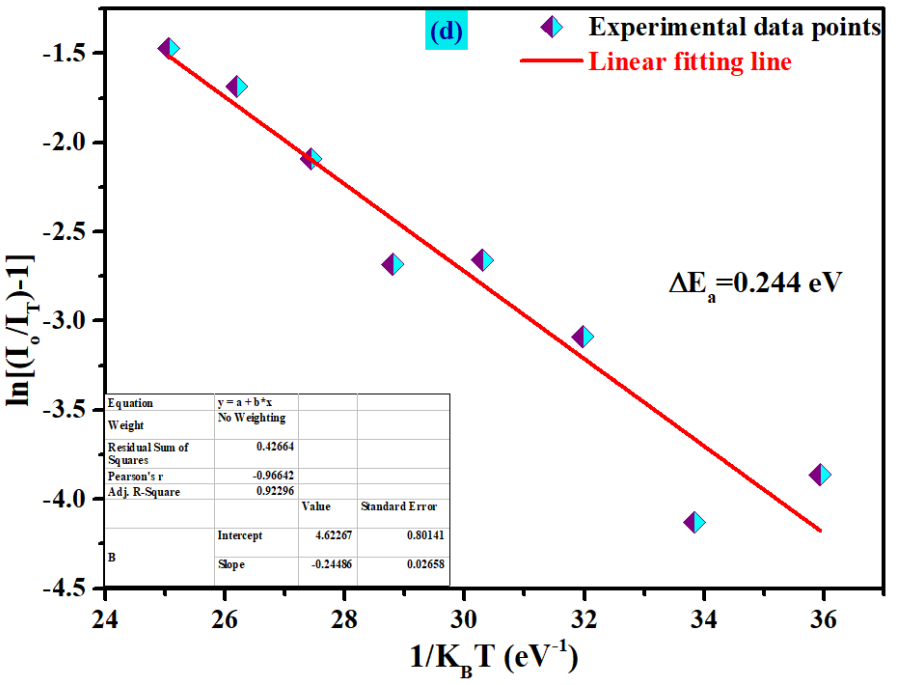

Fig. 5.11 ***(a)*** *Temperature-dependent PL spectra of 5.0 mol% Dy^{3+} doped $Na_4Ca_4Si_6O_{18}$ phosphor [inset:* ***(b)*** *shows the relative emission intensity variation in temperature range 303-463 K] and* ***(c)*** *zoom-in view of dominating emission intensity at 576 nm wavelength.* ***(d)*** *Plot of $ln\left(\frac{I_o}{I_T}-1\right)$ with $1/K_BT$ for 5.0 mol% Dy^{3+} doped $Na_4Ca_4Si_6O_{18}$ phosphor.*

Fig. 5.11 (b) represents the relative intensity of luminescence spectra of Dy^{3+} activated $Na_4Ca_4Si_6O_{18}$ phosphor with respect to temperature and prevail 89% intensity as temperature rises to 423 K (150 °C), indicating excellent thermal stability. In Fig. 5.11 (c) [zoom-in view of $^4F_{9/2}\rightarrow{}^6H_{13/2}$ transition], a gradual decrease in luminescent intensity with rise in temperature has been observed without varying the emission profile due to enhancement of non-radiative electronic transition and the effect is known as thermal quenching effect [212]. The non-radiative emission rate depending on the temperature can be expressed as follows [151]:

$$R_{nr} = Kexp\left(-\frac{\Delta E_a}{K_BT}\right) \quad (5.9)$$

where the above mentioned parameters, ΔE_a represent as activation energy relate with thermal quenching, K as a constant and K_B as Boltzmann's factor with the value 8.6173×10^{-5} eV/K. The relation between temperature and non- radiative emission rate shown in equation (5.9) clearly

explains the increase in non-radiative relaxation rate with rise in temperature, which supresses the emission intensity. To evaluate the activation energy (ΔE_a) of Dy^{3+} activated $Na_4Ca_4Si_6O_{18}$ phosphor, Arrhenius equation can be followed as given below [213]:

$$I_T = \frac{I_o}{1+\alpha exp\left(-\frac{\Delta E_a}{K_B T}\right)} \quad (5.10)$$

where, luminescent intensity at testing temperature and at initial temperature are represented as I_T and I_o, respectively while α denotes as a constant factor. The linear fitted plot between $\ln\left(\frac{I_o}{I_T}-1\right)$ and $1/K_BT$ aids to estimate activation energy as shown in Fig. 5.11 (d). Hence, the activation energy is discovered to be 0.244 eV from the slope of linearly fitted line. The obtained value of activation energy ($\Delta E_a = 0.244\ eV$) depicts the excellent thermal stability in comparison to various previously reported phosphors [214,215].

5.4. Conclusions

Near-UV excited yellow emitting NCMS phosphor have been successfully prepared through conventional solid-state reaction route. Pure phase has been achieved by thermally treated material at 950 °C temperature and confirmed through XRD patterns. The XRD studies depicted the well-matched pattern of $Na_4Ca_4Si_6O_{18}$ sample with standard JCPDS (card no. 75-1687) data. The FE-SEM micrographs represent the agglomerated particles morphology as well as the particle size falling in the micro-range suitable to fabricate w-LEDs. The excitation spectra observed by fixing emission wavelength at 576 nm and exhibit intense band at 348 nm and various bands in UV, near UV and blue spectral regions. The PL spectra manifests three characteristic peaks at 488, 576 and 675 nm under near UV excitation wavelength of 348 nm. The hypersensitive peak yield in the yellow region at 576 nm influenced by the crystal field environment and indicate the luminescence in yellow region of CIE chromaticity coordinates. Furthermore, the maximum emission intensity depending on the concentration was achieved at 5.0 mol% of Dy^{3+} ion, beyond which the intensity begins to suppress caused by concentration quenching effect. The CIE coordinates are falling in

yellow zone for all concentrations of NCMS phosphor. The average lifetime values for $^4F_{9/2}$ energy level of $Na_4Ca_4Si_6O_{18}$ phosphor under 348 nm excitation are found to be in micro second range. Moreover, the temperature dependent PL emission demonstrates the as-synthesized phosphor's excellent thermal stability. Based on the aforementioned findings, the NCMS phosphor has great potential to contribute as thermally stable yellow emitting phosphor in the w-LED applications.

Chapter 6

Energy transfer induced color-tunable bi-activated (Dy^{3+}/Eu^{3+}) alkaline earth metasilicate phosphor for luminescent devices

Solid state reaction methodology has been adopted to synthesize Dy^{3+}/Eu^{3+} co-activated thermally persistent $Na_4Ca_4Si_6O_{18}$ (NCMS) phosphors and investigated their structural, morphological and luminescence characteristics. Peaks appeared in the XRD pattern were compared to the peaks in the JCPDS standard pattern to confirm the pure phase of NCMS crystal structure. FE-SEM revealed the particle size and morphology. As-synthesized NCMS phosphors co-activated with Dy^{3+}/Eu^{3+} ions have been excited with near-ultraviolet light (λ_{ex}=348 nm) and shows the utmost energy transfer up to 97.80% from sensitizer to activator. Dy^{3+} activated NCMS phosphor shows the color shift from yellow to red region with varying the Eu^{3+} ions concentration and also observed color tunability by altering the excitation energy. Excellent thermal stability of bi-activated NCMS phosphor up to 92.21% at 423 K (~150 °C) temperature, have been examined. The Dy^{3+}/Eu^{3+} co-doped NCMS phosphors embrace tremendous thermally stable behaviour with flexible color tunability to emerge as a promising contender in the field of lighting and display technologies.

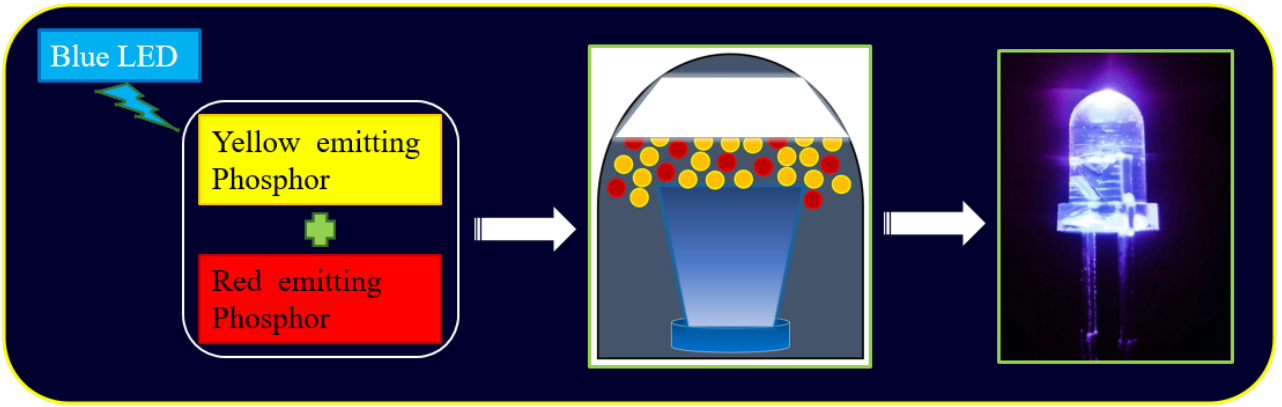

6.1. Introduction

Over the past few decades, inorganic materials based phosphor with extensive optical properties have been investigated to employ in various solid state lighting applications such as w-LEDs, multicolour displays, solar cells and temperature sensors etc. [216,217]. Phosphor converted inorganic luminescent devices, especially w-LEDs, have replaced the incandescent and fluorescent lamps [218].Owing to its plethora of merits, including their lifespan, high durability, affordability and environmental friendliness, phosphor converted luminous devices have grabbed the interest of researchers [219,220]. It is commonly known that commercial w-LEDs are fabricated by coating a yellow emitting YAG: Ce^{3+} (Ce^{3+} ion doped yttrium aluminium garnet) phosphor with reasonably broad spectrum on blue emitting InGaN LED chip. One such fabricated w-LED shows deprived value of color rendering index and correlated colour temperature caused by the dearth of red colour emitting component [221–223]. In order to achieve sufficient CRI and lower CCT with improved luminous stability, researchers and scientists have to delve into an alternative approach in which the suitable amalgamation of RGB (red: R, green: G and blue: B) mono phase phosphor on to UV/n-UV LED has been proposed. Nevertheless, the proclaimed approach is difficult to implement in practice since reabsorption of blue emission by RG phosphor [224,225]. Aforementioned glitches to produce white light can be resolved by developing the co-doped monophase phosphor combined with UV/n-UV LED chip. By transferring energy (sensitizer→activator) in the same host matrix, the single phase white light generating phosphors provide remarkable features such as appropriate CRI and CCT, spectral tunability, excellent colour reproducibility and appealing visual perception [226].

In contemplation of an efficient monophase phosphor, an adaptation of appropriate host matrix with suitable dopant ions are required to be investigated. Numerous inorganic oxide host matrices have been explored holding special redeeming features such as excellent physical and chemical stability, cost-effective, eco-friendly, remarkable optical thermal stability and facile

preparation [227]. Therefore, the aforementioned characteristics in host matrices including silicates, vanadates, borates, phophates, molybdates, niobates and tungstates engages the researchers to this fascinating field [123]. Among the above listed hosts, silicates drawn much attention owing to its significant attributes such as stable crystal matrix, cost effective preparation, excellent chemical and physical stability and employed in diverse applications specified as solar cell, wLEDs, display devices, optical-thermometry, indoor agricultural lighting and lasers [228]. However, metasilicate host exhibit excellent luminescent properties in combination with a small amount of rare earth ions as dopants [109]. In the recent era, colour tunable luminescent properties in the phosphor materials can also be achieved via incorporating dual RE ions into the host matrix. Therefore, a suitable combination of dopant ions is indeed the primary necessity to develop the desired phosphor that can be applied into appropriate domain such as display and lighting [229].

Among various available RE ions, trivalent dysprosium (Dy^{3+}) is one of the accessible ions and Dy^{3+} doped phosphor exhibit three foremost emission peaks in blue (B) and yellow (Y) region with a feeble peak in red region. Based on the ratio of emission intensity of two remarkable peaks i.e. Y/B, white light may be generated with Dy^{3+} doped phosphor. The white light produced through Dy^{3+} doped phosphor suffers from lower CRI and higher CCT value which is due to inadequacy of red component in the phosphor. Moreover, taking account of Eu^{3+} as an activator ion into the Dy^{3+} activated phosphor can improve the CRI value and results the tunable white light shifts from cool to warm region [230,231]. Therefore, in order to obtain spectral tunability via involving the energy transfer process between Dy^{3+} and Eu^{3+}, development of Dy^{3+}/Eu^{3+} bi-activated inorganic phosphors have been focused in the current research work.

The prime goal of the present work is to acquire a white light emitting single phase phosphor with effective features of colour tunability via varying the wavelength as well as the concentration of activator ions. In the current chapter, as-synthesized sodium calcium metasilicate ($Na_4Ca_4Si_6O_{18}$) phosphors activated with Dy^{3+} and Dy^{3+}/Eu^{3+} ions have been synthesized via well-

established solid state reaction route. Furthermore, the structural, morphological, optical, photoluminescence (PL) and decay studies have been investigated through distinct characterization techniques to explore the characteristic features of the as-synthesized phosphor. Most importantly, the PL and PL decay studies expand the excitation and emission spectra and also elaborate the energy transfer process between activator and sensitizer. The thermal stability and colorimetric properties of $Na_4Ca_4Si_6O_{18}$: Dy^{3+}/Eu^{3+} phosphor have also been investigated to reveal its practicability in the optoelectronic device applications.

6.2. Sample preparation and characterisation techniques

Microcrystalline sodium calcium metasilicate ($Na_4Ca_{4-x}Si_6O_{18}$) phosphor doped with Dy^{3+} and codoped with Eu^{3+} ions were synthesized using conventional solid-state reaction methodology as described in section 2.2.3. The detailed procedure is represented through the flow chart as shown in Fig. 2.1. Moreover, various characterization techniques have been carried out to investigate the crystalline, morphological and luminescent behaviour of the as synthesized phosphors, described in detail in section 2.3. (chapter 2). Each sample has indicated with a sample code and listed in Table 6.1.

6.3. Results and discussion

6.3.1. Phase identification, surface morphology and optical band gap studies

6.3.1.1. X-Ray Diffraction

Fig. 6.1. exhibits the XRD measurements of NCMS host (undoped), NCMS phosphors activated with Dy^{3+} and Dy^{3+}/Eu^{3+} ions. The diffraction peak profiles of all represented samples are well acceded with the standard XRD pattern (JCPDS card no. 75-1687) and do not reveal any extra peak. The peaks established in the diffraction patterns with non-appearance of impurity peaks endorses the pure phase of $Na_4Ca_4Si_6O_{18}$ host sample. Pure crystalline hexagonal $Na_4Ca_4Si_6O_{18}$ host is formed with $P3_2$ space group containing V=1249.42 $Å^3$ along with the value of lattice parameters as $a = b$= 10.46 Å; c =13.17 Å [154].

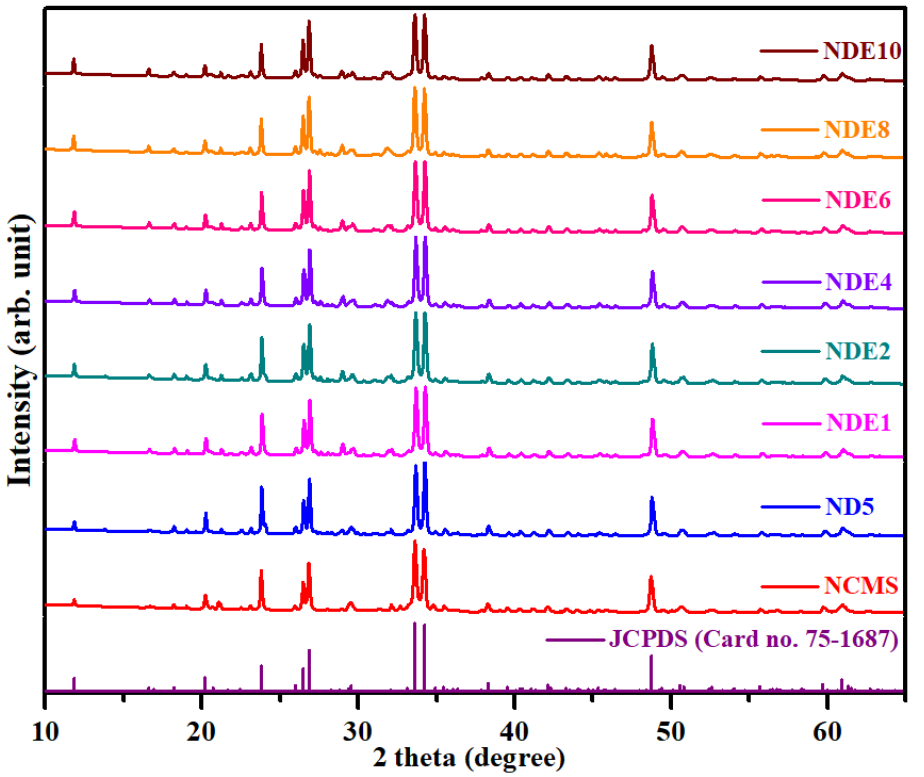

Fig. 6.1. *XRD patterns of undoped (NCMS), optimized Dy^{3+} doped (ND5) and Dy^{3+}/Eu^{3+} co-doped (NDE1, NDE2, NDE4, NDE6, NDE8 and NDE10) NCMS phosphors.*

XRD profiles of NCMS phosphors activated with Dy^{3+} and Dy^{3+}/Eu^{3+} ions have illustrated the virtuous agreement with standard XRD patterns, which implies that the crystal structure remains same even after adding dopants. Moreover, ionic radii of both sensitizer (Dy^{3+}: 0.912 Å) and activator (Eu^{3+}: 0.947 Å) ions are close to the ionic radii of Ca^{2+} (1.00 Å) ion. Therefore, it is expected that both dopants and co-dopants will occupy the place of Ca^{2+} site to exhibit superior results without altering the crystal structure. Average crystallite size (D_{hkl}) of all the prepared NCMS samples were evaluated via well-known Debye-Scherrer equation below [232]:

$$D_{hkl} = \frac{k\lambda}{\beta_{hkl} Cos\theta_{hkl}} \qquad (6.1)$$

where λ designates the incident x-ray wavelength, θ_{hkl} and β_{hkl} symbolizes the Bragg's diffraction angle and full width at half maxima (FWHM) of the represented diffraction peaks [233]. The average crystallite size and other parameters have been computed for all the samples using above formula and represented in the Table. 6.1.

Table 6.1. *Sample code, average crystallite size, Bragg's angle (θ_{hkl}), FWHM (β_{hkl}) of all undoped, Dy^{3+} doped and Dy^{3+}/Eu^{3+} co-doped NCMS phosphor.*

$Na_4Ca_4Si_6O_{18}$: xDy^{3+}/yEu^{3+} samples	Sample code	Average Crystallite size (nm)	θ_{hkl} (degrees)	β_{hkl} (degrees)
x=0.0 and y=0.0 mol%	NCMS (undoped)	51.89	33.63	0.254
			34.21	0.241
x=5.0 and y=0.0 mol%	ND5	51.20	33.63	0.209
			34.21	0.198
x=5.0 and y=1.0 mol%	NDE1	51.10	33.63	0.221
			34.21	0.206
x=5.0 and y=2.0 mol%	NDE2	50.28	33.63	0.221
			34.21	0.207
x=5.0 and y=4.0 mol%	NDE4	49.34	33.63	0.216
			34.21	0.202
x=5.0 and y=6.0 mol%	NDE6	48.19	33.63	0.221
			34.21	0.208
x=5.0 and y=8.0 mol%	NDE8	48.01	33.63	0.213
			34.21	0.203
x=5.0 and y=10.0 mol%	NDE10	47.37	33.63	0.220
			34.21	0.209

The size of undoped and ND5 are 51.89 and 51.20 nm, respectively, and the average crystallite size varies from NDE1 to NDE10 in a range of 51.10 to 47.37 nm after insertion of Eu^{3+}. It can be ascertained that the crystalline size decreases as the concentration of co-dopant ions increases which implies that the contraction in the lattice may takes place via occupying larger ionic radii site (Ca^{2+}) by smaller ionic radii (Dy^{3+} & Eu^{3+}) ions [234,235].

6.3.1.2. Morphological analysis with FE-SEM

Surface morphology and particle size of Dy^{3+}/Eu^{3+} co-doped NCMS phosphor (Dy^{3+}: 5.0 mol% and Eu^{3+}: 1.0 mol%) has been investigated with the help of FE-SEM micrographs, as exhibited in Fig. 2 (a & b). The FE-SEM images of as-prepared phosphors are observed to be

agglomerated morphology with irregular shapes which ascertains that the samples are prepared at high temperature [236]. Fig. 6.2 (a & b) represents the micrographs of Dy^{3+}/Eu^{3+} co-doped NCMS phosphor at 5 and 10 µm resolution. Fig. 6.2 (c) represents energy dispersive x-ray analysis (EDAX) of NCMS: Dy^{3+}/Eu^{3+} to disclose the elemental presence in the sample.

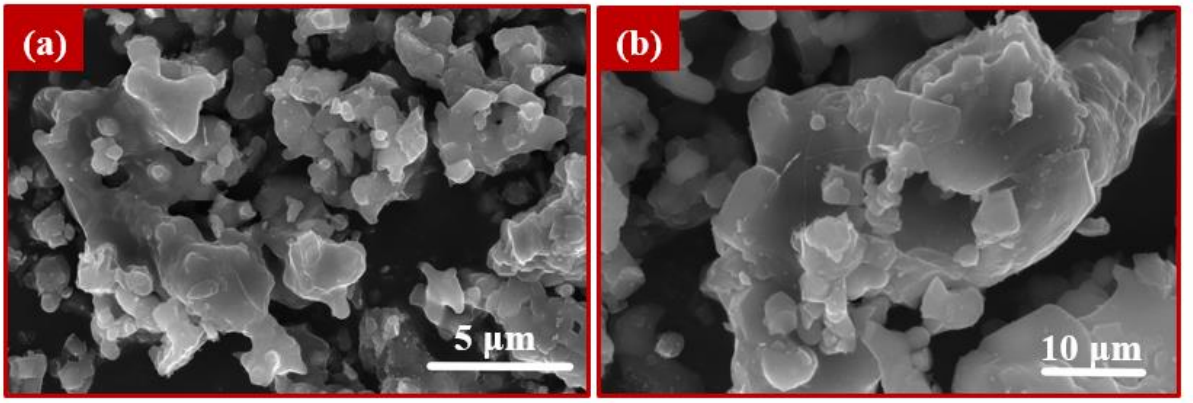

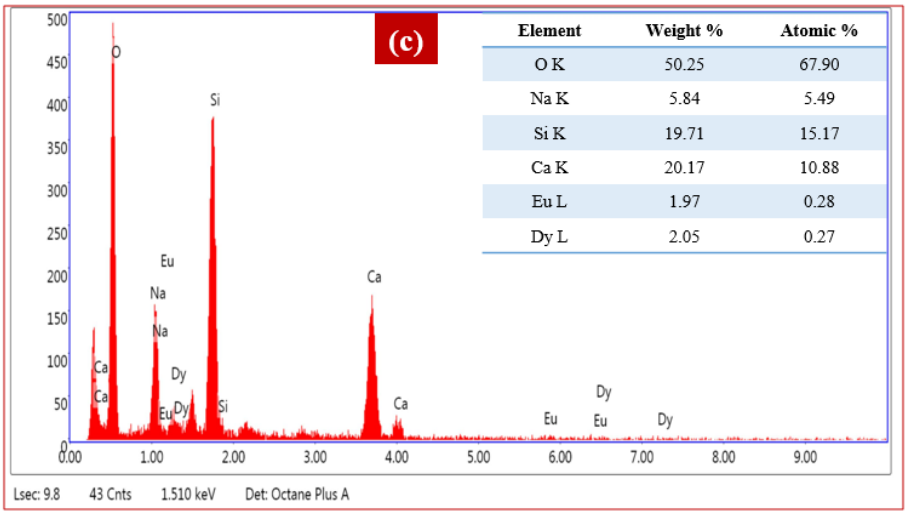

Element	Weight %	Atomic %
O K	50.25	67.90
Na K	5.84	5.49
Si K	19.71	15.17
Ca K	20.17	10.88
Eu L	1.97	0.28
Dy L	2.05	0.27

Fig. 6.2 ***(a-b)*** *FE-SEM micrographs of NCMS: Dy^{3+}/Eu^{3+} phosphor at different resolutions* ***(c)*** *Energy dispersive x-ray analysis (EDAX).*

6.3.1.3. Optical band gap studies

Fig. 6.3. depicts the band gap of Dy^{3+}/Eu^{3+} co-doped $Na_4Ca_4Si_6O_{18}$ phosphors whereas inset indicates the diffuse reflectance spectra with the intense reflectance band in the range of 200-300 nm wavelength [237]. Samples coded with NDE1 and NDE10 have shown the weak absorption bands positioned at 348 nm and 393 nm that are obtained due to f-f transition of Dy^{3+}

and Eu^{3+} ions. Moreover, energy band gap values for NDE1 and NDE10 have been evaluated using Kubelka-Munk (K-M) relation, which can be accompanied with Tauc equation and given as [238].

$$(F(R)h\upsilon) = B(h\upsilon - E_g)^n \quad (6.2)$$

where E_g denotes the band gap energy, F(R) as Kubelka-Munk function, *h* and B are the plancks constant and proportionality constant, respectively. Moreover, ν is the photon energy and *n* denote to specific values which ascertain the types of electronic transition.

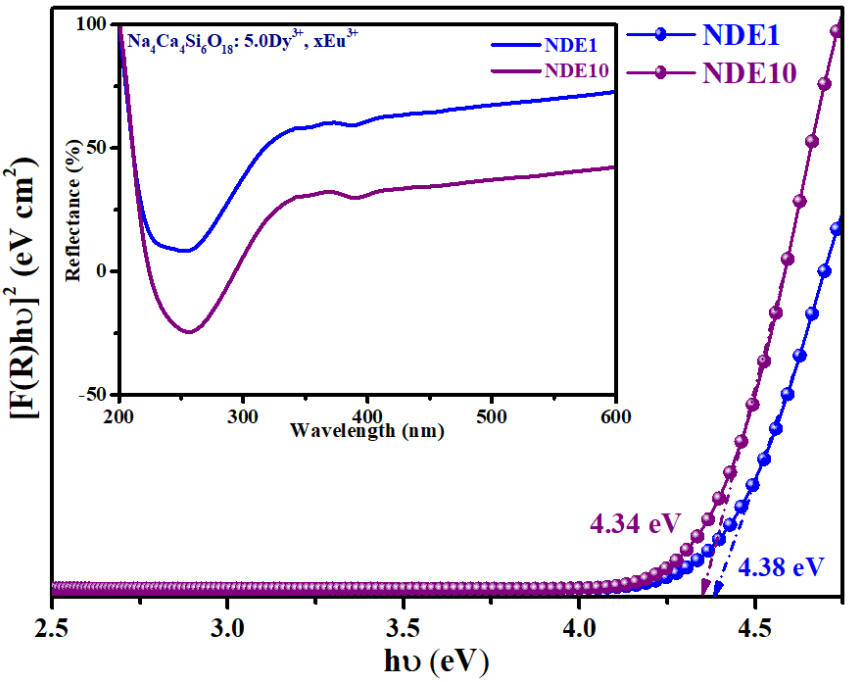

Fig. 6.3. *Band gap energy determination using K-M function for 5.0 Dy^{3+}/xEu^{3+} (x=1.0 and 10.0 mol%) co-doped $Na_4Ca_4Si_6O_{18}$ phosphors. Inset shows the diffuse reflectance spectra for the same samples.*

For instance, direct and indirect allowed transitions resemble to the values (*n*) of 1/2 and 2, while direct and indirect forbidden transitions correspond to 3/2 and 3, respectively. Fig. 6.3. represents the energy band gap values for NDE1 and NDE10 which are evaluated by the plot between $[F(R)h\upsilon]^2$ versus hυ, indicating the direct allowed transition band and are found to be 4.34 and 4.38 eV, respectively [239].

6.3.2. FT-IR spectroscopy

Fig. 6.4. exhibits FT-IR spectroscopy of NCMS: 5.0 Dy^{3+}/1.0 Eu^{3+} (NDE1) and NCMS: 5.0 Dy^{3+}/10.0 Eu^{3+} (NDE10) phosphors have been recorded in order to examine the functional

groups. From FT-IR spectra of NDE1 and NDE10, it can be observed that both the samples show analogous absorption peaks which indicate similar chemical compositions [240]. The peaks represented in FT-IR spectra have been depicted in the range of 500-1275 cm^{-1} and positioned at 529, 624 and 696 cm^{-1} owing to bending vibration modes of Si-O bond linkages [241].

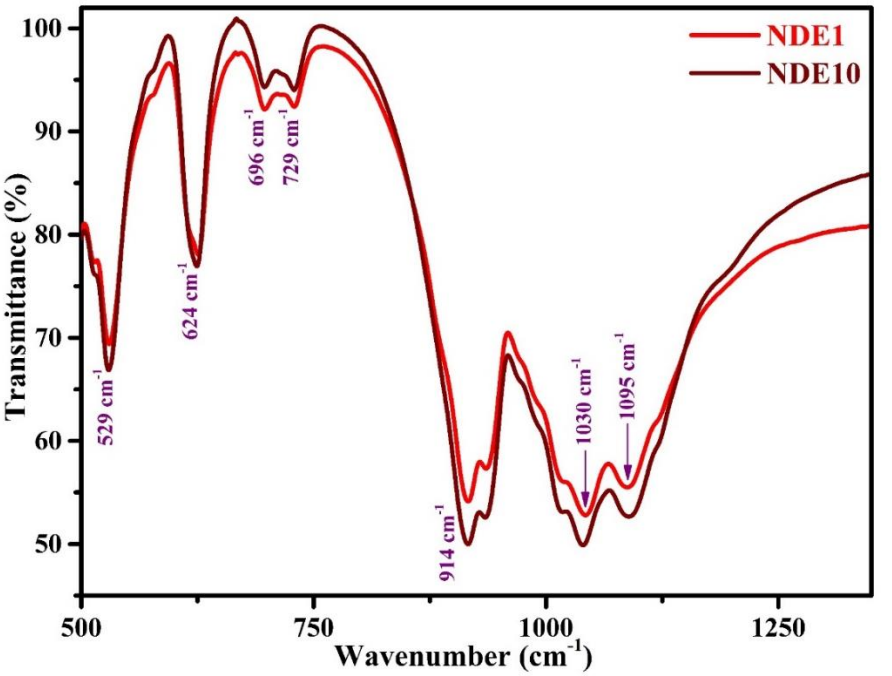

Fig. 6.4. *Fourier transform infrared spectroscopy of NCMS: 5.0 Dy^{3+}/1.0 Eu^{3+} (NDE1) and NCMS: 5.0 Dy^{3+}/10.0 Eu^{3+} (NDE10) phosphors.*

However, asymmetric and symmetric stretching in Si-O-Si resembles to 729 and 1030 cm^{-1}, respectively, while bands observed at 914 cm^{-1} is due to Si-O symmetric stretching mode [242]. The bands centred at 1095 cm^{-1} are exhibited due to the presence of vibrational mode of metal (Ca, Na) bonds with oxygen atoms (O) [243]. In both FT-IR spectra, there is no additional peaks which supporting the conclusion that addition of Dy^{3+} and Eu^{3+} dopant ions in NCMS phosphor had no discernible impact [153].

6.3.3. Luminescent studies of NCMS phosphors activated with Dy^{3+} and Dy^{3+}/Eu^{3+} ions

PL spectral measurements of NCMS phosphors activated with Dy^{3+} and Dy^{3+}/Eu^{3+} ions have been carried out to analyse photoluminescence properties. Fig. 6.5 (a) exhibit the photoluminescence excitation (PLE) spectrum of optimized 5.0 mol% of Dy^{3+} activated

$Na_4Ca_4Si_6O_{18}$ phosphor under emission wavelength 576 nm. In Fig. 6.5 (a), the excitation peaks positioned at 321, 348, 360, 382, 421, 450 and 476 nm, which begin from the lower energy state $^6H_{15/2}$ to a variety of excited states, including $^6P_{3/2}$, $^6P_{7/2}$, $^6P_{5/2}$, $^4F_{7/2}$, $^4G_{11/2}$, $^4I_{15/2}$ and $^4F_{9/2}$, respectively [244]. The peak at 348 nm has the highest intensity among all excitation peaks and thus indicates that the greatest possible amount of absorption energy is at this particular wavelength for Dy^{3+}. Hence, the photoluminescence (PL) profiles of Dy^{3+} (x=1.0, 3.0, 4.0, 5.0 and 6.0 mol%) doped $Na_4Ca_4Si_6O_{18}$ phosphors obtained at the strongest excitation wavelength 348 nm as shown in Fig. 6.5(b).

The bands in the PL spectra credited to pure Dy^{3+} transitions, which are attained at 488, 576 and 675 nm resembles to $^4F_{9/2}\rightarrow{}^6H_J$ (where J are 15/2, 13/2 and 11/2, respectively) as depicted in Fig. 6.5 (b) [245]. The intense peak is located at 576 nm ($^4F_{9/2}\rightarrow{}^6H_{13/2}$) attributed to forced electric dipole (ED) transition in which the dopants ions are situated at a location lacking of an inversion centre whereas second dominant peak is at 488 nm ($^4F_{9/2}\rightarrow{}^6H_{15/2}$) is owing to magnetic dipole (MD) transition [246]. Ca^{2+} site having low symmetry can easily access by Dy^{3+} ions with ease as the Dy^{3+} ionic radii is smaller than the Ca^{2+} ions [247].

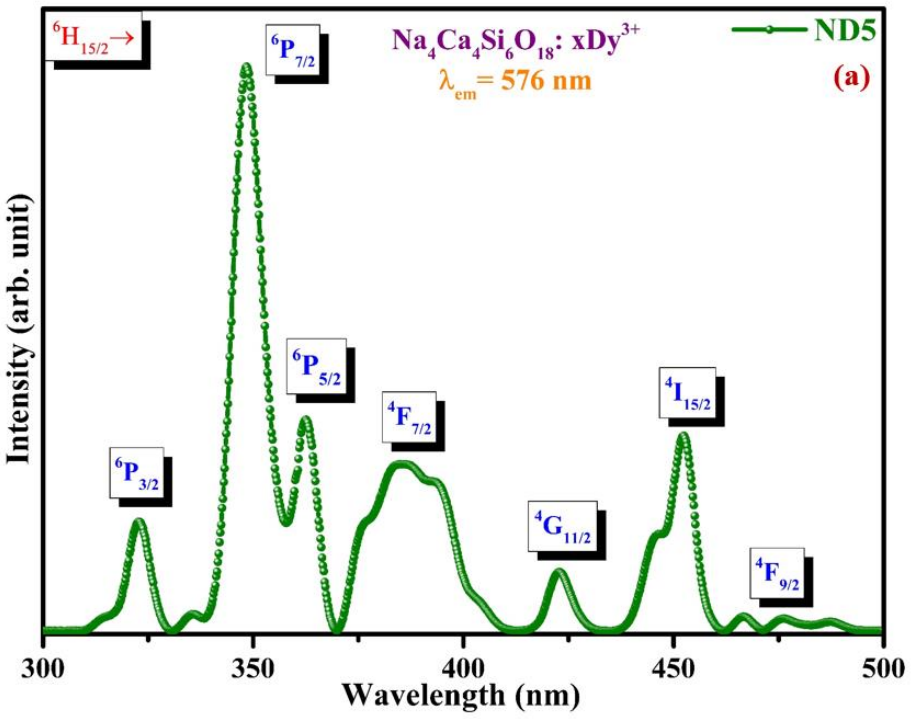

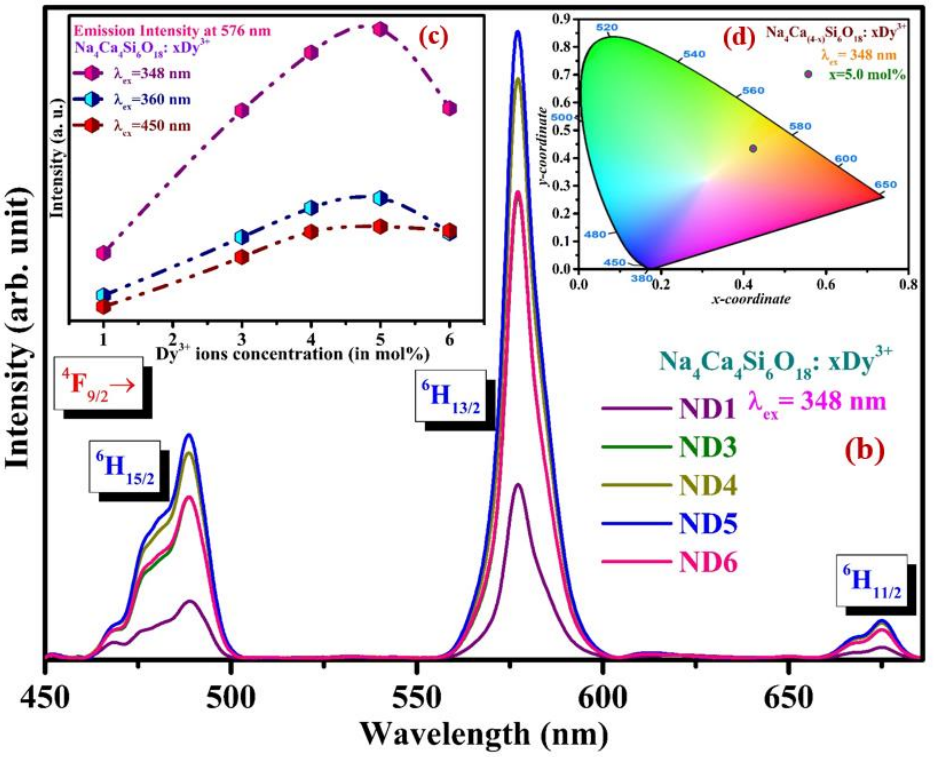

Fig. 6.5. ***(a & b)*** *PLE spectrum of Dy^{3+} (x=5.0 mol%) and PL emission spectra of ND1 to ND6 phosphors at λ_{em}= 576 nm and λ_{ex}= 348 nm* ***(c)*** *Variation of emission intensity at 576 nm with the concentration of Dy^{3+} ions at different excitation wavelengths* ***(d)*** *CIE chromaticity diagram of ND5 under 348 nm excitation wavelength.*

Furthermore, stark splitting of emission peaks have been observed for the transitions at 488 and 675 nm up to utmost of J+1/2 as a result of crystal field effect, where J is total angular momentum [248]. Fig. 6.5 (c) depicts the effect of concentration of Dy^{3+} ions on $^4F_{9/2}\rightarrow{}^6H_{13/2}$ intensity under different significant excitation wavelengths (348, 360 and 450 nm). The rise in concentration enhances the luminescence intensity until 5.0 mol% and further with concentration, the intensity declines due to widely known concentration quenching effect [249]. Owing to reduce in distance between the dopant (Dy^{3+}) ions at considerably larger dopant ion concentrations (beyond 5.0 mol%), it is more likely that the energy of absorbed ions is releasing non-radiatively despite of transmitted radiatively. Thus, the highly optimized Dy^{3+} concentration in NCMS host is observed to be 5.0 mol% (ND5) which falls in the yellow region under n-UV (λ_{ex}=348 nm) excitation as denoted in CIE chromaticity diagram (Fig. 6.5 (d)). The as-prepared Dy^{3+} ion induced

phosphor emit yellow colour along with feeble red emission band. Therefore, in order to achieve intense white light along with better CRI value and color tunability behaviour, Eu^{3+} was included as a co-dopant ion to the optimized yellow emitting (5.0 mol%) Dy^{3+} activated NCMS phosphor to accomplish the prerequisite red emission [250].

Thus, the PLE and PL spectra of 7.0 mol% of Eu^{3+} (optimized) activated NCMS phosphor have been measured as shown in Fig. 6.6 (a & b). Numerous excitation peaks from 300-500 nm range have been recognized at different excitation wavelengths attributed to the different transitions as 321 ($^7F_0 \rightarrow {}^5H_7$), 364 ($^7F_0 \rightarrow {}^5D_4$), 382 ($^7F_0 \rightarrow {}^5L_7$), 393 ($^7F_0 \rightarrow {}^5L_6$), 416 ($^7F_0 \rightarrow {}^5D_3$) and 464 nm ($^7F_0 \rightarrow {}^5D_2$). Two strongly intense peaks are captured in n-UV and blue region positioned at 393 and 464 nm, which implies that the as-synthesized NCMS: Eu^{3+} can be adequately excited with n-UV/blue light.

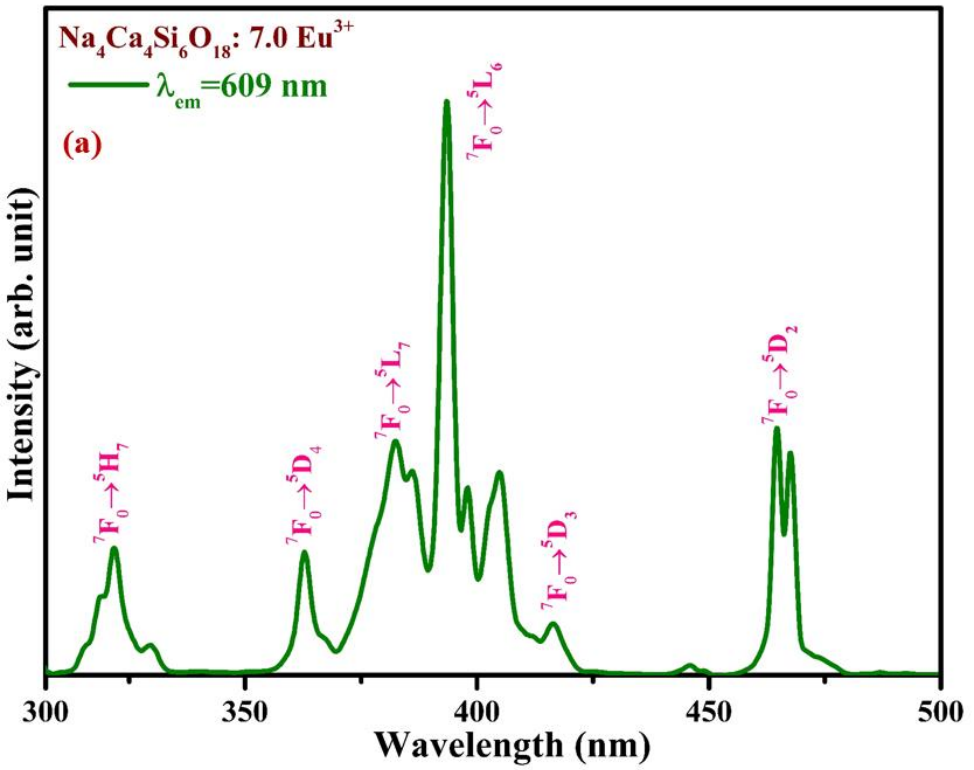

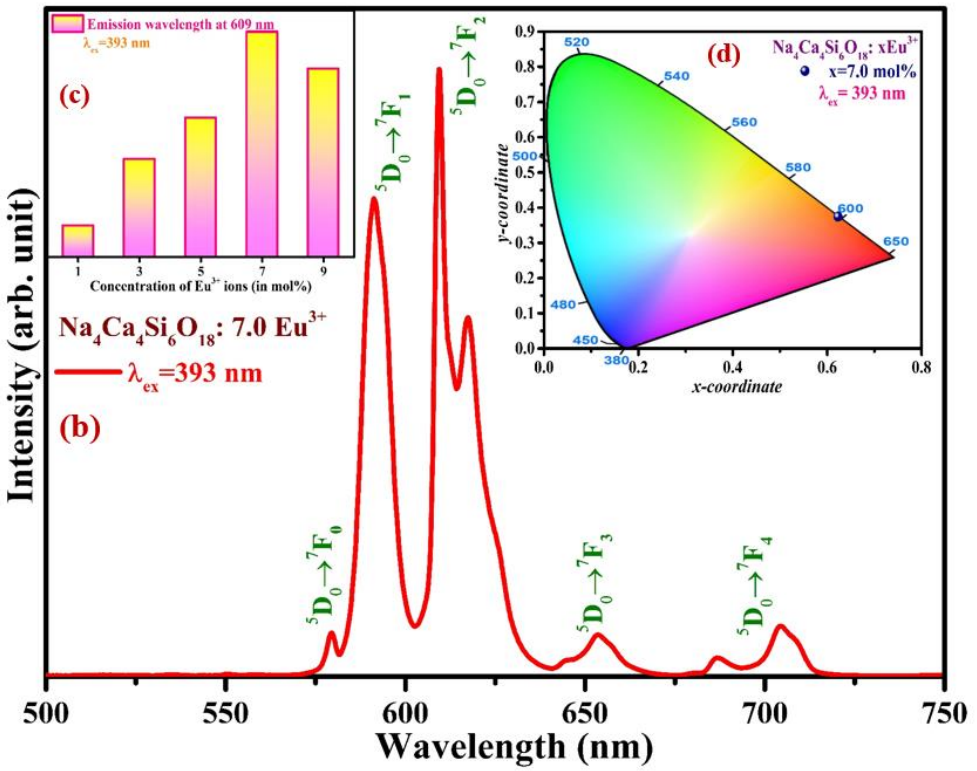

Fig. 6.6. ***(a & b)*** *PLE and PL spectrum of 7.0 mol% of Eu^{3+} activated NCMS phosphor;* ***(c)*** *Intensity of $^5D_0 \rightarrow {}^7F_2$ versus concentration of Eu^{3+} ions (in mol%);* ***(d)*** *CIE chromaticity diagram of the optimized Eu^{3+} activated NCMS phosphor under 393 nm excitation wavelength.*

Furthermore, the dominated excitation peak observed at 393 nm is chosen to record the PL spectrum of Eu^{3+} activated NCMS phosphor in a range of 500-750 nm, as represented in Fig. 6.6 (b). The emission peaks attained at 579, 591, 609, 653 and 704 nm reveals the transitions of Eu^{3+} ions under 393 nm excitation from the lower energy state $^5D_0$ to distinct excited states as $^7F_0$, $^7F_1$, $^7F_2$, $^7F_3$ and $^7F_4$, respectively [251]. In the PL spectrum, two peaks positioned at 591 (orange: O) and 609 nm (red: R) wavelengths are quite strong among five peaks. Highest peak at 609 nm attributed to forced electric dipole (ED) transition ($^5D_0 \rightarrow {}^7F_2$) complies the selection rule $\Delta J \leq 2$ and is inherently hypersensitive and strongly impacted by the crystal field environment. However, the peak positioned at 591 nm ascribed to magnetic dipole (MD) transition ($^5D_0 \rightarrow {}^7F_1$), obeys the selection rule $\Delta J = 1$ [252]. The red to orange (R/O) emission intensity ratio or asymmetric ratio quantifies the site symmetry of the dopant ions. Particularly for Eu^{3+} ions doped NCMS phosphor, the red to orange emission intensity ratio is found to be 1.42 for optimum concentration (7.0 mol%)

of Eu^{3+} ions, indicates that Eu^{3+} ions are placed at the low symmetry sites as the R/O ratio is greater than unity [253]. Fig. 6.6 (c) illustrates the optimum activator (Eu^{3+}) ions concentration in the host matrix with the highest emission intensity, after which the intensity begins to suppress through the effect of concentration quenching mechanism via expressing non-radiative energy transfer among the Eu^{3+} ions. The emission colour of the optimized concentration of Eu^{3+} doped NCMS phosphor falls under the red region with the CIE coordinates (0.631, 0.367) as shown in Fig. 6.6 (d).

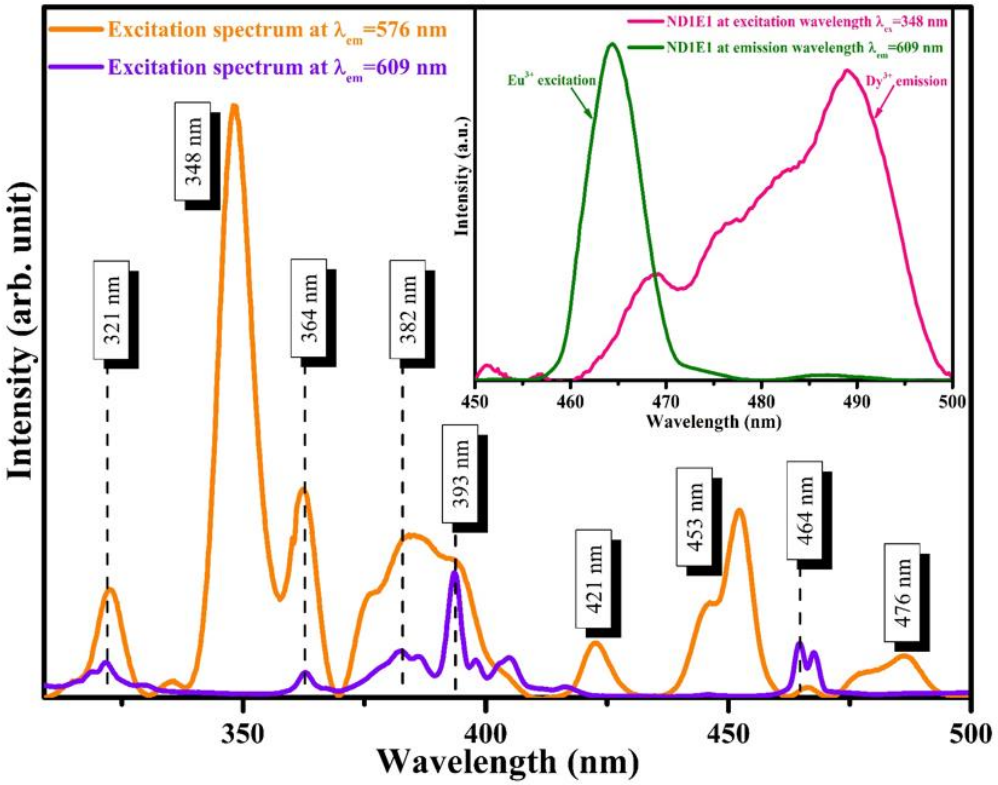

Fig. 6.7. *Photoluminescence excitation spectra for ND1E1 phosphor at emission wavelength 576 and 609 nm (Inset: Spectral overlap for emission of sensitizer (Dy^{3+}) and absorption of activator (Eu^{3+}).*

PLE spectra of ND1E1 (Dy^{3+}: 1.0 mol% doped and Eu^{3+}: 1.0 mol% co-doped NCMS phosphors) were measured by affixing at the highest emission wavelength of each dopant (Dy^{3+}: 576 nm) and (Eu^{3+}: 609 nm), as represented in Fig. 6.7. The excitation spectrum of ND1E1 phosphor exhibit characteristic absorption peaks of Dy^{3+} and Eu^{3+} in n-UV and blue region in a range of 300-500 nm. Furthermore, one of the crucial prerequisites for energy transfer from Dy^{3+} to Eu^{3+} is that the sensitizer emission (Donor: Dy^{3+}) overlap with the activator excitation

(Acceptor: Eu^{3+}), which was satisfied in the current work. To demonstrate the energy transfer mechanism along with colour tunability behaviour in bi-activated (Dy^{3+}/Eu^{3+}) NCMS phosphor, the sample has been excited at selected wavelengths at 348, 364, 393 and 464 nm. Based on the above results, ND1E1 phosphor may efficiently excite using n-UV and blue LEDs. Fig. 6.8 depicts the excitation spectra of co-activated xDy^{3+}/yEu^{3+} (where, x=5.0 mol% and y=1.0, 2.0, 4.0, 6.0, 8.0 and 10.0 mol%) $Na_4Ca_4Si_6O_{18}$ phosphors at 576 nm emission wavelength. The peaks obtained in the spectra are mixture of Dy^{3+} and Eu^{3+} ions positioned at 321, 348, 364, 382, 393, 421, 453, 464 and 476 nm correspond to the transitions from ground state of Dy^{3+} ($^6H_{15/2}$) and Eu^{3+} ($^7F_0$) to various excited states $^6P_{3/2}$ (Dy^{3+}), $^6P_{7/2}$ (Dy^{3+}), $^6P_{5/2}$ (Dy^{3+}), $^4F_{7/2}$ (Dy^{3+}), $^5L_6$ (Eu^{3+}), $^4G_{11/2}$ (Dy^{3+}), $^4I_{15/2}$ (Dy^{3+}), $^5D_2$ (Eu^{3+}) and $^4F_{9/2}$ (Dy^{3+}), respectively.

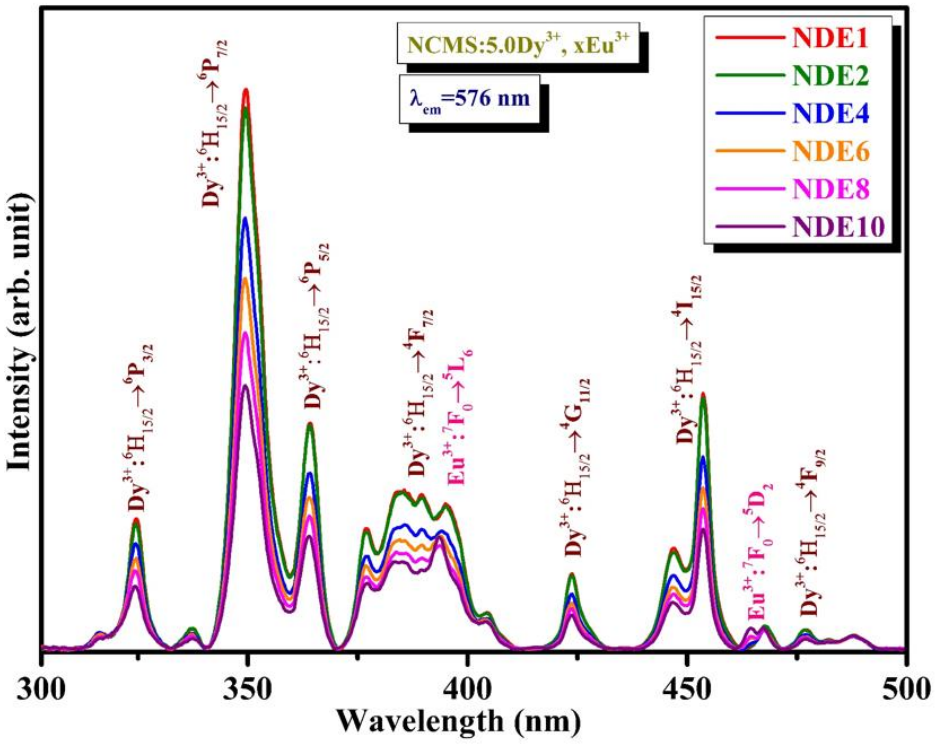

Fig. 6.8. *Photoluminescence excitation spectra of co-activated 5.0 mol% of Dy^{3+} and x mol% of Eu^{3+} (x=1.0, 2.0, 4.0, 6.0, 8.0 and 10.0 mol%) $Na_4Ca_4Si_6O_{18}$ phosphors under 576 nm emission wavelength.*

Fig. 6.9 (a-d) epitomizes PL spectra of Dy^{3+}/Eu^{3+} co-activated NCMS phosphors have been demonstrated under various excitation (348, 364, 393 and 464 nm) wavelengths. The emission peaks perceived in visible (blue: B, yellow: Y, orange: O and red: R) regions represented by energy

transitions between ground and excited levels of Dy^{3+} ($^4F_{9/2} \rightarrow {}^6H_J$, J= 15/2, 13/2 and 11/2) and Eu^{3+} ($^5D_0 \rightarrow {}^7F_J$, J= 1, 2, 3 and 4) ions as explained in the preceding graphs. Moreover, it is evident from Fig. 6.9 (a-d) that the emission peaks of Dy^{3+} & Eu^{3+} and their intensities can be strongly impacted by the excitation wavelengths and concentration of activator ions. According to Fig. 6.9 (a), the emission peaks ascribed to Dy^{3+} ions under 348 nm excitation wavelength exhibit decrement in emission intensities, while the increment in emission intensity observed for the peaks associated to Eu^{3+} ions. Here, the enhancement of absorption probability of Eu^{3+} ions and energy transfer from Dy^{3+} (sensitizer) to Eu^{3+} (activator) ions are responsible for the rise in Eu^{3+} emission intensity with the concentration [254].

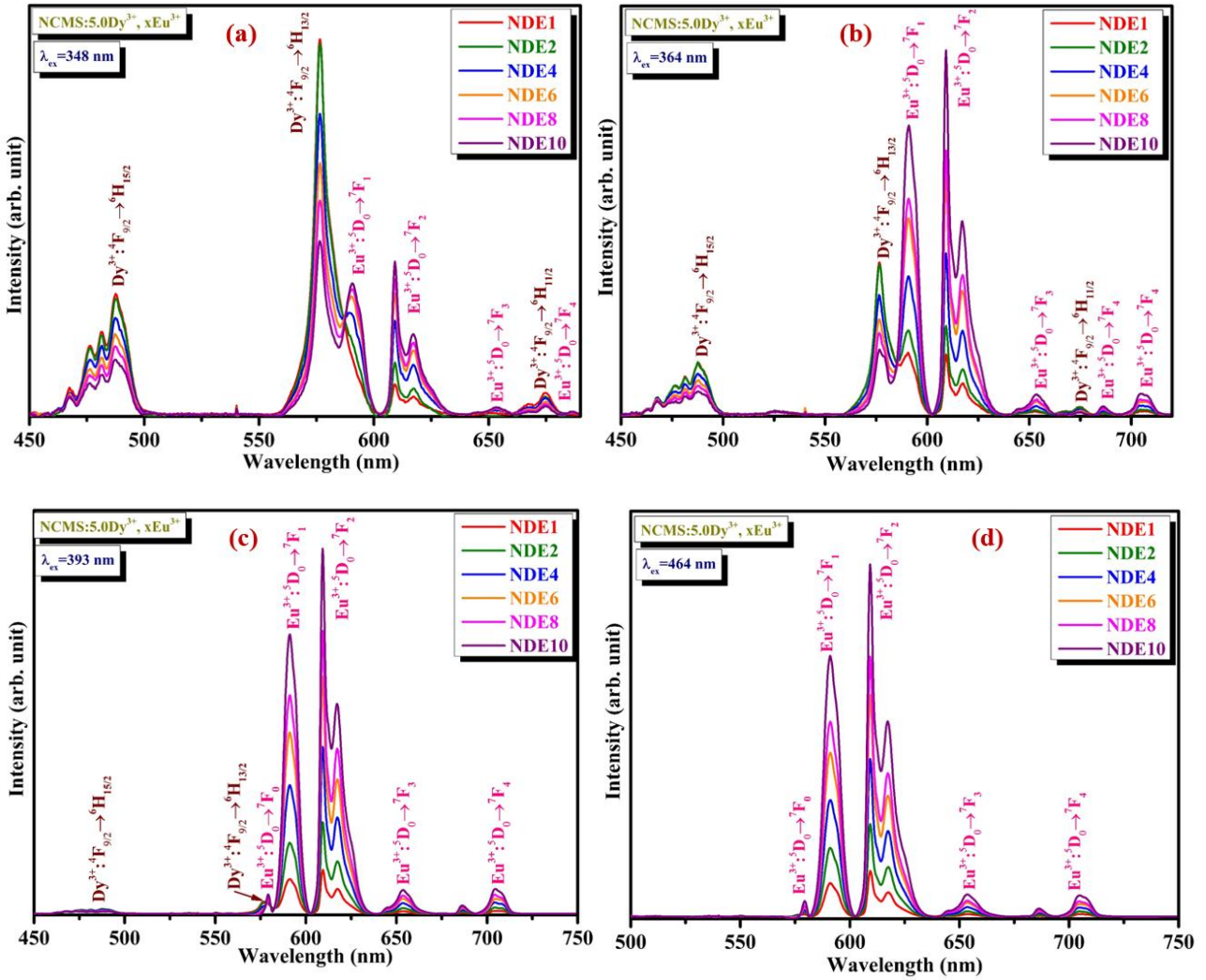

Fig. 6.9. ***(a-d)*** *Emission spectra of NDE1, NDE2, NDE4, NDE6, NDE8 and NDE10 phosphors under distinct excitation wavelengths* ***(a)*** λ_{ex}*= 348 nm* ***(b)*** λ_{ex}*= 364 nm* ***(c)*** λ_{ex}*= 393 nm* ***(d)*** λ_{ex}*= 464 nm.*

Energy transfer occurs from Dy^{3+} to Eu^{3+} is more prominent and conspicuous under pure Dy^{3+} excitation (348 nm) wavelengths. Under 364 nm excitation, the emission peaks intensity related to Dy^{3+} ions are dominated initially and later by the peaks of Eu^{3+} ions as the concentration of Eu^{3+} ion increases on account of energy transfer from sensitizer to activator ions [255]. Emission peaks appeared due to Eu^{3+} ions were quite intense under 393 nm excitation along with feeble peaks ascribed to Dy^{3+} ions which is due to the comparable excitation wavelengths of both the dopants. However, under the 464 nm excitation wavelength, the dominance of emission peaks corresponding to Eu^{3+} has been observed as the absorption intensity of Eu^{3+} ion is leading in comparison to Dy^{3+}, which substantiate that there is no reverse transfer of energy (i.e. Eu^{3+} to Dy^{3+}). Fig. 6.9 (a-d) portrays the increase in Eu^{3+} emission intensity until 10.0 mol% concentration of Eu^{3+} ions under all the excitation wavelengths and no quenching of emission intensity takes place. Moreover, color tunability could be achieved owing to energy transfer between dopant and co-dopant ions by tuning the excitation wavelength and varying the Eu^{3+} ions concentration which is clearly described in the forthcoming section.

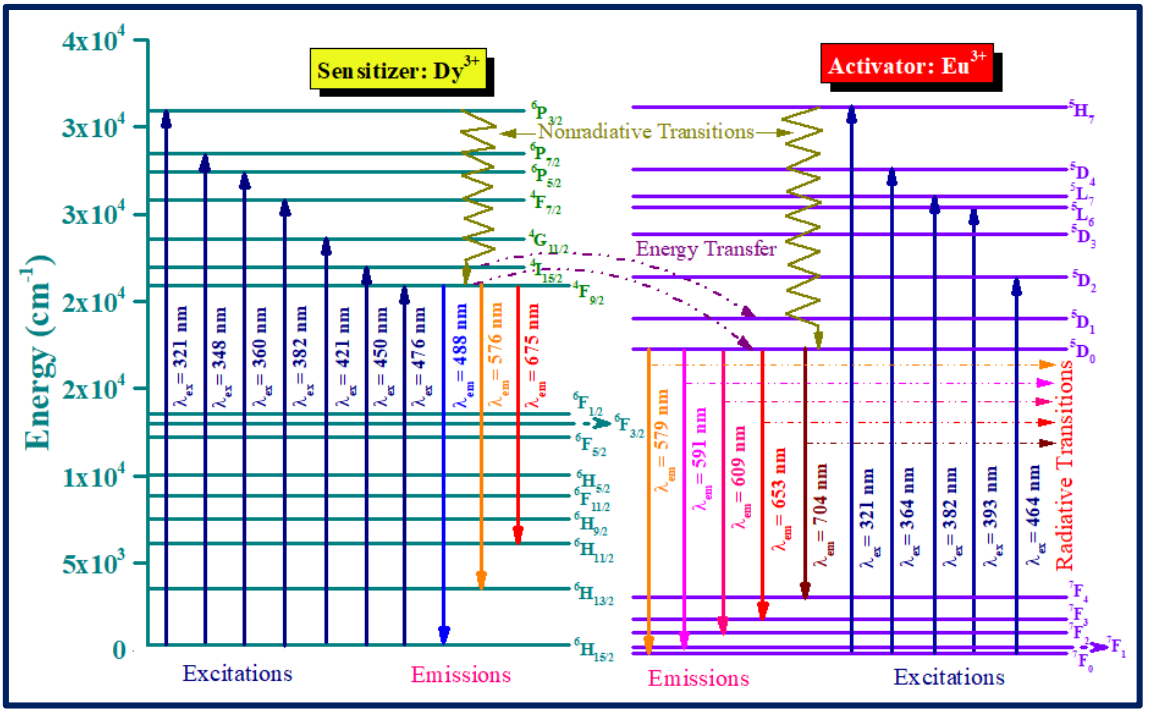

Fig. 6.10. *Partial energy level diagram illustrating energy transfer in Dy^{3+} activated and Dy^{3+}/Eu^{3+} co-activated $Na_4Ca_4Si_6O_{18}$ phosphors.*

Fig. 6.10. represents the schematic for partial energy level diagram with various energy levels, radiative and non-radiative energy transitions. The process evinces that when the light incident onto the Dy^{3+}/Eu^{3+} bi-activated NCMS phosphors, then the incident energy may be absorbed by Dy^{3+} ions at ground state ($^6H_{15/2}$) and excited to the distinct higher (i.e. $^6P_{3/2}$, $^6P_{7/2}$, $^6P_{5/2}$, $^4F_{7/2}$, $^4G_{11/2}$, $^4I_{15/2}$ and $^4F_{9/2}$) energy levels. Furthermore, the Dy^{3+} ions at excited state either relax non-radiatively (shown with zig zag arrow) or may transfer their energy to the nearest levels ($^5D_1$ & $^5D_0$) of activator ions (shown with horizontal arrows) along with their radiative emission transitions in the visible region [256]. Thus, the transfer of energy in co-doped NCMS: Dy^{3+}/Eu^{3+} phosphors may occur through higher excited states of Dy^{3+} ions to Eu^{3+} ions (sensitizer→activator) via phonon assisted non-radiative and photon accelerated radiative transition through activator ions to provide integrated emission in the visible region [257].

Moreover, non-radiative energy transfer from donor (Dy^{3+}) to an acceptor (Eu^{3+}) ions may be generated by the variety of mechanisms, such as exchange interaction or multipole-multipole interactions [258,259]. The exchange interaction ensues if the critical distance ($R_{Dy\text{-}Eu}$) value should be less than or equal to 5 Å. Using below mentioned formula in Eq. (3), the critical distance can be estimated [260]:

$$R_{Dy-Eu} = 2\left(\frac{3V}{4\pi x_c N}\right)^{\frac{1}{3}} \quad (6.3)$$

where V denotes for volume and N for number of cations fixed in the unit cell, respectively. However, for the current matrix V=1249.42 $Å^3$ (done) and N=3. To evaluate the critical concentration (x_c), the addition of fixed optimum Dy^{3+} (5.0 mol%) and Eu^{3+} (10.0 mol%) concentrations upon which the Dy^{3+} ion emission intensity persevered nearly half of its initial value, hence the value of critical concentration is taken as 0.15 mol [261]. Thus, using the above mentioned parameters in the given formula, the estimated $R_{Dy\text{-}Eu}$ value comes out to be 17.44 Å and affirms the multipolar-multipolar interaction. Thus, to recognize the type of multipolar interaction, Reisfield's and Dexter theory can be employed [262]. This expresses the relation of

quantum efficiencies (η_{s0} and η_s), where η_{s0} is the quantum efficiency of sensitizer (Dy^{3+}) emission without activator (Eu^{3+}) and η_s is quantum efficiency with activator ions, on the summation of sensitizer and activator concentrations ($C_{Dy^{3+}+Eu^{3+}}$) [263]:

$$\frac{\eta_{s0}}{\eta_s} \propto C^{\frac{n}{3}}_{Dy^{3+}+Eu^{3+}} \tag{6.4}$$

where n designates the type of multipolar interactions for which dipole-dipole (d-d) interaction with the value of 6, dipole-quadrupole (d-q) with 8 and quadrupole-quadrupole (q-q) interaction with 10. The value of quantum efficiency ratio $\left(\frac{\eta_{s0}}{\eta_s}\right)$ for Dy^{3+} ions emission without and with Eu^{3+} ions can be associated to the ratio of emission intensity $\left(\frac{I_{s0}}{I_s}\right)$ [264]:

$$\frac{I_{s0}}{I_s} \propto C^{\frac{n}{3}}_{Dy^{3+}+Eu^{3+}} \tag{6.5}$$

Here, I_{s0} and I_s represents the emission intensity of Dy^{3+} ions without and with Eu^{3+} ions, respectively, under 348 nm excitation wavelength. The plot shown in Fig. 6.11, depicts the $\frac{I_{s0}}{I_s}$ vs $C^{n/3}_{Dy^{3+}+Eu^{3+}}$ explicates the multipolar interaction takes place in the reported phosphor corresponds to the value of n to 6, 8 and 10.

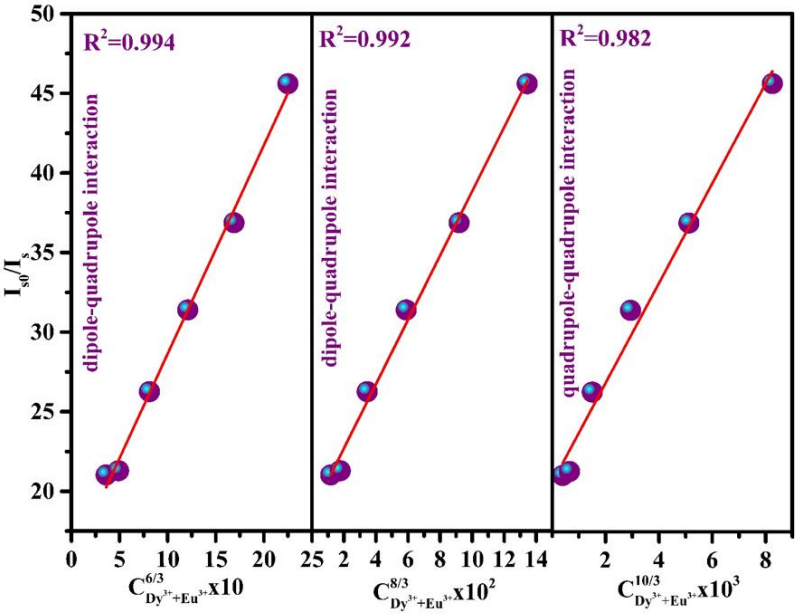

Fig. 6.11. *I_{s0}/I_s versus $C^{n/3}_{Dy^{3+}+Eu^{3+}}$ plot to reveal the type of interaction among dopant and co-dopant ions.*

Among all the values of *n*, plot unveils the best linear fitted at 6, indicating the contribution of d-d interaction to elaborate the energy transfer mechanism from Dy^{3+} to Eu^{3+} ions. Moreover, the energy transfer efficiency (η_{ET}) of corresponding donor (Dy^{3+}) to acceptor (Eu^{3+}) can be evaluated using below equation [265,266]:

$$\eta_{ET} = 1 - \frac{I_s}{I_{s0}} \tag{6.6}$$

The evaluated energy transfer efficiencies for NDE1, NDE2, NDE4, NDE6, NDE8 and NDE10 are listed in Table 6.2. The utmost efficiency is found to be 97.80% for NDE10 phosphor.

Table 6.2. *Energy transfer efficiency, energy transfer probability rate and average decay time of Dy^{3+} activated and Dy^{3+}/Eu^{3+} co-activated NCMS phosphors.*

Sample codes	ND5	NDE1	NDE2	NDE4	NDE6	NDE8	NDE10
Energy transfer efficiency (η_{ET} in %)	-	95.24	95.30	96.19	96.81	97.28	97.80
Energy transfer Probability (P)	-	-	0.31	0.36	0.41	0.62	0.73
Average decay time (μs)	2.22	-	1.30	1.22	1.15	0.93	0.84

6.3.4. CIE colorimetric studies

To elucidate the competence of white light emission and versatile color tunable behaviour of NCMS: Dy^{3+}/Eu^{3+} phosphors, color coordinates have been computed using the emission data and annotated them in CIE 1931 chromaticity diagram as expressed in Fig. 6.12 (a-f) [267]. The CIE color coordinates of the ND5 under 348 nm excitation wavelength and NDE1 under 348, 364, 393, 453 and 464 nm are marked in Fig. 6.12 (a). The color coordinates of NDE1 phosphor under the excitation wavelengths of 348 and 364 nm are found to be in a pure white domain while under 453 nm excitation wavelength, the emission color reflects in the yellow region and shows red emission under 393 and 464 nm. Further, the color coordinates from NDE1 to NDE10 phosphor

indicates the tunability in color from white domain to red region with rise in the Eu^{3+} ion concentration under the excitation of 348 and 364 nm (Fig. 6.12 (b & c)). The obtained color tunability may be the result of energy transfer from Dy^{3+} to Eu^{3+} ions. Furthermore, the chromaticity coordinates instantly shifted to the more prominent red color under 393 nm excitation wavelength represented in Fig. 6.12 (d). Under 453 nm excitation, the co-doped phosphor manifests shifting of color from yellow to red region and exhibit pure red emission under 464 nm excitation wavelength, which confirms that there is no reverse transfer of energy from Eu^{3+} to Dy^{3+} in the prepared phosphor, shown in Fig. 6.12 (e & f).

Table 6.3. *CIE chromaticity coordinates and CCT values of singly doped NCMS: Dy^{3+} and doubly doped NCMS: Dy^{3+}/Eu^{3+} phosphors under different excitation wavelengths.*

Sample codes	Excitation waveleng (nm)	CIE chromaticity coordinates (x, y)	CCT values (K)
ND5	348	(0.42, 0.44)	3536.11
NDE1	348	(0.43, 0.43)	3315.58
	464	(0.57, 0.37)	1732.00
NDE2	348	(0.44, 0.42)	3087.09
	464	(0.60, 0.37)	1852.72
NDE4	348	(0.47, 0.41)	2648.14
	464	(0.62, 0.37)	1959.64
NDE6	348	(0.49, 0.41)	2356.13
	464	(0.62, 0.37)	2011.51
NDE8	348	(0.50, 0.40)	2179.36
	464	(0.63, 0.37)	2028.12
NDE10	348	(0.52, 0.40)	1984.82
	464	(0.63, 0.36)	2054.13

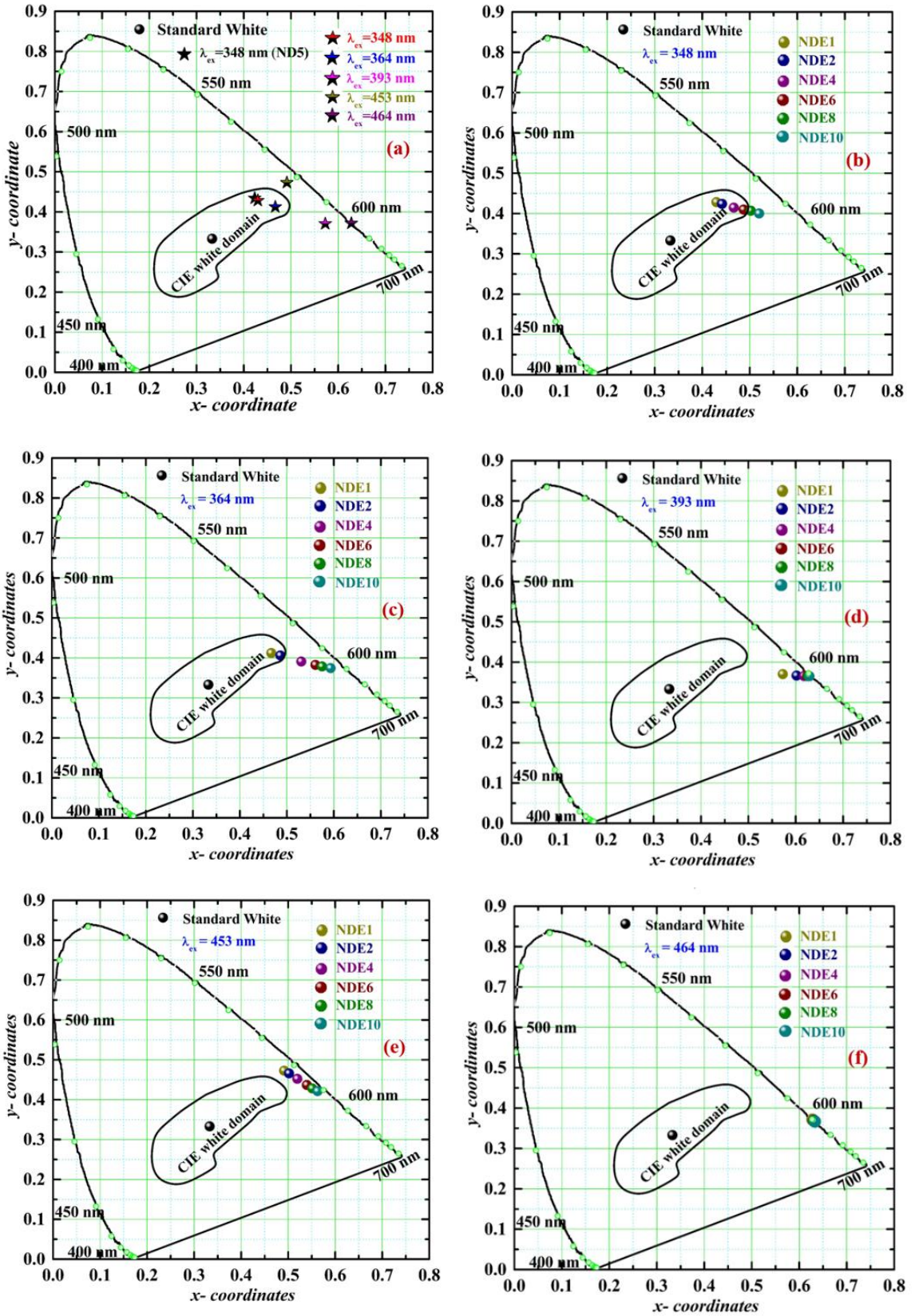

Fig. 6.12. ***(a)*** *CIE chromaticity coordinates of ND5 at 348 nm excitation wavelength and NDE1 at different wavelength (348, 364, 393, 453 and 464 nm)* ***(b-f)*** *CIE coordinates of NDE1, NDE2, NDE4, NDE6, NDE8 and NDE10 under 348, 364, 393, 453, and 464 nm excitation wavelength, respectively.*

Moreover, CIE and CCT (Correlated color temperature) values of single and bi-activated NCMS phosphors have been evaluated and represented in Table 6.3 under 348 and 464 nm excitation wavelengths. The CCT values are less than 5000 K indicate that the colour of the synthesized phosphors fall in warm white light region with incorporating Eu^{3+} ions under the excitation wavelengths of Dy^{3+}. The aforementioned colorimetric behaviour under n-UV/blue LED excitation source of the as-synthesized bi-activated NCMS: Dy^{3+}/Eu^{3+} phosphors have proved its ability to utilize in w-LEDs and color tunable display devices.

6.3.5. Decay measurement of NCMS: Dy^{3+}/Eu^{3+} phosphor

Fig. 6.13 (a & b) depicts the luminescence decay measurements which have been performed under 348 nm excitation wavelength by fixing the emission wavelength at 576 nm. The feasible fitted PL decay profiles of ND5, NDE2, NDE4, NDE6, NDE8 and NDE10 were achieved with the bi-exponential equation [268]:

$$I = I_o + ae^{\left(\frac{1}{\tau_1}\right)} + be^{\left(\frac{1}{\tau_2}\right)} \quad (6.7)$$

In the above equation, I and I_o implies the emission intensity resembles to specific time 't' and '0'. The parameters, τ_1 denotes as slow while τ_2 as the fast component of decay time with *a* and *b* as fitting constants, respectively. Further, average decay lifetime (τ_{avg}) for all the samples have been evaluated using the below equation:

$$\tau_{avg} = (a\tau_1^2 + b\tau_2^2)/(a\tau_1 + b\tau_2) \quad (6.8)$$

The evaluated lifetime value of bi-activated NCMS: Dy^{3+}/Eu^{3+} phosphors show the downtrend with increase in concentration of activator ion and confirms the energy transfer from sensitizer to activator (Dy^{3+} to Eu^{3+}) ions.

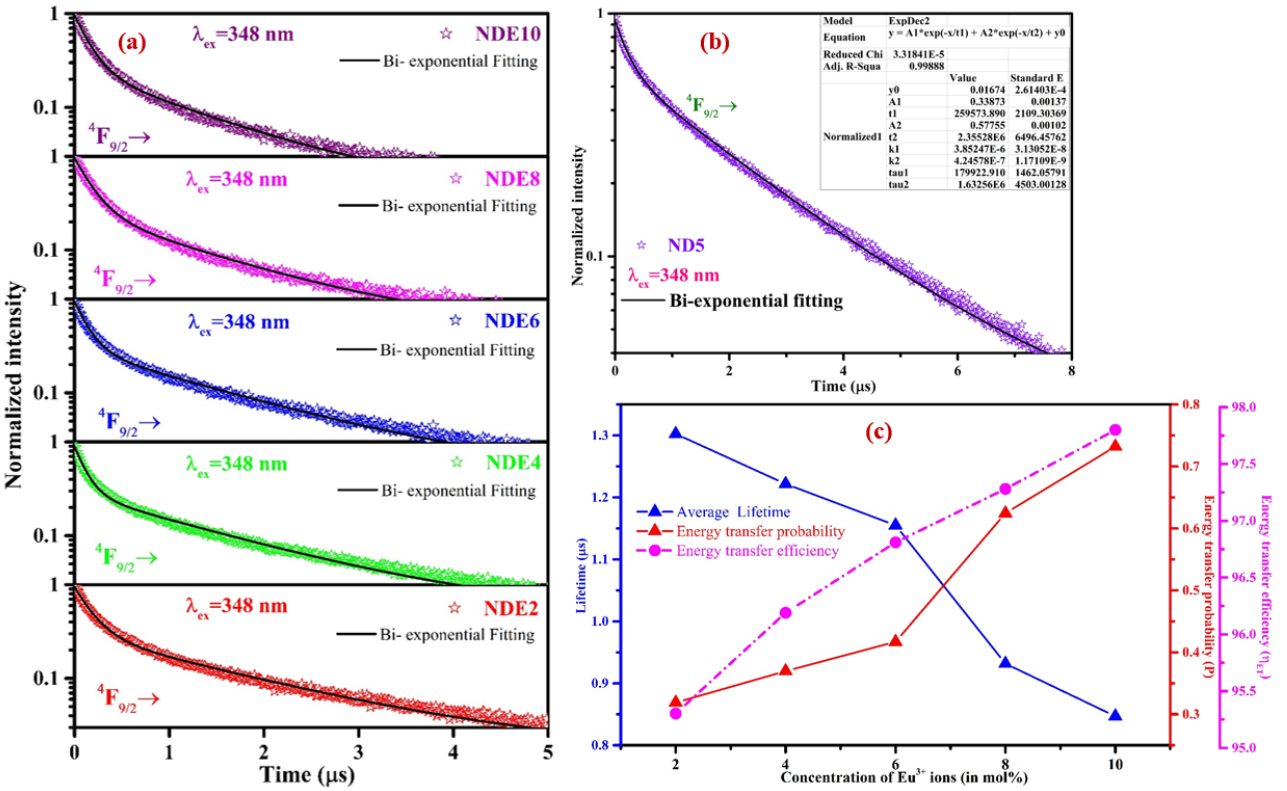

Fig. 6.13. ***(a)*** *Decay plots of NDE2, NDE4, NDE6, NDE8 and NDE10 phosphors for $^4F_{9/2}$ level under the excitation wavelength of 348 nm* ***(b)*** *Decay plot for ND5 phosphor under 348 nm excitation wavelength* ***(c)*** *Lifetime, energy transfer efficiency and energy transfer probability with increasing the concentration of Eu^{3+} ions at λ_{ex}= 348 nm and λ_{em}= 576 nm.*

Using decay time values such as τ_0 (without Eu^{3+} ions) and τ (with Eu^{3+} ions), probability rate (P) for dipole-dipole energy transfer in NCMS: Dy^{3+}/Eu^{3+} phosphors have been estimated as follow equation below [269]:

$$P = {}^{1}/_{\tau} - {}^{1}/_{\tau_0} \qquad (6.9)$$

The evaluated energy transfer probability rate with varying the activator ions (Eu^{3+} ions) concentration in NCMS phosphors are mentioned in Table 6.2. Moreover, Fig. 6.13 (c) epitomizes the plot for concentration of Eu^{3+} ions in ND5 phosphor versus decay time values along with the energy transfer efficiency and probability. The energy transfer probability rate and energy transfer efficiency upsurges with rising the concentration of activator ions in NCMS phosphors.

6.3.6. Thermal stability studies of Dy^{3+}/Eu^{3+} doped NCMS phosphor

Fig. 6.14 (a) illustrates thermal stability of the as-prepared phosphor to divulge the performance of materials at high temperature, as the working temperature for LEDs approaches to 150 °C very frequently. A better thermal stability makes the material proficient to implement in the fabrication of LEDs. Bi-activated NCMS: Dy^{3+}/Eu^{3+} phosphor (NDE1) under 348 nm excitation reflects slight drop in the emission intensity with the temperature interval of 20 °C. The constant increment in temperature in a range from RT to 463 K brings down the emission intensity of NDE1 up to 86.30%. Fig. 6.14 (b) depicts the variation in relative emission intensity with rising the temperature. The emission intensity of NDE1 phosphor sustained up to 92.21 and 86.30% at 423 (~150 °C) and 463 K (~190 °C), respectively indicates the superior thermal stability in comparison with the other reported samples [270–272]. Moreover, the thermal stability of other sort of materials such as perovskites and metal organic frameworks (MOFs) possess very less thermal stability [273,274]. Furthermore, the activation energy (ΔE_a) for thermal quenching has been evaluated using the following equation [275]:

$$I_T = \frac{I_o}{1+Aexp\left(\frac{E_a}{K_B T}\right)} \tag{6.10}$$

here, I_o is the initial emission intensity whereas I_T designates intensity at a specific temperature, respectively. Additionally, K_B is the Boltzmann's constant with the value 8.617×10^{-5} *eV/K* and *A* is the Arrhenius constant.

Table 6.4. *Comparison of thermal stability of NCMS: Dy^{3+}/Eu^{3+} phosphor with other reported results.*

Samples	Activation energy (in eV)	Thermal quenching a 423 K (in %)	References
$Na_4Ca_4Si_6O_{18}$: Dy^{3+}/Eu^{3+}	0.25	92.21	Present work
$Sr_3Gd(PO_4)_3$: Dy^{3+}/Eu^{3+}	0.188	80.0	[270]
$SrLaMgTaO_6$:Dy^{3+}/Eu^{3+}	-	83.34	[271]
$Ba_2LaV_3O_{11}$: Dy^{3+}/Eu^{3+}	0.23	50.0	[272]

The activation energy for thermal quenching of NDE1 phosphor has been estimated using plot between ln[(I_o-I_T)-1] and 1/K_BT, as displayed in Fig. 6.14 (c) and found the value as 0.25 eV. The present value is relatively higher than the various other reported phosphors as represented in Table 6.4.

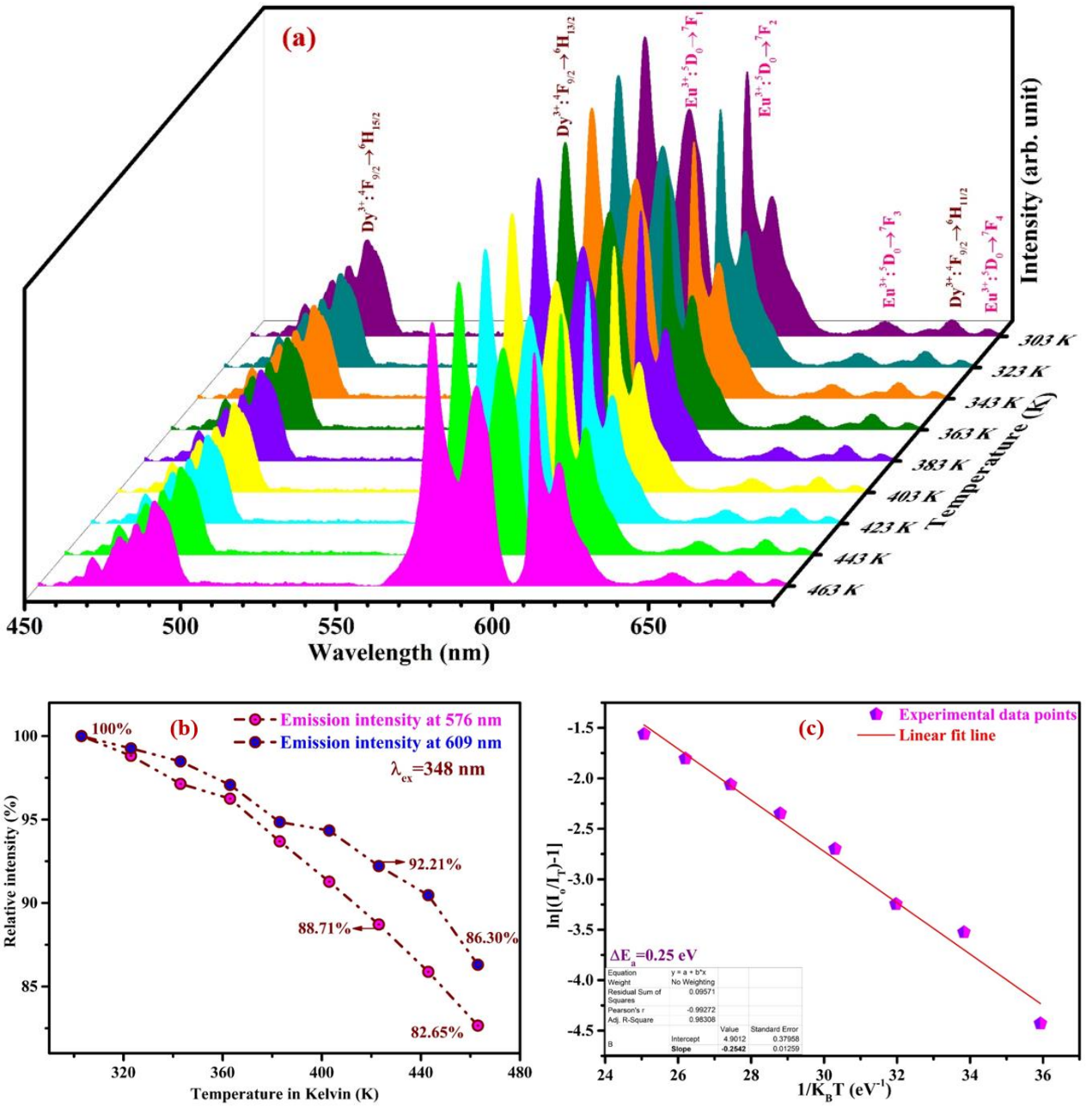

Fig. 6.14 ***(a)*** *Temperature dependent PL spectra of NDE1 phosphor under 348 nm excitation wavelength* ***(b)*** *Relative intensity vs temperature plot for emission peak wavelengths at 576 and 609 nm for NDE1 phosphor under 348 nm excitation wavelength* ***(c)*** *Plot of ln[(I_0/I_T)-1] vs 1/K_BT (eV^{-1}) for NDE1 phosphor.*

6.4. Conclusions

A sequence of NCMS phosphors activated with Dy^{3+} and Dy^{3+}/Eu^{3+} ions were synthesized using solid state reaction technique. Crystalline hexagonal phase of sodium calcium metasilicate phosphor material has been established via X-ray diffraction and the diffraction pattern for all samples are well agreed with specific JCPDS (card no. 75-1687) data. Morphological analysis has been done via observing FE-SEM micrograph that unveils the agglomerated micro sized particles with sharp edges of as-synthesized NDE1 phosphor. The optical band gap of phosphors such as NDE1 and NDE10 are estimated through diffuse reflectance spectra. The emission spectra of the optimized NCMS: Dy^{3+} phosphor illustrate strong intense peaks in yellow region and feeble intense peaks in blue and red region under 348 nm excitation wavelength whereas optimized Eu^{3+} doped NCMS phosphor reveals emission in red region under 393 nm excitation wavelength. The codoped NCMS: Dy^{3+}/Eu^{3+} phosphors represent the color tunability by altering the excitation wavelength and with concentration of Eu^{3+} ions. Moreover, the decay plot under 348 nm excitation expresses the bi-exponential fit with decrement in the decay time with increment in the concentration of activator ion. The Dy^{3+}/Eu^{3+} doubly doped NCMS (NDE1) phosphor shows outstanding thermal stability with higher activation energy demonstrate that this phosphor is the promising candidate for w-LEDs and colour tunable devices.

Chapter 7

Effect of sensitizer on the luminescence of thermally stable Eu^{3+} activated metasilicate phosphor for solar cell applications

Conventional solid state reaction methodology has been opted to synthesize microcrystalline pure phase Sm^{3+}/Eu^{3+} co-doped $Na_4Ca_4Si_6O_{18}$ (NCMS) phosphors. Pure phase has been obtained at the calcination temperature of 950 °C and confirmed via x-ray diffraction technique. The particle size and morphology of the samples have been shown through the micrograph captured using field emission scanning electron microscope. Photoluminescence studies of Sm^{3+} activated and Sm^{3+}/Eu^{3+} co-activated NCMS phosphor have been thoroughly investigated and discussed. The energy transfer mechanism in NCMS: Sm^{3+}/Eu^{3+} phosphors have been studied using PL and lifetime data to facilitate the emission in red region under n-UV excitation. The chromaticity coordinates of NCMS: Sm^{3+}/Eu^{3+} phosphors show the color tunability from orange to red region excited with n-UV/blue light as the concentration of activator ion increases. Moreover, improved luminescence and superior thermal stability of Sm^{3+}/Eu^{3+} co-activated NCMS phosphor demonstrates the viability of the phosphor to be utilized in solar cell applications.

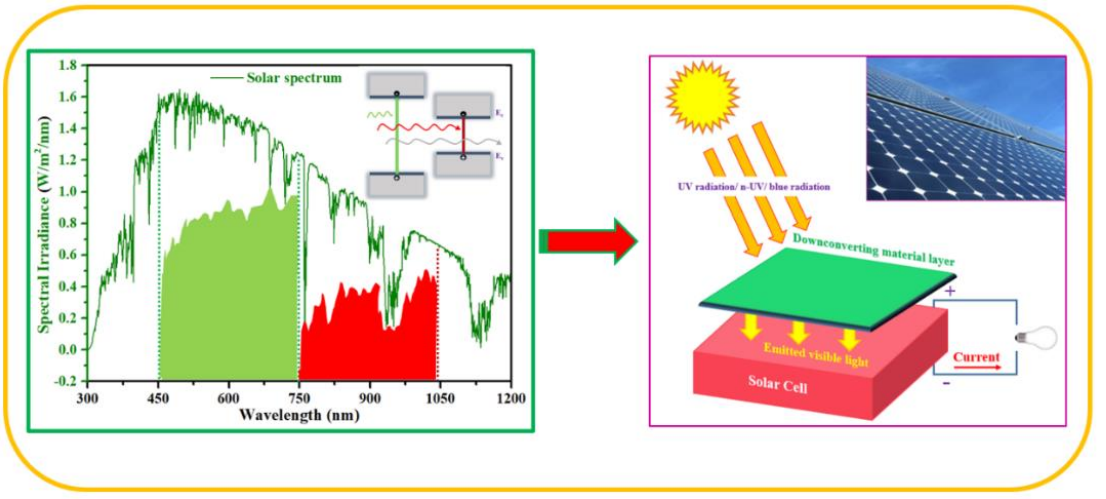

7.1. Introduction

In the modern era, due to overwhelming global population growth and their constant energy consumption, there has been an intense upsurge in the demand of energy. Solar energy has been ascended as a leading renewable energy source to accomplish the massive demand through amalgamating this energy source into technology [276,277]. The extensive and incessant availability of solar energy have drawn the attention of the researchers and scientists to develop the device with capability of converting solar energy into electrical energy and initiated the step towards bridging the gap between nature and technology [278,279]. Recently, the silicon based solar cells are most widely used at industrial horizon due to their benefits such as high stability, ease of massive fabrication and environmental friendliness [280]. However, the commercially available silicon-based solar cells utilize merely a small proportion of solar spectrum indeed have minimal propensity to convert solar energy into electrical energy. The theoretically calculated conversion efficiency of silicon- based solar cell has been reported with the band gap of 1.1 eV as 30%, whereas remaining 70% has been dissipated due to the solar cell response does not match with the solar spectrum which is widely known as spectral mismatch [281,282]. In general, spectral mismatch caused due to two substantial losses: predominant loss (i.e. transmittance loss) arises when the photon with lower energy transmitted through the solar cell without generating electron-hole pair as commercially available silicon has higher band gap energy. Moreover, secondary or thermalization loss occur due to relaxation of charge carriers in the form of thermal energy that absorbed by high energy photons and leads to declining the conversion efficiency of solar cell [283–285]. Thus, use of the luminescent materials could be a viable approach to reduce the spectral mismatch caused by losses and increase the conversion efficiency of solar cells. The luminescent materials especially downconversion/downshifting (DC/DS) materials, which absorbs energy in UV/n-UV region and releases energy in the visible region (without heat dissipation) have been discovered to utilize as a solar spectral convertor for photovoltaic applications [286]. However,

these luminescent materials or phosphors could be efficiently used in numerous other applications such as display devices, optical sensors, security ink, solid state lighting (w-LED) and bioimaging etc. [287].

Trivalent rare-earth (RE) ions listed as Eu^{3+}, Ce^{3+}, Ho^{3+}, Sm^{3+}, Tm^{3+}, Tb^{3+} and Dy^{3+} etc. doped into various host matrices mentioned as silicates, aluminates, phosphates, tungstates and germanates etc., have shown remarkable performance in terms of photovoltaic and w-LED applications [288]. It is a crucial to choose suitable host matrix and doped with appropriate RE ions for better luminescence results. Therefore, selecting the metasilicate as a host matrix seems to be a wise decision as it shows magnificent thermal and chemical stability with ease of synthesis under ambient condition. Singly rare earth ion doped phosphor is excited with UV/n-UV light, reflects an intense single color emission. For instance, Eu^{3+} ion doped materials may be employed as a red component in the generation of white light with improved CRI and CCT values. However, bi-activated phosphors illustrate the transfer of energy occur from sensitizer (donor) to activator (acceptor), which may extend excitation levels to improve the luminescence of the phosphor materials. Sm^{3+}/Eu^{3+} codoped zinc phosphate barium titanate (ZPBT) glasses have illustrated the enhanced luminescence intensity of Eu^{3+} ion via incorporating the Sm^{3+} as a sensitizer [289]. Thus, double ion doped or co-doped phosphors are quiet approachable practically in solar cell applications in order to achieve excellent results.

In the current work, a series of microcrystalline Sm^{3+}/Eu^{3+} co-activated $Na_4Ca_4Si_6O_{18}$ (NCMS) phosphors have been prepared through conventional synthesis methodology (i.e. solid state reaction route) and delved their structural, morphological, optical and photoluminescence behaviour. The emission intensity through activator ion has been enhanced by the incorporation of sensitizer ions and investigated in detail using photoluminescence spectra. Furthermore, the type of interaction among the dopant and co-dopant ions can be revealed by employing the Dexter's and Reisfeld's approximation. The admirable thermal stability of the material has been

acknowledged using temperature dependent photoluminescence spectra. The decay analysis and CIE chromaticity coordinates demonstrate the energy transfer as well as color tunability behaviour of as-prepared NCMS phosphor. The above stated research outcomes from Sm^{3+}/Eu^{3+} co-activated NCMS phosphor showcase its potential to utilise in solar cell application.

7.2. Sample preparation and characterisation techniques

Sodium calcium metasilicate ($Na_4Ca_{4-x}Si_6O_{18}$) phosphor doped with Sm^{3+} and codoped with Eu^{3+} ions were synthesized using conventional solid-state reaction methodology as described in the section 2.2.3. The detailed procedure is represented through the flow chart as shown in Fig. 2.1. Moreover, various characterization techniques have been carried out to investigate the crystalline, morphological and luminescent behaviour of the as synthesized phosphors, described in detailed in section 2.3 (chapter 2). Furthermore, the incorporated concentration of Sm^{3+} as dopant ion (i.e. 1.0, 2.0, 3.0, 4.0 and 5.0 mol%) in NCMS host matrix are named as NS1 to NS5. The Eu^{3+} as co-dopant ions have been added to the NS3 and are identified as NSE1, NSE2, NSE4, NSE6 and NSE8 for 1.0, 2.0, 4.0, 6.0 and 8.0 mol% concentration of Eu^{3+} ion.

7.3. Results and discussion

7.3.1. Structural, phase purity and strain measurement studies

Fig. 7.1 (a). depicts the X-ray diffraction (XRD) patterns of undoped, Sm^{3+} doped and Sm^{3+}/Eu^{3+} co-doped NCMS materials. Diffraction peaks of all the samples have shown the good agreement to the standard diffraction peaks of $Na_4Ca_4Si_6O_{18}$ (JCPDS card no.: 75-1687) materials that signified the absence of any impurity and confirmed the preparation of single phase crystalline hexagonal NCMS host matrix. The as-prepared NCMS crystal with pure hexagonal phase belongs to $P3_2$ space group and have unit cell parameters as a=b=10.46 Å; c=13.17 Å and V=1249.42 $Å^3$. However, the insertion of dopant (Sm^{3+}) and co-dopant (Eu^{3+}) ions into the host lattice may supplement the photoluminescence effect without changing the elementary crystal structure.

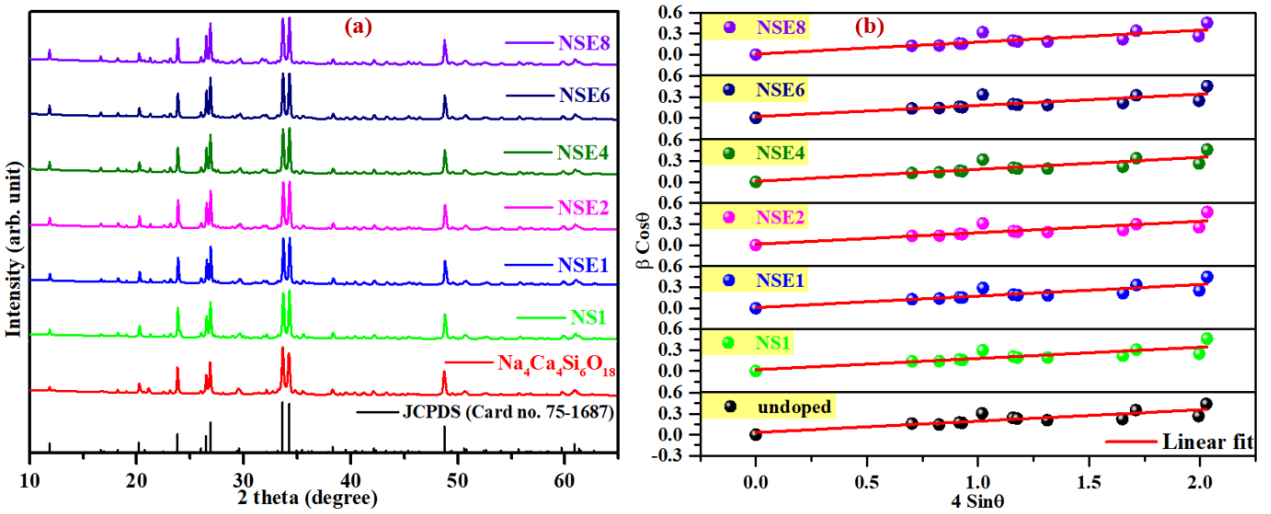

Fig. 7.1. ***(a)*** *X-ray diffraction patterns and* ***(b)*** *Williamson-Hall (W-H) of undoped, Sm^{3+} (1.0 mol%) and Sm^{3+}/Eu^{3+} (1.0, 2.0, 4.0, 6.0 and 8.0 mol% of Eu^{3+} ions) co-activated $Na_4Ca_4Si_6O_{18}$ phosphor.*

Since the XRD profile of Sm^{3+} activated and Sm^{3+}/Eu^{3+} co-activated NCMS phosphors have shown the well-matched diffraction peaks with the standard and undoped pattern of NCMS structure indicate the effective incorporation of dopant and co-dopant ions into the host lattice. Moreover, as the ionic radii of Sm^{3+} (0.96 Å) and Eu^{3+} (0.95 Å) having coordination number six is quite closer to the ionic radii of Ca^{2+} (1.00 Å) and can be easily replaced with these two dopant and co-dopant ions in the NCMS crystal framework. Furthermore, the average crystallite size (D_{hkl}) can be evaluated using illustrious Debye-Scherrer equation given below [290]:

$$D_{hkl} = \frac{k\lambda}{\beta_{hkl} Cos\theta_{hkl}} \tag{7.1}$$

Each parameter in the above equation such as *K*, λ, β and θ are designated as constant with value 0.94, wavelength of incident x-rays with the value of 1.54 Å, full width at half maxima (FWHM) and diffraction angle, respectively. Using above equation, the average crystallite size are computed for all the as-prepared samples and varies in a range of 44-49 nm [291]. The average crystallite size (D) and strain (ε) can also be estimated using Williamson-Hall (W-H) plot equation given below [292]:

$$\beta Cos\theta = {}^{K\lambda}/_{D_{hkl}} + 4\varepsilon\, Sin\theta \tag{7.2}$$

where most of the parameters such as *D*, *K*, λ, β and θ have already defined earlier and ε is the strain. The strain has been estimated using slope and intercept value after plotting a graph between $\beta Cos\theta$ and $4\,Sin\theta$, as represented in Fig. 7.1 (b). Using W-H plot, strain for the samples would lie in a range of 0.163 to 1.710 [293]. Moreover, the positive values of the slope reveal the tensile strain which also elevate with rise in the concentration of dopant and co-dopant ions in the samples.

7.3.2. Band gap measurement

To compute the optical band gap, diffuse reflectance spectra of NCMS: xSm^{3+}/yEu^{3+} (x=3.0 mol% & y=1.0 and 8.0 mol%) phosphors have been measured in UV, n-UV and visible regions (200-600 nm), as demonstrated in Fig. 7.2 (a & b). The spectra show few characteristic reflectance peaks are appeared in n-UV and visible region due to f-f transition among dopant and codopant ions [153]. Moreover, the band gap (E_g) energy have been reckoned using Kubelka-Munk (K-M) relation as represented below [294]:

$$F(R) = \frac{(1-R)^2}{2R} = \frac{K}{S} \tag{7.3}$$

where F(R) refers to K-M function, R (reflectance) tends to the reflectance of sample to reference sample (Standard: $BaSO_4$) ratio, K and S symbolizes the absorption and scattering coefficient. Furthermore, by equating Tauc equation with K-M relation provides the optical band gap (E_g) energy by following the value of *n* which elaborate the kind the electronic transitions through equation below [85]:

$$(F(R)h\upsilon) = B(h\upsilon - E_g)^n \tag{7.4}$$

Thus, the band gap energy for NCMS: xSm^{3+}/yEu^{3+} (x=3.0 mol% & y=1.0 and 8.0 mol%) phosphor have been calculated by extrapolating the line to x-axis in $[F(R)\,h\upsilon]^2$ vs $h\upsilon$ plot, exposed in the inserted plot of Fig. 7.2 (a & b). The direct allowed band gap with n=1/2 for NSE1 and NSE8 have been computed and found to be 4.41 and 4.40 eV, respectively [295].

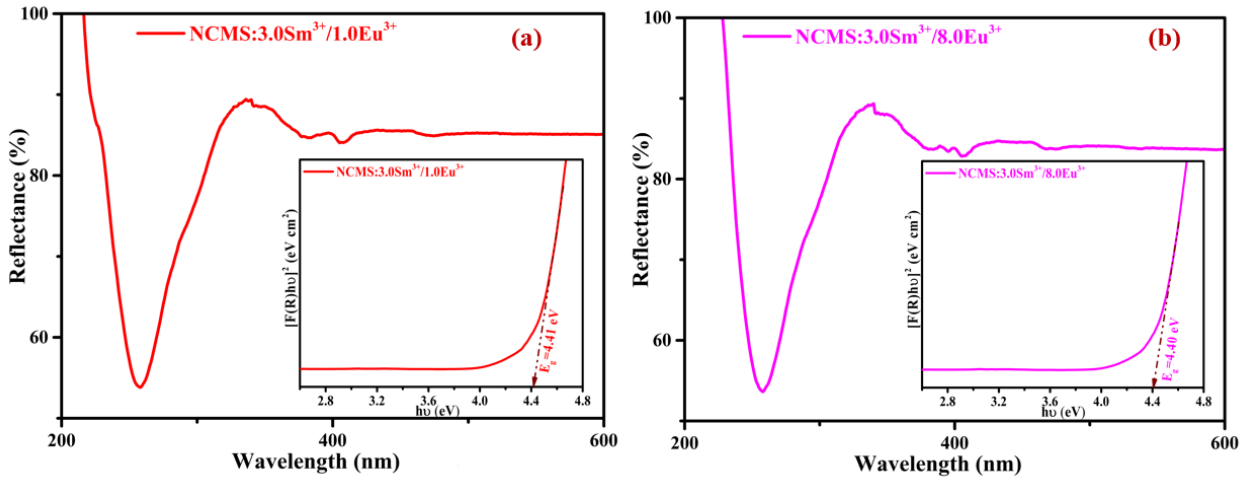

Fig. 7.2. ***(a & b)*** *Diffuse reflectance spectra of Sm^{3+}/Eu^{3+} co-activated $Na_4Ca_4Si_6O_{18}$ phosphors and inset shows the band gap plot of associated NCMS: Sm^{3+}/Eu^{3+} phosphors.*

7.3.3. Morphological studies

The shape, size and morphology of the undoped $Na_4Ca_4Si_6O_{18}$ (Fig. 3 (a-c)) and $Na_4Ca_4Si_6O_{18}$:$3.0Sm^{3+}/1.0Eu^{3+}$ (Fig. 7.3 (d-f)) phosphors have been unveiled by field emission scanning electron microscopy (FE-SEM) technique.

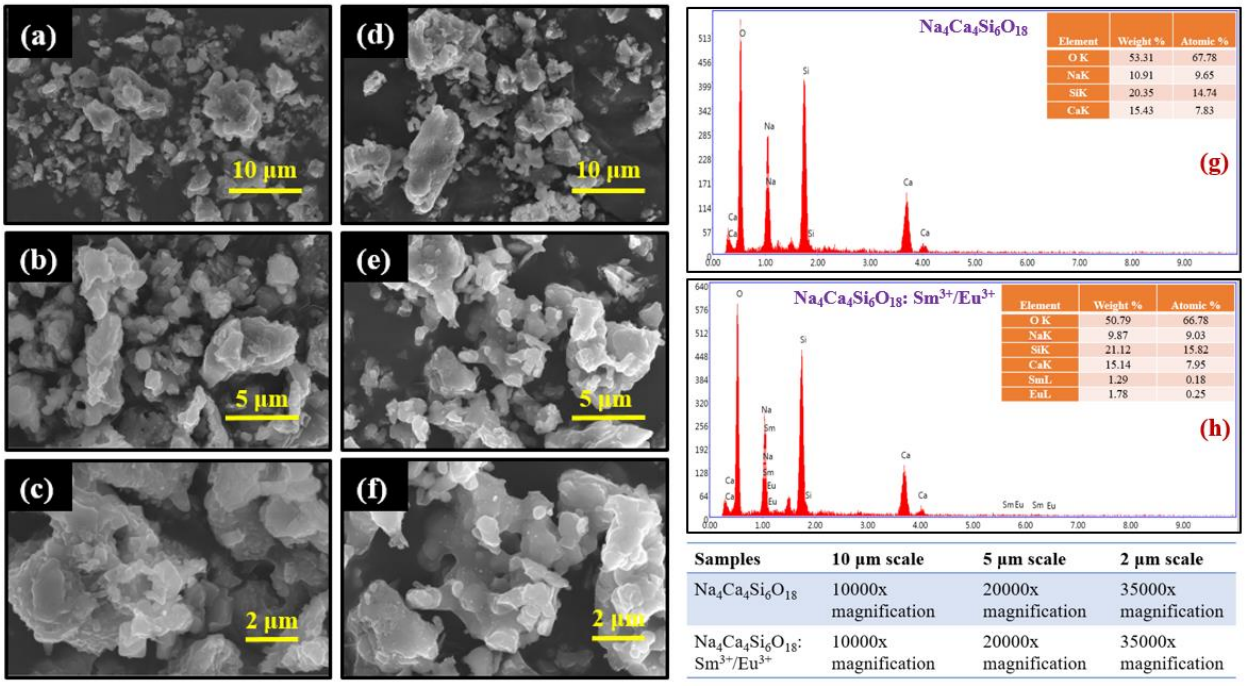

Samples	10 µm scale	5 µm scale	2 µm scale
$Na_4Ca_4Si_6O_{18}$	10000x magnification	20000x magnification	35000x magnification
$Na_4Ca_4Si_6O_{18}$: Sm^{3+}/Eu^{3+}	10000x magnification	20000x magnification	35000x magnification

Fig. 7.3. ***(a-f)*** *FE-SEM micrograph of undoped and NCMS: 3.0 $Sm^{3+}/1.0Eu^{3+}$ phosphor at different resolution mentioned in the table shown above.* ***(g & h)*** *Energy dispersive x-ray analysis (EDAX) of undoped and NCMS: 3.0 $Sm^{3+}/1.0Eu^{3+}$ phosphor.*

Each FE-SEM micrograph divulge the irregular and agglomerated particles in micron range which was observed due to high calcination temperature and taken at different resolutions, as depicted in Fig. 7.3 [296]. Energy dispersive x-ray analysis (EDAX) have also been done along with FE-SEM, which reveals the presence of atoms with weight and atomic percentage in the material, as represented in Fig. 7.3 (g & h).

7.3.4. Luminescent studies of NCMS: Sm^{3+}/Eu^{3+} phosphor

The photoluminescence (excitation and emission) spectra of Sm^{3+} doped $Na_4Ca_4Si_6O_{18}$ phosphors were captured in 300-500 excitation and 550-700 nm emission range, as represented in Fig. 7.4 (a & b), respectively. The recorded excitation spectra express multiple peaks at fixed emission wavelength of 602 nm. These multiple peaks were observed in excitation range having electronic transition from lower state $^6H_{5/2}$ to various excited states as $^4P_{1/2}$ (315nm), $^4H_{9/2}$ (344 nm), $^4D_{3/2}$ (361 nm), $^6P_{7/2}$ (375 nm), $^4G_{11/2}$ (388 nm), $^6P_{3/2}$ (403 nm), $^4M_{19/2}$ (416 nm), $^4G_{9/2}$ (441 nm), $^4M_{17/2}$ (450 nm), $^4I_{13/2}$ (467 nm) and $^4I_{9/2}$ (488 nm) [297]. Among all the excitation peaks highest intense peak is observed at 403 nm which attributes to $^6H_{5/2} \rightarrow {}^6P_{3/2}$ and have been chosen to record the emission spectra. Moreover, the monitored emission spectra affirm peak position at 564, 602, 650 and 714 nm implies to the transitions of Sm^{3+} ions from $^4G_{5/2}$ to $^6H_{5/2}$, $^6H_{7/2}$, $^6H_{9/2}$ and $^6H_{11/2}$, respectively. In addition to the intense emission peak at 602 nm, two less strong peaks identified at 564 and 650 nm obeys selection rule and ensues the magnetic dipole (MD) ($\Delta J=0, \pm1$) and electric dipole (ED) ($\Delta J \leq 6$; $\Delta J=2$, 4 and 6) transitions, respectively, where J is the total angular momentum [298]. The MD transition resembles to $^4G_{5/2} \rightarrow {}^6H_{5/2}$, and does not effect from crystal field environment wherein hypersensitive forced ED transition attributed to $^4G_{5/2} \rightarrow {}^6H_{9/2}$ is highly influenced with crystal field environment. Most effectively intense peak observed at 602 nm ($^4G_{5/2} \rightarrow {}^6H_{7/2}$) due to both partially MD and ED transitions by following the selection rule (where, $\Delta J= \pm1$) [299,300]. The information regarding the symmetric and asymmetric nature of local environment of the dopant ions in the host matrices is represented by the ratio of ED to MD

transitions [120]. Lower the intensity ratio indicates lesser distortion from the inversion symmetry. Hence, the estimated value for intensity ratio of ED to MD transition is 0.81 for optimized concentration and designates lesser distortion from the inversion symmetry or higher environmental symmetry [301]. Furthermore, the emission intensity for distinct Sm^{3+} ion concentrations incorporated into the host matrix increases up to 3.0 mol%, however, further increase in concentration leads to decrease in emission by the cause of concentration quenching mechanism, as represented in Fig. 7.4 (c) [302,303].

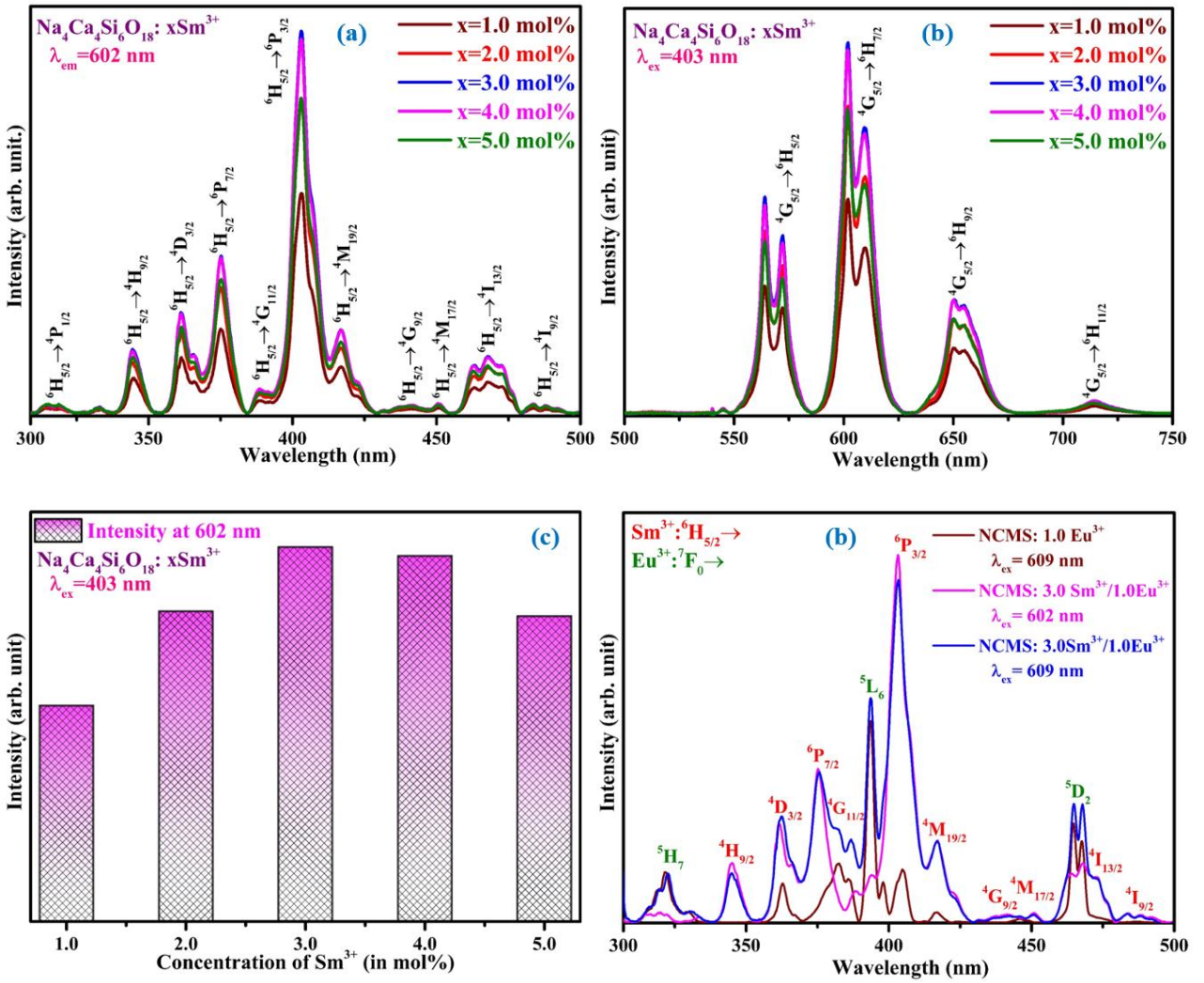

Fig. 7.4. ***(a & b)*** *PLE and PL spectra of Sm^{3+} (1.0, 2.0, 3.0, 4.0 and 5.0 mol%) doped $Na_4Ca_4Si_6O_{18}$ phosphors monitored with the λ_{em}=602 nm and λ_{ex}=403 nm, respectively.* ***(c)*** *Bar plot for intensity versus concentration of Sm^{3+} ions.* ***(d)*** *Compiled excitation plot of 1.0 mol% of Eu^{3+} doped & 3.0 Sm^{3+}/1.0 Eu^{3+} co-doped NCMS phosphor under λ_{em}=609 nm and λ_{em}=602 nm.*

Initially, the dopant (Sm^{3+}) concentration optimization in the as-prepared host matrix has been done to act as a sensitizer. Additionally, the Eu^{3+} ions (activators) added in the optimized sample in order to enhance the intensity. As a result, sensitizer has been proved to be essential in boosting the intensity of activator ion as shown in the excitation plot of Sm^{3+} and Sm^{3+}/Eu^{3+} co-activated NCMS phosphor in Fig. 7.4 (d) [304]. The excitation spectra of 1.0 mol% of Eu^{3+} ion activated and 3.0 mol% of Sm^{3+} doped with 1.0 mol% of Eu^{3+} co-activated NCMS phosphor have been taken under 602 and 609 nm emission wavelength.

Under both emission wavelengths several peaks are obtained due to Sm^{3+} and Eu^{3+} dopant ions located at 344, 361, 375, 388, 403, 416, 441, 450, 467 and 488 nm wavelength attributed to distinct levels from $^6H_{5/2}$ to $^4H_{9/2}$, $^4D_{3/2}$, $^6P_{7/2}$, $^4G_{11/2}$, $^6P_{3/2}$, $^4M_{19/2}$, $^4G_{9/2}$, $^4M_{17/2}$, $^4I_{13/2}$, $^4I_{9/2}$ (for Sm^{3+} ions) and 321, 393 and 464 nm resembles from $^7F_0$ to $^5H_7$, $^5L_6$, $^5D_2$ state (for Eu^{3+} ions) [305]. It can be espied that the augmented excitation peaks of Eu^{3+} ions at 393 ($^7F_0 \rightarrow {}^5L_6$) and 467 ($^7F_0 \rightarrow {}^5D_2$) nm have been achieved due to the insertion of Sm^{3+} ions whose sensitization effect has emerged onto the Eu^{3+} in Sm^{3+}/Eu^{3+} co-doped NCMS host matrices, as represented in Fig. 7.4 (d).

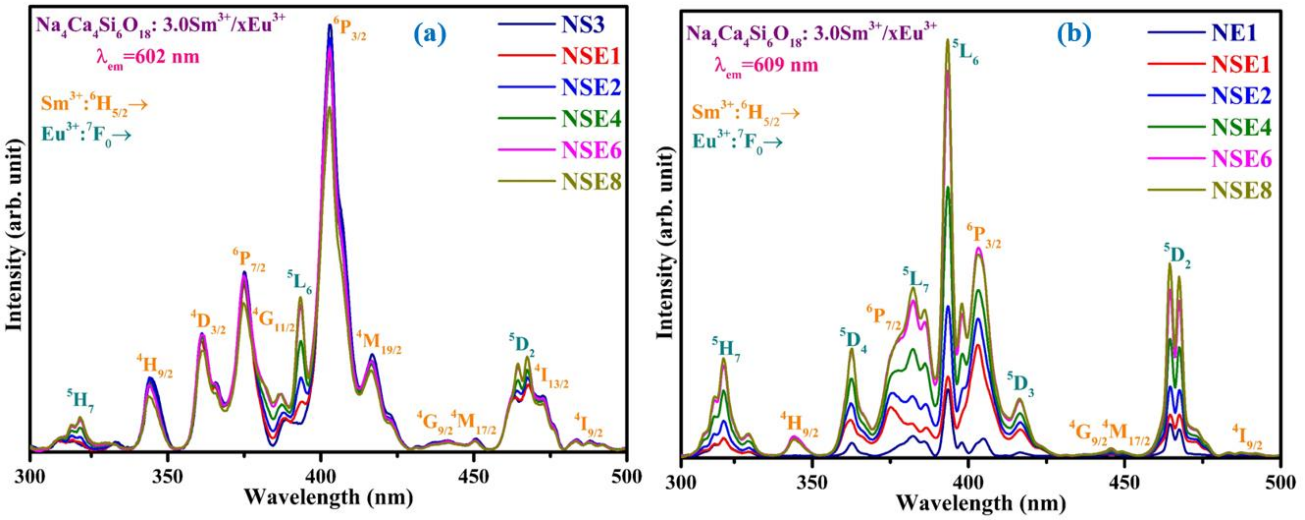

Fig. 7.5. ***(a & b)*** *Excitation spectra of Sm^{3+}, Eu^{3+} activated and Sm^{3+}/Eu^{3+} co-activated NCMS phosphor by monitoring the emission wavelength of λ_{em}=602 and 609 nm.*

The Fig. 7.5 (a & b) expresses the excitation spectra of Sm^{3+} activated and Eu^{3+} co-activated $Na_4Ca_4Si_6O_{18}$ phosphor at intense emission wavelength of Sm^{3+} (602 nm) and Eu^{3+} (609

nm) ions in order to elucidate the behaviour of peaks with incorporation of Eu^{3+} as a co-dopant. In the excitation spectra under 602 and 609 nm, mixed peaks of Sm^{3+} and Eu^{3+} ions are observed in a range of 300 to 500 nm, as discussed earlier in Fig. 7.4 (d). Considering the intense peaks enumerated at 375, 403, 467 and 393 nm in the excitation spectra in Fig. 7.5 (a & b), the emission profiles have been monitored in the visible spectral region as catalogued in Fig. 7.6 (a-d). The emission spectra recorded under 375 and 403 nm excitation wavelengths are quite similar as both the excitation wavelengths are of pure Sm^{3+} ions. Emission peaks positioned at 564, 602, 650 and 714 nm are attained due to the presence of Sm^{3+} ion acts as sensitizer in the host matrix and their intensity drops with simultaneous rise in the Eu^{3+} ions concentration. However, peaks obtained at 579, 591, 609, 653, 686 and 705 nm are due to insertion of Eu^{3+} as an activator ion and upsurges as followed with the concentration of Eu^{3+} ions. The peaks observed in a range of 635-675 nm due to Sm^{3+} ions are showing the random intensity behaviour and unable to distinguished which is because of the combined effect of Sm^{3+} and Eu^{3+} ions. Fig. 7.6 (c) depicts the emission spectra of NCMS: Sm^{3+}/Eu^{3+} phosphor at 467 nm excitation wavelength, which is second utmost intense as well as nearly common peaks emerged in the excitation range. It can be observed that the Sm^{3+} ion peaks are dropping down wherein the peaks position obtained due to Eu^{3+} ions are rising with its concentration. Fig. 7.6 (d) manifests that the emission spectra under 393 nm excitation wavelength for NCMS: Sm^{3+}/Eu^{3+} phosphor wherein the emission peaks of Eu^{3+} ions are rising with increase in the Eu^{3+} ions concentration. Moreover, inset of Fig. 7.6 (d) illustrates the emission peaks of NSE1 is elevated in comparison with NE1 phosphor indicated that the Sm^{3+} ion has aided to improve the emission intensity. It can extricate from the graph that few peaks positioned at 564 and 602 nm are appeared in emission spectra of NSE1 phosphor which signifies the presence of Sm^{3+} ions due to the fact that the excitation energy of Sm^{3+} and Eu^{3+} is nearby, which further vanishes with increase in Eu^{3+} ion concentration [306].

Dexter and Schulman express the ubiquitous phenomenon of concentration quenching effect during energy transfer from sensitizers (Sm^{3+}) to activators (Eu^{3+}) [307]. In general, there are two viable mechanisms by which energy can be transferred among rare earths, namely exchange and multipolar interaction. Predominantly, the exchange interaction appears if the critical distance (R_c) is smaller than the 5 Å, whereas the multipolar interaction occurs when the R_c is larger than 5 Å. According to Blasse, the critical distance (R_c) between sensitizer and activator ions can be evaluated using below equation [308]:

$$R_c = 2\left(\frac{3V}{4\pi x_c N}\right)^{\frac{1}{3}} \quad (7.5)$$

In the above-mentioned equation, various significant parameters such as the critical concentration *(x_c)* of sensitizer (Sm^{3+}) and activator (Eu^{3+}), volume *(V)* and number of cations in the unit cell *(N)*. For $Na_4Ca_4Si_6O_{18}$ matrix, the value of N is 3 and V is 1249.42 $Å^3$ inclusively, the critical concentration is taken where the emission intensity of sensitizer approaches to half of their own intensity i.e. 0.11 mol by taking Sm^{3+} as fixed at 3.0 mol% and Eu^{3+} as 8.0 mol%.

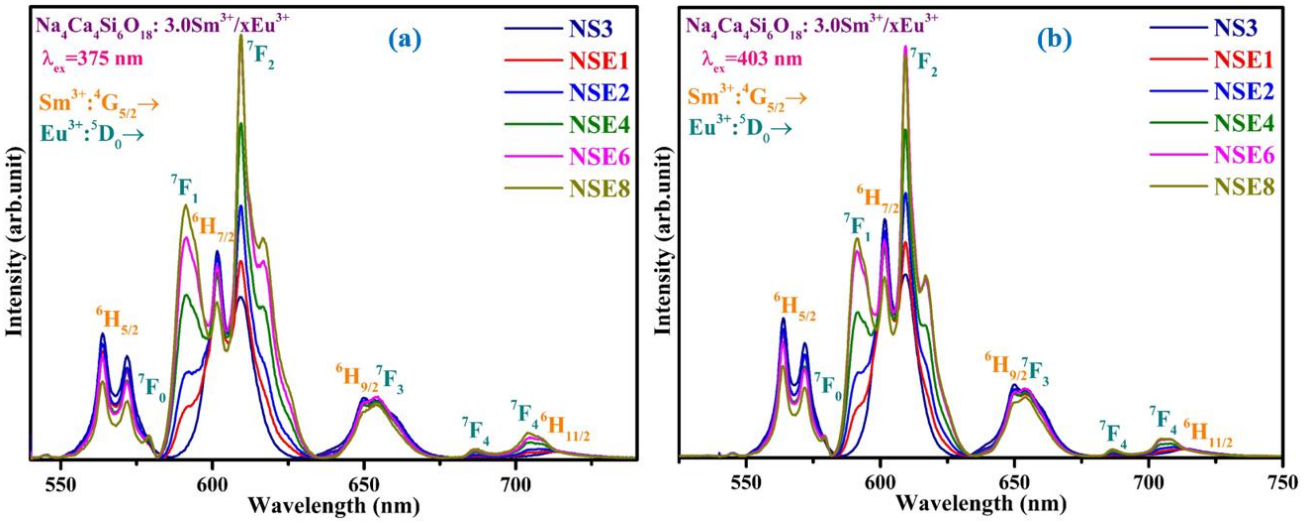

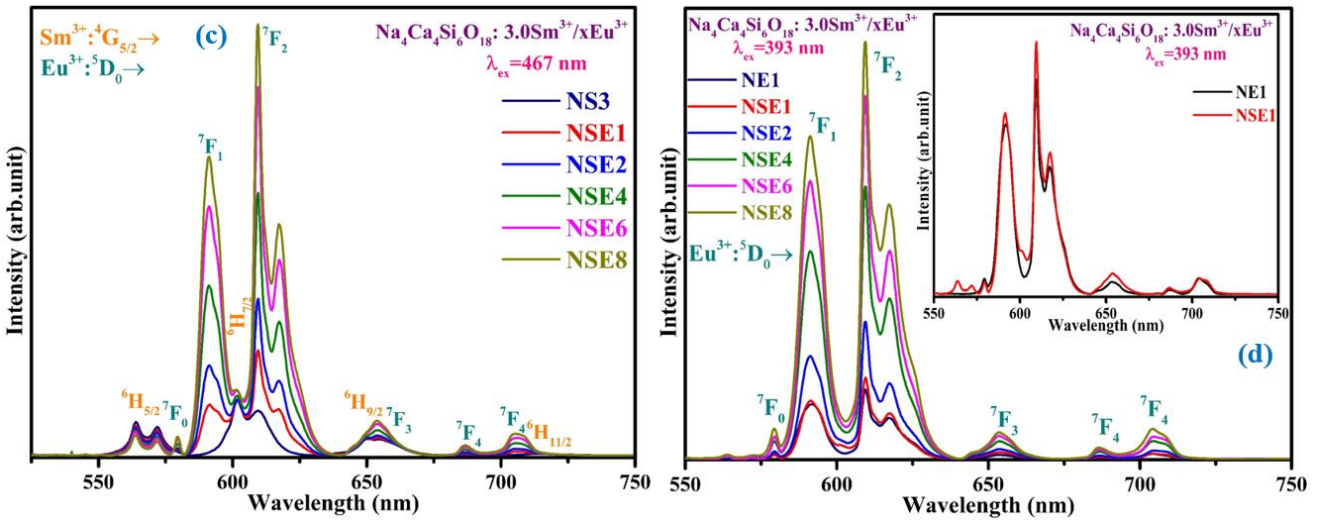

Fig. 7.6. ***(a)*** *PL spectra of Sm^{3+} activated and Sm^{3+}/Eu^{3+} co-activated NCMS phosphor under the excitation wavelengths λ_{ex}=375 nm* ***(b)*** *λ_{ex}=403 nm* ***(c)*** *λ_{ex}=467 nm and* ***(d)*** *λ_{ex}=393 nm with inset representing the comparison of emission spectra of 1.0 Eu^{3+} with 3.0Sm^{3+}/1.0Eu^{3+} co-doped NCMS phosphor.*

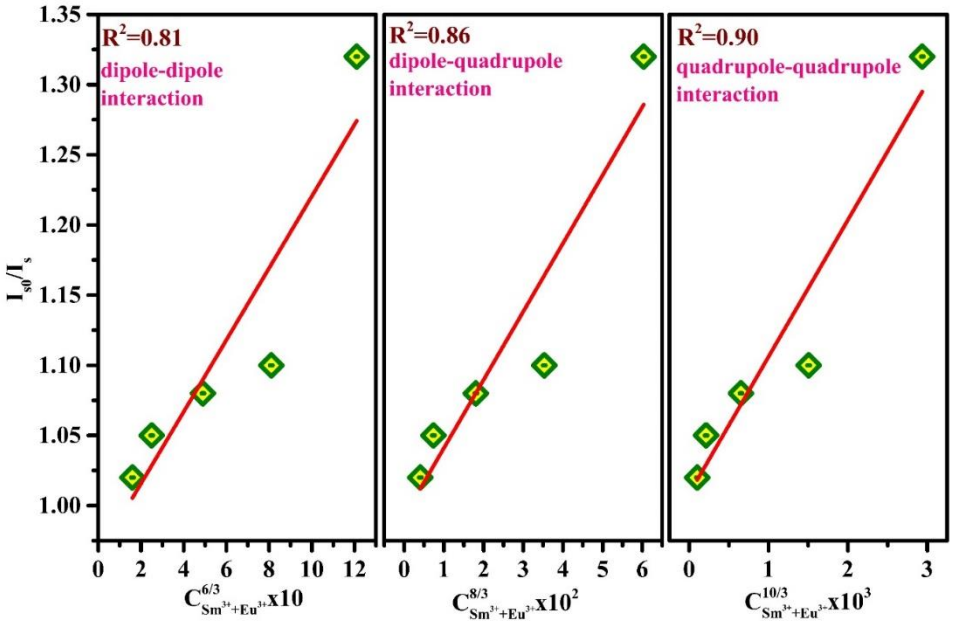

Fig. 7.7. *I_{s0}/I_s versus $C^{n/3}_{Sm^{3+}+Eu^{3+}}$ plot revealing the types of interactions among dopant and co-dopants ions in bi-activated NCMS phosphor.*

Finally, the critical distance is evaluated as 19.34 Å, which is higher than 5 Å, prone to allow multipolar interactions that includes dipole-dipole, dipole-quadrupole and quadrupole-quadrupole (i.e. d-d, d-q and q-q) interactions [309]. Thus, in order to inspect the sort of interaction

in the Sm^{3+}/Eu^{3+} co-doped NCMS phosphor sample, Dexter's and Reisfeld's approximation are employed according to the below equation [266]:

$$\frac{\eta_{s0}}{\eta_s} \propto C^{\frac{n}{3}}_{Sm^{3+}+Eu^{3+}} \tag{7.6}$$

where, η_{s0} is the luminescent quantum efficiency of sensitizer (no activator), η_s is the luminescent quantum efficiency of activator ions and *C* signifies as the sum of concentration of sensitizer and activator ions with the power of *n/3*, where *n* represents the type of interaction taking place depending on the values 6 (d-d), 8 (d-q) and 10 (q-q). The η_{s0}/η_s ratio can be equated to the ratio of associated luminescence intensity and represented as below [310]:

$$\frac{I_{s0}}{I_s} \propto C^{\frac{n}{3}}_{Sm^{3+}+Eu^{3+}} \tag{7.7}$$

Similar to the Dexter's and Reisfeld's approximation, here I_{so} and I_s is the intrinsic emission intensity of Sm^{3+} ion (without Eu^{3+} ion) and Sm^{3+} ion (with Eu^{3+} ion), respectively. Fig. 7.7. depicts that the value of *n* obtained after fitted linearly in I_{s0}/I_s versus $C^{n/3}_{Sm^{3+}+Eu^{3+}}$ plot is 10 under 403 nm. This signifies that the non-radiative energy transfer from donor to acceptor (sensitizer → activator) ions is caused by the quadrupole-quadrupole multipolar interaction [311].

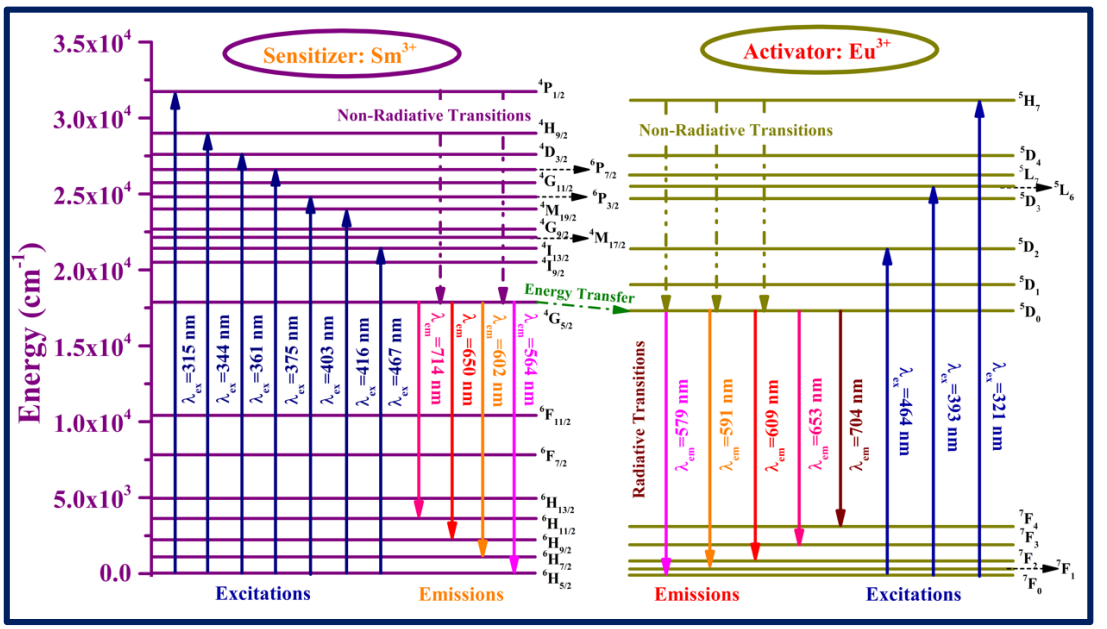

Fig. 7.8. *Partial Energy level diagram representing the energy transfer process in Sm^{3+} doped and Sm^{3+}/Eu^{3+} co-doped NCMS phosphor.*

The partial energy level diagram clearly illustrates the energy transfer mechanism among sensitizer and activator ions, as represented in Fig. 7.8. Initially the excited energy is absorbed by the Sm^{3+}/Eu^{3+} doped NCMS phosphor samples, which stimulates the ion from lower state to various excited states. Further, the ion attained to higher state later falls swiftly to the lower excited state through non-radiative relaxation represented by the dashed lines and then relaxes radiatively to the ground states. The lower excited state of Sm^{3+} and Eu^{3+}, i.e. $^4G_{5/2}$ and $^5D_0$ attribute to energy 17900 and 17286 cm^{-1}. The lower excited energy level of Sm^{3+} is nearly 614 cm^{-1} above than the lower excited level of Eu^{3+} ions. Hence, probably there may be a chance of transferring a part of energy from Sm^{3+} ions which leads to decline of emission obtained due to sensitizers, as represented in Fig. 7.8. Indeed, the minor distinction between the lower excited energy levels of sensitizer and activator ions allow the possible energy transfer from Sm^{3+} to Eu^{3+} ions. This transition acclaims that Sm^{3+} ions must behave as a sensitizer (donor) for activator (acceptor) ions in the current bi-activated NCMS crystal lattice [312].

7.3.5. Lifetime and energy transfer efficiency/probability analysis

Decay analysis for sensitizer and activator ions NCMS samples have been done under the excitation of 403 nm which attributes to the emission transition of $^4G_{5/2} \rightarrow {}^6H_{7/2}$ at 602 nm as shown in Fig. 7.9 (a-d). The decay profile of samples represents the declining trend with rise of Eu^{3+} ions concentration in the host matrix which implies the strong evidence of migration of partial energy from sensitizer to activator ions. The exponential decay curves were well fitted with bi-exponential equation after adopting different exponential equations. The optimized bi-exponential equation is as shown below [154]:

$$I = I_o + A_1 e^{\left(\frac{1}{\tau_1}\right)} + A_2 e^{\left(\frac{1}{\tau_2}\right)} \quad (7.8)$$

where I_o and I are denoted as the emission intensities at time t is 0 and t, respectively. The fitting constants are A_1 and A_2 and the lifetimes are represented as τ_1 and τ_2 which indicate slow and fast

lifetimes. Furthermore, the average lifetime can be evaluated from bi-exponential fitted data as given below [313]:

$$\tau_{avg} = \frac{A_1\tau_1^2 + A_2\tau_2^2}{A_1\tau_1 + A_2\tau_2} \tag{7.9}$$

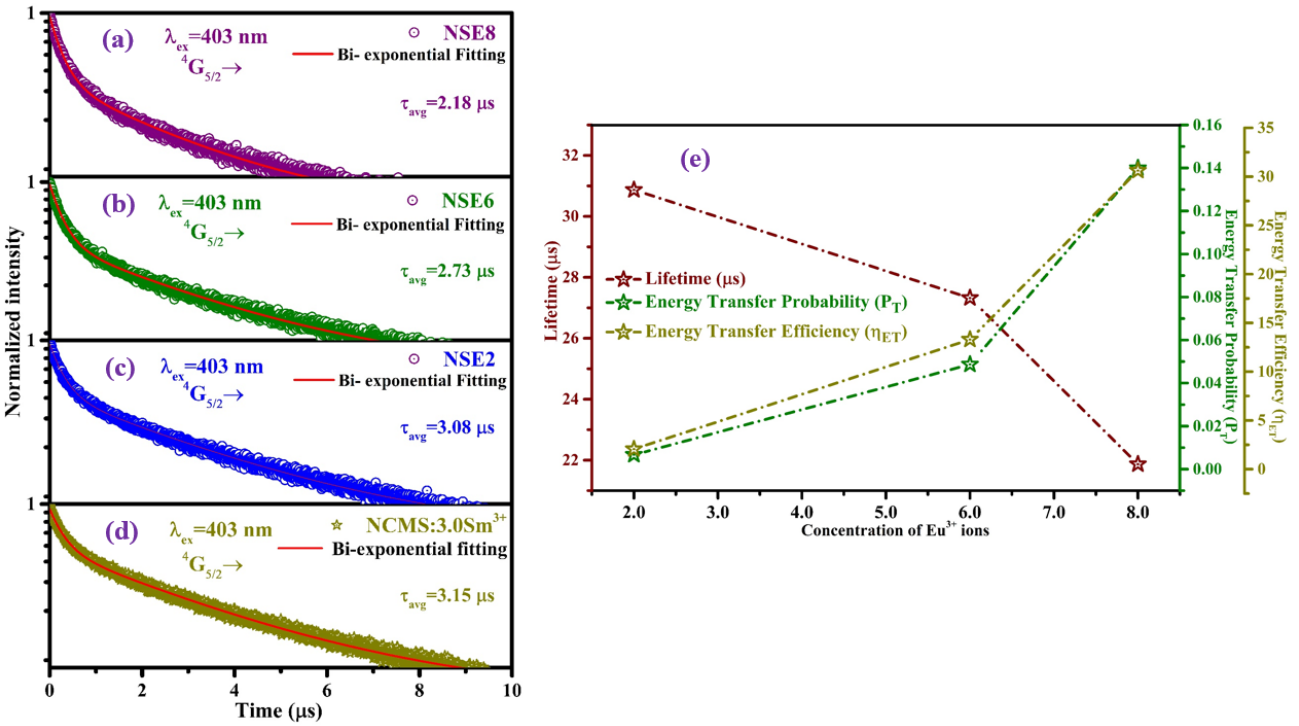

Fig. 7.9. ***(a-d)*** *Lifetime decay plot of 3.0Sm^{3+}/xEu^{3+} (x=2.0, 6.0 and 8.0 mol%) and 3.0 mol% of Sm^{3+} doped NCMS phosphor for $^4G_{5/2}$ under 403nm excitation wavelength.* ***(e)*** *Lifetime, energy transfer efficiency and energy transfer probability with increasing the concentration of Eu^{3+} ion at λ_{ex}=403 nm and λ_{em}= 602 nm.*

The evaluated average lifetime is in the range of 2.18 to 3.15 μs for undoped and co-doped phosphor expressed in Fig. 7.9 (a-d). The energy transfer efficiency and probability in terms of decay lifetime can be evaluated by the following equations [314]:

$$\eta_{T(Sm^{3+}\rightarrow Eu^{3+})} = 1 - \left(\frac{\tau_d}{\tau_{d_o}}\right) \tag{7.10}$$

$$P_{T(Sm^{3+}\rightarrow Eu^{3+})} = \left(\frac{1}{\tau_d}\right) - \left(\frac{1}{\tau_{d_o}}\right) \tag{7.11}$$

The parameters in above equations such as τ_{d_o} and τ_d are referred as the average decay time of Sm^{3+} without Eu^{3+} and with Eu^{3+}, respectively. The estimated values of energy transfer efficiency in terms of percentage for NSE2, NSE4 and NSE8 is found to be 2.06, 13.30 and 30.61% whereas

the values of energy transfer probability are 0.006, 0.048 and 0.139, respectively. The lifetime values, energy transfer efficiencies and energy transfer probability are comprehensively revealed in Fig. 7.9 (e). The assessed energy transfer efficiency and probability are increasing with rise in concentration of activator (Eu^{3+}) ions concentration, which signifies the transfer of energy from Sm^{3+} to Eu^{3+} ions in the host matrix.

7.3.6. CIE color coordinates

Commission International de L'Eclairage (CIE) coordinates manifest luminescent color performance of the as-synthesized NCMS: Sm^{3+}/Eu^{3+} co-doped phosphors under distinct excitations, as represented in Fig. 7.10 (a-c). On the basis of emission spectra of Sm^{3+}/Eu^{3+} bi-activated NCMS phosphor (NS3, NSE1, NSE2, NSE4, NSE6 and NSE8) samples, the CIE color coordinates are determined under the 375, 403 and 467 nm excitation wavelengths as summarized in Table 7.1. The chromaticity plot of bi-activated NCMS phosphors under 375, 403 and 467 nm excitation wavelength expresses the shift from orange to red luminescent region with the addition of Eu^{3+} ions concentration in the host lattice.

Table 7.1. *CIE chromaticity coordinates of singly doped NCMS: Sm^{3+} and doubly doped NCMS: Sm^{3+}/Eu^{3+} phosphors under different excitation wavelengths.*

Sample	CIE chromaticity coordinates different excitation wavelength		
	375 nm	403nm	467 nm
NS3	(0.579, 0.420)	(0.580, 0.418)	(0.581, 0.418)
NSE1	(0.591, 0.407)	(0.589, 0.409)	(0.607, 0.391)
NSE2	(0.597, 0.401)	(0.594, 0.404)	(0.617, 0.382)
NSE4	(0.608, 0.390)	(0.603, 0.395)	(0.625, 0.374)
NSE6	(0.613, 0.386)	(0.609, 0.390)	(0.628, 0.370)
NSE8	(0.618, 0.380)	(0.613, 0.386)	(0.630, 0.368)

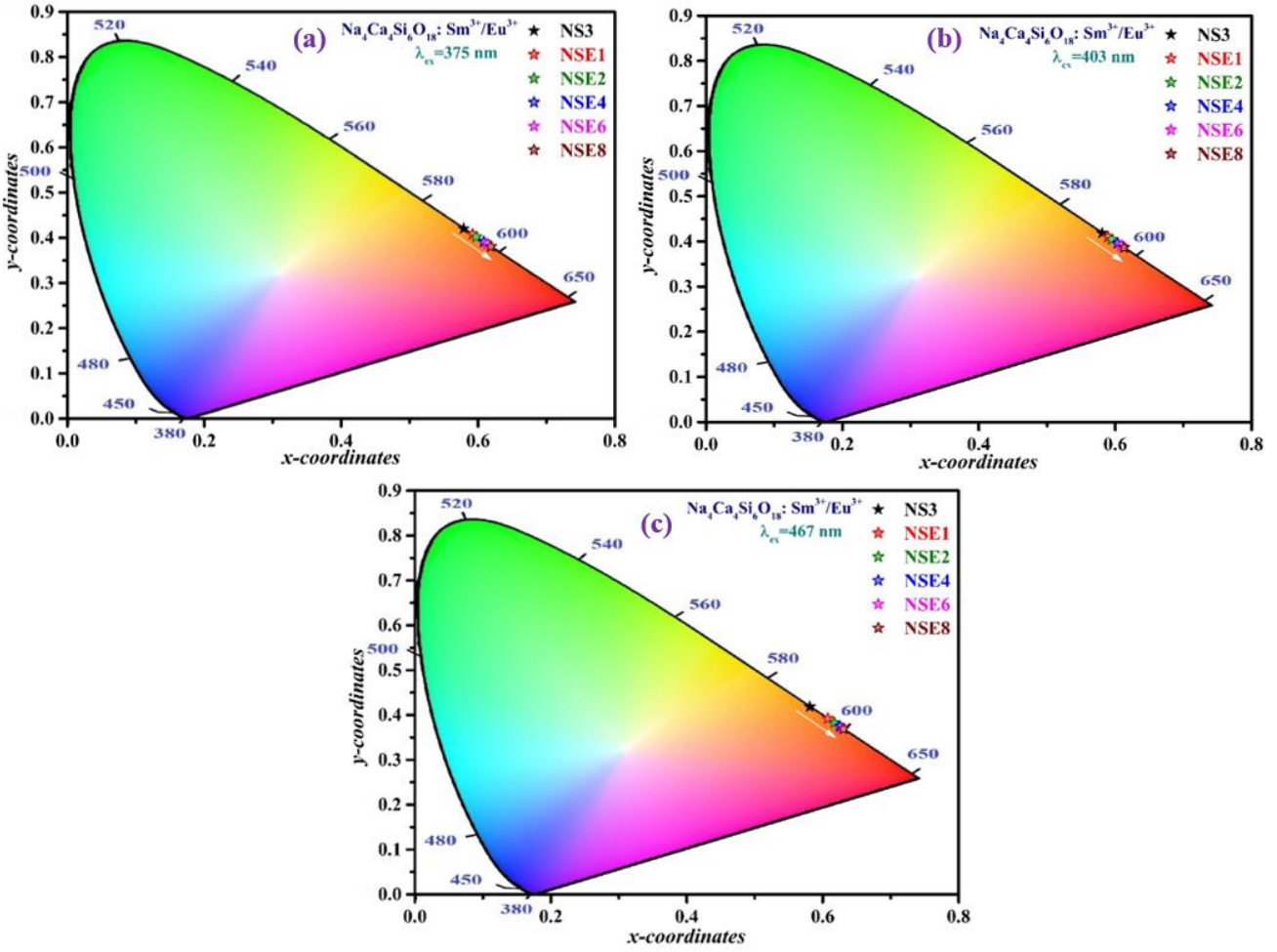

Fig. 7.10. ***(a)*** *CIE chromaticity coordinates of Sm^{3+} doped NCMS phosphor (optimized) and Sm^{3+}/Eu^{3+} biactivated NCMS phosphor under excitation wavelengths λ_{ex}=375 nm* ***(b)*** *λ_{ex}=403 nm* ***(c)*** *λ_{ex}=467 nm.*

In the NCMS: Sm^{3+}/Eu^{3+} bi-activated phosphor, the red shift under 375, 403 and 467 nm excitation wavelength occur due the appropriate energy transfer from Sm^{3+} to Eu^{3+} with increase in the concentration of Eu^{3+} ions. The CIE chromaticity coordinates for NSE8 phosphor found to be close to the available commercialized Y_2O_3: Eu^{3+} (0.647, 0.343) [315]. Fig. 7.11 (a) demonstrates spectral distribution of sunlight (300-1200 nm) at air mass 1.5 Global (AM 1.5G) with the excitation and emission spectrum of NSE8 phosphor at emission wavelength 602 and excitation wavelength at 403 nm. Since, the down-converting materials absorb the shorter wavelength (300-500 nm) and re-emit into higher wavelength, thus down-converting NCMS:Sm^{3+}/Eu^{3+} phosphor may apply directly onto the front surface of solar cell to utilize the

unused part of solar spectrum and can enhance efficiency of solar cell, as represented in Fig. 7.11 (b) [316].

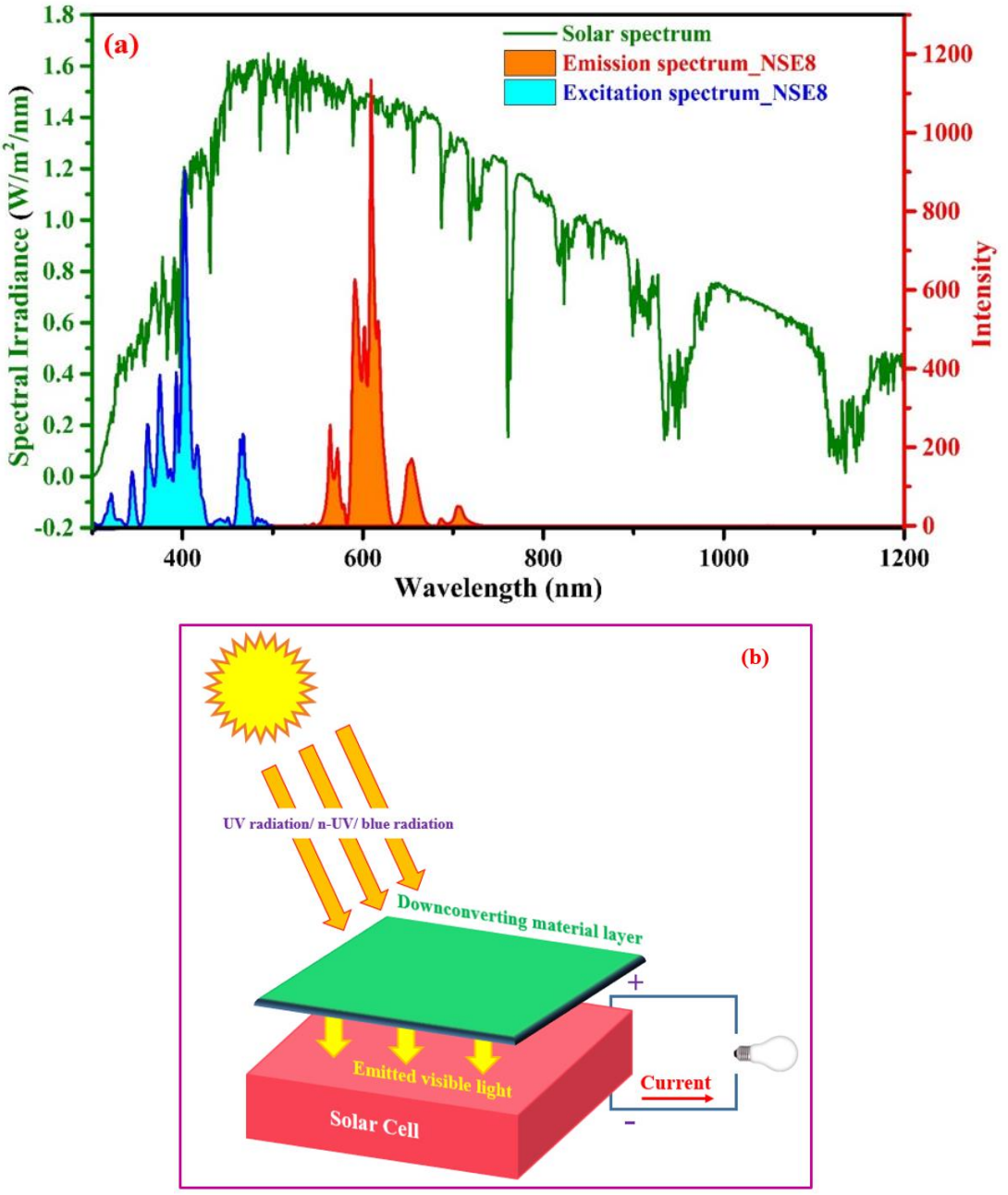

Fig. 7.11. ***(a)*** *The comparative plot for AM 1.5 solar spectrum, excitation and emission spectrum of NSE8 under λ_{em}= 602 nm and λ_{ex}=403 nm, respectively; (b) Schematic representation of solar cell with downconverting material.*

7.3.7. Thermal stability of NCMS: Sm^{3+}/Eu^{3+} phosphor

In order to fabricate devices with high power, exploration of thermal stability of the material is required. Fig. 7.12 (a) depicts the emission plot of NSE1 phosphor with respect to

temperature (ranging from 303 to 463K) measured under 403 nm excitation wavelength in a range of 550 to 750 nm. The emission intensity tends to decline with rise in temperature, and can be observed the emission intensity persist to 77.6 % at 423 K (150 °C) of initial intensity obtained at room temperature (i.e. 30 °C) as shown in the graph inserted in Fig. 7.12 (a).

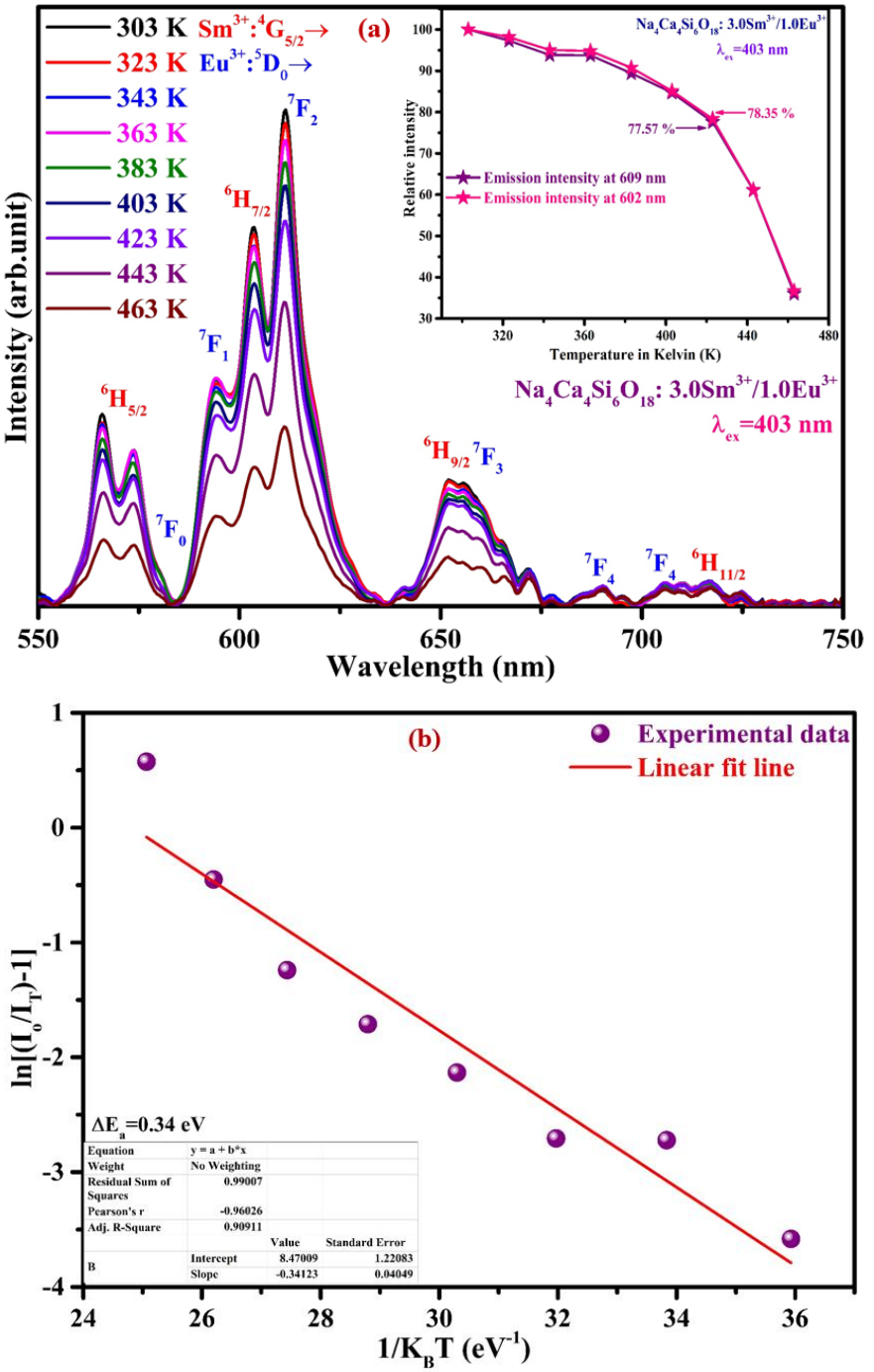

Fig. 7.12. ***(a)*** *Temperature dependent PL spectra of NCMS:3.0Sm^{3+}/1.0Eu^{3+} phosphor under 403 nm excitation wavelength; inset shows the relative intensity vs temperature plot at emission wavelength 602 and 609 nm for NSE1 phosphor under 403 nm excitation wavelength* ***(b)*** *Plot of ln[(I_0/I_T)-1] vs 1/K_BT (eV^{-1}) for NSE1 phosphor.*

Thus, the greater sustainability of integrated emission intensity at 423 K temperature indicates that the phosphor possesses excellent thermal stability [317]. Moreover, the activation energy (ΔE) of as synthesized NSE1 phosphor have been evaluated using the well-known Arrhenius equation [318]:

$$I_T = \frac{I_o}{1+\alpha exp\left(-\frac{\Delta E_a}{K_B T}\right)} \quad (7.12)$$

In the above mentioned formula, α and K_B (Boltzmann's constant=8.617×10^{-5} *eV/K*) are the constants, I_o and I_T denotes to the initial emission intensity and emission intensity at specific temperature (T) in K, respectively. Fig. 7.12 (b) represents the evaluated activation energy (ΔE) as 0.34 *eV* by plotting $ln[(I_o/I_T)-1]$ versus $1/K_BT$ and fitted linearly. In addition, the achieved activation energy of NSE1 phosphor is fairly higher than other phosphors reported earlier [319–321]. Thus, the as-prepared phosphor has shown tremendous thermal stability and motivated to implement in solar cell applications.

7.4. Conclusions

A series of microcrystalline Sm^{3+} activated and Sm^{3+}/Eu^{3+} bi-activated NCMS phosphors have been synthesized by following the high temperature solid state reaction approach. Hexagonal pure phase has been obtained at high temperature and confirmed through x-ray diffraction technique, in which all diffraction patterns are well agreed with the standard JCPDS diffraction pattern. Emission spectra of Sm^{3+} doped NCMS phosphors have been articulated through excited with n-UV light and optimized the Sm^{3+} ions concentration in the host matrix as 3.0 mol%. Furthermore, PL spectra of Sm^{3+}/Eu^{3+} bi-activated phosphor under 375, 403 and 467 nm excitation wavelength revealed the declining intensity of emission peaks associated with Sm^{3+} ion while increment in the peaks related to Eu^{3+} ion with rising in the concentration of Eu^{3+} ion. The decay curve of NCMS: Sm^{3+}/Eu^{3+} phosphors exhibits the decrement with enhancement in the Eu^{3+} ions concentration as a result of energy transfer from the sensitizer (Sm^{3+}) to activator (Eu^{3+}) ions at

403 nm excitation. Based on the aforementioned investigations, the notable chromaticity coordinates, down-converting features of thermally stable NCMS: Sm^{3+}/Eu^{3+} phosphors are highly preferred for solar cell and other optoelectronic applications.

Chapter 8

Summary and future scope of the work

This chapter provides an overview of the pertinent findings and the current status of the research work. The overall results of the thesis are concentrated on the production of thermally stable metasilicate based phosphor owing efficient white light emission along with the color tunability behaviour under UV/n-UV/blue excitation source for optoelectronics applications. The produced phosphor divulges effective luminescent features in a desired spectral region to be anticipated in the w-LEDs and solar cell applications. This chapter also focused on the future scope of research work in a versatile fields.

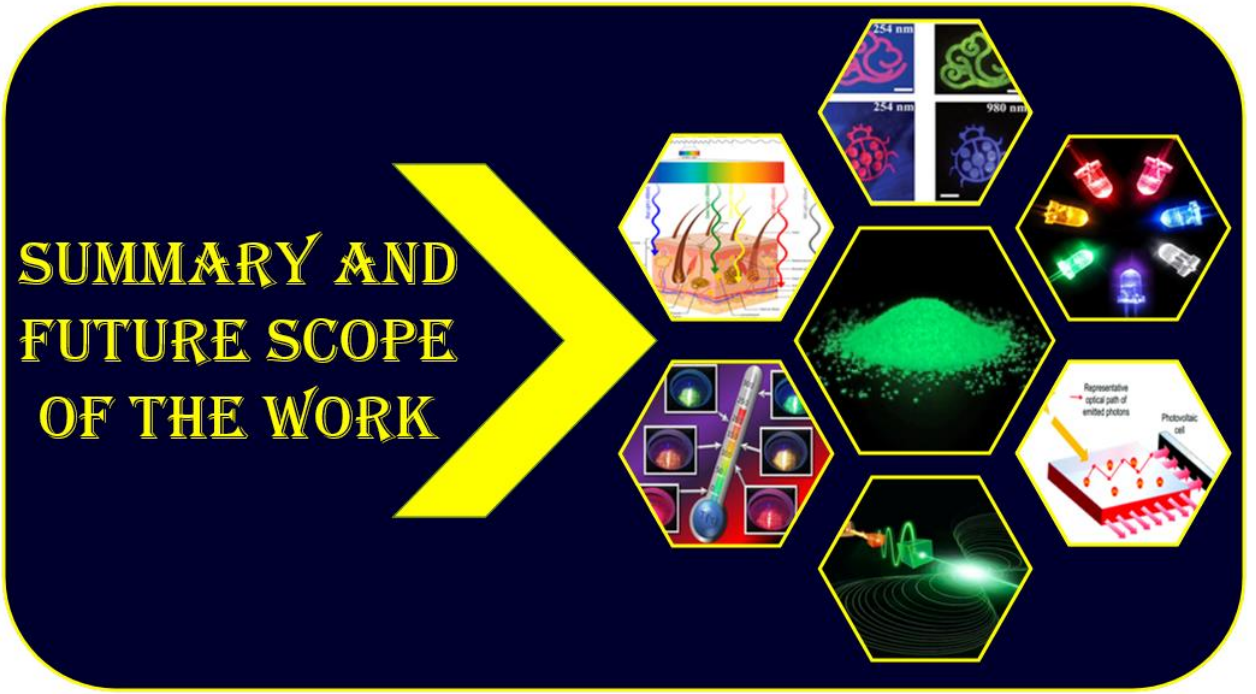

8.1. Summary of the work

The significant focus of this thesis is altogether on the synthesis and analysis of the structural, morphological, optical and luminescence studies of RE^{3+} ions doped $Na_4Ca_4Si_6O_{18}$ micro-phosphors for deployment in the wLED and solar cell applications. The results were investigated with the multiple RE ions and the combination of RE ions (Tb^{3+}, Pr^{3+}, Dy^{3+}, Sm^{3+} and Eu^{3+}) doped in the NCMS phosphor and synthesized using solid state reaction (SSR) method. The noteworthy encouragement on the enhancement of luminescence have been considered and make it functional by varying the dopant ions and its concentration as well as use of co-dopant as an activator ion. Since, it has been discussed in the previous sections that the pc-LEDs have recently received enormous interest owing to their unique features such as better energy efficiency, durability, ecological sustainability and alluring luminous characteristics. In this regard, it is necessary to work on the materials which hold such impressive properties to utilize in phosphor converted based LEDs and in various other applications such as safety signals, thermal sensors, display devices and artificial lighting as well as in efficient energy conversion solar cell applications. The abovementioned attractive features motivated for developing new phosphor and investigate their structural, optical, morphological and photoluminescent properties. Thus, a single phase green emitting Tb^{3+} doped NCMS phosphors under UV/n-UV excitation have been successfully synthesized via SSR approach. Furthermore, either a mixture of green and red phosphors via blue LED chip or a mixture of blue-green-red phosphors via UV/near(n)-UV LED chip can provide effective white light with higher values of CRI and lower CCT values. Therefore, Tb^{3+} activated phosphor can be used as a green component to fabricate white light emitting phosphor converted LEDs. In addition, we have focused on the Pr^{3+} doped intense red emitting NCMS phosphor prepared via SSR synthesis route to develop red component. Pr^{3+} activated NCMS phosphor emits intense red color in order to develop white light with high CRI and low CCT value, since, white light can also be generated via exciting a yellow emitting phosphor with

blue LED to prevent the loss or reabsorption of energy. In general, Dy^{3+} doped phosphors are prominent to emit yellow color. Thus, Dy^{3+} activated NCMS phosphor possesses yellow emission coated on to the blue LEDs to produce white emission. However, white light occurs from yellow phosphor exhibit low CRI and high CCT value which can be mended via including red emitting phosphor. Therefore, Dy^{3+}-Eu^{3+} co-activated red emitting NCMS phosphors have been successfully synthesized. Color tunable behaviour obtained in Eu^{3+} co-activated phosphor under varying excitation wavelength as well as activator ion concentration accomplished by energy transfer process due to the spectral overlap between the emission of Dy^{3+} and excitation of Eu^{3+} ion. Moreover, phosphor materials are essentially embracing in solar cell application to improve the conversion efficiency of existing solar cells by modulating the spectral region. To accomplish the aforementioned objective, Sm^{3+}/Eu^{3+} co-activated NCMS phosphor has been synthesized through SSR route. All the qualitative outcomes led to the conclusion that sodium calcium metasilicate doped with distinct RE ions would be an appropriate candidate for w-LEDs and solar cell applications.

8.1.1. Important findings

To accomplish the investigation begins from synthesis to analysis of $Na_4Ca_4Si_6O_{18}$ phosphor doped with RE^{3+} ions, each step has taken in a systematic manner. Predominantly, the thermal analysis was carried out for which an un-sintered sample of $Na_4Ca_4Si_6O_{18}$ powder was heated to examine the crystallization temperature. The $Na_4Ca_4Si_6O_{18}$ powder was prepared through solid state reaction (SSR) method and by following the thermal results, calcination temperature has been determined. The prepared samples were calcined at 950 °C temperature with the preceding step of 650 °C especially for the removal of water molecules, carbonates and carbon monoxide. Therefore, the samples initially treated at 650 °C for 1 h and then calcined at 950 °C for 3h. Pure phase of NCMS samples was obtained at optimized temperature (950 °C) and confirmed by the XRD pattern which has shown the good agreement with the standard diffraction

JCPDS (card no. 75-1687) data. Hence, the structural properties such as phase purity, crystallinity, crystallite size and strain smeared on the structure for as-prepared NCMS samples (doped with various RE^{3+} ions) have been investigated. Furthermore, all the samples exhibit irregular shape and agglomerated massive particle formation since the samples were prepared abstemiously at high temperature using solid state reaction route.

Moving ahead to explore the photoluminescence properties of NCMS phosphor doped with RE^{3+} ions, the major aspects of the present thesis are summarized as follows:

The luminescence studies of Tb^{3+} activated $Na_4Ca_4Si_6O_{18}$ phosphor at various concentrations excited with UV/n-UV range have been examined. PLE spectra of NCMS: xTb^{3+} (x= 1.0, 3.0, 5.0, 7.0, 9.0 and 11.0 mol%) exhibit strong excitation peaks located at 232 (UV region) and 378 (n-UV region) nm by monitoring the emission wavelength at 542 nm. PL emission observed in two ranges due to the transitions from $^5D_3$ (350-475) and $^5D_4$ (475-650) excited levels to various ^7F_J ground state levels. The emission intensity reduces with an increase in the concentration of dopant ions till 11.0 mol% in the range of 350-475 nm under 232 nm (UV) excitation. The decrease in emission intensity from $^5D_3$ state and increase in the intensity of $^5D_4$ level with an increment in dopant ion concentration is due to cross relaxation. However, the PL intensity under 378 nm (n-UV) excitation wavelength rises up to 9.0 mol% concentration of Tb^{3+} ions and then begin to decrease due to the effect of concentration quenching. The similar effect observed under 232 nm excitation in the wavelength range of 475-650 nm. Hence, the optimized concentration is estimated to be 9.0 mol% for the Tb^{3+} ions doped $Na_4Ca_4Si_6O_{18}$ phosphor. PL spectra and CIE coordinates revealed the tunable blue to green emission by exciting under UV light while intense green emission was obtained via n-UV excitation source. The features mentioned above indicate that Tb^{3+} doped $Na_4Ca_4Si_6O_{18}$ phosphor could be a viable choice to be utilized as a green emitting component in the development of w-LED applications.

Furthermore, the luminescent features of Pr^{3+} doped NCMS phosphor have been investigated in order to develop red emitting phosphor for w-LED applications. The excitation spectrum shows three characteristic peaks in the blue region and the strongest excitation peak emerge at 480 nm ($^3H_4 \rightarrow {}^3P_0$) is used to record the emission spectra of NCMS: Pr^{3+} phosphor. The emission spectrum for 1.0 mol% of Pr^{3+} doped NCMS phosphor depicts the various radiative peaks obtained under 480 nm excitation wavelength with the highest intensity at 611 nm wavelength. The concentration of dopant ion in the host matrix has been finalized at 1.0 mol% due to the effect of concentration quenching phenomenon. Dexter's theory expresses the type of interaction among the dopant ions in NCMS phosphor as dipole-quadrupole interaction. Chromaticity coordinates illustrate the emitting color of the optimized Pr^{3+} doped NCMS phosphor as intense red with the high color purity of 97.0%. Hence, the above-mentioned studies indicate the promising features of thermally stable red emitting Pr^{3+} doped NCMS phosphor for w-LED applications.

Moreover, single phase n-UV excited Dy^{3+} doped NCMS phosphors have been prepared and explored their luminescent features. The excitation spectra observed by fixing emission wavelength at 576 nm and exhibit intense band at 348 nm and various band in UV, near UV and blue spectral regions. The PL spectra manifests three characteristic peaks at 488, 576 and 675 nm under near UV excitation wavelength of 348 nm. The hypersensitive peak yield in the yellow region at 576 nm influenced by the crystal field environment and indicate the luminescence in yellow region. Furthermore, the maximum emission intensity depending on the concentration was achieved at 5.0 mol% of Dy^{3+} ion, beyond which the intensity begins to suppress caused by concentration quenching effect. The CIE coordinates are falling in yellow zone for all concentrations of NCMS phosphor. The average lifetime values for $^4F_{9/2}$ energy level of $Na_4Ca_4Si_6O_{18}$ phosphor under 348 nm excitation are found to be in micro second range. Moreover, the temperature dependent PL emission demonstrates the as-synthesized phosphor's excellent

thermal stability. Based on the aforementioned findings, the NCMS phosphor has great potential to contribute as thermally stable yellow emitting phosphor in the w-LED applications.

In general, the single phase white light generating Dy^{3+} doped phosphors possess low CRI and CCT values. An additional ion required to be incorporated for developing the efficient phosphor with high CRI and low CCT values. Furthermore, Dy^{3+}/Eu^{3+} co-activated NCMS phosphors have been prepared which possess remarkable features such as appropriate CRI and CCT, spectral tunability, excellent colour reproducibility and appealing visual perception. The emission spectra of the optimized NCMS: Dy^{3+} phosphor illustrate strong intense peaks in yellow region and feeble intense peaks in blue and red region under 348 nm excitation wavelength whereas optimized Eu^{3+} doped NCMS phosphor reveals emission in red region under 393 nm excitation wavelength. The codoped NCMS: Dy^{3+}/Eu^{3+} phosphors represent the color tunability by altering the excitation wavelength and with concentration of Eu^{3+} ions. Energy transfer occurs from Dy^{3+} to Eu^{3+} is more prominent and conspicuous under pure Dy^{3+} excitation (348 nm) wavelengths. Under 364 nm excitation, the emission peaks intensity related to Dy^{3+} ions are dominated initially and later by the peaks of Eu^{3+} ions as the concentration of Eu^{3+} ion increases on account of energy transfer from sensitizer to activator ions. Emission peaks appeared due to Eu^{3+} ions were quite intense under 393 nm excitation along with feeble peaks ascribe to Dy^{3+} ions which is due to the comparable excitation wavelengths of both the dopants. However, under the 464 nm excitation wavelength, the dominance of emission peaks corresponding to Eu^{3+} has been observed as the absorption intensity of Eu^{3+} ion is leading in comparison to Dy^{3+}, which substantiate that there is no reverse transfer of energy (i.e. Eu^{3+} to Dy^{3+}). Furthermore, increase in Eu^{3+} emission intensity until 10.0 mol% concentration of Eu^{3+} ions under all the excitation wavelengths and no quenching of emission intensity takes place. Color tunability could be achieved owing to energy transfer between dopant and co-dopant ions by tuning the excitation wavelength and varying the Eu^{3+} ions concentration. The decay plot under 348 nm excitation

expresses the bi-exponential fit with decrement in the decay time with increment in the concentration of activator ion. The Dy^{3+}/Eu^{3+} doubly doped NCMS (NDE1) phosphor shows outstanding thermal stability with higher activation energy demonstrate that this phosphor is the promising candidate for w-LEDs and colour tunable devices.

Furthermore, the photoluminescence properties of a series of microcrystalline Sm^{3+} activated and Sm^{3+}/Eu^{3+} bi-activated NCMS phosphors have been explored for solar cell application. Emission spectra of Sm^{3+} doped NCMS phosphors have been articulated through excited with n-UV light and optimized the Sm^{3+} ions concentration in the host matrix as 3.0 mol%. Furthermore, PL spectra of Sm^{3+}/Eu^{3+} bi-activated phosphor under 375, 403 and 467 nm excitation wavelength revealed the declining intensity of emission peaks associated with Sm^{3+} ion while increment in the peaks related to Eu^{3+} ion with rising in the concentration of Eu^{3+} ion. Considering the intense peaks enumerated at 375, 403, 467 and 393 nm in the excitation spectra, the emission profiles have been monitored in the visible spectral region. Emission peaks positioned at 564, 602, 650 and 714 nm are attained due to the presence of Sm^{3+} ion acts as sensitizer in the host matrix and their intensity drops with simultaneous rise in the Eu^{3+} ions concentration. However, peaks obtained at 579, 591, 609, 653, 686 and 705 nm are due to insertion of Eu^{3+} as an activator ion and upsurges as followed with the concentration of Eu^{3+} ions. Dexter and Schulman express the phenomenon of concentration quenching effect during energy transfer from sensitizers (Sm^{3+}) to activators (Eu^{3+}). Moreover, the decay curve of NCMS: Sm^{3+}/Eu^{3+} phosphors exhibit the decrement with enhancement in the Eu^{3+} ions concentration as a result of energy transfer from the sensitizer (Sm^{3+}) to activator (Eu^{3+}) ions at 403 nm excitation. Based on the aforementioned investigations, the notable chromaticity coordinates, down-converting features of thermally stable NCMS: Sm^{3+}/Eu^{3+} phosphor are highly preferred for solar cell and other optoelectronic applications.

The noteworthy findings discussed in the thesis validate that the $Na_4Ca_4Si_6O_{18}$ phosphor activated with distinct RE ions (dopant/co-dopant) possess extensive use in w-LEDs and solar cell applications.

8.2. Future scope of the work

- To synthesize efficient RE doped metasilicate nanophosphor with optimized shape, size and crystallinity using various synthesis techniques to improve the chemical and optical properties of the materials.
- To synthesize upconversion phosphors using specific RE^{3+} (Er^{3+}, Ho^{3+}, Yb^{3+} and Nd^{3+} etc.) ions in order to explore versatile optoelectronic applications.
- To synthesize phosphors utilizing appropriate flux (KX, NaX and NH_4X etc., where X=halides) to enhance the photoluminescent features.
- To explore the utility of optimized metasilicate phosphors in a variety of applications such as thermal sensing, bio-imaging, photocatalysis, finger printing and counter-anticounterfeiting along with solid state lighting applications.
- Finally, to fabricate the prototype phosphor converted w-LED using UV/n-UV excited RE doped $Na_4Ca_4Si_6O_{18}$ phosphor.

References

[1] Y. Zhuo, J. Brgoch, J. Phys. Chem. Lett. 12 (2021) 764–772.

[2] M.A. Esteso, A.C.F. Ribeiro, S.C. George, A.R. Abraham, A.K. Haghi, T&F Group (2021) 518.

[3] C. Ronda, A. Srivastava, Electrochem. Soc. Interface 15 (2006) 55–57.

[4] T.H. Fereja, A. Hymete, T. Gunasekaran, ISRN Spectrosc. 2013 (2013) 1–12.

[5] P. Chansri, S. Arunrungrusmi, T. Yuji, N. Mungkung, Int. J. Photoenergy 2017 (2017).

[6] M. Souli, M. Reghima, M. Secu, C. Bartha, M. Enculescu, A. Mejri, N. Kamoun-Turki, P. Badica, Superlattices Microstruct. 126 (2019) 103–119.

[7] H.L. Li, Z.L. Wang, J.H. Hao, IOP Conf. Ser. Mater. Sci. Eng. 1 (2009) 012010.

[8] M. Ilhan, I.Ç. Keskin, Dalt. Trans. 47 (2018) 13939–13948.

[9] M. Kumar Mishra, P.M. Mishra, V. Dubey, I. Khan, T. Sachdev, Adv. Mater. Lett. 12 (2021) 1–9.

[10] A.D. Sontakke, A.J. Van Bunningen, F.T. Rabouw, S. Meijers, A. Meijerink, J. Phys. Chem. C 124 (2020) 13902–13911.

[11] R.S. Yadav, Monika, S.B. Rai, S.J. Dhoble, Prog. Solid State Chem. 57 (2020) 100267.

[12] I. Gupta, S. Singh, S. Bhagwan, D. Singh, Ceram. Int. 47 (2021) 19282–19303.

[13] H.W. Chen, J.H. Lee, B.Y. Lin, S. Chen, S.T. Wu, Light Sci. Appl. 7 (2018) 17168.

[14] S.J. Park, B.S. Je, J.W. Jang, M.S. Oh, M.S. Koo, S.J. Yang, H.K. Yang, J. Alloys Compd. 789 (2019) 367–374.

[15] H. Zhang, H. Zhang, A. Pan, B. Yang, L. He, Y. Wu, Adv. Mater. Technol. 6 (2021) 1–26.

[16] Y.C. Lin, M. Karlsson, M. Bettinelli, Top. Curr. Chem. 374 (2016) 374–421.

[17] R.K. Sharma, A.V. Mudring, P. Ghosh, J. Lumin. 189 (2017) 44–63.

[18] J.H. Wi, J.Y. Jung, S.G. Park, Materials 15 (2022) 1–9.

[19] D.R. Taikar, S.J. Dhoble, Optik 261 (2022) 169215.

[20] P.C. De Sousa Filho, J.F. Lima, O.A. Serra, J. Braz. Chem. Soc. 26 (2015) 2471–2495.

[21] J.E. Lowther, Phys. Status Solidi 77 (1976) 359–366.G

[22] C. Yang, Q. Liu, D. Huang, X. Li, X. Zhang, Z. Bai, X. Wang, J. Mater. Sci. Mater. Electron. 30 (2019) 5544–5554.

[23] G.B. Kumar, B.V. Rao, B.C. Babu, G. Hungerford, S.H. Nandyalad, J.D. Santose, Material Research Forum, (2016) 159–189.

[24] S. Nan, F. Hong, H. Xu, J. Dou, G. Liu, X. Dong, J. Wang, W. Yu, J. Mater. Sci. Mater. Electron. 31 (2020) 13688–13695.

[25] L. Robindro Singh, R.S. Ningthoujam, V. Sudarsan, I. Srivastava, S. Dorendrajit Singh, G.K. Dey, S.K. Kulshreshtha, Nanotechnology 19 (2008) 55201.

[26] A. Nadort, J. Zhao, E.M. Goldys, Nanoscale 8 (2016) 13099–13130.

[27] Y. Liu, T. Wang, Z. Tan, J. Meng, W. Huang, Y. Huang, S. Liao, H. Zhang, Ceram. Int. 45 (2019) 6243–6249.

[28] F.K. Fong, M.M. Miller, Chem. Phys. Lett. 10 (1971) 408–411.

[29] R. Cao, T. Chen, Y. Ren, T. Chen, H. Ao, W. Li, G. Zheng, J. Alloys Compd. 780 (2019) 749–755.

[30] J. Shao, J. Yan, X. Li, S. Li, T. Hu, Dye. Pigment. 160 (2019) 555–562.

[31] E.F. Schubert, J.K. Kim, H. Luo, J.Q. Xi, Reports Prog. Phys. 69 (2006) 3069–3099.

[32] M. Cao, Y. Xu, P. Li, Q. Zhong, D. Yang, Q. Zhang, J. Mater. Chem. C 7 (2019) 14412–14440.

[33] M. Loi, A. Villani, F. Paciolla, G. Mulè, C. Paciolla, Antioxidants 10 (2021) 1–35.

[34] T.H. Kim, W. Wang, Q. Li, Front. Chem. Sci. Eng. 6 (2012) 13–26.

[35] B.R. Sharma, Himal. Phys. 6 (2017) 115–118.

[36] A.G. Bispo-Jr, L.F. Saraiva, S.A.M. Lima, A.M. Pires, M.R. Davolos, J. Lumin. 237 (2021) 118167.

[37] C.C. Lin, A. Meijerink, R.S. Liu, J. Phys. Chem. Lett. 7 (2016) 495–503.

[38] J. Cho, J.H. Park, J.K. Kim, E.F. Schubert, Laser Photonics Rev. 11 (2017) 1600147.

[39] P. Tadge, R.S. Yadav, P.K. Vishwakarma, S.B. Rai, T.M. Chen, S. Sapra, S. Ray, J. Alloys Compd. 821 (2020) 153230.

[40] Z.R. Abrams, A. Niv, X. Zhang, J. Appl. Phys. 109 (2011) 114905.

[41] P. Tumram, P.D. Sahare, S. V. Moharil, J. Lumin. 199 (2018) 78–81.

[42] X.Y. Huang, J.X. Wang, D.C. Yu, S. Ye, Q.Y. Zhang, X.W. Sun, J. Appl. Phys. 109 (2011) 1–8.

[43] K. Li, R. Van Deun, Dye. Pigment. 162 (2019) 990–997.

[44] D.C. Yu, X.Y. Huang, S. Ye, M.Y. Peng, Q.Y. Zhang, Sol. Energy Mater. Sol. Cells 101 (2012) 303–307.

[45] J. Day, S. Senthilarasu, T.K. Mallick, Renew. Energy 132 (2019) 186–205.

[46] C. Yen-Chi, H. Woan-Yu, C. Teng-Ming, J. Rare Earths 29 (2011) 907–910.

[47] G. Shao, C. Lou, D. Xiao, J. Lumin. 157 (2015) 344–348.

[48] W.J. Mir, T. Sheikh, H. Arfin, Z. Xia, A. Nag, NPG Asia Mater. 12 (2020) 9.

[49] M.B. de la Mora, O. Amelines-Sarria, B.M. Monroy, C.D. Hernández-Pérez, J.E. Lugo, Sol. Energy Mater. Sol. Cells 165 (2017) 59–71.

[50] M. Dhanalakshmi, R.B. Basavaraj, G.P. Darshan, S.C. Sharma, H. Nagabhushana, Microchem. J. 145 (2019) 226–234.

[51] T.Y. Seong, J. Han, H. Amano, H. Morkoç, 126 (2013) 1.

[52] H. Wu, Z. Sun, S. Gan, L. Li, J. Photochem. Photobiol. A Chem. 368 (2019) 258–262.

[53] C. Ronda, Prog. Electromagn. Res. 147 (2014) 81–93.

[54] A. Dwivedi, M. Srivastava, A. Srivastava, C. Upadhyay, S.K. Srivastava, Sci. Rep. 12 (2022) 1–15.

[55] C.S. McCamy, Color Res. Appl. 17 (1992) 142–144.

[56] M.E. Coltrin, J.Y. Tsao, Sandia Report (2006) 2-38.

[57] J.I. Shim, D.S. Shin, Nanophotonics 7 (2018) 1601–1615.

[58] Z. Lu, Y. Meng, L. Wen, M. Huang, L. Zhou, L. Liao, D. He, Dye. Pigment. 160 (2019) 395–402.

[59] R.M. MacFarlane, J. Lumin. 40–41 (1988) 3–6.

[60] T. Lu, Z. Ma, C. Du, Y. Fang, H. Wu, Y. Jiang, L. Wang, L. Dai, H. Jia, W. Liu, H. Chen, Sci. Rep. 4 (2014) 1–7.

[61] I.I. Fabrikant, H. Hotop, J. Chem. Phys. 128 (2008) 124308.

[62] N. An, F. Xu, Q. Guo, L. Liao, L. Mei, H. Liu, RSC Adv. 10 (2020) 11608–11614.

[63] M. Xia, X. Wu, Y. Zhong, H.T. Bert Hintzen, Z. Zhou, J. Wang, J. Mater. Chem. C 7 (2019) 2927–2935.

[64] H. Ohsato, Y. Takéuchi, I. Maki, Acta Crystallogr. Sect. B 46 (1990) 125–131.

[65] K. Narita, Phosphor handbook, T&F. Group, (2006) 82.

[66] R. Vajtai, Springer Handbook of Nanomaterials, 2013.

[67] M.S.H. Akash, K. Rehman, Essentials of Pharmaceutical Analysis, 2019.

[68] A.W Coats and J.P.Redfern, Analyst. 88 (1963) 906-924.

[69] R. Bottom, Princ. Appl. Therm. Anal. (2008) 87–118.

[70] C. Peninsula, C. Town, S. Africa, 2 (2017) 3–21.

[71] O.O. Olatunji, S.A. Akinlabi, M.P. Mashinini, S.O. Fatoba, O.O. Ajayi, IOP Conf. Ser. Mater. Sci. Eng. 423 (2018) 12175.

[72] M. Shiraishi, M. Inagaki, X-Ray Diffraction Methods to Study Crystallite Size and Lattice Constants of Carbon Materials, Elsevier Ltd, (2003) 161-173.

[73] R. Jenkins, Encycl. Anal. Chem. (2006) 1–20.

[74] J. Martin, M. Beauparlant, J. Lesage, H.T. Van, Powder Diffraction. 27 (2012) 12-19.

[75] L. Henriksen, Radiat. Eff. 11 (1971) 59–59.

[76] U. Holzwarth, N. Gibson, Nat. Nanotechnol. 6 (2011) 534.

[77] A. González, Compr. Biophys. 1 (2012) 64–91.

[78] A. Popelka, S. Zavahir, S. Habib, Morphology Analysis, INC Polymer Science and Innovative Application, 2020 21-68.

[79] L.E. Franken, K. Grunewald, E.J. Boekema, M.C. Stuart, Small 16 (2020) 1906198.

[80] L. Kumari, W.Z. Li, C.H. Vannoy, R.M. Leblanc, D.Z. Wang, Mater. Res. Bull. 45 (2010) 190–196.

[81] N. Ural, Open Geosci. 13 (2021) 197–218.

[82] J.S. Heslop Harrison, C. Energy, F. Linskens, S.B. Heidelberg. (1990) 1–2.

[83] S. Petit, J. Madejova, Fourier Transform Infrared Spectroscopy, 2nd ed., Elsevier Ltd., 2013.

[84] J. Singh, M. Kumar, A. Sharma, G. Pandey, K. Chae, S. Lee, Intech 11 (2016) 13.

[85] A. Escobedo-Morales, I.I. Ruiz-López, M. de L. Ruiz-Peralta, L. Tepech-Carrillo, M. Sánchez-Cantú, J.E. Moreno-Orea, Heliyon 5 (2019) 1–19.

[86] C.R. Wie, Mater, Sci. Eng.:R: Rep. 13 (1994) 1–56.

[87] C. Cao, S. Wei, Y. Zhu, T. Liu, A. Xie, H.M. Noh, J.H. Jeong, Mater. Res. Bull. 126 (2020) 110846.

[88] R.W. Yeung, C.E. Shannon, Source (2010) 3–9.

[89] S. Eaton-Magaña, C.M. Breeding, Gems Gemol. 52 (2016) 2–17.

[90] M.H.V. Werts, Sci. Prog. 88 (2005) 101–131.

[91] A. Nevin, A. Cesaratto, S. Bellei, C. D'Andrea, L. Toniolo, G. Valentini, D. Comelli, Sensors 14 (2014) 6338–6355.

[92] J.P. Creasey, G.C. Tyrrell, Rare-Earth-Doped Mater. Devices IV 3942 (2000) 114.

[93] A. Siwach, D. Kumar, Chem. Phys. Lett. 772 (2021) 138547.

[94] X. Huang, C. He, X. Wen, Z. Huang, Y. Liu, M. Fang, X. Wu, X. Min, Opt. Mater. 95 (2019) 109191.

[95] A.D. Sontakke, K. Biswas, K. Annapurna, J. Lumin. 129 (2009) 1347–1355.

[96] K. Li, D. Zhu, H. Lian, J. Alloys Compd. 816 (2020) 152554.

[97] K. Li, D. Zhu, C. Yue, J. Mater. Chem. C 1 (2022) 6603–6610.

[98] M.H. Weng, R.Y. Yang, Y.M. Peng, J.L. Chen, Ceram. Int. 38 (2012) 1319–1323.

[99] A. Potdevin, G. Chadeyron, R. Mahiou, Chem. Phys. Lett. 490 (2010) 50–53.

[100] M.K. Sahu, J. Mula, J. Am. Ceram. Soc. 102 (2019) 6087–6099.

[101] N.T. Hien, N.X. Ca, N.T. Kien, N.T. Luyen, P. V. Do, L.D. Thanh, H.T. Van, S. Bharti, Y. Wang, N.T.M. Thuy, P.M. Tan, J. Phys. Chem. Solids 147 (2020) 109638.

[102] J. Suresh Kumar, K. Pavani, T. Sasikala, M. Jayasimhadri, K. Jang, L. Rama Moorthy, Oxide-Based Mater. Devices II 7940 (2011) 79401.

[103] F. Liao, Y. Zhang, J. Hu, J. Lumin. 231 (2021) 117791.

[104] S. Zhang, Z. Mu, Y. Lv, L. Fan, Y. Li, G. Ju, Y. Hu, J. Alloys Compd. 729 (2017) 418–425.

[105] T. Yu, L. Wang, X. Yang, W. Ding, Q. Zhang, Electron. Mater. Lett. 15 (2019) 18–26.

[106] G.J. Talwar, C.P. Joshi, S. V. Moharil, S.M. Dhopte, P.L. Muthal, V.K. Kondawar, J. Alloys Compd. 509 (2011) 8742–8747.

[107] H. Ohsato, Y. Takeuchi, I. Maki, 42 (1986) 934–937.

[108] R.X. Fischer, E. Tillmanns, Acta Cryst. 43 (1987) 1852–1854.

[109] D. Singh, S. Sheoran, V. Tanwar, S. Bhagwan, J. Mater. Sci. Mater. Electron. 28 (2017) 3243–3253.

[110] N.H. Jamil, M.M. Al Bakri Abdullah, F.C. Pa, H. Mohamad, W.M.A.W. Ibrahim, J. Chaiprapa, J. Mater. Res. Technol. 9 (2020) 14922–14932.

[111] R. Ullah, B.K. Deb, M. Yousuf, A. Mollah, Int. J. Compos. Mater. 4 (2014) 135–145.

[112] W. Hami, A. Zegzouti, M. Daoud, D. Zambon, M. Rossi, A. Vergara, F. Capitelli, A. Altomare, R. Rizzi, Ceram. Int. 44 (2018) 19184–19190.

[113] P. Biswas, V. Kumar, Kamni, Mater. Today Proc. 28 (2019) 1018–1023.

[114] A. Raja, G. Annadurai, D. Joseph Daniel, P. Ramasamy, J. Alloys Compd. 683 (2016) 654–660.

[115] S. Panda, P. Vinodkumar, U. Madhusoodanan, B.S. Panigrahi, Luminescence 34 (2019) 887–894.

[116] M. Xia, W. Zhao, J. Zhong, P. Shi, Z. Liao, X. Liu, J. Song, L. Luo, L. Ma, Z. Nie, J. Lumin. 220 (2020) 116957.

[117] Y. Jin, Y. Hu, Mater. Res. Bull. 61 (2015) 16–21.

[118] M.K. Sahu, M. Jayasimhadri, J. Lumin. 227 (2020) 117570.

[119] J. Tauc, Mat. Res. Bull. 3 (1968) 37.

[120] Deepali, R. Bisi, Vandana, H. Kaur, M. Jayasimhadri, J. Mater. Sci. Mater. Electron. 32 (2021) 1650–1658.

[121] F. Zhang, Y. Wang, Y. Tao, J. Lumin. 136 (2013) 51–56.

[122] X. Guo, J. He, M. Huang, R. Shi, Y. Chen, Y. Huang, J. Zhang, Z.Q. Liu, Mater. Res. Bull. 118 (2019) 110523.

[123] X. Zhang, H.J. Seo, Mater. Res. Bull. 47 (2012) 2012–2015.

[124] S. Kaur, A.S. Rao, M. Jayasimhadri, V.V. Jaiswal, D. Haranath, J. Alloys Compd. 826 (2020) 154212.

[125] Y. Fu, Y. Hu, J. Mater. Sci. Mater. Electron. 27 (2016) 3867–3872.

[126] S. Devi, A. Khatkar, A. Hooda, V.B. Taxak, P. Boora, P. Dhankhar, S.P. Khatkar, J. Solid State Chem. 288 (2020) 121333.

[127] S.K. Gupta, P.S. Ghosh, A.K. Yadav, N. Pathak, A. Arya, S.N. Jha, D. Bhattacharyya, R.M. Kadam, Inorg. Chem. 55 (2016) 1728–1740.

[128] S. Ray, A. Patra, P. Pramanik, Opt. Mater. 30 (2007) 608–616.

[129] Z. Hao, J. Zhang, X. Zhang, S. Lu, X. Wang, J. Electrochem. Soc. 156 (2009) 193.

[130] Y.C. Fang, X.R. Huang, Y. Der Juang, S.Y. Chu, J. Am. Ceram. Soc. 95 (2012) 1613–1618.

[131] B. V. Ratnam, M. Jayasimhadri, G. Bhaskar Kumar, K. Jang, S.S. Kim, Y.I. Lee, J.M. Lim, D.S. Shin, T.K. Song, J. Alloys Compd. 564 (2013) 100–104.

[132] R.G. Nair, S. Nigam, V. Sudarsan, R.K. Vatsa, V.K. Jain, J. Lumin. 195 (2018) 271–277.

[133] X. Huang, B. Li, H. Guo, J. Alloys Compd. 695 (2017) 2773–2780.

[134] L.G. Van Uitert, J. Electrochem. Soc. 114 (1967) 1048.

[135] H. Kaur, M. Jayasimhadri, Ceram. Int. 45 (2019) 15385–15393.

[136] M. Peddaiah, P. Ankoji, B.H. Rudramadevi, Mater. Today Proc. 46 (2021) 184–189.

[137] C. Liang, H. You, Y. Fu, X. Teng, K. Liu, J. He, Optik 131 (2017) 335–342.

[138] S. Kaur, N. Deopa, A. Prasad, R. Bajaj, A.S. Rao, Opt. Mater. 84 (2018) 318–323.

[139] R. Kokate, G.B. Nair, S.J. Dhoble, H. Jeong, H. Jeong, R. Boddula, V. Singh, Optik 241 (2021) 166633.

[140] J. Yang, H. Wu, L. Song, X. Wang, J. Dong, S. Gan, L. Zou, J. Lumin. 204 (2018) 533–538.

[141] R. Kokate, P. Rohilla, S. Kaur, A.S. Rao, V. Singh, Optik 243 (2021) 167391.

[142] V. Singh, A.R. Kadam, S.J. Dhoble, Optik 243 (2021) 167437.

[143] I. Ahemen, F.B. Dejene, R. Botha, J. Lumin. 201 (2018) 303–313.

[144] F.B. Xiong, H.F. Lin, X.G. Meng, H.X. Shen, W.Z. Zhu, Optik 159 (2018) 102–107.

[145] L.G. Teoh, M.T. Tsai, Y.C. Chang, Y.S. Chang, Ceram. Int. 44 (2018) 2656–2660.

[146] L.X. Lovisa, Y.L.R.L. Fernandes, L.M.P. Garcia, B.S. Barros, E. Longo, C.A. Paskocimas, M.R.D. Bomio, F. V. Motta, Opt. Mater. 96 (2019) 109332.

[147] N. Oshime, Y. Shimizu, H. Takashima, Ceram. Int. 45 (2019) 21011–21014.

[148] H.L. Chen, L.K. Wei, Y.S. Chang, J. Electron. Mater. 47 (2018) 6649–6654.

[149] T. Raghu Raman, Y.C. Ratnakaram, B. Deva Prasad Raju, Optik 225 (2021) 165758.

[150] D. Wei, H.J. Seo, Y. Liu, X. Yang, J. Lumin. 253 (2023) 119488.

[151] H. Kaur, M. Jayasimhadri, J. Am. Ceram. Soc. 104 (2021) 5764–5775.

[152] V. Vidyadharan, K.P. Mani, M.S. Sajna, C. Joseph, N. V. Unnikrishnan, P.R. Biju, Spectrochim. Acta - Part A Mol. Biomol. Spectrosc. 133 (2014) 767–772.

[153] Deepali, M. Jayasimhadri, Luminescence 37 (2022) 1465–1474.

[154] Deepali, M. Jayasimhadri, J. Mater. Sci. Mater. Electron. 33 (2022) 19218–19230.

[155] J. Wang, N. Chen, J. Li, Q. Feng, R. Lei, H. Wang, S. Xu, J. Lumin. 238 (2021) 118240.

[156] M. Ilhan, R. Samur, H. Demirer, F. Mindivan, Metalurgija 54 (2015) 407–410.

[157] J.P. Zuniga, S.K. Gupta, M. Pokhrel, Y. Mao, New J. Chem. 42 (2018) 9381–9392.

[158] N. Mohamed, J. Hassan, K.A. Matori, R.S. Azis, Z.A. Wahab, Z.M.M. Ismail, N.F.

Baharuddin, S.S.A. Rashid, Results Phys. 7 (2017) 1202–1206.

[159] X. Kang, W. Lü, Z. Zhu, C. Jia, J. Rare Earths 41 (2022) 666.

[160] M.Y.A. Yagoub, H.C. Swart, P. Bergman, E. Coetsee, AIP Adv. 6 (2016).

[161] N.N. Zhang, X.X. Jiang, Y.N. Wang, X.R. Pan, Y.Y. Zhang, B. Liu, Y.G. Yang, X.P. Wang, J. Alloys Compd. 932 (2023) 167626.

[162] G. Blasse, Phys. Lett. A 28 (1968) 444–445.

[163] D.L. Dexter, J. Chem. Phys. 21 (1953) 836–850.

[164] E. Sreeja, V. Vidyadharan, S.K. Jose, A. George, C. Joseph, N. V. Unnikrishnan, P.R. Biju, Opt. Mater. 78 (2018) 52–62.

[165] A. Kumar, J. Manam, Mater. Sci. Semicond. Process. 148 (2022) 106828.

[166] L. Li, P. Yang, W. Xia, Y. Wang, F. Ling, Z. Cao, S. Jiang, G. Xiang, X. Zhou, Y. Wang, Ceram. Int. 47 (2021) 769–775.

[167] D. Zeng, Y. Chen, Y. Cai, C. Peng, S. Peng, J. Lumin. 206 (2019) 376–379.

[168] R. Gopal, J. Manam, Ceram. Int. 48 (2022) 30724–30733.

[169] Y.L. Xue, A.Y. Zhang, D. Zhao, R.J. Zhang, J. Zhao, Y.P. Fan, Z. Ma, Optik 179 (2019) 1189–1194.

[170] L. Lakshmi Devi, C. Basavapoornima, S.R. Depuru, V. Venkatramu, C.K. Jayasankar, J. Lumin. 250 (2022) 119059.

[171] Y. Zhang, J. Xu, Q. Cui, B. Yang, Sci. Rep. 7 (2017) 1–12.

[172] Q. Wang, M. Xie, M. Fang, X. Wu, Y. Liu, Z. Huang, K. Xi, X. Min, Molecules 24 (2019) 1296.

[173] P. Sehrawat, R.K. Malik, N. Kumari, M. Punia, S.P. Khatkar, V.B. Taxak, Chem. Phys. Lett. 770 (2021) 138438.

[174] R. Anbarasan, P. Eniya, J. Kalyana Sundar, J. Electron. Mater. 48 (2019) 7686–7695.

[175] K.M. Girish, S.C. Prashantha, H. Nagabhushana, J. Sci. Adv. Mater. Devices 2 (2017) 360–370.

[176] N.P. Singh, N.R. Singh, Y.R. Devi, B. Singh Sh, T.D. Singh, N.R. Singh, N.M. Singh, Solid State Sci. 102 (2020) 106172.

[177] S. Hu, X. Qin, G. Zhou, X. Liu, C. Lu, Z. Xu, S. Wang, J. Alloys Compd. 664 (2016) 304–310.

[178] P.S. Babu, P.P. Rao, S.K. Mahesh, T.L. Francis, T.S. Sreena, Mater. Lett. 170 (2016) 196–198.

[179] M. Song, Y. Liu, Y. Liu, L. Wang, N. Zhang, X. Wang, Z. Huang, C. Ji, J. Lumin. 211 (2019) 218–226.

[180] T. Yu, L. Wang, X. Yang, W. Ding, Q. Zhang, Electron. Mater. Lett. 15 (2019) 18–26.

[181] T. Sivakumar, M. Anna Lakshmi, R. Anbarasan, P. Eniya, S. Vignesh, J. Kalyana Sundar, Mater. Technol. 00 (2021) 1–13.

[182] T. Bongkarn, W. Khiawwangthong, Adv. Mater. Res. 55–57 (2008) 181–184.

[183] I.O. Ali, T.M. Salama, M.S. Thabet, K.S. El-Nasser, A.M. Hassan, Mater. Chem. Phys. 140 (2013) 81–88.

[184] S.N.F. Syed Adam, R. Shamsudin, S.R. Zainuddin, B. Johar, F. Zainuddin, Sains Malaysiana 47 (2018) 1025–1031.

[185] R. Kheshtzar, A. Berenjian, S.M. Taghizadeh, Y. Ghasemi, A.G. Asad, A. Ebrahiminezhad,

Green Process. Synth. 8 (2019) 846–855.

[186] I.M. Alibe, K.A. Matori, H.A.A. Sidek, Y. Yaakob, U. Rashid, A.M. Alibe, M.H.M. Zaid, S. Nasir, M.M. Nasir, J. Therm. Anal. Calorim. 136 (2019) 2249–2268.

[187] K. Munirathnam, K. Mallikarjuna, R. Vijaya, P.C. Nagajyothi, K.R. Reddy, M. Srinivas, J. Rare Earths 40 (2021) 218-225.

[188] R. Mahajan, R. Prakash, S. Kumar, V. Kumar, R.J. Choudhary, D.M. Phase, Optik 225 (2021) 165717.

[189] M. Jayasimhadri, B. V. Ratnam, K. Jang, H.S. Lee, B. Chen, S.S. Yi, J.H. Jeong, L.R. Moorthy, J. Am. Ceram. Soc. 93 (2010) 494–499.

[190] G.R. Revannasiddappa, R.B. Basavaraj, M.S. Rudresha, G. Nagaraju, S. Kumar, N. Sasidhar, Vacuum 184 (2021) 109940.

[191] A.K. Kunti, N. Patra, S.K. Sharma, H.C. Swart, J. Alloys Compd. 735 (2018) 2410–2422.

[192] C. Ma, Y. Wang, J. Zhang, Y. Hu, Z. Zhai, J. Wu, W. Zhou, X. Lv, Spectrochim. Acta - Part A Mol. Biomol. Spectrosc. 254 (2021) 119636.

[193] S. Som, S.K. Sharma, J. Phys. D. Appl. Phys. 45 (2012) 415102.

[194] M.K. Mahata, K. Kumar, V.K. Rai, Spectrochim. Acta - Part A Mol. Biomol. Spectrosc. 124 (2014) 285–291.

[195] M.S. Pathak, N.O. Gopal, N. Singh, M. Mohapatra, J.L. Rao, J.K. Lee, V. Singh, J. Non. Cryst. Solids 500 (2018) 266–271.

[196] C.C. Kee, B.C. Ang, H.S.C. Metselaar, Ceram. Int. 47 (2021) 4803–4812.

[197] L. Yang, M. Fang, L. Du, Z. Zhang, L. Ren, X. Yu, Mater. Res. Bull. 43 (2008) 2538–2543.

[198] S. Katyayan, S. Agrawal, Jom 71 (2019) 2899–2905.

[199] R. Mahajan, S. Kumar, R. Prakash, V. Kumar, R.J. Choudhary, D.M. Phase, J. Alloys Compd. 777 (2019) 562–571.

[200] D. V. Sunitha, H. Nagabhushana, S.C. Sharma, B.M. Nagabhushana, B. Daruka Prasad, R.P.S. Chakradhar, Spectrochim. Acta - Part A Mol. Biomol. Spectrosc. 127 (2014) 381–387.

[201] V. Kumar, M. Manhas, A.K. Bedyal, H.C. Swart, Mater. Res. Bull. 91 (2017) 140–147.

[202] M. Gökçe, D. Koçyiğit, Opt. Mater. 89 (2019) 568–575.

[203] G. Ram Banjare, D.P. Bisen, N. Brahme, C. Belodhiya, Mater. Sci. Eng. B Solid-State Mater. Adv. Technol. 263 (2021) 114882.

[204] T. Manohar, S.C. Prashantha, H.P. Nagaswarupa, R. Naik, H. Nagabhushana, K.S. Anantharaju, K.R.V. Mahesh, H.B. Premkumar, J. Lumin. 190 (2017) 279–288.

[205] N. Basavaraju, S.C. Prashantha, H. Nagabhushana, C. Pratapkumar, C.R. Ravikumar, M.R.A. Kumar, B.S. Surendra, T.R.S. Shekhar, H.B. Premkumar, H.P. Nagaswarupa, Ceram. Int. 47 (2021) 10370–10380.

[206] K. Jha, M. Jayasimhadri, J. Alloys Compd. 688 (2016) 833–840.

[207] M. Sheoran, P. Sehrawat, N. Kumari, S.P. Khatkar, R.K. Malik, Chem. Phys. Lett. 773 (2021) 138608.

[208] G. Ramakrishna, H. Nagabhushana, K. Hareesh, D. V. Sunitha, Solid State Sci. 69 (2017) 56–63.

[209] A. Balakrishna, O.M. Ntwaeaborwa, Sensors Actuators, B Chem. 242 (2017) 305–317.

[210] S. Pradhan, H. Kaur, M. Jayasimhadri, Ceram. Int. 47 (2021) 27694–27701.

[211] R. Mi, J. Chen, Y. Liu, L. Mei, J. Yuan, Y. Xia, Z. Huang, M. Fang, Mater. Res. Bull. 86

(2017) 146–152.

[212] A.K. Bedyal, A.K. Kunti, V. Kumar, H.C. Swart, J. Alloys Compd. 806 (2019) 1127–1137.

[213] S. Liu, J. He, Z. Wu, J.H. Jeong, B. Deng, R. Yu, J. Lumin. 200 (2018) 164–168.

[214] S.K. Hussain, T.T.H. Giang, J.S. Yu, J. Alloys Compd. 739 (2018) 218–226.

[215] G. Zhang, L. Zhao, F. Fan, Y. Bai, B. Ouyang, W. Chen, Y. Li, L. Huang, Spectrochim. Acta - Part A Mol. Biomol. Spectrosc. 223 (2019) 117343.

[216] W.P. Lustig, Z. Shen, S.J. Teat, N. Javed, E. Velasco, D.M. O'Carroll, J. Li, Chem. Sci. 11 (2020) 1814–1824.

[217] B. Li, G. Annadurai, J. Liang, L. Sun, S. Wang, Q. Sun, X. Huang, RSC Adv. 8 (2018) 33710–33716.

[218] W. Wu, Y. Zhang, Y. Zhang, J. Hu, Dalt. Trans. 50 (2021) 5287–5300.

[219] S.K. Hussain, J.S. Yu, RSC Adv. 7 (2017) 13281–13288.

[220] S. Liu, B. Deng, J. Chen, H. Liu, C.S. Zhou, R. Yu, IOP Conf. Ser. Earth Environ. Sci. 295 (2019) 4–7.

[221] J. Deng, H. Zhang, X. Zhang, M.S. Molokeev, J. Qiu, Y. Liu, B. Lei, L. Ma, X. Wang, J. Mater. Chem. C 6 (2018) 4077–4086.

[222] L. Zhang, Y. Xu, X. Wu, S. Yin, H. You, Mater. Adv. 3 (2022) 2591–2597.

[223] Y.L. Yang, J.Y. Yuan, Y.T. Fan, D.Y. Wan, Q.L. Li, J.T. Zhao, Z.J. Zhang, Dalt. Trans. 50 (2021) 11130–11136.

[224] S. Som, P. Mitra, V. Kumar, V. Kumar, J.J. Terblans, H.C. Swart, S.K. Sharma, Dalt. Trans. 43 (2014) 9860–9871.

[225] S.K. Hussain, J.S. Yu, J. Lumin. 183 (2017) 39–47.

[226] K. Mondal, J. Manam, J. Lumin. 195 (2018) 259–270.

[227] Z. Zhang, Y. Wang, J. Zhang, Mater. Lett. 62 (2008) 846–848.

[228] D. Golja, F. Dejene, Chem. Phys. Lett. 741 (2020) 137122.

[229] S. Kaur, A.S. Rao, M. Jayasimhadri, Mater. Res. Bull. 116 (2019) 79–88.

[230] B. Devakumar, P. Halappa, C. Shivakumara, Dye. Pigment. 137 (2017) 244–255.

[231] P. Du, J.S. Yu, J. Alloys Compd. 653 (2015) 468–473.

[232] W. Li, W. Zhang, W. Li, Y. Gan, P. Zhang, J. Mater. Sci. Mater. Electron. 30 (2019) 658–666.

[233] A. Kumar, J. Manam, Opt. Mater. 96 (2019) 109373.

[234] J.S. Revathy, N.S.C. Priya, K. Sandhya, D.N. Rajendran, Bull. Mater. Sci. 44 (2021) 1–8.

[235] A.M. Khachatourian, F. Golestani-Fard, H. Sarpoolaky, C. Vogt, E. Vasileva, M. Mensi, S. Popov, M.S. Toprak, J. Lumin. 169 (2016) 1–8.

[236] C. Wang, J. Jiang, S. Xin, Y. Shi, G. Zhu, J. Lumin. 214 (2019) 116521.

[237] K.M. Girish, S.C. Prashantha, R. Naik, H. Nagabhushana, K.S. Anantharaju, SN Appl. Sci. 1 (2019) 1–9.

[238] Y. Deng, S. Yi, J. Huang, J. Xian, W. Zhao, Mater. Res. Bull. 57 (2014) 85–90.

[239] M. Jiao, Q. Xu, C. Yang, H. You, RSC Adv. 7 (2017) 28647–28654.

[240] W. Wang, J. Li, Z. Zhang, Z. Liu, J. Lumin. 207 (2019) 114–122.

[241] M.A. Mickens, Z. Assefa, J. Lumin. 145 (2014) 498–506.

[242] M. Manca, A. Cannavale, L. De Marco, A.S. Aricò, R. Cingolani, G. Gigli, Langmuir 25 (2009) 6357–6362.

[243] R. Choudhary, S. Koppala, S. Swamiappan, J. Asian Ceram. Soc. 3 (2015) 173–177.

[244] Y. Wu, Y. Yang, B. Liu, M. Hu, X. Min, Y. Wu, Z. Liu, L. Yu, Luminescence 36 (2021) 914–922.

[245] J. Li, Y. Liu, W. Cao, Y. Gao, W. Zhang, X. Lai, Integr. Ferroelectr. 179 (2017) 1–9.

[246] S. Das, A. Amarnath Reddy, S. Surendra Babu, G. Vijaya Prakash, J. Mater. Sci. 46 (2011) 7770–7775.

[247] L. Jiang, C. Chang, D. Mao, J. Alloys Compd. 360 (2003) 193–197.

[248] K. Jha, A.K. Vishwakarma, M. Jayasimhadri, D. Haranath, K. Jang, J. Non. Cryst. Solids 553 (2021) 120516.

[249] A.N. Meza-Rocha, I. Camarillo, R. Lozada-Morales, U. Caldiño, J. Lumin. 183 (2017) 341–347.

[250] M.M. Rodríguez-García, J.A.G. Williams, I.R. Evans, J. Mater. Chem. C 7 (2019) 7779–7787.

[251] J. Xiao, C. Wang, X. Min, X. Wu, Y. Liu, Z. Huang and M. Fang, Nanomaterials, 2020, **10**, 1249.

[252] Y. Il Jeon, L. Krishna Bharat, J.S. Yu, J. Alloys Compd. 620 (2015) 263–268.

[253] H. Kaur, M. Jayasimhadri, Solid State Sci. 122 (2021) 106776.

[254] T. Leow, H. Liu, R. Hussin, Z. Ibrahim, K. Deraman, H.O. Lintang, W.N.W. Shamsuri, J. Rare Earths 34 (2016) 21–29.

[255] P. Du, S. Wu, J.S. Yu, J. Lumin. 173 (2016) 192–198.

[256] V.R. Bandi, B.K. Grandhe, H.J. Woo, K. Jang, D.S. Shin, S.S. Yi, J.H. Jeong, J. Alloys Compd. 538 (2012) 85–90.

[257] T.S. Atabaev, Y.H. Hwang and H.K. Kim, Nanoscale Res. Lett., 2012, **7**, 556.

[258] Y. Ma, S. Fu, Y. Zhao, C. Liu, L. Li, Z. Wang, H. Suo, D. Wang, J. Zhao, P. Li, RSC Adv. 12 (2021) 420–428.

[259] M. Xu, L. Wang, D. Jia, H. Zhao, Phys. Chem. Chem. Phys. 17 (2015) 28802–28808.

[260] A. George, S.K. Jose, A. Jose, C. Joseph, P.R. Biju, Opt. Laser Technol. 151 (2022) 108029.

[261] F. Xu, L. Fang, X. Zhou, H. Xia, J. Zhang, H. Song, B. Chen, Opt. Mater. 108 (2020) 110222.

[262] X.Y. Sun, T.T. Han, D.L. Wu, F. Xiao, S.L. Zhou, Q.M. Yang, J.P. Zhong, J. Lumin. 204 (2018) 89–94.

[263] X. Wu, W. Bai, O. Hai, Q. Ren, F. Lin, Y. Jiao, J. Solid State Chem. 265 (2018) 109–116.

[264] X. Wu, B. Yin, Q. Ren, J. zheng, Y. Ren, O. Hai, J. Alloys Compd. 822 (2020) 153562.

[265] K.N. Kumar, J.S. Kim, M. Cho, J. Shim, B.K. Gupta, M. Kang, J. Alloys Compd. 721 (2017) 554–562.

[266] M. Fhoula, T. Koubaa, M. Dammak, Opt. Laser Technol. 130 (2020) 106352.

[267] R. Vijayakumar, H. Guo, X. Huang, Dye. Pigment. 156 (2018) 8–16.

[268] Z.Y. Wang, B.L. Shen, K.H. Yu, Z. Yang, R.L. Zheng, E.T. Hu, J.J. Zheng, W. Wei, J. Alloys Compd. 791 (2019) 833–838.

[269] K. Jha, A.K. Vishwakarma, M. Jayasimhadri, D. Haranath, J. Alloys Compd. 719 (2017) 116–124.

[270] B. Fan, W. Zhao, L. Han, Appl. Phys. A Mater. Sci. Process. 126 (2020) 1–10.

[271] Y. Guo, B.K. Moon, B.C. Choi, J.H. Jeong, J.H. Kim, Mater. Res. Bull. 88 (2017) 166–173.

[272] H. Patnam, S.K. Hussain, L.K. Bharat, J.S. Yu, Dye. Pigment. 162 (2019) 583–589.

[273] R. Liu, J. Yang, D. Zhao, W. Liu, G. Li, W. Yan, W. Zhang, Inorg. Chem. 60 (2021) 17878–17888.

[274] C. Pareja-Rivera, D. Morett, D. Barreiro-Argüelles, P. Olalde-Velasco, D. Solis-Ibarra, JPhys Energy 3 (2021) 32014.

[275] S. Dutta, T.M. Chen, RSC Adv. 7 (2017) 40914–40921.

[276] S. Razzaq, A. Asghar, C. Lou, H. Diao, S. Huang, Y. Yin, J. Alloys Compd. 907 (2022) 164512.

[277] Y. Tan, Y. Yan, H. Du, X. Hu, G. Li, Y. Kuang, M. Li, D. Guo, Opt. Mater. 85 (2018) 538–544.

[278] M. Yu, H. Xu, Y. Li, Q. Dai, G. Wang, W. Qin, J. Colloid Interface Sci. 559 (2020) 162–168.

[279] J. Sahariya, P. Kumar, A. Soni, Mater. Chem. Phys. 199 (2017) 257–264.

[280] W.J. Ho, S.K. Feng, J.J. Liu, Y.C. Yang, C.H. Ho, Appl. Surf. Sci. 439 (2018) 868–875.

[281] W. Bin Hung, T.M. Chen, Sol. Energy Mater. Sol. Cells 133 (2015) 39–47.

[282] D.C. Yu, S. Ye, M.Y. Peng, Q.Y. Zhang, J.R. Qiu, J. Wang, L. Wondraczek, Sol. Energy Mater. Sol. Cells 95 (2011) 1590–1593.

[283] F. Zhang, Y. Wang, Y. Tao, Mater. Res. Bull. 48 (2013) 1952–1956.

[284] W.J. Ho, Y.T. Shen, Y.J. Deng, C.W. Yeh, R.S. Sue, Thin Solid Films 618 (2016) 141–145.

[285] P. Kumar, Kanika, S. Singh, R. Lahon, A. Gundimeda, G. Gupta, B.K. Gupta, J. Lumin. 196 (2018) 207–213.

[286] W.J. Ho, W. Bin Bai, J.J. Liu, H.P. Shiao, Thin Solid Films 660 (2018) 651–656.

[287] A.R. Kadam, S.J. Dhoble, J. Alloys Compd. 884 (2021) 161138.

[288] P.K. Tawalare, P.D. Belsare, S. V. Moharil, Opt. Mater. 100 (2020) 109668.

[289] K. Jha, M. Jayasimhadri, J. Lumin. 194 (2018) 102–107.

[290] R. Yantake, A. Sidike, T. Yusufu, J. Rare Earths 40 (2022) 390–397.

[291] R. Sagheer, M. Khalil, V. Abbas, Z.N. Kayani, U. Tariq, F. Ashraf, Optik 200 (2020) 163428.

[292] K. Rawat, A.K. Vishwakarma, K. Jha, Mater. Res. Bull. 124 (2020) 110750.

[293] T. Tatarchuk, M. Bououdina, W. Macyk, O. Shyichuk, N. Paliychuk, I. Yaremiy, B. Al-Najar, M. Pacia, Nanoscale Res. Lett. 12 (2017).

[294] J. Zheng, X. Wu, Q. Ren, W. Bai, Y. Ren, M. Wang, O. Hai, Opt. Laser Technol. 122 (2020) 105857.

[295] D. Jiang, L. Geng, S. Zhou, Y. Wang, Inorg. Chem. Commun. 142 (2022) 109668.

[296] Z. Xie, X. Liu, W. Zhao, J. Mater. Sci. Mater. Electron. 31 (2020) 7114–7122.

[297] Z. Wang, P. Li, Z. Yang, Q. Guo, J. Lumin. 151 (2014) 170–175.

[298] F. Zhang, W. Zhang, Z. Zhang, Y. Huang, Y. Tao, J. Lumin. 152 (2014) 160–164.

[299] R.N. Perumal, A.X. Lopez, G. Subalakshmi, Optik 170 (2018) 125–131.

[300] J. Jeong, V.R. Bandi, B.K. Grandhe, K. Jang, H.S. Lee, S.S. Yi, J.H. Jeong, J. Korean Phys. Soc. 58 (2011) 306–310.

[301] S. Kaur, A.S. Rao, M. Jayasimhadri, Ceram. Int. 43 (2017) 7401–7407.

[302] H. Kaur, M. Jayasimhadri, M.K. Sahu, P.K. Rao, N.S. Reddy, Ceram. Int. 46 (2020) 26434–26439.

[303] G. Ramakrishna, H. Nagabhushana, S.C. Prashantha, S.C. Sharma, B.M. Nagabhushana, Spectrochim. Acta - Part A Mol. Biomol. Spectrosc. 136 (2015) 356–365.

[304] M.K. Sahu, M. Jayasimhadri, K. Jha, B. Sivaiah, A.S. Rao, D. Haranath, J. Lumin. 202 (2018) 475–483.

[305] K.B. Morebodi, L. Reddy, A. Balakrishna, L.J.B. Erasmus, H.C. Swart, P.L. Masiteng, Solid State Sci. 134 (2022) 107059.

[306] H.X. Jiang, S.C. Lü, Mater. Res. Bull. 111 (2019) 140–145.

[307] D.L. Dexter, J.H. Schulman, J. Chem. Phys. 22 (1954) 1063–1070.

[308] W.J. Yang, L. Luo, T.M. Chen, N.S. Wang, Chem. Mater. 17 (2005) 3883–3888.

[309] Q. Chen, X. Yang, G. Zhang, Q. Ma, S. Han, B. Ma, Opt. Mater. 111 (2021) 110585.

[310] N.P. Rajesh, G. Subalakshmi, C.K. Jayasankar, Opt. Mater. 85 (2018) 464–473.

[311] X. Min, Z. Huang, M. Fang, Y. Liu, C. Tang, X. Wu, 53 (2014) 6060-6065.

[312] S. Lou, P. Zhang, Y. Chen, Q. Xiong, K. Qiu, Ceram. Int. 47 (2021) 10174–10184.

[313] S. Song, J. Si, J. Zhang, G. Cai, RSC Adv. 9 (2019) 1029–1035.

[314] K. Saidi, M. Dammak, RSC Adv. 10 (2020) 21867–21875.

[315] C. Huang, T. Kuo, T. Chen, Opt. Express. 19 (2011) 238–241.

[316] R. Datt, S. Bishnoi, D. Hughes, P. Mahajan, A. Singh, R. Gupta, S. Arya, V. Gupta, W.C. Tsoi, Sol. RRL 6 (2022).

[317] H. Guo, Q. Shi, K. V. Ivanovskikh, L. Wang, C. Cui, P. Huang, Mater. Res. Bull. 126 (2020) 110836.

[318] S.J. Dai, Dan Zhao, R.J. Zhang, L. Jia, Q.X. Yao, J. Alloys Compd. 891 (2022) 161973.

[319] S. Yi, X. Hu, B. Liang, G. Hu, W. Zhao, Y. Wang, J. Lumin. 207 (2019) 105–113.

[320] J. Wu, C. Liu, H. Jia, Y. Qi, Z. Liu, Y. Hu, F. Feng, J. Lumin. 245 (2022) 118791.

[321] Y. Ding, N. Guo, M. Zhu, W. Lv, R. Ouyang, Y. Miao, B. Shao, Mater. Res. Bull. 129 (2020) 110869.